Study of electron spin relaxation in photo-excited organic molecules towards quantum sensing

山内, 朗生

Study of electron spin relaxation in photo-excited organic molecules towards quantum sensing

Akio Yamauchi

Department of Applied Chemistry

Graduate School of Engineering

Kyushu University

2024

Study of electron spin relaxation in photo-excited organic molecules towards quantum sensing

Author

Akio Yamauchi

Supervisor

Tsuyohiko Fujigaya

Department of Applied Chemistry

Graduate School of Engineering

Kyushu University

December 2024

Acknowledgements

The research in this thesis was conducted under the supervision of Professor Nobuo Kimizuka, Professor Nobuhiro Yanai, and Professor Tsuyohiko Fujigaya at the Department of Applied Chemistry, Graduate School of Engineering, Kyushu University, between April 2019 and March 2025.

I would like to express the sincerest gratitude to Professor Nobuhiro Yanai (The University of Tokyo) for his precious suggestions, valuable discussion. I would also like to thank Professor Nobuo Kimizuka for his helpful suggestions, warm encouragement and reviewing my dissertation. I am also grateful to Professor Tsuyohiko Fujigaya for reviewing my dissertation and taking care of the various matters about relocating the lab.

I am highly appreciative to the Japan Society for the Promotion of Science (JSPS) and JST SPRING for financial support.

I am deeply indebted to Professor Teppei Yamada (The University of Tokyo), Professor Shigenori Fujikawa, Assistant Professor Yoichi Sasaki, Assistant Professor Koki Nishimura, Assistant Professor Takuya Shimajiri, Assistant Professor Bhavesh Parmer, Assistant Professor Shinobu Arikawa, Assistant Professor Masa-aki Morikawa, and Assistant Professor Joseph Ka Ho Hui for their helpful advice and meaningful discussions. I would like to thank Technical Staff Ms. Mamiko Kunitomo, Ms. Kazumi Matsuno, Ms. Ryo Maeda, and Ms. Chihoko Fukakusa for their warm encouragement and support.

I sincerely appreciate the great collaborators, Dr. Tomohiro Uesaka, Dr. Kenichiro Tateishi (RIKEN), Dr. Toshikazu Nakamura, Dr. Mizue Asada, Dr. Motoyasu Fujiwara (IMS), Associate Professor Yuh Hijikata, Assistant Professor Jenny Pirillo (Nagoya University), Professor Ken Onda, Associate Professor Kiyoshi Miyata, Dr. Masaki Saigo, Mr. Tomohiro Ryu (Kyushu University), Professor Yasuhiro Kobori, Assistant Professor Masaaki Fuki, Mr. Ryota Kusumoto, Professor Harumi Sato, and Dr. Nami Ueno (Kobe University) for giving me valuable insights and discussions.

I also wish to thank all the members that I have worked together in Kimizuka laboratory and Yanai laboratory Dr. Biplab Joarder, Dr. Arijit Mallick, Dr. Gurbir Singh, Dr. Baljeet Singh, Dr. Bibhisan Roy, Dr. Manpreet Singh, Dr. Tsubasa Kashino, Dr. Yimin Liang, Dr. Hironori Kouno, Dr. Keisuke Okumura, Dr. Ryosuke Yamamoto, Dr. Saiya Fujiwara, Dr. Yuki Nagai, Dr. Yusuke

Kawashima, Dr. Hirotaka Inoue, Dr. Kana Orihashi, Dr. Naoyuki Harada, Ms. Rena Haruki, Ms. Mika Kinoshita, Mr. Takashi Kobayashi, Mr. Tetsuro Kobayashi, Mr. Keisuke Hayashi, Ms. Risa Iwami, Mr. Donggyu Kwak, Ms. Mio Koharagi, Ms. Mone Sakata, Mr. Yuichiro Seki, Mr. Issei Maruyama, Ms. Kanae Izumi, Mr. Jumpei Kondo, Mr. Kentaro Tanaka, Mr. Ryoichi Tomomatsu, Mr. Tomoyuki Hamachi, Mr. Fumitoshi Matoba, Mr. Shuta Waki, Ms. Naura Fakhira Antariksa, Ms. Hikari Ishihara, Mr. Masanori Uji, Ms. Tae Tamemoto, Mr. Udai Danyoshi, Mr. Yuma Nakashima, Ms. Yuka Masunaga, Mr. Naoto Matsumoto, Mr. Keita Sakamoto, Mr. Kodai Matsumoto, Mr. Reiya Yabuki, Mr. Yuta Yamanaka, Mr. Yuya Watanabe, Mr. Mai Lam Bac, Mr. Wataru Ishii, Ms. Miku Inoue, Mr. Yuta Sawada, Ms. Sakura Nakagawa, Ms. Jiarui Song, and Mr. Toshiteru Tada for their warm supports and discussion.

I would like to thank my friends and all the wonderful works that have supported me emotionally. Finally, I wish to offer special thanks to my family for their financial supports and warm encouragement all through my student life.

Akio Yamauchi
Department of Applied Chemistry
Graduate School of Engineering, Kyushu University
December 2024

Table of Contents

Chapter 2. Development of novel porphyrin-based qubit

Chapter 3. Guest responsive triplet quantum coherence in a flexible MOF towards quantum sensing

Chapter 1. General introduction

1-1. Quantum information science (QIS)

Here comes a second quantum revolution. In the first quantum revolution, methods to observe or measure quantum were developed, such as a nuclear magnetic resonance (NMR) and an electronic microscopy. In addition to detect them, the control of individual quantum systems and the quantum properties such as quantum coherence or quantum entanglement were investigated in the second quantum revolution to enable more powerful applications of quantum information. These fields are called as quantum information science (QIS), which views the quantum particles as units of information.

1-1-1. Quantum bit (qubit)

A bit is a fundamental concept in information theory, and a classical bit is represented by two values, 0 and 1. In QIS, the concept of bits are extended to discrete quantum levels, and two discrete quantum levels are considered as quantum bit (qubit). While a classical bit can only take one state, 0 or 1, a qubit can take not only $|0\rangle$ and $|1\rangle$ but also their superposition state (Figure 1-1).

$$|\psi\rangle = \alpha|0\rangle + \beta|1\rangle \tag{1.1}$$

Where $|\ \rangle$ is "Dirac notation", and α, β are coefficient of each state, respectively. The concept of qubit can be applied for more advanced systems. When the quantum levels are consisted by three or more levels, these are called qutrit of qudit.

There are several candidates of qubits. One of the typical examples of qubit are the two-level systems of anharmonic oscillators, such as ground states and first excited states of atoms or Josephson function on superconducting circuits.[1-2] Other examples of qubit are spins, which has two-level systems of upward and downward spins, such as electron and nuclear spins.[3-7] The superposition state properties of qubits can be applied to quantum technologies.

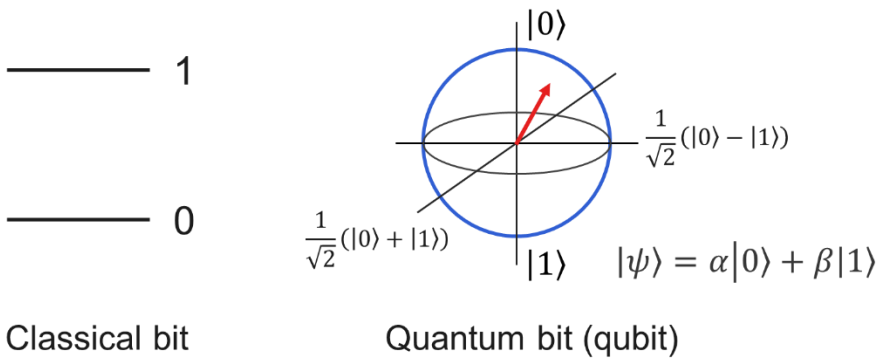

Figure 1-1. The difference of a classical bit and a quantum bit (qubit). A qubit can take $|0\rangle$, $|1\rangle$ and these superposition state while a classical bit can take only 0 or 1.

1-1-2. Quantum technologies

The superposition of states in qubit are called as quantum coherence. The quantum coherence of qubit can be generated by qubit manipulation of electromagnetic waves like microwave, radio wave, or visible light. When there are couplings between qubits, the quantum states of qubits can be mixed to form quantum entanglement, which is also unique to quantum mechanics. Utilizing these quantum phenomena, QIS realize quantum technologies, quantum computing,[1-2] quantum communication,[8-9] and quantum sensing,[10-12] for example. Quantum computing is expected to allow certain types of calculations to be performed faster. Quantum communication is considered to improve the security and the speed of communication. Quantum sensing is anticipated to make sensors having better superior sensitivity and resolution.

1-1-3. Quantum sensing

The quantum coherence are fragile and easily lost by environmental fluctuations, but in other words, they can detect even slight stimulus. In addition, the size of qubits are microscopic (< μm ~ nm), and higher spatial resolution can be expected. By using the quantum properties effectively, quantum sensing obtains an improved sensitivity or resolution comparing to the classical ones (Figure 1-2), which realizes detections of emergent matters and phenomena such as single molecules or dark matters, bringing a large impact for various fields.[13-15]

According to Degen et al., quantum sensing is defined as satisfying one or, in a narrower sense,

all of the following three conditions.[11]

(1) Use quantum objects which have quantized energy levels to measure physical quantities.

(2) Use quantum coherence (superposition states) to measure physical quantities.

(3) Use quantum entanglement to improve the sensitivity and accuracy of measurements, preferably beyond the classical limit.

Although the first two definitions are broader than the last definition and contain systems which are not strictly quantum such as classical wave interference, the quantum sensors belonging the definitions (1) and (2) are often closer to the applications.

The advantages of using quantum entanglement can be explained as follows: One of the typical quantum entangled states are called the Bell state or EPR state[16] and composed of the following four wave functions.

$$|\beta_{00}\rangle = \frac{1}{\sqrt{2}}(|00\rangle + |11\rangle) \tag{1.2}$$

$$|\beta_{01}\rangle = \frac{1}{\sqrt{2}}(|01\rangle + |10\rangle) \tag{1.3}$$

$$|\beta_{10}\rangle = \frac{1}{\sqrt{2}}(|00\rangle - |11\rangle) \tag{1.4}$$

$$|\beta_{11}\rangle = \frac{1}{\sqrt{2}}(|01\rangle - |10\rangle) \tag{1.5}$$

Taking $|\beta_{00}\rangle$ as an example, if the result of the measurement of the first qubit is $|0\rangle$, the state of the other qubit is also found to be $|0\rangle$. On the other hand, if the first qubit is $|1\rangle$, the other qubit is also found to be $|1\rangle$. Thus, by using a quantum entangled state, it is possible to measure all other entangled qubits by measuring the state of one qubit among multiple entangled qubits. The sensitivity of quantum sensing can be improved by utilizing a quantum entanglement, for example, N entangled qubit systems can enhance the sensitivity by a factor of $\sqrt{N}$ in a Ramsey relaxometry protocol, which is a method to determine the resonance frequency of particles in magnetic resonance.[11]

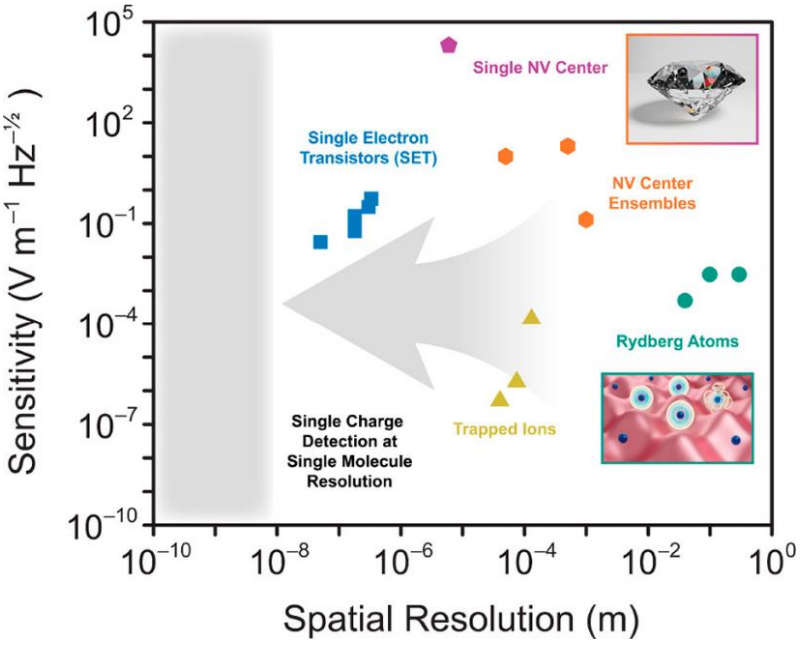

Figure 1-2. Electric field sensitivity (V m^{-1} Hz$^{-1/2}$) of quantum sensor candidates. The gray area is the sensitivity and the spatial resolution desirable for single charge detection. Reproduced with permission from reference 17. Copyright 2021 American Chemical Society.

1-2. Quantum sensors

The qubits used for quantum sensing are called quantum sensors. Quantum sensor should not only work as qubit like other quantum technologies, but also respond to the external environment as a sensor.

1-2-1. Criteria of qubits for quantum sensing

The requirements for a qubit for quantum sensing are as follows (Figure 1-3):

(1) Qubit must be able to be initialized.

(2) Qubit must have sufficiently long coherence time.

(3) Qubit can change its quantum state by interacting with the sensing target.

Firstly, qubits should from well-defined initial state. The quantum coherence is generated from the initialized state, and the degree of the quantum coherence is determined by the purity of initialized state.

For the second requirement, a coherence time, which is a duration of the superposition state, is an important parameter of quantum sensing. Because the quantum coherence will be lost by fluctuations from environments during the qubit manipulation, a long coherence time is desirable to obtain a better sensitivity. For example, the sensitivity (defined as the minimum detectable signal per unit time) of Ramsey interferometry is proportional to the 1/2 to 3/2 power of the coherence time.[11]

Although above two requirements are also essential for other quantum technologies, the third criteria is specific to quantum sensing. The quantum state of qubit such as the energy between quantum levels, the coherent states, or the entangled states should be altered by some stimulus. These changes in the quantum states were readout by qubit manipulation as well as the generation of the quantum coherence.

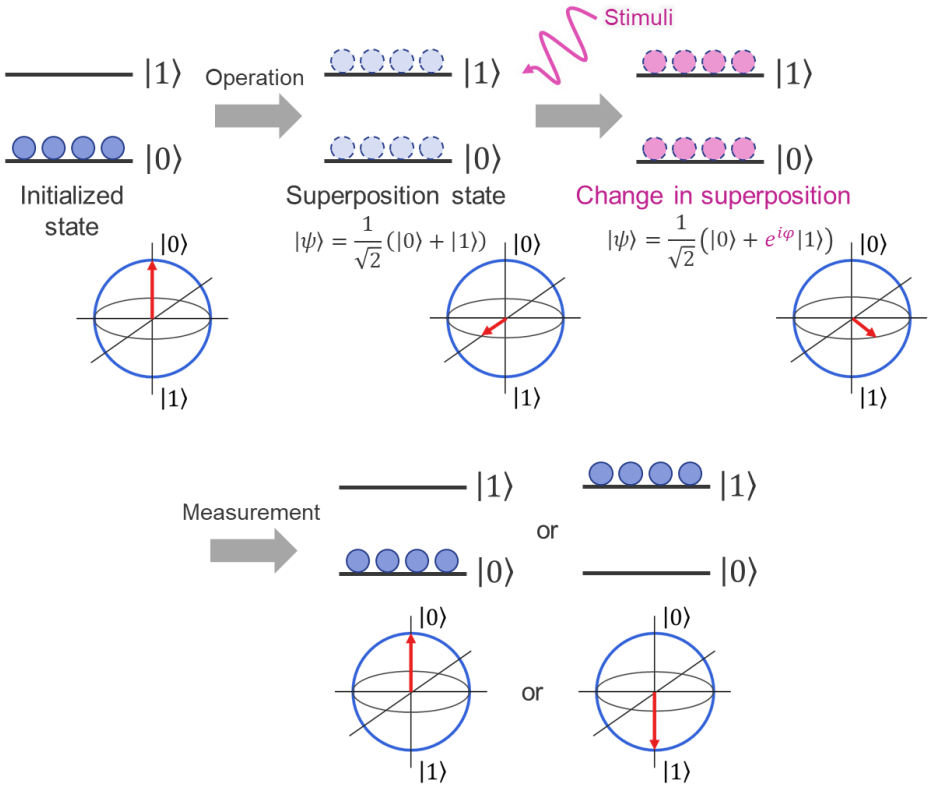

Figure 1-3. Schematic image of an example of quantum sensing. The qubit is firstly initialized to the well-defined state and then converted to the superposition state. The superposition state is altered by external stimulus, which is appeared as the change in the phase of the state. Finally, the superposition state is readout as $|0\rangle$ and $|1\rangle$, and the output varies with the phase.

1-2-2. Electron spin-based qubits

There are several quantum sensors satisfying above mentioned criteria, trapped ions, Rydberg atoms, and atomic vapor, for example.[18-21] Among the various systems, electron-spin based qubits are widely studied as quantum sensors. For typical spin-1/2 systems such as radicals, the downward spins and the upward spins can be considered as $|0\rangle$ and $|1\rangle$, respectively, and these states are controlled by microwave as electron paramagnetic resonance (EPR).

1-2-2-1. Quantum coherence and operation of electron spin-based qubits

The energy difference of these levels are mainly determined by Zeeman splitting, which is an energy splitting derived from the interaction between a spin and a magnetic field. In Bloch sphere, the direction parallel to the orientation of upward and downward spins are defined as z axis (Figure 1-4). For electron spins having a negative gyromagnetic ratio in the thermal equilibrium state, the number (population) of downward spins are larger than that of upward spins, thus the overall spin direction are aligned to antiparallel to the magnetic field. This can works as an initial state of qubits.

When a microwave that resonate the energy difference is applied to spin systems, the directions of spins rotate in a Bloch sphere. For the strong microwave, the flip angle β_p of spins is proportional to the intensity (ω_{nut}) and the length (τ_p) of the microwave:

$$\beta_p = \omega_{nut}\tau_p \tag{1.6}$$

This microwave-induced spin rotation is known as Rabi oscillation (or nutation), and the frequency of the oscillation is Rabi frequency (nutation frequency). Rabi oscillation is often measured to show that the system is available as a qubit. The frequency is determined by the spin multiplicity S and the quantum number of spin sublevels m_s as follows:

$$\omega_{nut} = \frac{g\mu_B B_1}{\hbar}\sqrt{S(S+1) - m_s(m_s \pm 1)} \tag{1.7}$$

Where g, μ_B, B_1, and $\hbar$ are g value of electron spin, Bohr magneton of electron, the microwave field strength, and Dirac constant, respectively. Since the direction of spin rotation can be controlled by the direction of microwave, by proper microwave irradiations, the spins are operated arbitrary in the sphere.

These operations by microwave are correspond to basic logic gate operations. NOT gate is a gate that inverts $|0\rangle$ and $|1\rangle$, and also called as X gate. X gate is represented as follows:

$$\boldsymbol{X} = \begin{pmatrix} 0 & 1 \\ 1 & 0 \end{pmatrix} \tag{1.8}$$

Denote the quantum state in (1.1) as follows:

$$\alpha|0\rangle + \beta|1\rangle \equiv \begin{pmatrix} \alpha \\ \beta \end{pmatrix} \tag{1.9}$$

When X gate is applied to this state, the output of the gate operation is given as

$$\boldsymbol{X}\begin{pmatrix} \alpha \\ \beta \end{pmatrix} = \begin{pmatrix} 0 & 1 \\ 1 & 0 \end{pmatrix}\begin{pmatrix} \alpha \\ \beta \end{pmatrix} = \begin{pmatrix} \beta \\ \alpha \end{pmatrix} \tag{1.10}$$

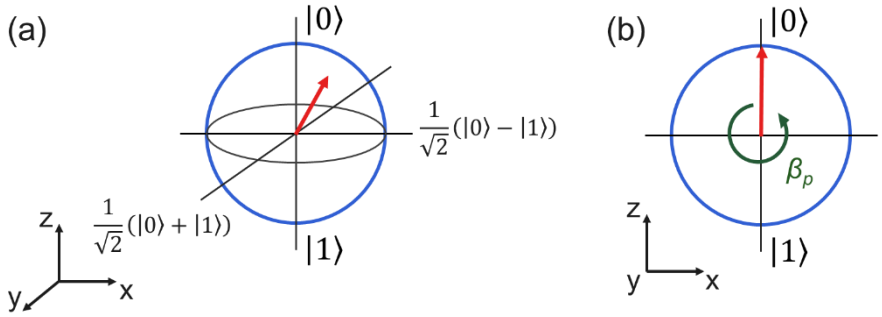

Figure 1-4. (a) Bloch sphere and (b) its operation. When microwave is applied to the system, the spins rotate about an axis in the direction of the microwave irradiation. In (b), microwave is applied from y-axis direction. The flip angle (β_p) and the speed (ω_{nut}) are determined by the length and the strength of the microwave.

Y gate and *Z* gate are represented as

$$\boldsymbol{Y} = \begin{pmatrix} 0 & -i \\ i & 0 \end{pmatrix} \tag{1.11}$$

$$\boldsymbol{Z} = \begin{pmatrix} 1 & 0 \\ 0 & -1 \end{pmatrix} \tag{1.12}$$

These operations are corresponded to rotating the spin by 180 degrees about an axis in each direction on the Bloch sphere (called as π pulse in the field of magnetic resonance).

Hadamard gate (*H*) is an operation to convert $|0\rangle$ and $|1\rangle$ to superposition states.

$$\boldsymbol{H} = \frac{1}{\sqrt{2}}\begin{pmatrix} 1 & 1 \\ 1 & -1 \end{pmatrix} \tag{1.13}$$

When this gate is applied to $|0\rangle$, the output of the gate operation is given as

$$\boldsymbol{H}\begin{pmatrix} 1 \\ 0 \end{pmatrix} = \frac{1}{\sqrt{2}}\begin{pmatrix} 1 & 1 \\ 1 & -1 \end{pmatrix}\begin{pmatrix} 1 \\ 0 \end{pmatrix} = \frac{1}{\sqrt{2}}\begin{pmatrix} 1 \\ 1 \end{pmatrix} \tag{1.14}$$

This means $|0\rangle$ is altered to superposition of $|0\rangle$ and $|1\rangle$.

By adjusting the angle of rotation as in equation (1.6), arbitrary operations are possible for a one-qubit system. Rotation around *x*-axis, *y*-axis, and *z*-axis are written as

$$\boldsymbol{R}_x(\theta) = \begin{pmatrix} \cos\frac{1}{2}\theta & -i\sin\frac{1}{2}\theta \\ -i\sin\frac{1}{2}\theta & \cos\frac{1}{2}\theta \end{pmatrix} \tag{1.15}$$

$$\boldsymbol{R}_y(\theta) = \begin{pmatrix} \cos\frac{1}{2}\theta & -\sin\frac{1}{2}\theta \\ \sin\frac{1}{2}\theta & \cos\frac{1}{2}\theta \end{pmatrix} \tag{1.16}$$

$$\boldsymbol{R}_z(\varphi) = \begin{pmatrix} \exp(-\frac{i}{2}\varphi) & 0 \\ 0 & \exp\frac{i}{2}\varphi \end{pmatrix} \tag{1.17}$$

where θ and φ are rotation angle around *x*-axis or *y*-axis, and *z*-axis, respectively. In EPR measurement, a microwave pulse that is correspond to the quarter rotation in the Bloch sphere ($\pi/2$ pulse) converts the spins aligned in *z*-axis to *xy*-plane, this is equivalent to produce quantum coherence of qubits. For example, quantum coherence is generated by applying $\pi/2$ pulse to $|0\rangle$ around *y*-axis.

$$\boldsymbol{R}_y\left(\frac{\pi}{2}\right)\begin{pmatrix}1\\0\end{pmatrix} = \begin{pmatrix} \cos\frac{1}{4}\pi & -\sin\frac{1}{4}\pi \\ \sin\frac{1}{4}\pi & \cos\frac{1}{4}\pi \end{pmatrix}\begin{pmatrix}1\\0\end{pmatrix} = \frac{1}{\sqrt{2}}\begin{pmatrix}1 & -1\\1 & 1\end{pmatrix}\begin{pmatrix}1\\0\end{pmatrix} = \frac{1}{\sqrt{2}}\begin{pmatrix}1\\1\end{pmatrix} \tag{1.18}$$

Hadamard gate is formed by a combination of $\pi/2$ rotation along *y*-axis and π rotation along *x*-axis.

1-2-2-2. Generation of quantum entanglement

For the operations of two or more qubits, arbitrary operations can be performed by using single qubit gates mentioned above and controlled NOT (CNOT) gate, which is a representative two qubit gate.[22] In CNOT gate operation, one of the two qubits is used as a control qubit while the another is used as a target qubit. When the state of the control qubit is $|0\rangle$, the state of the target qubit is not altered, but when the control qubit is $|1\rangle$, the state of the target qubit is inverted. Thus, CNOT gate is represented as

$$\boldsymbol{CNOT} = \begin{pmatrix} 1 & 0 & 0 & 0 \\ 0 & 1 & 0 & 0 \\ 0 & 0 & 0 & 1 \\ 0 & 0 & 1 & 0 \end{pmatrix} \tag{1.19}$$

where each line means conversions for $|00\rangle$, $|01\rangle$, $|10\rangle$, and $|11\rangle$, respectively. Therefore, $|00\rangle$ and $|01\rangle$ are unchanged by CNOT gate, while $|10\rangle$ and $|11\rangle$ are inverted. Entanglement of qubits can be generated by using $\pi/2$ pulse following CNOT operation. Take $|00\rangle$ as an example, the qubits change as follows:

$$\boldsymbol{R}_{1y}\left(\frac{\pi}{2}\right)\begin{pmatrix}1\\0\\0\\0\end{pmatrix} = \frac{1}{\sqrt{2}}\begin{pmatrix}1&0&-1&0\\0&0&0&0\\1&0&1&0\\0&0&0&0\end{pmatrix}\begin{pmatrix}1\\0\\0\\0\end{pmatrix} = \frac{1}{\sqrt{2}}\begin{pmatrix}1\\0\\1\\0\end{pmatrix} \tag{1.20}$$

$$\boldsymbol{CNOT}\frac{1}{\sqrt{2}}\begin{pmatrix}1\\0\\1\\0\end{pmatrix} = \frac{1}{\sqrt{2}}\begin{pmatrix}1&0&0&0\\0&1&0&0\\0&0&0&1\\0&0&1&0\end{pmatrix}\begin{pmatrix}1\\0\\1\\0\end{pmatrix} = \frac{1}{\sqrt{2}}\begin{pmatrix}1\\0\\0\\1\end{pmatrix} \tag{1.21}$$

where

$$\boldsymbol{R}_{1y}\left(\frac{\pi}{2}\right) = \boldsymbol{R}_{y}\left(\frac{\pi}{2}\right)\otimes\begin{pmatrix}1&0\\0&1\end{pmatrix} = \frac{1}{\sqrt{2}}\begin{pmatrix}1&-1\\1&1\end{pmatrix}\otimes\begin{pmatrix}1&0\\0&1\end{pmatrix} = \begin{pmatrix}1&0&-1&0\\0&0&0&0\\1&0&1&0\\0&0&0&0\end{pmatrix} \tag{1.22}$$

The symbol $\otimes$ means a direct product of the two matrices. Bell state in equation (1.2)-(1.5) can be obtained from above operations. In this sequence, the first π/2 pulse is applied to only the control qubit, meaning selective pulse operation and the different resonance frequency are required for the generation of entanglement.

1-2-2-3. Readout of quantum coherence

The quantum coherence of electron spins can be readout by a microwave (Figure 1-5). Typical way of microwave readout is using pulse sequence called as spin echo (also called as Hahn echo). In the spin echo sequence, firstly the quantum coherence is generated by π/2 pulse, and this quantum coherence is operated by following a π pulse that inverses the direction of spins is applied after a certain time interval τ from the first π/2 pulse. As a result, after a same interval τ from the π pulse, an echo signal is obtained with the information of the coherent state.

In section 1-2-2-1, only a single spin was treated, but there are many spins in the system and the average of the ensemble should be considered. This will be possible by introducing a density operator $\boldsymbol{\rho}$. The density operator is defined as

$$\boldsymbol{\rho} = \overline{|\psi\rangle\langle\psi|} \tag{1.23}$$

where the overbar means the average over the ensemble. For spin-1/2 systems, the density operator are written as

$$\boldsymbol{\rho} = \begin{pmatrix}\rho_0 & \rho_{10}\\ \rho_{01} & \rho_1\end{pmatrix} \tag{1.24}$$

using the populations of each level ρ_0 and ρ_1, and the coherence between two levels ρ_{10} and ρ_{01}. The diagonal part of the density operator shows the population of the system, and the non-diagonal part shows the coherence. The rotation of the density operator is denoted as

$$\boldsymbol{\rho}_f = \boldsymbol{R}_x(\theta)\,\boldsymbol{\rho}_i \boldsymbol{R}_x(-\theta) \tag{1.25}$$

The same is applicable for rotations in other directions. The spin echo sequence is explained using the density operator. Assume the population of $|0\rangle$ is unity in the initial state $\boldsymbol{\rho}_a$, i.e.

$$\boldsymbol{\rho}_a = \begin{pmatrix} 1 & 0 \\ 0 & 0 \end{pmatrix} \tag{1.26}$$

The density operator just after the first π/2 pulse is

$$\boldsymbol{\rho}_b = R_y\left(\frac{\pi}{2}\right)\boldsymbol{\rho}_a R_y\left(-\frac{\pi}{2}\right) = \frac{1}{\sqrt{2}}\begin{pmatrix} 1 & -1 \\ 1 & 1 \end{pmatrix}\begin{pmatrix} 1 & 0 \\ 0 & 0 \end{pmatrix}\frac{1}{\sqrt{2}}\begin{pmatrix} 1 & 1 \\ -1 & 1 \end{pmatrix} = \frac{1}{2}\begin{pmatrix} 1 & 1 \\ 1 & 1 \end{pmatrix} \tag{1.27}$$

The generated coherence rotate in *xy*-plane by Larmor precession and the density operator changes as follows between the interval τ:

$$\boldsymbol{\rho}_c = \boldsymbol{\rho}_b \exp\left\{\left(-i\omega_0 - \frac{1}{T_2}\right)\tau\right\} = \frac{1}{2}\exp\left\{\left(-i\omega_0 - \frac{1}{T_2}\right)\tau\right\}\begin{pmatrix} 1 & 1 \\ 1 & 1 \end{pmatrix} \tag{1.28}$$

where ω_0 is Larmor frequency of each spin and T_2 is spin–spin relaxation time (same as coherence time for electron spin). The value ω_0 is different by spins because of inhomogeneity of local magnetic fields. Therefore, the quantum coherence lost quickly by two factors: magnetic inhomogeneity and spin–spin relaxation, making it difficult to observe quantum coherence directly by a single π/2 pulse. It is possible to vanish the effect due to the inhomogeneous factors by applying spin echo sequence. The density operator after the π pulse is

$$\begin{aligned} \boldsymbol{\rho}_d = \boldsymbol{R}_x(\pi)\boldsymbol{\rho}_c\boldsymbol{R}_x(-\pi) &= \frac{1}{2}\exp\left\{\left(-i\omega_0 - \frac{1}{T_2}\right)\tau\right\}\begin{pmatrix} 0 & -i \\ -i & 0 \end{pmatrix}\begin{pmatrix} 1 & 1 \\ 1 & 1 \end{pmatrix}\begin{pmatrix} 0 & i \\ i & 0 \end{pmatrix} \\ &= \frac{1}{2}\exp\left\{\left(-i\omega_0 - \frac{1}{T_2}\right)\tau\right\}\begin{pmatrix} 1 & 1 \\ 1 & 1 \end{pmatrix} \end{aligned} \tag{1.29}$$

The direction of the precession is inverted in the second interval by the π pulse, and the density operator evolves

$$\begin{aligned} \boldsymbol{\rho}_e = \boldsymbol{\rho}_d \exp\left\{\left(+i\omega_0 - \frac{1}{T_2}\right)\tau\right\} &= \frac{1}{2}\exp\left\{\left(+i\omega_0 - \frac{1}{T_2}\right)\tau\right\}\exp\left\{\left(-i\omega_0 - \frac{1}{T_2}\right)\tau\right\}\begin{pmatrix} 1 & 1 \\ 1 & 1 \end{pmatrix} \\ &= \frac{1}{2}\exp\left(-\frac{2\tau}{T_2}\right)\begin{pmatrix} 1 & 1 \\ 1 & 1 \end{pmatrix} \end{aligned} \tag{1.30}$$

The echo signal is independent to the magnetic inhomogeneity and only depends on the coherence time of the spins.

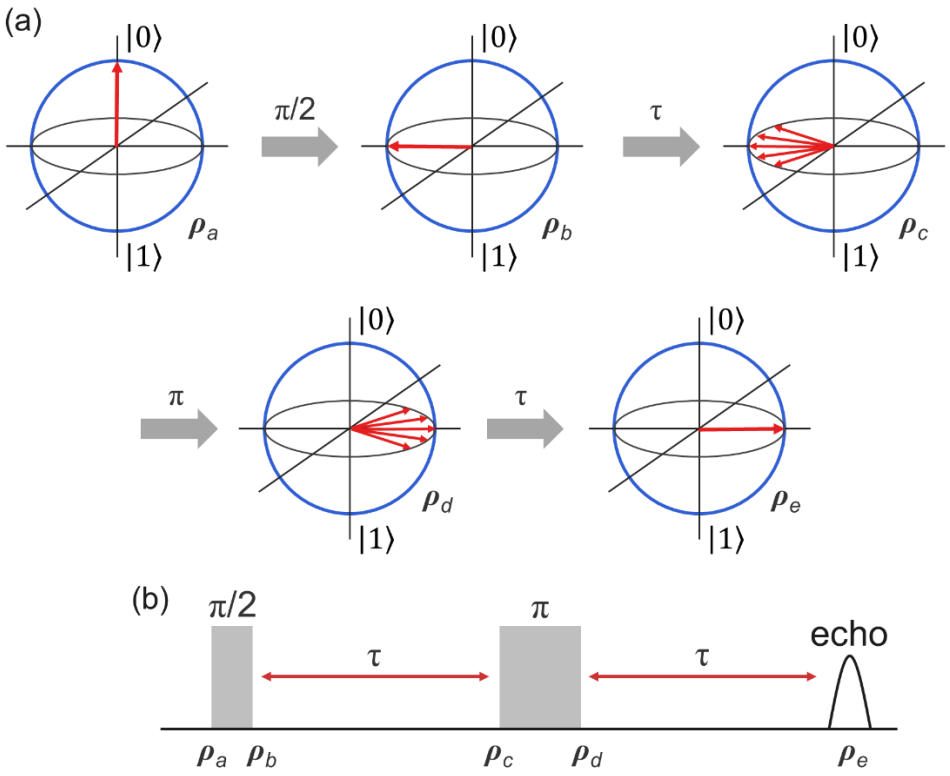

Figure 1-5. (a) Schematic illustration of spin echo method and (b) its pulse sequence. The quantum coherence is generated by π/2 pulse from the initial state. While the quantum coherence is quickly lost by the inhomogeneity of the surrounding environment around the spins, the following a π pulse that inverses the direction of spins and cancel out the effect of the inhomogeneity. As a result, the spins are refocused, and echo signal is obtained after a same interval between π/2 and π pulses.

In addition to a microwave-based method, an optical method is also available for the readout. When the qubits have spin-selective pathways in their dynamics like a fluorescence process, the intensity of the optical emission changes by irradiating a microwave. Therefore, the information about the spins can be readout indirectly from the emission intensity. This method is called as optically detected magnetic resonance (ODMR). The optical readout is preferable in viewpoints of the resolution and the sensitivity since a (visible) light has shorter wavelength and larger energy than a microwave avoiding the scattering and the noise.[23]

1-2-2-3. Coherence times of electron spin-based qubits

The coherence time of electron qubits are approximately correspond to the spin–spin relaxation time T_2. The quantum coherence of electron spins are lost during the pulse sequence manipulation, thus, T_2 should be comparable or longer than the sequence for efficient readout. Since the microwave operation of electron spins needs more than 100 ns, it is difficult to detect the species with short T_2 less than 100 ns. For quantum sensing, the coherence time is a crucial factor of the sensitivity as mentioned above, and the long T_2 of longer than several microseconds is desirable.

1-2-3. Nitrogen-vacancy (NV) centers in nanodiamonds

Among the various qubit systems, defect center-based systems such as the nitrogen-vacancy (NV) centers in diamond, are in a spotlight, because of their long coherence time and ability to sense wide range of targets, for example, temperature, magnetic fields, electric fields (Figure 1-6).[24-25] Moreover, NV centers are capable for optical detection, making it possible to sense the physical quantities in microscopic areas such as cells.

Although NV centers can detects various analytes, they have a difficulty especially in field of chemical sensing, which detects chemical substances like molecules, ions, or atoms. NV centers detects these chemical substances through nuclear magnetic resonance,[26] but there is a limitation. The NV centers in deep part of diamond have long T_2 that reaches order of millisecond at room temperature,[27] but they cannot detect the target due to the nominal interaction to them. On the other hand, the ones close to the surface (~ several nanometers) can sense molecules near the diamond, but the T_2 becomes shorter (around 1 ~ 100 μs, depending on the fabrication method and particle size),[28] and the sensitivity is not necessarily high. They also suffer in their inhomogeneous structure, making the fabrication processes difficult to control the defect positions.

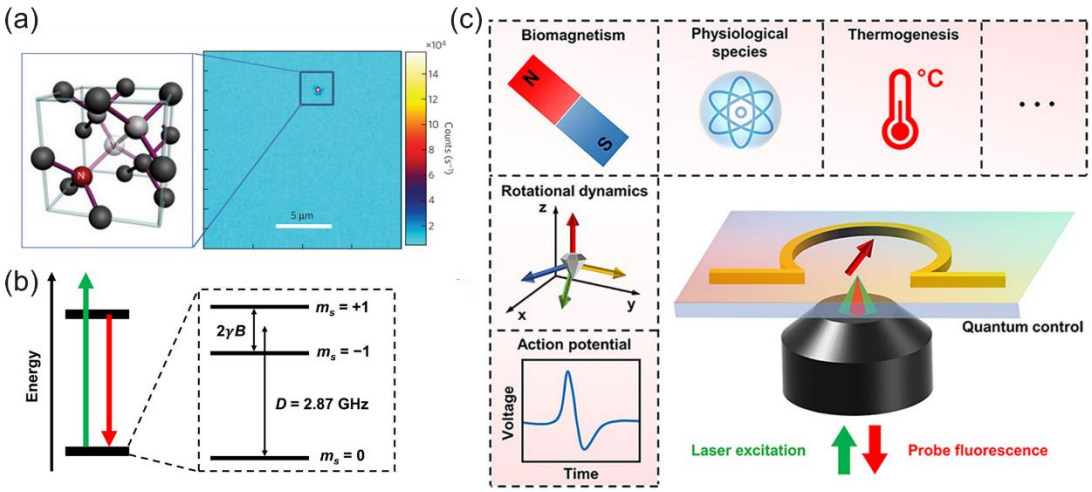

Figure 1-6. (a) Structure and (energy levels) of nitrogen-vacancy (NV) centers of nanodiamonds. (c) Sensing analytes of NV centers. Reproduced with permission from reference 25. Copyright 2021 American Chemical Society.

1-2-4. Molecular qubits

On the contrary, electron spins of molecules (molecular qubits) can interact with analyte molecules directly because of their smaller size (~ nanometer) than defect-based systems.[29-38] In addition, molecules has homogenous structure and their properties as qubits can be precisely tuned by chemical modifications. For example, the coherence time of molecular qubits can be elongated by elaborate control of the structures.[30, 32, 34] Molecular qubits can be broadly divided into two types: paramagnetic metal ion-based systems (Figure 1-7a) and organic molecule-based systems. The former ones utilize metal complex as qubit. There are variety of combination of the central metal ion and the organic ligand, giving high degrees of tunability.[29, 31, 39-40] The latter ones are consisted by free radicals (Figure 1-7b) or photoexcited spins in organic molecules (Figure 1-7c).[30, 32-35, 38] Opposite to metal ion-based qubits which generally contain heavy metal atoms, organic systems is composed from light atoms that does not enhance the decoherence by spin–orbit coupling between electron spin qubits and molecular orbitals. Hence, longer coherence times exceeding 1 μs is sometimes observed for organic molecule-based qubits even at room temperature, while the reports of quantum coherence of metal ion-based systems were quite limited at ambient temperature.[30, 32, 37]

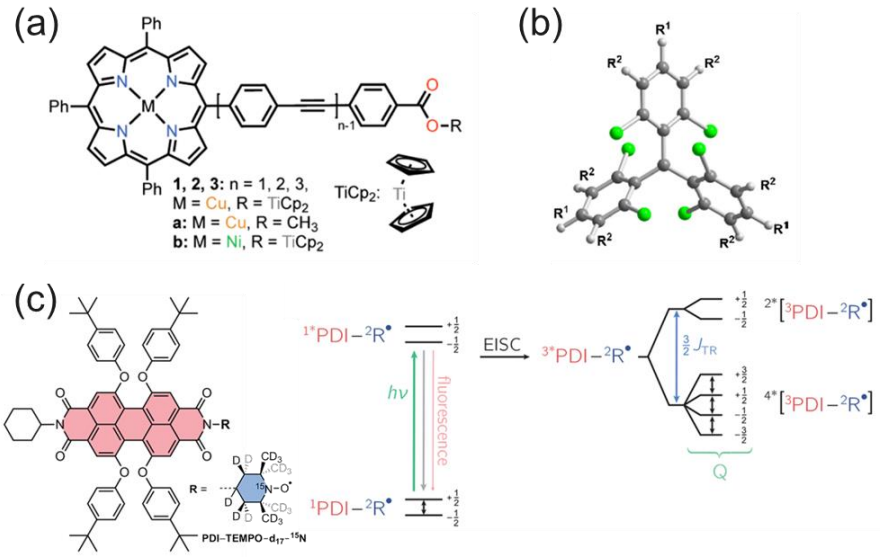

Figure 1-7. Examples of molecular qubits. (a) Molecular qubit consisted of metal complexes. (b) Organic radical-based molecular qubit. (c) Molecular qubit using spins generated by photoexcitation. Reproduced with permission from reference 31, 30, and 32. Copyright 2021 American Chemical Society. Copyright 2018 John Wiley & Sons. Copyright 2023 American Chemical Society.

1-2-5. Metal-organic frameworks (MOFs) as platform for quantum sensing

Major molecular qubit systems were evaluated in frozen glasses,[31] crystals,[41] and films,[30] but these systems are not suitable for molecular sensing because of their low guest accessibilities. Molecular qubit can work not only at bulk systems but also at porous systems like metal-organic frameworks (MOFs) and covalent-organic frameworks (COFs).[42-44] MOF is a porous material that consisted by metal ions and organic ligands. MOFs are excellent scaffolds of molecular qubit systems, especially for quantum sensing applications (Figure 1-8). The rigid frameworks of MOFs are helpful to suppress a spin relaxation due to the molecular motions. The strictly controlled structure permits the orientation of the qubits to be aligned. Furthermore, the porous structure and its tunability of MOF ensures the selective encapsulation of analyte guest molecules, this can be a superiority over other porous materials.

There are several ways to introduce molecular qubits into MOFs. Most popular way is to incorporate molecular qubits as ligands.[33, 36, 38] This method is appliable for various qubit systems

such as metal complexes, organic radicals, and photoexcited spins. Since the position and the orientation of ligand can be predicted from the topology of the MOF, these parameters of qubits are also controlled easily. Other way is using the metal centers as qubits.[45] Paramagnetic metal ions such as coppers can work as qubit. Accommodation of qubits as guests is also possible. The first way need the chemical modification of the coordination site to qubits, but the latter ways do not need the pre-modifications of qubits. In all cases, all parts of MOFs other than qubits should be consisted with diamagnetic species, which do not enhance the spin relaxation.

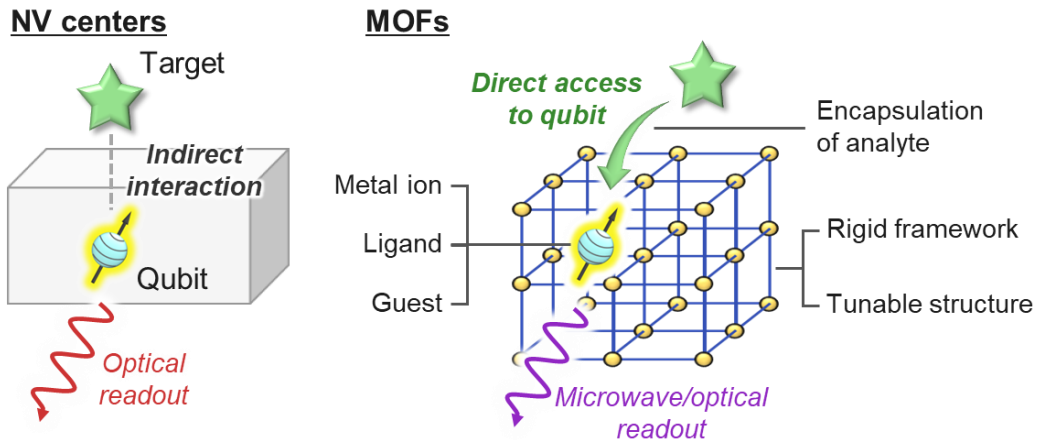

Figure 1-8. The advantages of MOF-based quantum sensing systems and the comparison to NV centers. MOF-based systems allow more direct interaction between the qubits and the analytes than NV centers. MOF-based systems also have high freedom of the structure, the topology, and the qubit species enabling sophisticated tuning of the systems.

1-3. Spin polarization in molecular qubits

1-3-1. Spin polarization

The difference in number of upward spins and that of downward spins divided by that of total spins are called as spin polarization. The polarization P is formed by following equation using population of each sublevels $N_{\uparrow}$, $N_{\downarrow}$.

$$P = \frac{N_{\uparrow} - N_{\downarrow}}{N_{\uparrow} + N_{\downarrow}} \tag{1.31}$$

The polarization expresses the percentage of available spins of whole spins. This is an important parameter of quantum sensing since this largely affects the sensitivity. The initial state is converted to the coherent state by qubit operations, but the efficiency of the quantum coherence generation is proportional to the spin polarization of the initial state (Figure 1-9). In other words, to create pure superposition state of spins, the generation of the spin polarization is required.

In a thermal equilibrium state, the spin polarization is written as follows:[46]

$$P = \tanh\frac{\gamma h B}{4\pi k_B T} \tag{1.32}$$

Where γ, h, B, k_B, and T are a gyromagnetic ratio of electron spins, Planck constant, magnetic field, Boltzmann constant, and temperature, respectively. The spin polarization of electron spin is around 0.07 % under 300 mT (~ 9 GHz) at room temperature. Thus, most part of spins do not work as qubits using thermalized spins at ambient condition.

When the spins are in the quantum entangled state, the requirement of spin polarization become more stringent than non-entangled qubit. For instance, consider an entangled qubit-pair consist by two spins. If one of the spins is not spin-polarized, the well-defined entangle state will not be formed unless the directions happen to coincide. Thus, the number of available entangled pairs in n-qubit system are proportional to the nth power of the polarization P, and the spin polarization should be close to unity to use the entanglement efficiently.

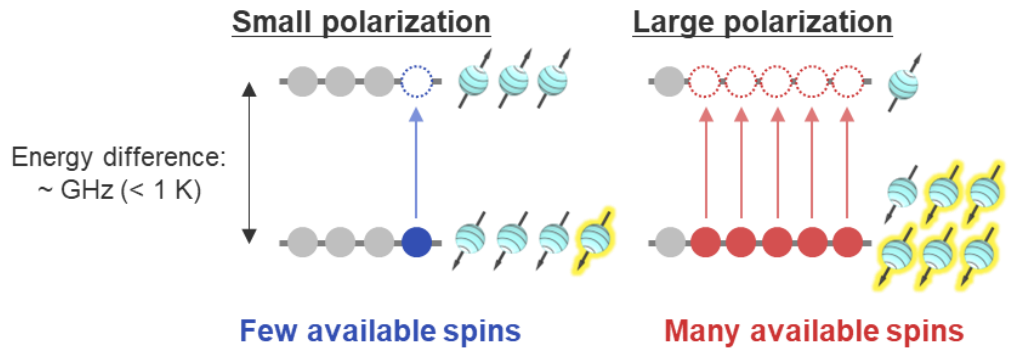

Figure 1-9. The relationship between the spin polarization and the availability of the qubits. When the spin polarization is small, only small amount of the spins are available while large part of the spins can work when the spin polarization is large. Because the energy difference between the energy levels is much smaller than the thermal energy at room temperature, a cryogenic condition or a non-equilibrium state are required to obtain large polarization.

1-3-2. Spin-selective intersystem crossing (ISC)

On of the ways to obtain large spin polarization at room temperature is utilizing spin-selective pathways of molecules. Some molecules are known to generate spin-polarized electron spins in their triplet states by spin-selective the intersystem crossing (ISC) from the singlet state (Figure 1-10a).[47-49] The selectivity of the ISC is determined by the anisotropy of the spin–orbit coupling of the molecule. For pentacene, which is typical chromophore that shows the spin-selective ISC, the population of each triplet sublevel are $P_x : P_y : P_z = 0.76 : 0.16 : 0.08$, respectively, and the spin polarization exceeds 70 %.[47]

1-3-3. Singlet fission (SF)

Singlet fission (SF) is a phenomenon that generates two triplet excitons from one singlet exciton between two close chromophores (Figure 1-10b).[50] While the most hitherto research about SF focused on the application of solar cells since the efficiency can overcome the previous theoretical limit,[51-53] the use for qubits are recently proposed.[54-56] In SF, the energy of S_1 state is firstly shared in two molecules to from singlet character triplet pair (^{1}TT). This ^{1}TT is converted to two triplet excitons directly or quintet character triplet pair (^{5}TT) with $S = 2$ as an intermediate

state of SF process. The spin conversion during ^{1}TT and ^{5}TT are spin-selective, so polarized spins can be obtained in the quintet sublevels.

The four spins in the ^{5}TT state strongly coupled, and there are entanglement among these electron qubits, allowing the improvement of the sensitivity. In addition, high spin of $S = 2$ increase the Rabi frequency, reducing the operation time of microwave. Furthermore, the information about ^{5}TT state can be readout optically as fluorescence from S_1 through triplet-triplet annihilation, which is reverse SF process.

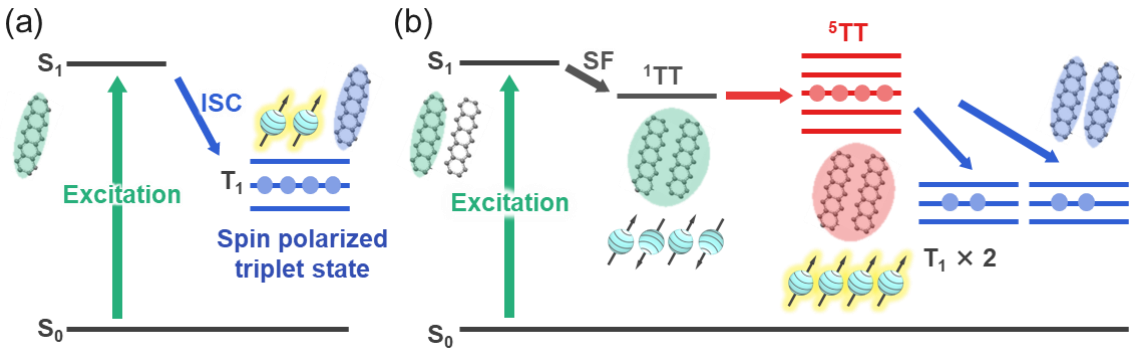

Figure 1-10. Schematic images of (a) spin-selective intersystem crossing (ISC) and (b) singlet fission (SF). In (a), the anisotropic spin–orbit coupling induce the spin-selective intersystem crossing, resulting the spin polarization in the triplet state. In (b), firstly singlet triplet pair (^{1}TT) is generated from singlet excited state (S_1) and converted to quinte triplet pair (^{5}TT) to form spin polarization.

1-3-4. EPR of triplet state

The EPR spectra of triplet state is obtained by calculating the energies of the states from Hamiltonian. The Hamiltonian of triplet is given as[57]

$$\boldsymbol{H}_T = \boldsymbol{H}_{Zeeman} + \boldsymbol{H}_{ZFS} \tag{1.33}$$

Each term can be written with spin operators formed by 3×3 Pauli matrices.

$$\hat{\boldsymbol{S}}_x = \frac{1}{\sqrt{2}}\begin{pmatrix} 0 & 1 & 0 \\ 1 & 0 & 1 \\ 0 & 1 & 0 \end{pmatrix} \tag{1.34}$$

$$\hat{\boldsymbol{S}}_y = \frac{1}{\sqrt{2}}\begin{pmatrix} 0 & -i & 0 \\ i & 0 & -i \\ 0 & i & 0 \end{pmatrix} \tag{1.35}$$

$$\widehat{\boldsymbol{S}}_z = \begin{pmatrix} 1 & 0 & 0 \\ 0 & 0 & 0 \\ 0 & 0 & -1 \end{pmatrix} \tag{1.36}$$

The spin operator are summarized as

$$\widehat{\boldsymbol{S}} = \begin{pmatrix} \widehat{\boldsymbol{S}}_x \\ \widehat{\boldsymbol{S}}_y \\ \widehat{\boldsymbol{S}}_z \end{pmatrix} \tag{1.37}$$

The first term is Zeeman interaction and given as

$$\boldsymbol{H}_{Zeeman} = g\mu_B B\widehat{\boldsymbol{S}}_Z \tag{1.38}$$

using g factor and Bohr magneton μ_B. The second term is a from zero-field splitting (ZFS) interaction which is described the later section. The Hamiltonian is denoted as follows by using ZFS parameters D and E that determines the strength of the interaction:

$$\begin{aligned} \boldsymbol{H}_{ZFS} &= \begin{pmatrix} \widehat{\boldsymbol{S}}_{x'} & \widehat{\boldsymbol{S}}_{y'} & \widehat{\boldsymbol{S}}_{z'} \end{pmatrix} \begin{pmatrix} -D/3+E & 0 & 0 \\ 0 & -D/3-E & 0 \\ 0 & 0 & 2D/3 \end{pmatrix} \begin{pmatrix} \widehat{\boldsymbol{S}}_{x'} \\ \widehat{\boldsymbol{S}}_{y'} \\ \widehat{\boldsymbol{S}}_{z'} \end{pmatrix} \\ &= \widehat{\boldsymbol{S}}^T \boldsymbol{R}(\alpha,\beta,\gamma)^T \boldsymbol{D} \boldsymbol{R}(\alpha,\beta,\gamma) \widehat{\boldsymbol{S}} \end{aligned} \tag{1.39}$$

where $S_{x'}$, $S_{y'}$, $S_{z'}$ are spin operators in the molecular frame, $\boldsymbol{D}$ is ZFS tensor, and $\boldsymbol{R}$ (α, β, γ) is a rotation matrix, respectively.

$$\boldsymbol{D} = \begin{pmatrix} -D/3+E & 0 & 0 \\ 0 & -D/3-E & 0 \\ 0 & 0 & 2D/3 \end{pmatrix} \tag{1.40}$$

$$\boldsymbol{R}(\alpha,\beta,\gamma) = \begin{pmatrix} \cos\gamma & \sin\gamma & 0 \\ -\sin\gamma & \cos\gamma & 0 \\ 0 & 0 & 1 \end{pmatrix} \begin{pmatrix} 1 & 0 & 0 \\ 0 & \cos\beta & \sin\beta \\ 0 & -\sin\beta & \cos\beta \end{pmatrix} \begin{pmatrix} \cos\alpha & \sin\alpha & 0 \\ -\sin\alpha & \cos\alpha & 0 \\ 0 & 0 & 1 \end{pmatrix} \tag{1.41}$$

The rotation angles of α, β, γ are Euler angles and $\boldsymbol{R}^T$ is a transpose matrix of $\boldsymbol{R}$, respectively. Since the ZFS is an interaction based on the molecular axis, it needs to convert the spin operators to the laboratory frame. The energy levels (E_T) and EPR spectrum are calculated by diagonalizing the Hamiltonian as in Figure 1-11.

$$\boldsymbol{H}_T|T_n\rangle = \boldsymbol{E}_T|T_n\rangle \tag{1.42}$$

$|T_n\rangle$ represents the eigenstates of triplet state and n = +1, 0, -1 are characters of their sublevels, respectively. Because the Hamiltonian is orientation-sensitive, the spectra of random-orientated sample is broaden as powder pattern.

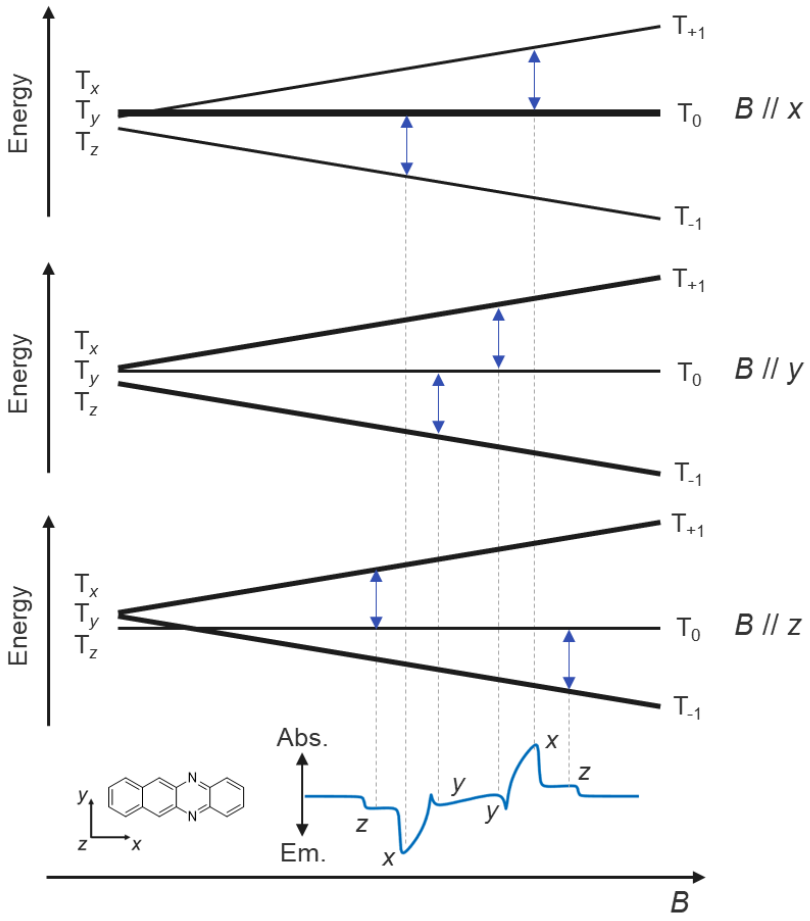

Figure 1-11. The energy diagram of triplet sublevels against the magnetic field. The energies of sublevels (T_x, T_y, and T_z) split to high-field basis (T_{+1}, T_0, T_{-1}) depending on the orientation to the magnetic field. Simulated EPR spectrum of diazatetracene in chapter 3 is also shown. The parameters of $P_x : P_y : P_z = 1.0 : 0 : 0$, $D = 1610$ MHz, and $E = -160$ MHz were used.

1-3-5. EPR of quintet triplet pair

The EPR spectra of quintet state is also obtained from the Hamiltonian written as below.[51]

$$\boldsymbol{H}_{TT} = \boldsymbol{H}_{TTZeeman} + \boldsymbol{H}_{TTZFS} + \boldsymbol{H}_{TTex} \tag{1.43}$$

The first two terms are similar to triplet, and the third term is related to the exchange coupling J.

$$\boldsymbol{H}_{TTZeeman} = \mu_B B(g_1\hat{\boldsymbol{S}}_{1Z} + g_2\hat{\boldsymbol{S}}_{2Z}) \tag{1.44}$$

$$\boldsymbol{H}_{TTZFS} = \hat{\boldsymbol{S}}_1{}^T\boldsymbol{R}_1{}^T\boldsymbol{D}_1\boldsymbol{R}_1\hat{\boldsymbol{S}}_1 + \hat{\boldsymbol{S}}_2{}^T\boldsymbol{R}_1{}^T\boldsymbol{D}_2\boldsymbol{R}_1\hat{\boldsymbol{S}}_2 \tag{1.45}$$

$$\boldsymbol{H}_{TTex} = -2J\hat{\boldsymbol{S}}_1\hat{\boldsymbol{S}}_2 \tag{1.46}$$

$\hat{\boldsymbol{S}}_i = (\hat{\boldsymbol{S}}_{ix}, \hat{\boldsymbol{S}}_{iy}, \hat{\boldsymbol{S}}_{iz})$ are the spin operators for the individual i-th triplet ($i = 1, 2$) and defined as follows using a 3×3 identity matrix $\hat{\mathbf{1}}$:

$$\widehat{\boldsymbol{S}}_{1x} = \widehat{\boldsymbol{S}}_x \otimes \widehat{\mathbf{1}} \tag{1.47}$$

$$\widehat{\boldsymbol{S}}_{1y} = \widehat{\boldsymbol{S}}_y \otimes \widehat{\mathbf{1}} \tag{1.48}$$

$$\widehat{\boldsymbol{S}}_{1z} = \widehat{\boldsymbol{S}}_z \otimes \widehat{\mathbf{1}} \tag{1.49}$$

$$\widehat{\boldsymbol{S}}_{2x} = \widehat{\mathbf{1}} \otimes \widehat{\boldsymbol{S}}_x \tag{1.50}$$

$$\widehat{\boldsymbol{S}}_{2y} = \widehat{\mathbf{1}} \otimes \widehat{\boldsymbol{S}}_y \tag{1.51}$$

$$\widehat{\boldsymbol{S}}_{2z} = \widehat{\mathbf{1}} \otimes \widehat{\boldsymbol{S}}_z \tag{1.52}$$

These operators are applicable for low-field systems ($|++\rangle$, $|+0\rangle$, $|+-\rangle$, …), and to apply the spin operators for high-field systems, the conversion to the high-field basis ($\left|\,{}^1TT_0\right\rangle$, $\left|\,{}^3TT_{+1}\right\rangle$, $\left|\,{}^3TT_0\right\rangle$, $\left|\,{}^3TT_{-1}\right\rangle$, $\left|\,{}^5TT_{+2}\right\rangle$, $\left|\,{}^5TT_{+1}\right\rangle$, $\left|\,{}^5TT_0\right\rangle$, $\left|\,{}^5TT_{-1}\right\rangle$, and $\left|\,{}^5TT_{-2}\right\rangle$) by the conversion matrix.

$$\widehat{\boldsymbol{S}}_{high\ field} = \boldsymbol{U}\widehat{\boldsymbol{S}}\boldsymbol{U}^{\boldsymbol{T}} \tag{1.53}$$

where

$$\boldsymbol{U} = \begin{pmatrix} 0 & 0 & -1/\sqrt{3} & 0 & 1/\sqrt{3} & 0 & -1/\sqrt{3} & 0 & 0 \\ 0 & 0 & 0 & 0 & 0 & -1/\sqrt{2} & 0 & 1/\sqrt{2} & 0 \\ 0 & 0 & 1/\sqrt{2} & 0 & 0 & 0 & -1/\sqrt{2} & 0 & 0 \\ 0 & 1/\sqrt{2} & 0 & -1/\sqrt{2} & 0 & 0 & 0 & 0 & 0 \\ 0 & 0 & 0 & 0 & 0 & 0 & 0 & 0 & 1 \\ 0 & 0 & 0 & 0 & 0 & 1/\sqrt{2} & 0 & 1/\sqrt{2} & 0 \\ 0 & 0 & 1/\sqrt{6} & 0 & 2/\sqrt{6} & 0 & 1/\sqrt{6} & 0 & 0 \\ 0 & 1/\sqrt{2} & 0 & 1/\sqrt{2} & 0 & 0 & 0 & 0 & 0 \\ 1 & 0 & 0 & 0 & 0 & 0 & 0 & 0 & 0 \end{pmatrix} \tag{1.54}$$

By diagonalizing the Hamiltonian, the energies (E_{TT}) and EPR spectrum are obtained.

$$\boldsymbol{H}_{TT}\left|{}^mTT_n\right\rangle = \boldsymbol{E}_{TT}\left|{}^mTT_n\right\rangle \tag{1.55}$$

$|T_n\rangle$ represents the eigenstates of the triplet pair. m = 1, 3, 5, and n = 0 (for m = 1), -1, 0, +1 (for m = 3), -2, -1, 0, +1, +2 (for m = 5) are characters of their sublevels, respectively. Similar to the triplet, the spectrum shows powder pattern.

1-4. Spin relaxation and spin interactions

The generated spin polarization is not in equilibrium, in other words it is temporal. Thus, the polarization is lost over time as well as the quantum coherence. These loss of spin information are called as spin relaxation and related to the interactions between spins or their surrounding environments.[58-59] The suppression of spin relaxation and the utilization the spin interactions are important for quantum sensing.

1-4-1. Spin–lattice relaxation

A spin–lattice relaxation is a relaxation of a spin polarization (Figure 1-12a). The population of spin-polarized state return to the thermal equilibrium state with the time constant of a spin–lattice relaxation time (T_1). Because the spin polarization is formed as a longitudinal arrow aligned to the z-axis in Bloch sphere, a spin–lattice relaxation is called as a longitudinal relaxation. Using the magnetization (the overall spin orientation), spin–lattice relaxation process is written as follows:[60]

$$M_z(t) = (M_z(0) - M_0)\exp\left(-\frac{t}{T_1}\right) + M_0 \tag{1.56}$$

where $M_z(t)$, $M_z(0)$, and M_0 are longitudinal magnetization at time t, initial longitudinal magnetization, and longitudinal magnetization in thermal equilibrium state, respectively. The magnetization is oriented parallel to the z-axis and its magnitude approaches to the that in equilibrium state.

An inversion recovery (uses π pulse for the first pulse) or a saturation recovery (uses π/2 pulse for the first pulse) pulse sequences are typical methods for evaluation of T_1 (Figure 1-12c). In these sequences, the first pulse invert (or saturate) the longitudinal magnetization to create non-equilibrium state. The operated magnetization goes back to the equilibrium state due to the spin–lattice relaxation. This transient magnetization of z-component is readout by a π/2 pulse (In actual cases, the spin echo sequence is often used for readout instead of single π/2 pulse). By changing the interval between two pulses, the magnetization just before π/2 pulse is also altered, and the time constant of the signal intensity recovery corresponds to the T_1.

The density operator in the thermal equilibrium state is formed by using the thermal spin polarization P_{eq}.

$$\boldsymbol{\rho}_{eq} = \begin{pmatrix} \frac{1}{2} + P_{eq} & 0 \\ 0 & \frac{1}{2} - P_{eq} \end{pmatrix} \tag{1.57}$$

The spin-lattice relaxation process in density matrix is written as

$$\boldsymbol{\rho}(t) = \left(\boldsymbol{\rho}(0) - \boldsymbol{\rho}_{eq}\right) \exp\left(-\frac{t}{T_1}\right) + \boldsymbol{\rho}_{eq} \tag{1.58}$$

Consider an inversion recovery sequence for the state in equation (1.26), the density operator just after the first π pulse is

$$\boldsymbol{\rho}_b = \boldsymbol{R}_x(\pi)\boldsymbol{\rho}_a\boldsymbol{R}_x(-\pi) = \begin{pmatrix} 0 & -i \\ -i & 0 \end{pmatrix}\begin{pmatrix} 1 & 0 \\ 0 & 0 \end{pmatrix}\begin{pmatrix} 0 & i \\ i & 0 \end{pmatrix} = \begin{pmatrix} 0 & 0 \\ 0 & 1 \end{pmatrix} \tag{1.59}$$

The evolution of the density operator between τ is

$$\boldsymbol{\rho}_c = \left(\boldsymbol{\rho}_b - \boldsymbol{\rho}_{eq}\right) \exp\left(-\frac{\tau}{T_1}\right) + \boldsymbol{\rho}_{eq} = \begin{pmatrix} -\frac{1}{2} - P & 0 \\ 0 & \frac{1}{2} + P \end{pmatrix} \exp\left(-\frac{t}{T_1}\right) + \boldsymbol{\rho}_{eq} \tag{1.60}$$

The remaining pulses are same as spin echo and the echo intensity is proportional to the population. Since the population converges to thermal equilibrium by the time constant of T_1, it is possible to obtain T_1 by plotting the echo intensity against the interval τ.

Spin interactions such as spin–orbit coupling and dipolar–dipolar spin coupling usually enhance the spin–lattice relaxation.[58, 61] To reduce these effects, molecules with heavy metal atoms or locally distributed electron spins should be avoided.

1-4-2. Spin–spin relaxation

Similar to a spin–lattice relaxation, a spin–spin relaxation is a relaxation of a quantum coherence (Figure 1-12b). The quantum coherence return to zero with the time constant of a spin–spin relaxation time (T_2). Since the quantum coherence of electron qubit is expressed as a transverse arrow aligned to the *xy*-plane in Bloch sphere, a spin–spin relaxation is called as a transverse relaxation. The magnetization in *xy*-plane is converted to zero as follows:[60]

$$M_{xy}(t) = M_{xy}(0)\exp\left(-\frac{t}{T_2}\right) \tag{1.61}$$

where $M_{xy}(t)$ and $M_{xy}(0)$ are transverse magnetization at time *t* and initial transverse magnetization, respectively.

At the first moment just after the quantum coherence is generated, the orientation of all spins are aligned in *xy*-plane, and spins start to rotate in *xy*-plane by Larmor oscillation. The precession

frequencies of each spin are slightly different each other due to the difference in the local environments. Then the phase of each spin become inhomogeneous over time, and overall magnetization is diminished. Therefore, the information about the quantum coherence is lost in the spin–spin relaxation process.

Similar to the T_1 measurement, the T_2 can be measured by modifying the pulse interval (Figure 1-12d). As shown in equations (1.26)-(1.30), the T_2 is evaluated by varying the intervals between the π/2 pulse and the π pulse, and between the π pulse and the detection in the spin echo sequence. The obtained echo intensity is decreased by increasing the interval because the longer interval induce the spin–spin relaxation process more. T_2 is estimated as the decay constant of echo intensity against the interval τ.

The spin–lattice relaxation process is involved in the spin–spin relaxation process, and T_2 is generally shorter than T_1. The relationship between T_2 and T_1 (and other factors) can approximately be written as follows for organic molecules:[30, 43]

$$\frac{1}{T_2} = \frac{1}{2T_1} + \frac{1}{T_{ee}} + \frac{1}{T_{en}} \tag{1.62}$$

where T_{ee} and T_{en} are relaxation time constant induced from electron–electron spin coupling and electron–nuclear spin coupling (hyperfine coupling), respectively. To elongate coherence time T_2, the tuning of each term is essential. Note that the latter two factors also contributes spin–lattice relaxation process, so suppression of these factors are also important for the elongation of T_1.

Since the relaxation times contain the information of these factors, the environment around qubits can be estimated from their relaxation properties. For example, when the relaxation is dominated by the hyperfine coupling due to the nuclear spins around qubits, the concentration of the species can be calculated from the relaxation time of qubits.[43] This method is called as relaxometry.

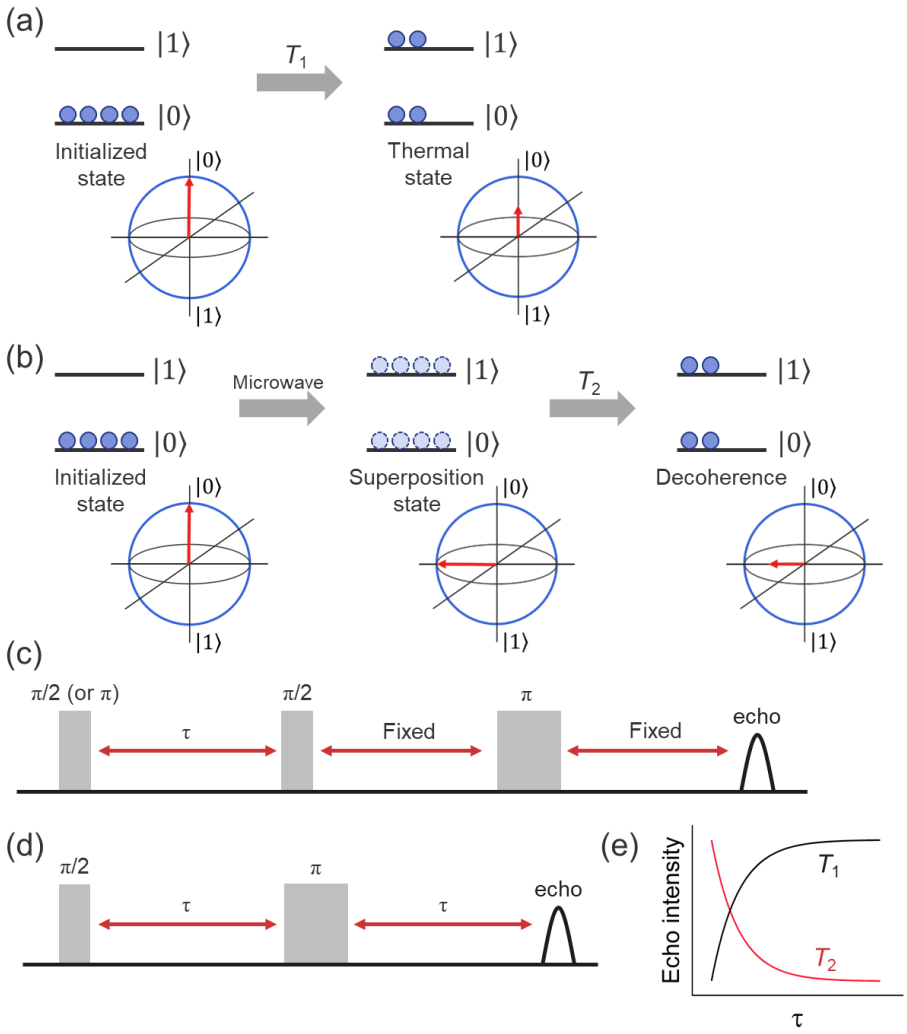

Figure 1-12. (a) Spin–lattice relaxation and (b) spin–spin relaxation of electron spins. In spin–lattice relaxation, a longitudinal magnetization returns to its thermal equilibrium value with a time constant of T_1. In spin–spin relaxation, a transverse magnetization returns to zero with a time constant of T_2. (c) T_1 and (d) T_2 measurements. In (b), a saturation recovery method uses a π/2 pulse for creating non-equilibrium state while an inversion recovery method uses a π pulse. For the readout sequence, a spin echo method is used instead of single π/2 pulse. (e) Plot of the echo intensity against the interval τ for each measurement.

1-4-3. Hyperfine coupling

The spin coupling between electron spins and nuclear spin are called as hyperfine coupling (Figure 1-13a). Some nuclei such as ^{1}H, ^{13}C, ^{14}N, and ^{19}F have spin as well as electrons, and it behaves as a small magnet. This interaction changes the Larmor frequencies of electron spins, and the motion of nuclear spins fluctuates the strength of the interaction, resulting the randomization of the phase in the coherent state.

The strength of hyperfine coupling is depends on following factors: (i) the gyromagnetic ratio of nuclear spins and (ii) the overlap of the electron spin orbitals and the nuclei. The hyperfine coupling constant is generally large with the atoms having a large gyromagnetic ratio, such as ^{1}H or ^{19}F spins. Therefore, to decrease the effect of hyperfine coupling, those nuclides that are in the high electron spin density position should be replaced to other nuclides with a smaller gyromagnetic ratio such as ^{2}D, ^{35}Cl or ^{37}Cl. Especially, high mobility functional groups like methyl group also affects the coherence time significantly. These groups usually facilitate spin decoherence and should also be substituted.

Hyperfine couplings to nuclear spins of surrounding molecules also contribute to relaxation. These intermolecular hyperfine interactions are important for quantum sensing of chemicals because qubits can detect the analytes by the coupling from the relaxation time or the decay profile of the echo signal called as electron spin echo envelope modulation (ESEEM).

1-4-4. Electron spin dipolar coupling

The dipolar spin coupling between electron spins can reduce the coherence time (Figure 1-13a). There are two types of electron–electron spin coupling.

The first one is an intermolecular dipolar coupling, which is the interaction of electron spins among different molecules. Paramagnetic species such as metal ions and radicals work as relaxation sources. Therefore, materials in the system other than qubits should be consisted with diamagnetic species, which do not enhance the spin relaxation. Qubits are also paramagnetic and can interact when they are close, so the qubits need to be separated each other. For MOFs, thus large amount of diamagnetic metal ions/ligands is required as dilutant to reduce the spin interactions between qubits.[42, 44]

The second one is an intramolecular dipolar coupling, zero-field splitting (ZFS). When there are two or more spins in a single molecule, they interacts each other to split the energy levels.

Consider a triplet state ($S = 1$), which having two electrons. These two electrons interact to split the degenerated triplet levels into three sublevels as T_x, T_y, and T_z. The energy gaps are represented as ZFS parameters D and E. ZFS parameters reflect the degree of localization of electron spins (Figure 1-123). When the electrons are localized and in close, ZFS parameters tends to be large, i.e., the electrons interacts strongly. For example, in acene molecules, the ZFS parameters become smaller with the increase of aromatic rings, and spin–lattice relaxation times become longer.[61] For high-spin quartet ($S = 3/2$) or quintet ($S = 2$) states that have more spins, the effects of intramolecular interaction is more significant, and usually the relaxation times are shorter than low-spin species.[32]

These two types of electron dipolar couplings are important relaxation sources since the gyromagnetic ratio of electron spins are much larger than that of nuclear spins (about 660 times of ^{1}H).

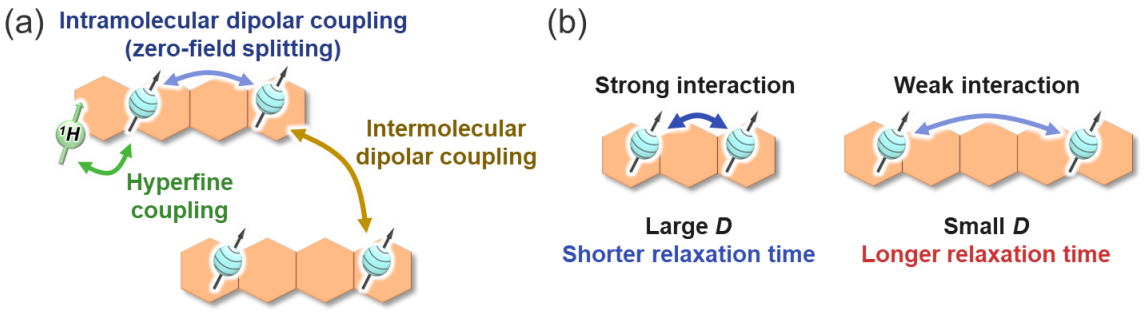

Figure 1-13. (a) Interactions that affects qubit properties. Intermolecular and intramolecular dipolar coupling are caused by magnetic interactions between electron spins. A hyperfine coupling is induced by interaction between electron spins and nuclear spins. (b) A relationship between the localization of the electron spins and the zero-field splitting (ZFS) parameters. The relaxation time tend to be shorter when the electron spins are in close and ZFS parameter is large. On the contrary, the relaxation time become longer when the interaction between spins are weak due to the delocalization.

1-4-5. Mobility of qubit system

Not only the strength of interactions, but also the degree of their fluctuations are important for relaxation. At higher temperature, the qubit molecules and surroundings have some mobilities, this can enhance relaxation. The strength of intermolecular interactions such as dipolar coupling between qubits or hyperfine interaction to surroundings are weakened (or strengthened) by changing the distance due to the rotational or the translational motions of the matrices. For anisotropic intramolecular interactions including ZFS interactions, molecular motions are also effective. Since the orientation of molecules to the magnetic field is altered by rotational motions, the interactions are modulated. These fluctuations due to molecular motions are important especially for applications at room temperature, so the motions of qubits and their surroundings, in general, should be suppressed as possible. Moreover, in porous systems like MOFs that the density around the qubits is altered by guests, the degree of the qubit motion can also be modulated, making it possible to detect analytes from fluctuations mentioned above (Figure 1-14) as the changes in relaxation times or interactions.

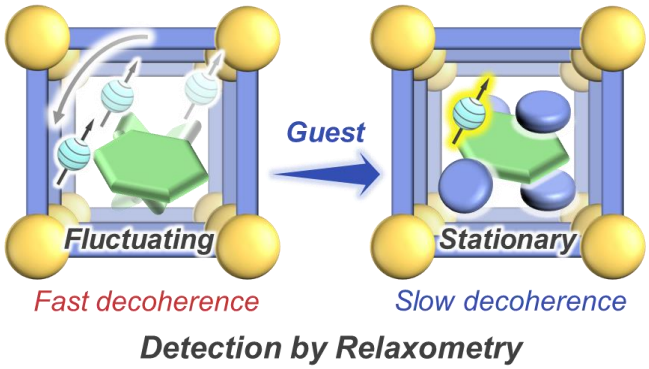

Figure 1-14. Schematic image of a relaxometry-based detection of molecular motions in MOFs. When qubits are incorporated in MOF, the qubit motion is affected by the density in the pore. The difference in the degree of the motion results the change in the relaxation time. Reproduced with permission from reference 62. Copyright 2024 American Chemical Society.

1-5. Conventional molecular qubit-based quantum sensing

Quantum sensing with molecular qubits is a recently emerging field with few examples of research, but there have been several reports on chemical sensing.

1-5-1. Molecular qubit-based quantum sensing in solution

Quantum sensing of electric fields using molecular qubits in solution are reported by Wasielewski et al. in 2023.[35] The group utilized spin-correlated radical pair (SCRP) that is a weakly interacting radicals generated in donor-acceptor pair as qubits (Figure 1-15). There are dipolar interaction between the radicals. Since the strength of the interaction depends on the distance between the radical spins, when the electric field is applied to the systems to alter the distance as the electric interaction between the host and the guest molecules, the interaction is also modified. This can be readout from the changes of electron spin echo envelope modulation (ESEEM) frequency, which is a modulation of echo intensity in pulsed EPR measurements.

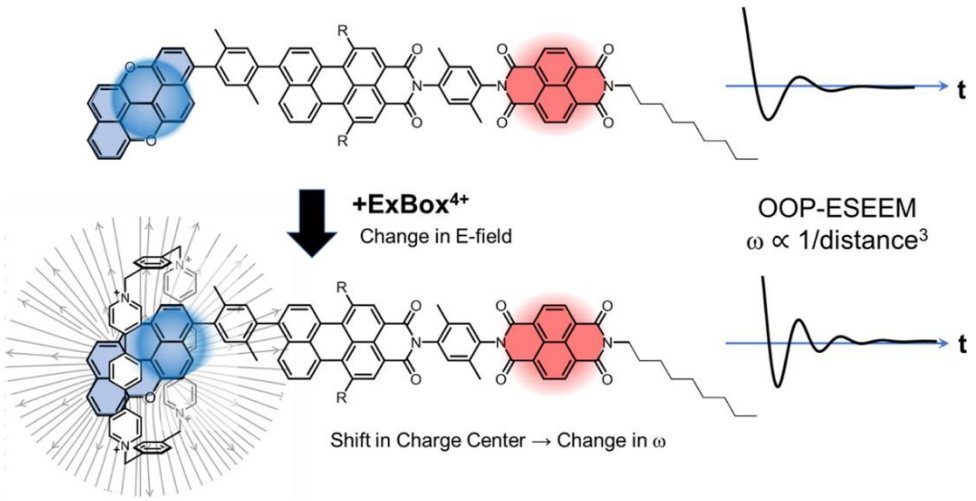

Figure 1-15. Schematic implementation quantum sensing of electric field with spin-correlated radical pair (SCRP). The electric field is modified by the positive charge of guest molecules, altering the spin distribution on the donor. The change in the spin distribution is readout as ESEEM frequency, which reflects the distance of electron spins. Reproduced with permission from reference 35. Copyright 2023 American Chemical Society.

1-5-2. Molecular qubit-based quantum sensing in MOF

As mentioned in previous section, MOFs are excellent materials for quantum sensing with molecular qubits. So far, several groups have reported the quantum sensing in MOFs. First example was reported by Kultaeva and the coworkers in 2022.[45] They employed Cu^{2+} ions doped in HKUST-1 as qubits to sense ^{1}H spins in butane molecules. By analyzing the orientation dependence of electron-nuclear double-resonance (ENDOR) signals, information on the spatial distribution of hydrogen atoms in the MOF was obtained. However, metal ion-based quantum sensors suffer from fast spin relaxation caused by strong spin-orbit coupling and require cryogenic conditions (< 10 K) to maintain quantum coherence long enough to obtain ENDOR signals.

Instead of metal ion-based qubits, Sun et al. reported the quantitative sensing of Li^{+} ions at room temperature using organic radicals generated by the partial oxidation of ligands (Figure 1-16).[43] They leveraged the hyperfine interaction between lithium nuclear spins and electron spins of organic radical qubits inside a two-dimensional MgHOTP MOF. The T_1, T_2, and ESEEM intensity changed depending on the lithium concentration, allowing for quantitative sensing.

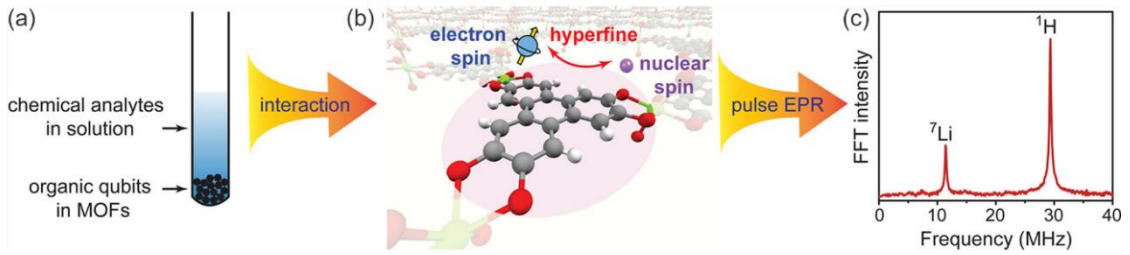

Figure 1-16. Room-temperature quantum sensing of Li^{+} ions in MOFs. (a) MOF particles containing organic radical qubits are soaked in the solution of Li^{+} analytes in THF. (b) The adsorbed Li^{+} ions interact with radicals through hyperfine coupling. (c) The interaction are identified by hyperfine spectrum obtained from fast Fourier transform (FFT) of ESEEM signal. Reproduced with permission from reference 43. Copyright 2022 American Chemical Society.

1-6. Overview of the thesis

As overviewed in previous sections, quantum sensing with molecular qubit was recently achieved at room temperature, however, there are several problems remained (Table 1-1). Solution-based systems have difficulty in elaborate tuning and not suitable for chemical sensing. On the contrary, MOF-based systems have high tunability of the structure, but non-spin-polarized qubits such as metal ions or radicals in the thermal state were used. Importantly, both systems only utilized interactions between the qubit each other or the qubits and nuclear spins of the guests, and detectable targets were limited. In the SCRP-based solution systems,[35] the analyte of electric fields was only detectable through the interaction between specific hosts and guests. For the MOF-based system reported by Sun et al.,[43] there was a major challenge in that they could not distinguish compounds composed of the same nuclear species, such as benzene and toluene, for example. In addition, the T_2 were short and not suitable for effective qubit operations at room temperature for both systems. Therefore, strategies of the material design and the sensing method are lacking for room-temperature quantum sensing of various chemicals.

Table 1-1. Comparison of the report about quantum sensing in molecular qubit-based systems at room temperature.

Qubit	Matrix	Polarization	Method	T_2	Target
SCRP	Solution	○	Dipolar	~ 200 ns [a)]	Electric field (Needs specific guest)
Radical	MOF	×	Hyperfine	153 ns	Specific ion (Li^+)

a: Estimated from a figure since correct value was not described.

In this thesis, the author discuss design guidelines for room-temperature qubits and strategies for sensing various molecules toward the realization of quantum chemical sensing.

Chapter 2 describes the strategy to achieve both the large spin polarization and the long relaxation time in photoexcited molecular qubit systems.[63] The electron withdrawing fluorine atoms were substituted to zinc porphyrins to reduce the spin density on the zinc atom, resulting relatively long relaxation time with keeping the large spin polarization of zinc porphyrins.

In chapter 3, a new methodology was proposed to recognize analytes through the change in the mobility of the qubits.[64] By hybridizing triplet qubits in flexible MOFs, the mobility of the qubits were controlled by analyte guests and reflected as the change in the relaxation time, showing a concept of molecular motion-based sensing.

Chapter 4 describes the first example of room-temperature quantum coherence of 4-spin entangled quintet qubits.[65] The coherent quintet state was generated through minimum motion of qubits by arranging the chromophores in the MOF densely suppressing the relaxation from the molecular motions.

In chapter 5, the thesis was summarized, and future remarks were discussed.

1-7. References

(1) Ladd, T. D.; Jelezko, F.; Laflamme, R.; Nakamura, Y.; Monroe, C.; O'Brien, J. L. Quantum computers. *Nature* **2010,** *464*, 45-53.

(2) Arute, F.; Arya, K.; Babbush, R.; Bacon, D.; Bardin, J. C.; Barends, R.; Biswas, R.; Boixo, S.; Brandao, F.; Buell, D. A.; Burkett, B.; Chen, Y.; Chen, Z.; Chiaro, B.; Collins, R.; Courtney, W.; Dunsworth, A.; Farhi, E.; Foxen, B.; Fowler, A.; Gidney, C.; Giustina, M.; Graff, R.; Guerin, K.; Habegger, S.; Harrigan, M. P.; Hartmann, M. J.; Ho, A.; Hoffmann, M.; Huang, T.; Humble, T. S.; Isakov, S. V.; Jeffrey, E.; Jiang, Z.; Kafri, D.; Kechedzhi, K.; Kelly, J.; Klimov, P. V.; Knysh, S.; Korotkov, A.; Kostritsa, F.; Landhuis, D.; Lindmark, M.; Lucero, E.; Lyakh, D.; Mandra, S.; McClean, J. R.; McEwen, M.; Megrant, A.; Mi, X.; Michielsen, K.; Mohseni, M.; Mutus, J.; Naaman, O.; Neeley, M.; Neill, C.; Niu, M. Y.; Ostby, E.; Petukhov, A.; Platt, J. C.; Quintana, C.; Rieffel, E. G.; Roushan, P.; Rubin, N. C.; Sank, D.; Satzinger, K. J.; Smelyanskiy, V.; Sung, K. J.; Trevithick, M. D.; Vainsencher, A.; Villalonga, B.; White, T.; Yao, Z. J.; Yeh, P.; Zalcman, A.; Neven, H.; Martinis, J. M. Quantum supremacy using a programmable superconducting processor. *Nature* **2019,** *574*, 505-510.

(3) Warren, W. S. The Usefulness of NMR Quantum Computing. *Science* **1997,** *277*, 1688-1690.

(4) Jones, J. A. NMR quantum computation. *Prog. Nucl. Magn. Reson. Spectrosc.* **2001,** *38*, 325-360.

(5) Wedge, C. J.; Timco, G. A.; Spielberg, E. T.; George, R. E.; Tuna, F.; Rigby, S.; McInnes, E. J.; Winpenny, R. E.; Blundell, S. J.; Ardavan, A. Chemical engineering of molecular qubits. *Phys. Rev. Lett.* **2012,** *108*, 107204.

(6) Gaita-Arino, A.; Luis, F.; Hill, S.; Coronado, E. Molecular spins for quantum computation. *Nat. Chem.* **2019,** *11*, 301-309.

(7) Kothe, G.; Lukaschek, M.; Yago, T.; Link, G.; Ivanov, K. L.; Lin, T. S. Initializing 2^{14} Pure 14-Qubit Entangled Nuclear Spin States in a Hyperpolarized Molecular Solid. *J. Phys. Chem. Lett.* **2021,** *12*, 3647-3654.

(8) Muralidharan, S.; Li, L.; Kim, J.; Lutkenhaus, N.; Lukin, M. D.; Jiang, L. Optimal architectures for long distance quantum communication. *Sci. Rep.* **2016,** *6*, 20463.

(9) Bhaskar, M. K.; Riedinger, R.; Machielse, B.; Levonian, D. S.; Nguyen, C. T.; Knall, E. N.; Park, H.; Englund, D.; Loncar, M.; Sukachev, D. D.; Lukin, M. D. Experimental demonstration of memory-enhanced quantum communication. *Nature* **2020,** *580*, 60-64.

(10) Maze, J. R.; Stanwix, P. L.; Hodges, J. S.; Hong, S.; Taylor, J. M.; Cappellaro, P.; Jiang, L.; Dutt, M. V.; Togan, E.; Zibrov, A. S.; Yacoby, A.; Walsworth, R. L.; Lukin, M. D. Nanoscale magnetic sensing with an individual electronic spin in diamond. *Nature* **2008,** *455*, 644-647.

(11) Degen, C. L.; Reinhard, F.; Cappellaro, P. Quantum sensing. *Rev. Mod. Phys.* **2017,** *89*, 035002.

(12) Guo, X.; Breum, C. R.; Borregaard, J.; Izumi, S.; Larsen, M. V.; Gehring, T.; Christandl, M.; Neergaard-Nielsen, J. S.; Andersen, U. L. Distributed quantum sensing in a continuous-variable entangled network. *Nat. Phys.* **2019,** *16*, 281-284.

(13) Romach, Y.; Muller, C.; Unden, T.; Rogers, L. J.; Isoda, T.; Itoh, K. M.; Markham, M.; Stacey, A.; Meijer, J.; Pezzagna, S.; Naydenov, B.; McGuinness, L. P.; Bar-Gill, N.; Jelezko, F. Spectroscopy of surface-induced noise using shallow spins in diamond. *Phys. Rev. Lett.* **2015,** *114*, 017601.

(14) Hochberg, Y.; Zhao, Y.; Zurek, K. M. Superconducting Detectors for Superlight Dark Matter. *Phys. Rev. Lett.* **2016,** *116*, 011301.

(15) Wu, T.; Blanchard, J. W.; Centers, G. P.; Figueroa, N. L.; Garcon, A.; Graham, P. W.; Kimball, D. F. J.; Rajendran, S.; Stadnik, Y. V.; Sushkov, A. O.; Wickenbrock, A.; Budker, D. Search for Axionlike Dark Matter with a Liquid-State Nuclear Spin Comagnetometer. *Phys. Rev. Lett.* **2019,** *122*, 191302.

(16) Braunstein, S. L.; Mann, A.; Revzen, M. Maximal violation of Bell inequalities for mixed states. *Phys. Rev. Lett.* **1992,** *68*, 3259-3261.

(17) Yu, C. J.; von Kugelgen, S.; Laorenza, D. W.; Freedman, D. E. A Molecular Approach to Quantum Sensing. *ACS Cent. Sci.* **2021,** *7*, 712-723.

(18) Kominis, I. K.; Kornack, T. W.; Allred, J. C.; Romalis, M. V. A subfemtotesla ultichannel atomic magnetometer. *Nature* **2003,** *422*, 596-599.

(19) Budker, D.; Romalis, M. Optical agnetometry. *Nat. Phys.* **2007,** *3*, 227-234.

(20) Reiter, F.; Sorensen, A. S.; Zoller, P.; Muschik, C. A. Dissipative quantum error correction and application to quantum sensing with trapped ions. *Nat. Commun.* **2017,** *8*, 1822.

(21) Heckötter, J.; Aßmann, M.; Bayer, M. Rydberg excitons and quantum sensing. *MRS Bulletin* **2024,** *49*, 948-957.

(22) Nielsen, M. A.; Chuang, I. L., *Quantum Computation and Quantum Information*. Cambridge University Press: Cambridge, **2000**.

(23) Bayliss, S. L.; Laorenza, D. W.; Mintun, P. J.; Kovos, B. D.; Freedman, D. E.; Awschalom, D. D. Optically addressable molecular spins for quantum information processing. *Science* **2020,** *370*, 1309–1312.

(24) Rembold, P.; Oshnik, N.; Müller, M. M.; Montangero, S.; Calarco, T.; Neu, E. Introduction to quantum optimal control for quantum sensing with nitrogen-vacancy centers in diamond. *AVS Quantum Sci.* **2020,** *2*.

(25) Zhang, T.; Pramanik, G.; Zhang, K.; Gulka, M.; Wang, L.; Jing, J.; Xu, F.; Li, Z.; Wei, Q.; Cigler, P.; Chu, Z. Toward Quantitative Bio-sensing with Nitrogen-Vacancy Center in Diamond. *ACS Sens.* **2021,** *6*, 2077-2107.

(26) Staudacher, T.; Shi, F.; Pezzagna, S.; Meijer, J.; Du, J.; Meriles, C. A.; Reinhard, F.; Wrachtrup, J. Nuclear Magnetic Resonance Spectroscopy on a (5-Nanometer)^3 Sample Volume. *Science* **2013,** *339*, 561-563.

(27) Herbschleb, E. D.; Kato, H.; Maruyama, Y.; Danjo, T.; Makino, T.; Yamasaki, S.; Ohki, I.; Hayashi, K.; Morishita, H.; Fujiwara, M.; Mizuochi, N. Ultra-long coherence times amongst room-temperature solid-state spins. *Nat. Commun.* **2019,** *10*, 3766.

(28) Ohashi, K.; Rosskopf, T.; Watanabe, H.; Loretz, M.; Tao, Y.; Hauert, R.; Tomizawa, S.; Ishikawa, T.; Ishi-Hayase, J.; Shikata, S.; Degen, C. L.; Itoh, K. M. Negatively charged nitrogen-vacancy centers in a 5 nm thin 12C diamond film. *Nano. Lett.* **2013,** *13*, 4733-4738.

(29) Zadrozny, J. M.; Gallagher, A. T.; Harris, T. D.; Freedman, D. E. A Porous Array of Clock Qubits. *J. Am. Chem. Soc.* **2017,** *139*, 7089-7094.

(30) Dai, Y. Z.; Dong, B. W.; Kao, Y.; Wang, Z. Y.; Un, H. I.; Liu, Z.; Lin, Z. J.; Li, L.; Xie, F. B.; Lu, Y.; Xu, M. X.; Lei, T.; Sun, Y. J.; Wang, J. Y.; Gao, S.; Jiang, S. D.; Pei, J. Chemical Modification toward Long Spin Lifetimes in Organic Conjugated Radicals. *Chemphyschem* **2018,** *19*, 2972-2977.

(31) von Kugelgen, S.; Krzyaniak, M. D.; Gu, M.; Puggioni, D.; Rondinelli, J. M.; Wasielewski, M. R.; Freedman, D. E. Spectral Addressability in a Modular Two Qubit System. *J. Am. Chem. Soc.* **2021,** *143*, 8069-8077.

(32) Maylander, M.; Thielert, P.; Quintes, T.; Vargas Jentzsch, A.; Richert, S. Room Temperature Electron Spin Coherence in Photogenerated Molecular Spin Qubit Candidates. *J. Am. Chem. Soc.* **2023,** *145*, 14064-14069.

(33) Orihashi, K.; Yamauchi, A.; Fujiwara, S.; Asada, M.; Nakamura, T.; Ka-Ho Hui, J.; Kimizuka, N.; Tateishi, K.; Uesaka, T.; Yanai, N. Spin-Polarized Radicals with Extremely Long Spin-Lattice Relaxation Time at Room Temperature in a Metal-Organic Framework. *J. Am. Chem. Soc.* **2023,** *145*, 27650-27656.

(34) Qiu, Y.; Eckvahl, H. J.; Equbal, A.; Krzyaniak, M. D.; Wasielewski, M. R. Enhancing Coherence Times of Chromophore-Radical Molecular Qubits and Qudits by Rational Design. *J. Am. Chem. Soc.* **2023,** *145*, 25903-25909.

(35) Xie, F.; Mao, H.; Lin, C.; Feng, Y.; Stoddart, J. F.; Young, R. M.; Wasielewski, M. R. Quantum Sensing of Electric Fields Using Spin-Correlated Radical Ion Pairs. *J. Am. Chem. Soc.* **2023,** *145*, 14922-14931.

(36) Inoue, M.; Yamauchi, A.; Parmar, B.; Orihashi, K.; Singh, M.; Asada, M.; Nakamura, T.; Yanai, N. Guest-responsive coherence time of radical qubits in a metal-organic framework. *Chem. Commun.* **2024,** *60*, 6130-6133.

(37) Kopp, K.; Westhofen, L.; Hett, T.; Felix Schwering-Sohnrey, M.; Maylander, M.; Richert, S.; Schiemann, O. Synthesis and dark state EPR properties of PDI-trityl dyads and triads. *Chem. Euro. J.* **2024,** *30*, e202303635.

(38) Orihashi, K.; Yamauchi, A.; Inoue, M.; Parmar, B.; Fujiwara, S.; Kimizuka, N.; Asada, M.; Nakamura, T.; Yanai, N. Radical qubits photo-generated in acene-based metal-organic frameworks. *Dalton Trans.* **2024,** *53*, 872-876.

(39) Bader, K.; Winkler, M.; van Slageren, J. Tuning of molecular qubits: very long coherence and spin-lattice relaxation times. *Chem. Commun.* **2016,** *52*, 3623-3626.

(40) Yu, C. J.; Krzyaniak, M. D.; Fataftah, M. S.; Wasielewski, M. R.; Freedman, D. E. A concentrated array of copper porphyrin candidate qubits. *Chem. Sci.* **2019,** *10*, 1702-1708.

(41) Jacobberger, R. M.; Qiu, Y.; Williams, M. L.; Krzyaniak, M. D.; Wasielewski, M. R. Using Molecular Design to Enhance the Coherence Time of Quintet Multiexcitons Generated by Singlet Fission in Single Crystals. *J. Am. Chem. Soc.* **2022,** *144*, 2276-2283.

(42) Yamabayashi, T.; Atzori, M.; Tesi, L.; Cosquer, G.; Santanni, F.; Boulon, M. E.; Morra, E.; Benci, S.; Torre, R.; Chiesa, M.; Sorace, L.; Sessoli, R.; Yamashita, M. Scaling Up Electronic Spin Qubits into a Three-Dimensional Metal-Organic Framework. *J. Am. Chem. Soc.* **2018,** *140*, 12090-12101.

(43) Sun, L.; Yang, L.; Dou, J. H.; Li, J.; Skorupskii, G.; Mardini, M.; Tan, K. O.; Chen, T.; Sun, C.; Oppenheim, J. J.; Griffin, R. G.; Dinca, M.; Rajh, T. Room-Temperature Quantitative Quantum Sensing of Lithium Ions with a Radical-Embedded Metal-Organic Framework. *J. Am. Chem. Soc.* **2022,** *144*, 19008-19016.

(44) Oanta, A. K.; Collins, K. A.; Evans, A. M.; Pratik, S. M.; Hall, L. A.; Strauss, M. J.; Marder, S. R.; D'Alessandro, D. M.; Rajh, T.; Freedman, D. E.; Li, H.; Bredas, J. L.; Sun, L.; Dichtel, W. R. Electronic Spin Qubit Candidates Arrayed within Layered Two-Dimensional Polymers. *J. Am. Chem. Soc.* **2023,** *145*, 689-696.

(45) Kultaeva, A.; Poppl, A.; Biktagirov, T. Atomic-Scale Quantum Sensing of Ensembles of Guest Molecules in a Metal-Organic Framework with Intrinsic Electron Spin Centers. *J. Phys. Chem. Lett.* **2022,** *13*, 6737-6742.

(46) Tateishi, K.; Negoro, M.; Nishida, S.; Kagawa, A.; Morita, Y.; Kitagawa, M. Room temperature

hyperpolarization of nuclear spins in bulk. *Proc. Natl. Acad. Sci. U.S.A.* **2014,** *111*, 7527-7530.

(47) Sloop, D. J.; Yu, H.-L.; Lin, T.-S.; Weissman, S. I. Electron spin echoes of a photoexcited triplet: Pentacene in *p*-terphenyl crystals. *J. Chem. Phys.* **1981,** *75*, 3746-3757.

(48) Kouno, H.; Kawashima, Y.; Tateishi, K.; Uesaka, T.; Kimizuka, N.; Yanai, N. Nonpentacene Polarizing Agents with Improved Air Stability for Triplet Dynamic Nuclear Polarization at Room Temperature. *J. Phys. Chem. Lett.* **2019,** *10*, 2208-2213.

(49) Wang, Y.-X.; Liu, Z.; Fang, Y.-H.; Zhou, S.; Jiang, S.-D.; Gao, S. Coherent manipulation and quantum phase interference in a fullerene-based electron triplet molecular qutrit. *npj Quantum Information* **2021,** *7*.

(50) Smith, M. B.; Michl, J. Singlet Fission. *Chem. Rev.* **2010,** *110*, 6891–6936.

(51) Nagashima, H.; Kawaoka, S.; Akimoto, S.; Tachikawa, T.; Matsui, Y.; Ikeda, H.; Kobori, Y. Singlet-Fission-Born Quintet State: Sublevel Selections and Trapping by Multiexciton Thermodynamics. *J. Phys. Chem. Lett.* **2018,** *9*, 5855-5861.

(52) Einzinger, M.; Wu, T.; Kompalla, J. F.; Smith, H. L.; Perkinson, C. F.; Nienhaus, L.; Wieghold, S.; Congreve, D. N.; Kahn, A.; Bawendi, M. G.; Baldo, M. A. Sensitization of silicon by singlet exciton fission in tetracene. *Nature* **2019,** *571*, 90-94.

(53) Budden, P. J.; Weiss, L. R.; Muller, M.; Panjwani, N. A.; Dowland, S.; Allardice, J. R.; Ganschow, M.; Freudenberg, J.; Behrends, J.; Bunz, U. H. F.; Friend, R. H. Singlet exciton fission in a modified acene with improved stability and high photoluminescence yield. *Nat. Commun.* **2021,** *12*, 1527.

(54) Kobori, Y.; Fuki, M.; Nakamura, S.; Hasobe, T. Geometries and Terahertz Motions Driving Quintet Multiexcitons and Ultimate Triplet-Triplet Dissociations via the Intramolecular Singlet Fissions. *J. Phys. Chem. B* **2020,** *124*, 9411-9419.

(55) Smyser, K. E.; Eaves, J. D. Singlet fission for quantum information and quantum computing: the parallel JDE model. *Sci. Rep.* **2020,** *10*, 18480.

(56) Reid, O. G.; Johnson, J. C.; Eaves, J. D.; Damrauer, N. H.; Anthony, J. E. Molecular Control of Triplet-Pair Spin Polarization and Its Optoelectronic Magnetic Resonance Probes. *Acc. Chem. Res.* **2024,** *57*, 59-69.

(57) Richert, S.; Tait, C. E.; Timmel, C. R. Delocalisation of photoexcited triplet states probed by transient EPR and hyperfine spectroscopy. *J. Magn. Reson.* **2017,** *280*, 103-116.

(58) Jackson, C. E.; Moseley, I. P.; Martinez, R.; Sung, S.; Zadrozny, J. M. A reaction-coordinate perspective of magnetic relaxation. *Chem. Soc. Rev.* **2021,** *50*, 6684-6699.

(59) Mirzoyan, R.; Kazmierczak, N. P.; Hadt, R. G. Deconvolving Contributions to Decoherence in Molecular Electron Spin Qubits: A Dynamic Ligand Field Approach. *Chem. Euro. J.* **2021,** *27*, 9482-9494.

(60) Levitt, M. H., *Spin Dynamics: Basics of Nuclear Magnetic Resonance. 2nd ed.* John Wiley & Sons Ltd,: The Atrium, Southern Gate, Chichester, **2008**.

(61) Yu, H.-L.; Lin, T.-S.; Weissman, S. I.; Sloop, D. J. Time resolved studies of pentacene triplets by electron spin echo spectroscopy. *J. Chem. Phys.* **1984,** *80*, 102-107.

(62) Yamauchi, A.; Yanai, N. Toward Quantum Noses: Quantum Chemosensing Based on Molecular Qubits in Metal-

Organic Frameworks. *Acc. Chem. Res.* **2024,** *57*, 2963-2972.

(63) Yamauchi, A.; Fujiwara, S.; Nishimura, K.; Sasaki, Y.; Tateishi, K.; Uesaka, T.; Kimizuka, N.; Yanai, N. Design Guidelines to Elongate Spin-Lattice Relaxation Times of Porphyrins with Large Triplet Electron Polarization. *J Phys Chem A* **2021,** *125*, 4334-4340.

(64) Yamauchi, A.; Fujiwara, S.; Kimizuka, N.; Asada, M.; Fujiwara, M.; Nakamura, T.; Pirillo, J.; Hijikata, Y.; Yanai, N. Modulation of triplet quantum coherence by guest-induced structural changes in a flexible metal-organic framework. *Nat. Commun.* **2024,** *15*, 7622.

(65) Yamauchi, A.; Tanaka, K.; Fuki, M.; Fujiwara, S.; Kimizuka, N.; Ryu, T.; Saigo, M.; Onda, K.; Kusumoto, R.; Ueno, N.; Sato, H.; Kobori, Y.; Miyata, K.; Yanai, N. Room-temperature quantum coherence of entangled multiexcitons in a metal-organic framework. *Sci. Adv.* **2024,** *10*, eadi3147.

Chapter 2. Development of zinc-based porphyrins towards room-temperature molecular qubit

2-1. Introduction

Porphyrins have been widely known as chromophore for their excellent stability, biocompatibility, and strong absorption of visible range.[1-2] Porphyrins are also known to generate a spin-polarization in their triplet states as acene-based chromophores such as pentacene and tetracene[3] and have higher stability to light and oxygen than acenes.[4-6] Although the triplets have excellent properties, the use for qubit was mainly limited to low temperature.[7-9] Free-base porphyrins have relatively long spin–lattice relaxation time of several microseconds at room temperature, but their polarization are about 50 to 70 %, smaller than that of pentacene.[10] On the contrary, metalloporphyrins such as zinc porphyrins exhibit higher polarization that reaches almost unity due to the anisotropic spin–orbit coupling attributed to the *d*-orbitals.[6] Nevertheless, the reports of metalloporphyrin-based qubits are limited to lower temperature, because the strong spin–orbit coupling enhance the relaxation of spins at the same time. As a results, it was remain unclear how to use the metalloporphyrins as room-temperature qubits.

In this chapter, the modifications to the phenyl group of porphyrins were employed to realize both large polarization and long relaxation time for room-temperature qubits. Electron-withdrawing fluorine substituents were introduced into porphyrins derivatives to control the electronic condition of triplet excited state (Figure 2-1a). In magnesium porphyrin, which shows similar polarization properties to free-base porphyrin, the change in the triplet electron spin polarization generation mechanism by fluorination has already been reported,[11] but the relationship to the relaxation time has not been investigated. The effects of fluorine substitutions to the polarization and the relaxation were systematically studied by changing the number of the substituents using TR-EPR in a glass matrix at room temperature.

The substitution of fluorine groups to free-base porphyrins leads to both the decrease of their relaxation time and the changes in the polarization patterns. However, the zinc porphyrins elongated their spin relaxation time by fluorine modification while the large polarization were not affected (Figure 2-1b). Density functional theory (DFT) calculations suggested that the introduction of fluorine atoms reduces the spin density around the Zn atom, which enables the coexistence of large polarization and long spin–lattice relaxation time.

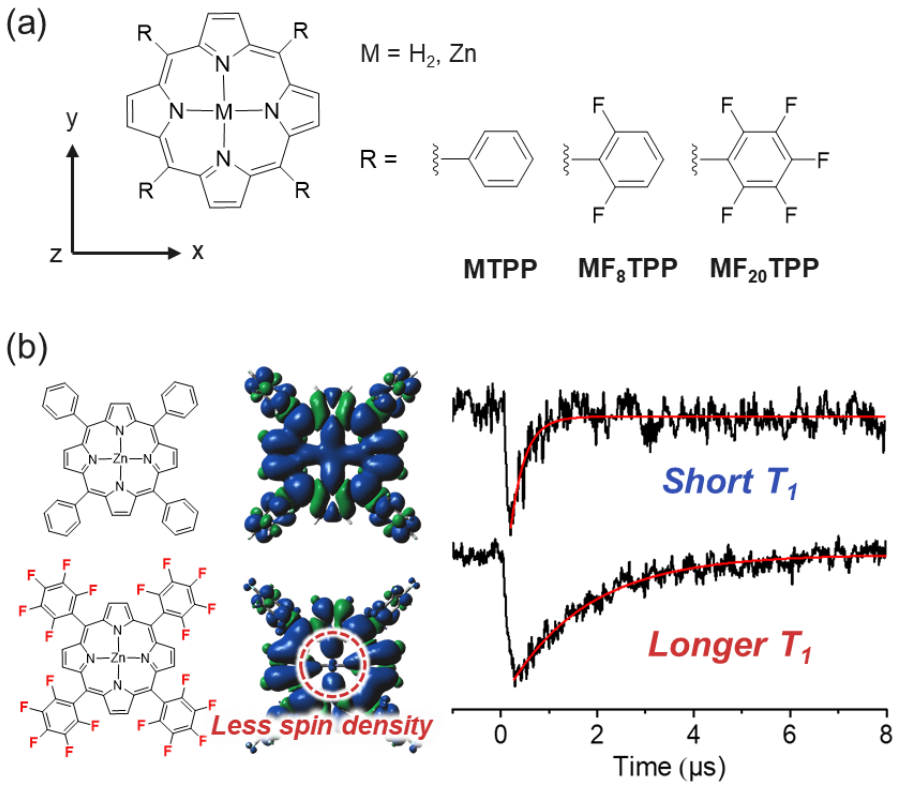

Figure 2-1. (a) Chemical structures of meso-tetraphenylporphyrins MTPP, MF_8TPP, and $MF_{20}TPP$ (M = H_2 and Zn). (b) Relationship between fluorine substitution on zinc porphyrins and the spin–lattice relaxation time.

2-2. Experimental section

2-2-1. Materials

All reagents were used without further purifications. Zinc acetate was purchased from Kishida chemical. Pyrrole, 2,6-difluorobenzaldehyde, *p*-chloranil, *β*-estradiol, Free-base tetraphenylporphyrin (H_2TPP) and free-base tetrakis(pentafluorophenyl)porphyrin (H_2F_{20}TPP) were purchased from TCI. Zinc tetraphenylporphyrin (ZnTPP) was purchased from Frontier Scientific.

2-2-2. Characterizations

^{1}H NMR (400 MHz) spectra were measured on a JEOL JNM-ECZ400 spectrometer using TMS as the internal standard. UV-Vis absorption spectra were recorded on a JASCO V-670 spectrophotometer. Fluorescence and phosphorescence spectra were measured by using a JASCO FP-8700 fluorescence spectrometer. Powder X-ray diffraction (PXRD) patterns were measured on a Bruker D2 Phaser (Cu-Kα, 30 kV, 10 mA). Transient absorption measurements were conducted by using a UNISOKU TSP-2000 system.

2-2-3. Time-resolved EPR measurements

Time-resolved EPR measurements were carried out using a home-built ~9 GHz dielectric resonator with a window for laser irradiation at a magnetic field generated by an electromagnet. Samples were photoexcited by using Spectra Physics Quanta-Lay Nd:YAG (wavelength and repetition rate were 532 nm and 10 Hz, respectively). An electromagnet was purchased from Takano (MC160A-16). The gap and the pole size were 50 mm and 120 mm, respectively. A power supply PAG60-55 (Kikusui) with the stability of 10^{-4} was used. A microwave was generated from SG22000Pro (DS instruments) with the power of ~10 μW. The EPR signal was converted to DC using diode detector, amplified with a low noise amp (ALN0905-12-3010, Dynamic RF Inc.), and detected by an oscilloscope (DSOX3024T, Keysight). The samples were put into capillaries and measured at room temperature. The zero-field populations and zero-field splitting parameters were determined by the simulations of spectra by using MATLAB[12] and Easyspin.[13]

2-2-4. DFT calculations

The optimized structures of porphyrins in the ground state and the lowest triplet state were obtained with the B3LYP exchange-correlation functional as implemented in the Gaussian 16 software using the 6-31G* basis set. Time-dependent DFT for the calculation of the energies and the configurations was performed with the B3LYP/SDD for Zn, EPR-II for others. Molecular orbitals and spin density were visualized by GaussView 6.0.[14]

2-2-5. Synthesis of porphyrins

Free-base tetrakis(2,6-difluorophenyl)porphyrin (H_2F_8TPP), zinc tetrakis(2,6-difluorophenylporphyrin (ZnF_8TPP), and zinc tetrakis(pentafluorophenyl)porphyrin ($ZnF_{20}TPP$) were prepared by following the literature methods,[15,16] and characterized by ^{1}H-NMR , ^{19}F-NMR and mass spectroscopy.

2-2-5-1. Synthesis of H_2F_8TPP

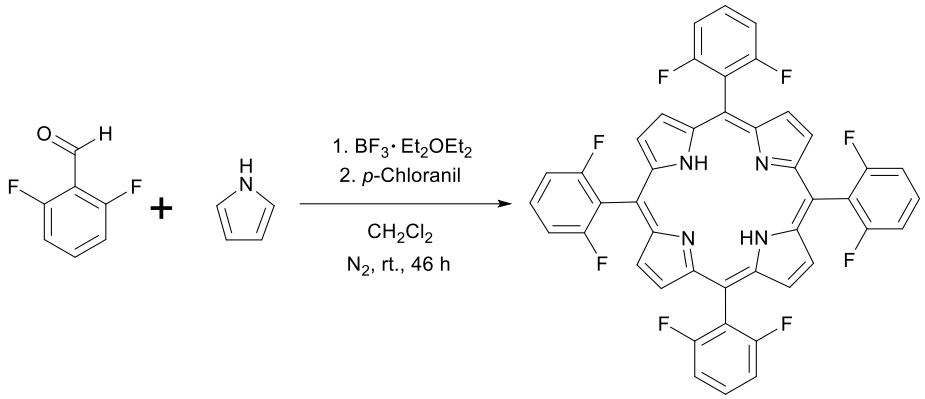

Figure 2-2. Synthetic scheme of H_2F_8TPP.

Pyrrole (340 μL, 4.04 mmol) and 2,6-difluorobenzaldehyde (550 mg, 3.87 mmol) were dissolved in 80 mL of dry CH_2Cl_2 under N_2. $BF_3 \cdot O(Et)_2$ (60 μL, 0.476 mmol) was then added and stirred at room temperature for 1 day. After adding *p*-Chloranil (390 mg, 1.59 mmol), the reaction mixture was stirred at room temperature for 18 h. After the reaction, the product was washed with methanol. The residue was purified by silica gel column chromatography (eluent: chloroform/hexane (8:2 v/v)). Yield: 13%. ^{1}H NMR (400 MHz, $CDCl_3$, TMS): δ = 7.35-7.40 (t, 8H), 7.75-7.83 (quin, 4H), 8.86 (s, 8H), -2.77 (s, 2H). ^{19}F NMR (376 MHz, $CDCl_3$) δ = -108.08 (s, 8F). MALDI-TOF-MAS (dithranol, *m/z*): calcd: 758.17, Found: 758.23.

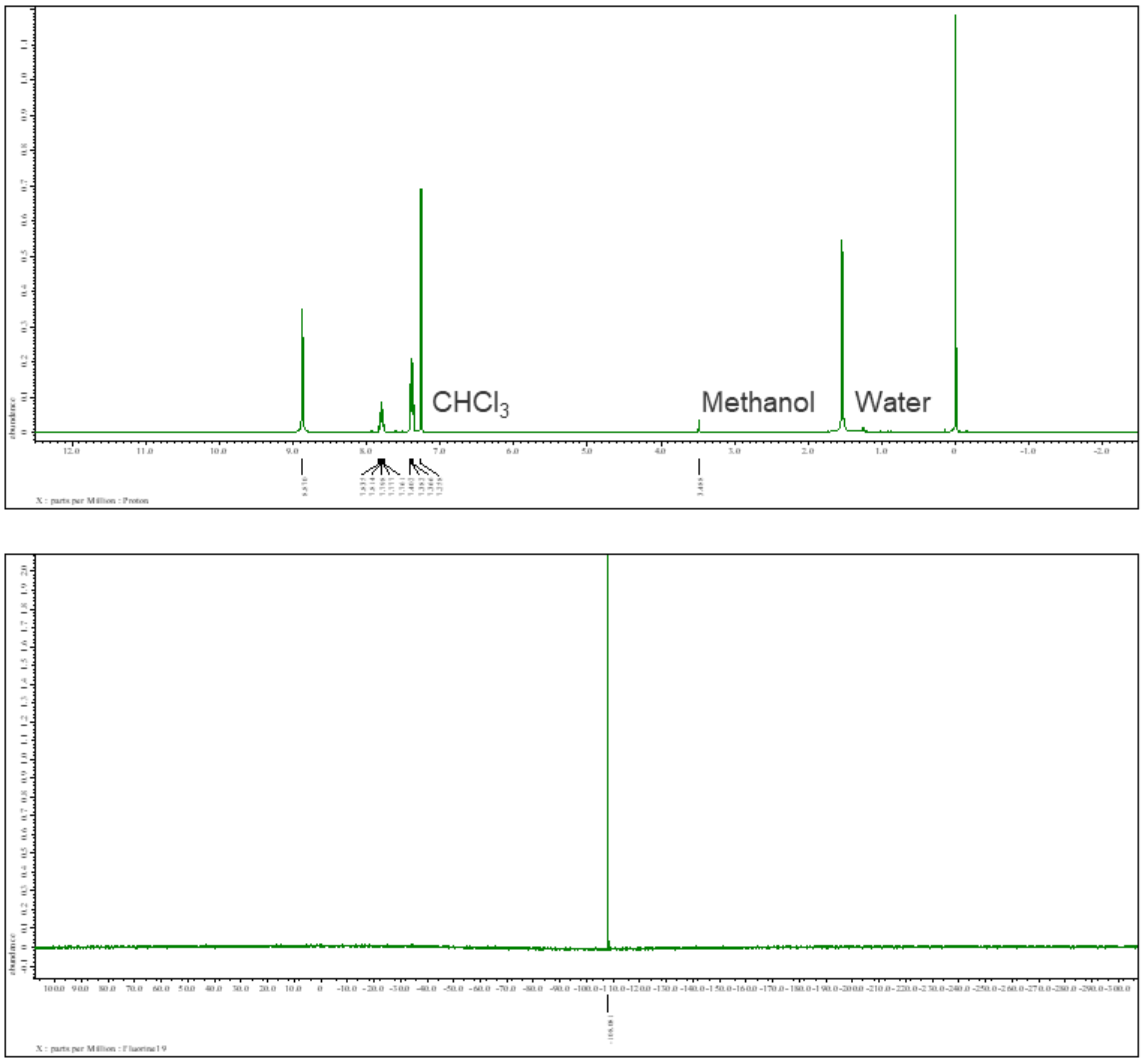

Figure 2-3. ^{1}H NMR (above) and ^{19}F NMR (bottom) spectra (9.4 T, $CDCl_3$) of H_2F_8TPP.

2-2-5-2. Synthesis of ZnF_8TPP

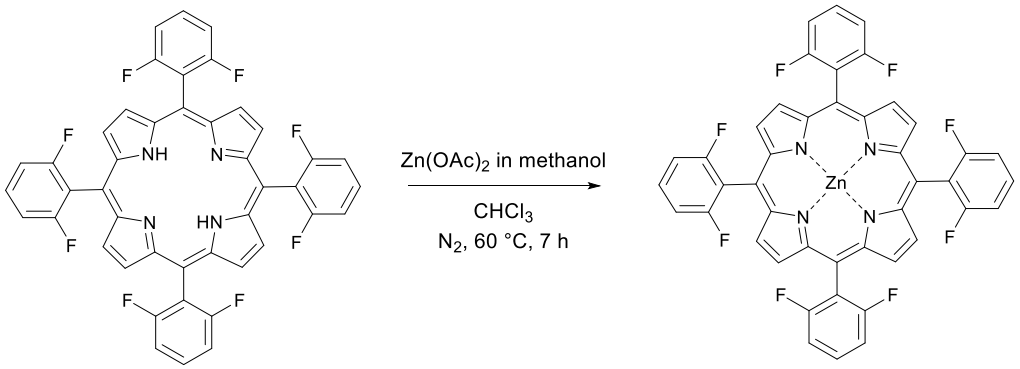

Figure 2-4. Synthetic scheme of ZnF_8TPP.

A saturated solution of zinc acetate in methanol (2 mL) was added to H_2F_8TPP (50 mg) in $CHCl_3$ (10 mL). The reaction mixture was refluxed for 7 hours. The progress of the reaction was confirmed by the disappearance of the Q-band in UV-Vis absorption measurements. After the reaction, the obtained crude was filtered, washed with water, dried over anhydrous Na_2SO_4, and purified by silica gel column chromatography (eluent: chloroform). Yield: 54%. ^1H NMR (400 MHz, $CDCl_3$, TMS): δ = 7.36-7.41 (t, 8H), 7.76-7.84 (quin, 4H), 8.97 (s, 8H). ^{19}F NMR (376 MHz, $CDCl_3$) δ = -108.40 (s, 8F). MALDI-TOF-MAS (dithranol, *m/z*): calcd: 820.09, Found: 820.17.

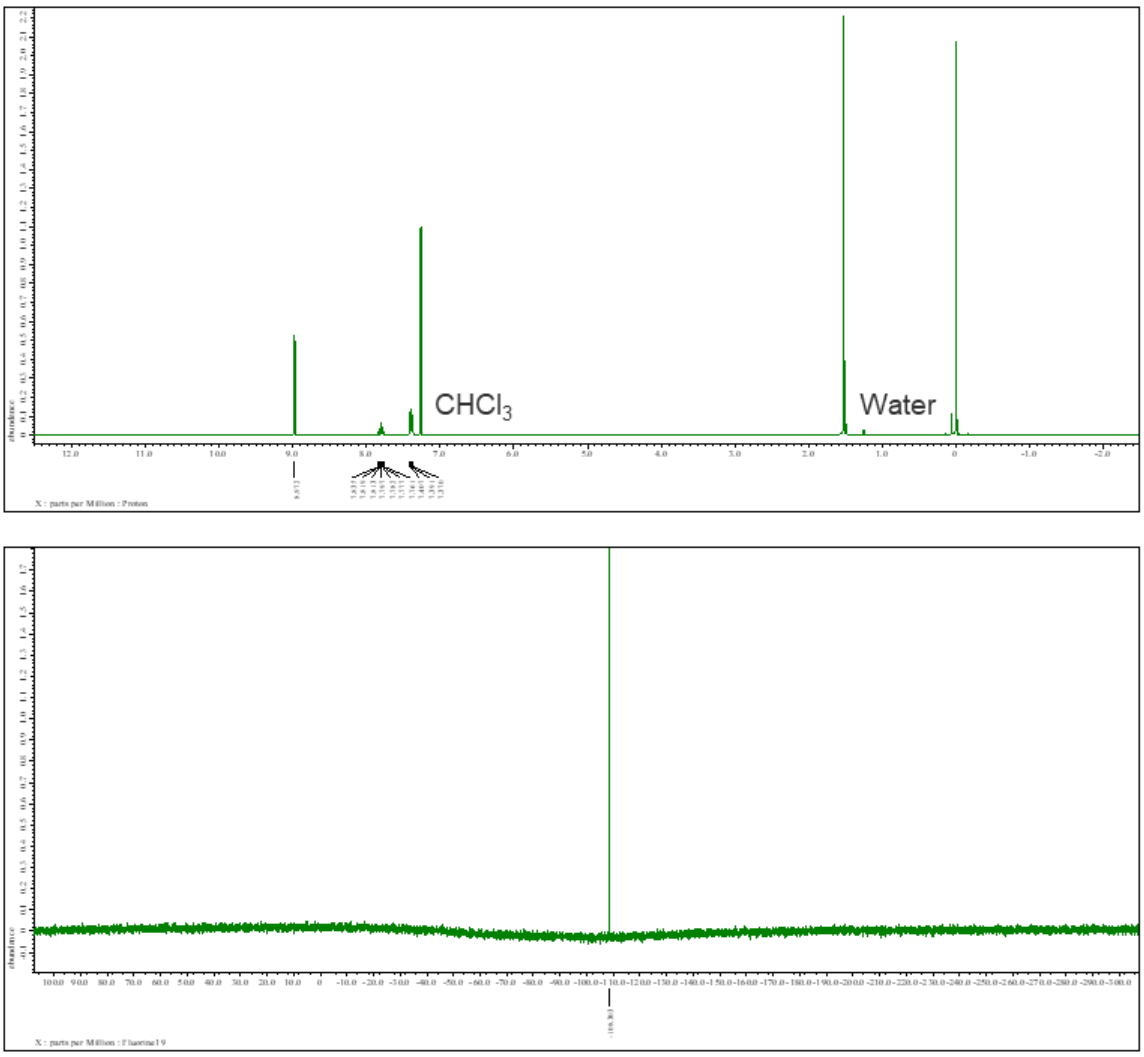

Figure 2-5. ^{1}H NMR (above) and ^{19}F NMR (bottom) spectra (9.4 T, $CDCl_3$) of ZnF_8TPP.

2-2-5-3. Synthesis of $ZnF_{20}TPP$

Figure 2-6. Synthetic scheme of $ZnF_{20}TPP$.

A saturated solution of zinc acetate in methanol (2 mL) was added to $H_2F_{20}TPP$ (50 mg) in $CHCl_3$ (10 mL). The reaction mixture was refluxed for 11.5 hours. The progress of the reaction was confirmed by the disappearance of the Q-band in UV-Vis absorption measurements. After the reaction, the obtained crude was filtered, washed with water, dried over anhydrous Na_2SO_4, and purified by silica gel column chromatography (eluent: chloroform/hexane (2:1 v/v)). Several reprecipitations (methanol/water) were performed to obtain the final compound. Yield: 68%. ^1H NMR (400 MHz, $CDCl_3$, TMS): δ = 9.00 (s, 8H). ^{19}F NMR (376 MHz, $CDCl_3$) δ = -136.63-136.70 (d, 8F), -151.66-151.72 (d, 4F), -161.48-161.70 (t, 8F). MALDI-TOF-MAS (dithranol, *m/z*): calcd: 1035.97, Found: 1035.87.

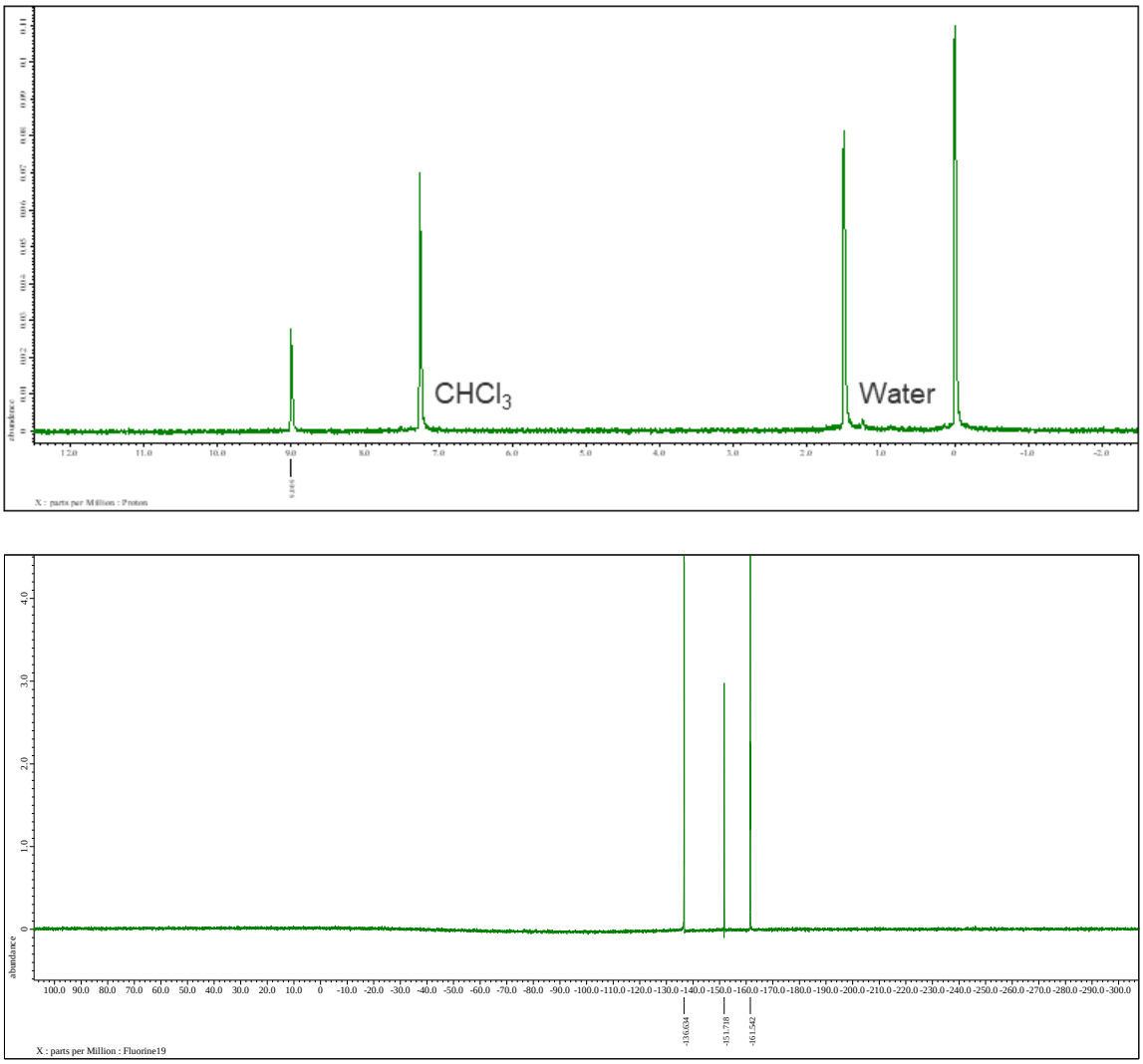

Figure 2-7. ^{1}H NMR (above) and ^{19}F NMR (bottom) spectra (9.4 T, $CDCl_3$) of $ZnF_{20}TPP$.

2-3. Results and discussion

2-3-1. General characterizations of porphyrins in toluene solution

The electronic structures of porphyrins were characterized in toluene by measuring absorption and fluorescence spectra at room temperature and phosphorescence spectra at 77 K (Figure 2-8). It is well documented that Zn porphyrins have approximate D_{4h} symmetry, with two highest occupied molecular orbital (HOMO)s and two lowest unoccupied molecular orbital (LUMO)s degenerated, but in free-base porphyrins, the symmetry drops to D_{2h}, and the HOMO and LUMO degenerations are resolved. Accordingly, ZnTPP showed one prominent absorption peak in the Q-band region, whereas H_2TPP showed separated peaks due to the symmetry breaking. The absorption and fluorescence peaks of free-base and Zn porphyrins in toluene were slightly blue-shifted by introducing the fluorine substituents due to the stabilization of HOMOs by fluorine substitution via inductive effect[17]. A similar substituent effect was also observed in the triplet state, where the phosphorescence peak positions of free-base and Zn porphyrins were blue-shifted by the fluorine substitution.

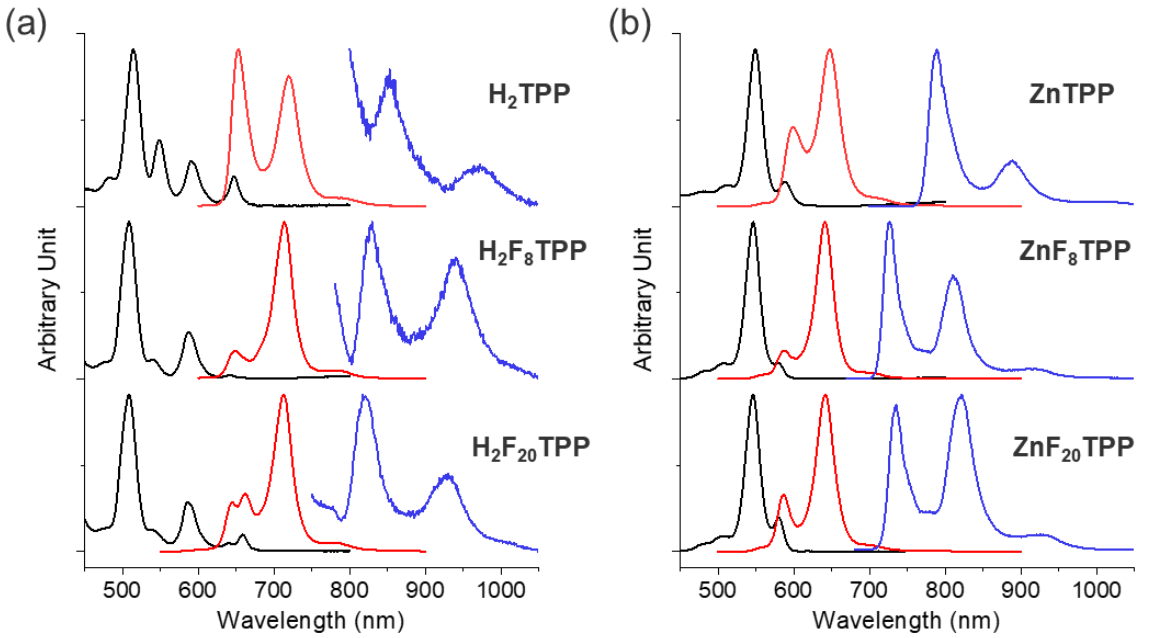

Figure 2-8. UV-vis absorption (black) and fluorescence (red) spectra at room temperature and phosphorescence spectra at 77 K (blue) of (a) H_2TPP, H_2F_8TPP and $H_2F_{20}TPP$ (top to bottom), (b) ZnTPP, ZnF_8TPP and $ZnF_{20}TPP$ (top to bottom) in toluene (20 μM for UV-vis absorption and fluorescence, 1 mM for phosphorescence). The shoulders on the short wavelength side of the phosphorescence spectra of free-base porphyrins are due to fluorescence.

2-3-2. General characterizations of porphyrins in *β*-estradiol matrix

To characterize the room-temperature polarization properties, all the porphyrins were dispersed in a *β*-estradiol glass matrix at room temperature. *β*-estradiol was employed since its rigid room-temperature glass has the excellent ability to disperse various dyes and to avoid the oxygen quenching of the photo-excited triplet state.[18,19] 0.1 mol% of porphyrins were dissolved in a *β*-estradiol melt at 300 ℃ above the melting point of *β*-estradiol (T_m = 176 ℃) and then quenched with liquid nitrogen (Figure 2-9). This process provided room-temperature glass with high transparency doped with porphyrins. Powder X-ray diffraction (PXRD) measurements of the porphyrin-doped *β*-estradiol samples did not show any sharp crystalline peaks, confirming the amorphous structure of the glass matrix (Figure 3-9).

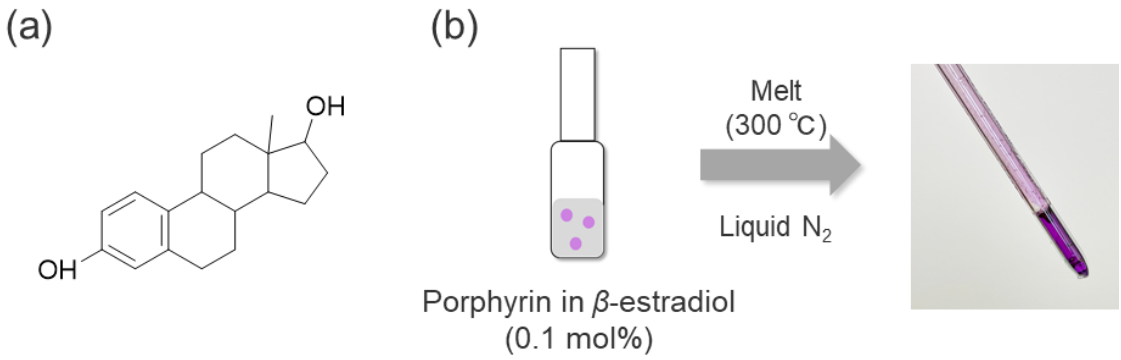

Figure 2-9. (a) Chemical structure of *β*-estradiol. (b) Picture of *β*-estradiol glass doped with 0.1 mol% $ZnF_{20}TPP$.

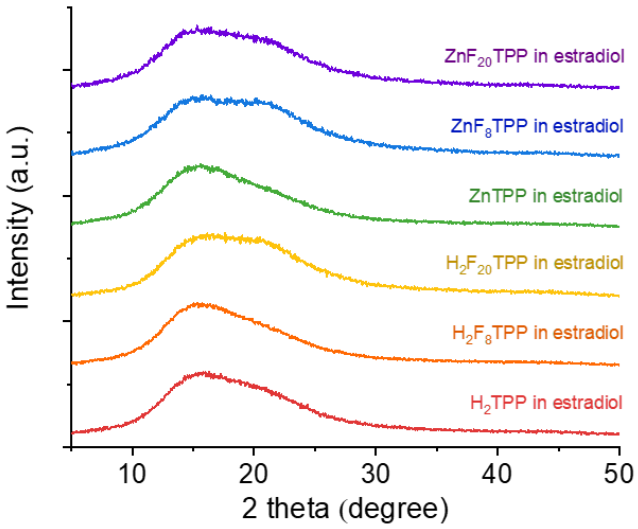

Figure 2-10. PXRD patterns of *β*-estradiol glass doped with 0.1 mol% H_2TPP (red), H_2F_8TPP (orange), $H_2F_{20}TPP$ (yellow), ZnTPP (green), ZnF_8TPP (blue) and $ZnF_{20}TPP$ (purple).

The dispersibility of the porphyrins in the *β*-estradiol glass matrix was examined by comparing absorption and fluorescence spectra of the porphyrins in toluene solution, *β*-estradiol glass, and neat solid at room temperature. The absorption spectra of all the porphyrins were red-shifted and broadened in the neat state compared to the solution state, suggesting the presence of inter-chromophore interactions in the neat sample (Figure 2-11). The absorption spectra of the three free-base porphyrins in *β*-estradiol glass did not change from the solution state, suggesting that they are in the molecularly dispersed state. The three Zn porphyrins showed a change in the shape of their spectra in *β*-estradiol glass compared to the solution state, but the broadening did not occur in *β*-estradiol glass as much as in the neat state. The change of the absorption spectra would be due to the slight structural distortion in *β*-estradiol glass.

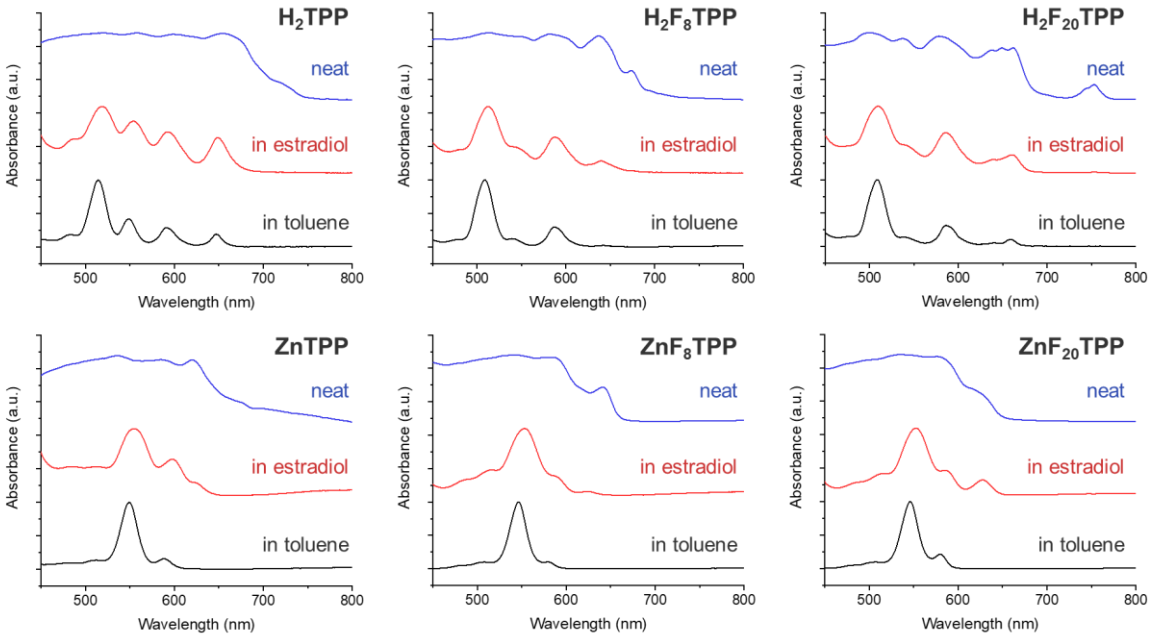

Figure 2-11. UV−vis absorption spectra of (a) H_2TPP, (b) H_2F_8TPP, (c) $H_2F_{20}TPP$, (d) ZnTPP, (e) ZnF_8TPP and (f) $ZnF_{20}TPP$ in toluene (20 μM, black line) in *β*-estradiol glass (0.1 mol%, red line) and neat solid (blue line).

In the fluorescence spectra, all the porphyrins showed a red shift in the neat state compared to the solution state, but the shape of the spectra in the *β*-estradiol glass was similar to that in the solution state, supporting their molecularly dispersed state in the glass (Figure 2-12).

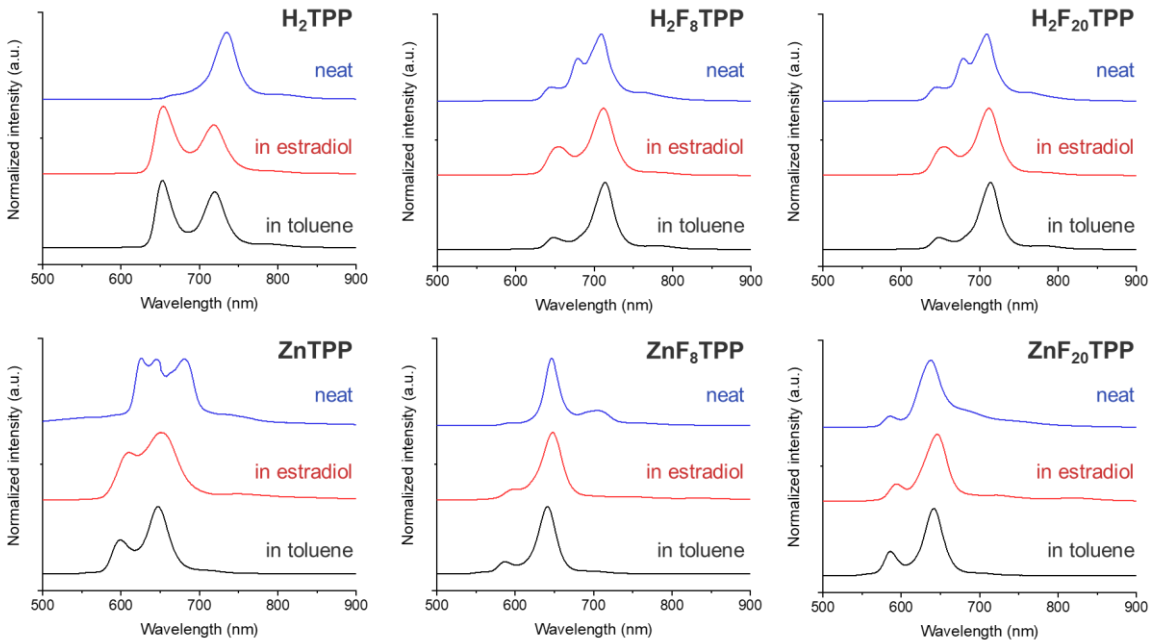

Figure 2-12. Fluorescence spectra of (a) H_2TPP, (b) H_2F_8TPP, (c) $H_2F_{20}TPP$, (d) ZnTPP, (e) ZnF_8TPP and (f) $ZnF_{20}TPP$ in toluene (20 μM, black line), in *β*-estradiol glass (0.1 mol%, red line) and neat solid (blue line). Excitation wavelength was 400-420 nm.

The lifetime of lowest triplet state of porphyrins was measured by transient absorption (Figure 2-13). It was found that the lifetime of free-base porphyrins was about a millisecond, whereas the lifetime of zinc porphyrins was about tens of milliseconds. The longer lifetime of the free-base porphyrin, despite the presence of the heavy atom effect of the zinc atom, may be due to the difference of the mobility of porphyrin ring.

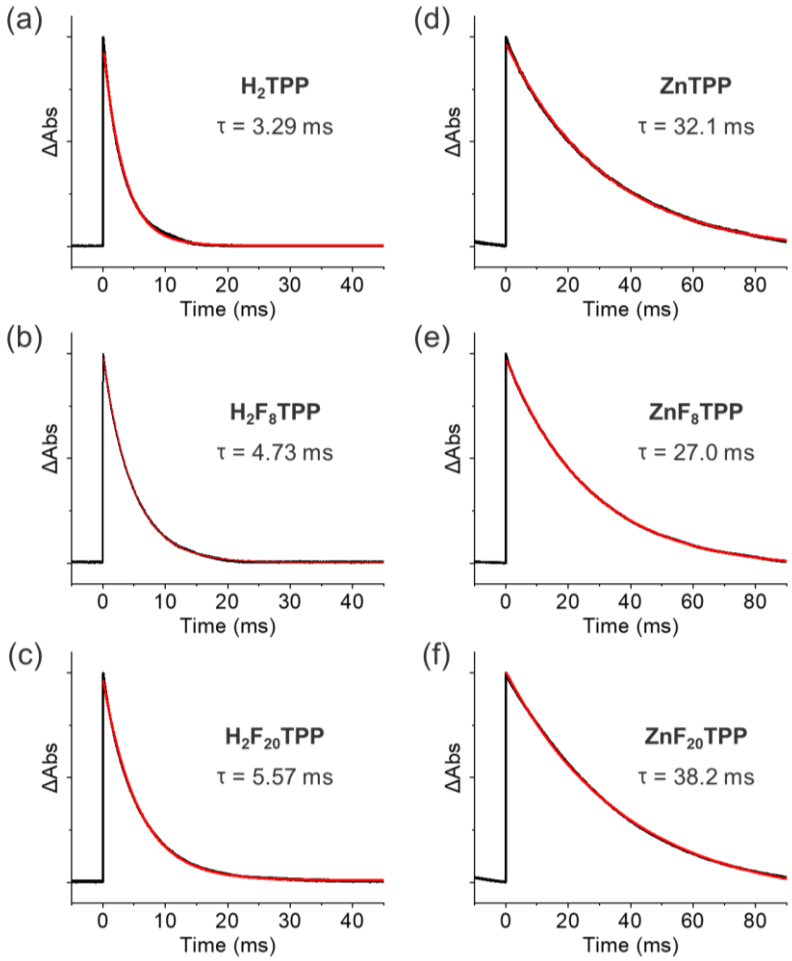

Figure 2-13. Transient absorption decays (black lines) of (a) H_2TPP (λ_{ex} = 515 nm, λ_{em} = 490 nm), (b) H_2F_8TPP (λ_{ex} = 515 nm, λ_{em} = 450 nm), (c) $H_2F_{20}TPP$ (λ_{ex} = 515 nm, λ_{em} = 460 nm), (d) ZnTPP (λ_{ex} = 550 nm, λ_{em} = 510 nm), (e) ZnF_8TPP (λ_{ex} = 550 nm, λ_{em} = 510 nm) and (f) $ZnF_{20}TPP$ (λ_{ex} = 550 nm, λ_{em} = 510 nm) in β-estradiol glass (0.1 mol%). The results of single exponential fittings are shown as red lines.

2-3-3. Spin properties of porphyrins in triplet states

The Time-resolved EPR spectra and fitting results of the porphyrins doped in *β*-estradiol glass at room temperature are shown in Figure 2-14. The relative population, zero-field splitting parameters, and spin–lattice relaxation time T_1 are summarized in Table 2-1. Since the lifetime of triplet excited state of porphyrins was in the millisecond scale (Figure 2-13), the decay constant of time-resolved EPR was treated as T_1. It has been known that in-plane sublevels are dominantly populated for free base porphyrins due to the in-plane components of spin–orbit coupling (SOC).[20] We also observed the in-plane (P_x and P_y) selective population for H_2TPP and H_2F_8TPP. For H_2F_{20}TPP, some population of out-of-plane (P_z) sublevel was also generated.

Since *n* and *σ* orbitals of the F atoms are oriented in various directions, they can also contribute to the production of P_z population.[11,21] Due to the strong interaction between *d*-orbital of central Zn ion and *π** orbital of the porphyrin ligand, the strong out-of-plane component of SOC is generated ($P_x : P_y : P_z = 0 : 0 : 1.0$).[22] Importantly, this highly selective population of out-of-plane sublevel was maintained in the fluorinated Zn porphyrins.

The spin–lattice relaxation time T_1 was obtained by single exponential fitting of the EPR decays. As the number of fluorine substitution increases, T_1 of free-base porphyrins became shorter from 9.3 μs to 4.9 μs. This trend is consistent with the change of *D* value that became larger from 1125 MHz to 1292 MHz with the increase of the number of fluorine atoms. The similar trend, a shorter T_1 and a larger *D* value by fluorine substitution, was also observed for ZnTPP and ZnF_8TPP. It has been reported that the modulation of electron spin dipolar interaction is mainly responsible for the spin–lattice relaxation of photo-excited triplets of organic molecules without any heavy atoms, and the spin–lattice relaxation rate is proportional to the square of zero-field splittings.[23,24] Interestingly, a totally different behavior was observed for ZnF_{20}TPP that showed much longer T_1 of 1.7 μs than ZnTPP (0.30 μs) and ZnF_8TPP (0.17 μs). This unexpected result cannot be explained by the *D* value since the *D* value of ZnF_{20}TPP (961 MHz) was close to that of ZnTPP (955 MHz). Rather, this behavior can be explained by changes in the spin–orbit interaction, as discussed later. It is remarkable that ZnF_{20}TPP achieves both of the large polarization and the long T_1 over 1 μs.

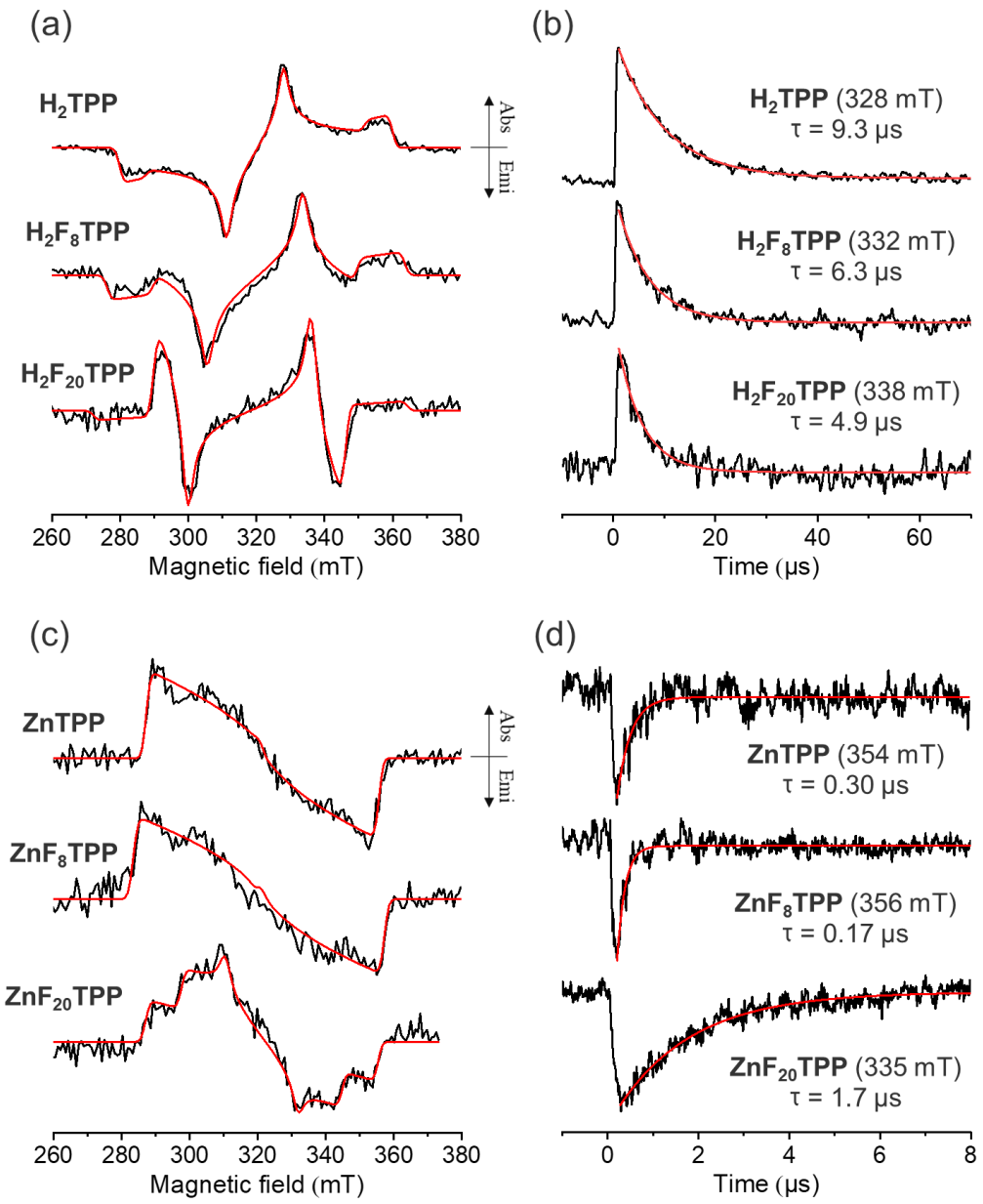

Figure 2-14. (a, c) Time-resolved EPR spectra and (b, d) decays of the EPR peaks of the free-base porphyrins and Zn porphyrins. Black lines are experimental data and red lines are fitting results. The EPR decays were recorded at 328 mT, 332 mT, 338 mT, 354 mT, 356 mT and 335 mT for H_2TPP, H_2F_8TPP, $H_2F_{20}TPP$, ZnTPP, ZnF_8TPP and $ZnF_{20}TPP$, respectively.

Table 2-1. Relative zero-field populations, zero-field splitting parameters, and spin–lattice relaxation time T_1 of the free-base and Zn porphyrins.

Compound	$P_x : P_y : P_z$	$\|D\|$ (MHz)	$\|E\|$ (MHz)	T_1 (μs)
H_2TPP	0.29 : 0.71 : 0	1125	221	9.3
H_2F_8TPP	0.18 : 0.82 : 0	1219	147	6.3
H_2F_{20}TPP	0 : 0.75 : 0.25	1292	93	4.9
ZnTPP	0 : 0 : 1.00	955	316	0.30
ZnF_8TPP	0 : 0 : 1.00	1046	352	0.17
ZnF_{20}TPP	0 : 0 : 1.00	961	121	1.7

2-3-4. Calculations of configurations of porphyrins in their triplet state

The stronger dipole-dipole interactions between electrons in the fluorinated free-base porphyrins, which is indicated by the larger *D* value,[25,26] would result in the shorter spin–lattice relaxation time T_1. It has been reported that the larger *D* value in the fluorinated Mg porphyrins is due to the enhanced mixing of $^3(a_{2u}e_g)$ and $^3(a_{1u}e_g)$ configurations by the fluorine substitution.[11] DFT calculations were performed for free-base porphyrins using B3LYP/6-31G* for geometry optimizations and B3LYP/EPR-II[27] for time-dependent DFT calculations.[28] The four frontier orbitals in the lowest triplet state are shown in Figure 2-15. In the triplet state, both HOMO and LUMO are singly occupied molecular orbital (SOMO)s, but the ground state labeling was retained for clarity. The fluorine substituents largely increased the excitation energy to the lowest triplet state (Table 2-2). The main configuration of the lowest triplet state of H_2TPP was (LUMO ← HOMO), but the contribution the (LUMO+1 ← HOMO-1) configuration (HOMO-1: the second highest molecular orbital, LUMO+1 the second lowest unoccupied molecular orbital) was increased with fluorination. The increased excitation energy to the triplet state and the enhanced contribution of the (LUMO+1 ← HOMO-1) configuration by the fluorine substitutions are consistent with the observed blue shift of the phosphorescence peaks (Figure 2-8).[11] Therefore, it was expected that the larger *D* value by the fluorine substitutions of the free-base porphyrins derives from the mixing of the configurations.

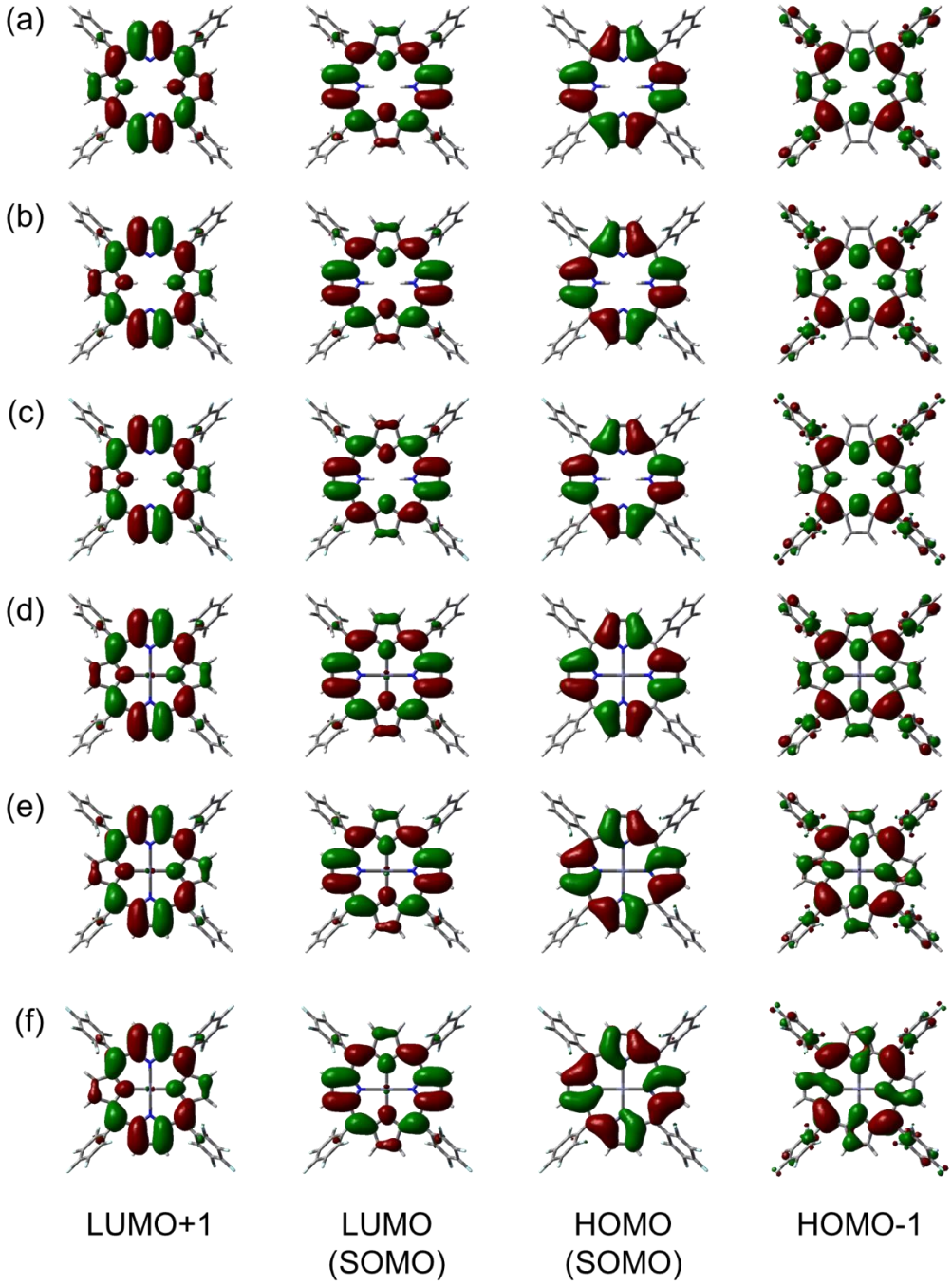

Figure 2-15. The four frontier orbitals (isovalue = 0.02) of (a) H_2TPP, (b) H_2F_8TPP, (c) $H_2F_{20}TPP$, (d) ZnTPP, (e) ZnF_8TPP and (f) $ZnF_{20}TPP$ in the lowest triplet state calculated by B3LYP/6-31G*.

Table 2-2. The excitation energies and main configurations (weight) of the porphyrins in the lowest triplet state calculated with B3LYP/SDD for Zn, EPR-II for others.

Compound	Excitation energy (eV)	HOMO → LUMO	HOMO → LUMO+1	HOMO-1 → LUMO	HOMO-1 → LUMO+1
H_2TPP	1.366	0.830	-	-	0.148
H_2F_8TPP	1.393	0.761	-	-	0.219
H_2F_{20}TPP	1.412	0.726	-	-	0.254
ZnTPP	1.649	0.421	0.421	0.075	0.075
ZnF_8TPP	1.684	0.167	0.167	0.328	0.328
ZnF_{20}TPP	1.695	0.220	0.220	0.272	0.272

2-3-5. Calculations of spin density of zinc porphyrins

The much shorter T_1 of 0.30 μs was observed for ZnTPP compared with H_2TPP (9.3 μs). Since D value of ZnTPP was smaller than that of H_2TPP, another relaxation mechanism that is not dipole-dipole interaction should be occurring to Zn porphyrins. In the case of organic molecules without heavy atoms, the effect of spin–orbit interaction on spin–lattice relaxation is known to be insignificant.[24,29] On the other hand, in the case of Zn porphyrins, the large spin–orbit interaction between the electrons and the heavy Zn atom may have a significant effect on spin–lattice relaxation. The T_1 of ZnF_8TPP (0.17 μs) was shorter compared to that of ZnTPP (0.30 μs). The DFT calculation results show that the mixing of the configurations were observed by fluorine substitution, which may result in the increase of D value and the shortening of T_1, similar to the case of free-base porphyrins.

On the other hand, by increasing the number of fluorine atoms, a significantly longer T_1 of 1.7 μs was observed for ZnF_{20}TPP than ZnTPP and ZnF_8TPP, which cannot be explained by the change of D value. To understand the observed large elongation of T_1 by the fluorine substitutions on Zn porphyrins, spin density in their lowest triplet state was estimated. The spin density of Zn atoms in ZnF_{20}TPP was significantly reduced compared to other Zn porphyrins (Figure 2-16, Table 2-3). Therefore, the long T_1 of ZnF_{20}TPP can be attributed to the electron-withdrawing fluorine substituents that reduce the spin density on Zn atoms and weaken the spin–orbit interaction. In free-base porphyrins, no large change in spin density was observed due to fluorine substitution, suggesting that the mixing of configurations does not affect the spin density significantly.

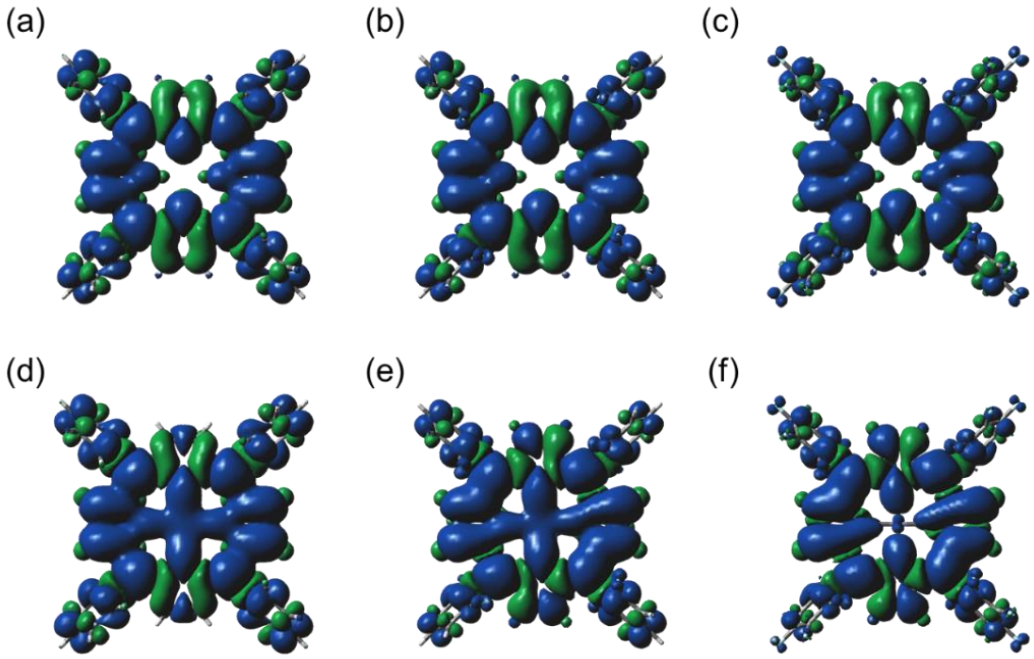

Figure 2-16. The spin density (isovalue = 0.00015) of (a) H_2TPP, (b) H_2F_8TPP, (c) H_2F_{20}TPP, (d) ZnTPP, (e) ZnF_8TPP and (f) ZnF_{20}TPP in the lowest triplet state calculated by B3LYP/6-31G*.

Table 2-3. Spin density of the porphyrins in the lowest triplet state calculated with B3LYP/6-31G*.

Compound	Porphyrin ring	Phenyl ring	Zn atom
H_2TPP	1.9901	0.0099	-
H_2F_8TPP	1.9987	0.0013	-
H_2F_{20}TPP	1.9980	0.0020	-
ZnTPP	1.9739	0.0125	0.0136
ZnF_8TPP	1.9785	0.0122	0.0093
ZnF_{20}TPP	1.9896	0.0136	-0.0031

2-4. Conclusion

In this chapter, it is succeeded to obtain longer spin–lattice relaxation time T_1 was obtained while maintaining the large polarization ($P_x : P_y : P_z = 0 : 0 : 1.0$) of metalloporphyrins. Although the spin–orbit coupling, that generates the polarization, shortens the relaxation time, the relaxation time can be successfully extended keeping a large polarization by optimizing the strength of the interaction. Metalloporphyrins have been considered to be difficult to utilize as qubits at room temperature, but it suggested that this problem can be overcome by the proper molecular design.

2-5. References

(1) Spellane, P. J.; Gouterman, M.; Antipas, A.; Kim, S.; Liu, Y. C. Porphyrins. 40. Electronic spectra and four-orbital energies of free-base, zinc, copper, and palladium tetrakis(perfluorophenyl)porphyrins. *Inorganic Chemistry* **2002,** *19*, 386-391.

(2) Berg, K.; Selbo, P. K.; Weyergang, A.; Dietze, A.; Prasmickaite, L.; Bonsted, A.; Engesaeter, B. O.; Angell-Petersen, E.; Warloe, T.; Frandsen, N.; Hogset, A. Porphyrin-related photosensitizers for cancer imaging and therapeutic applications. *J Microsc* **2005,** *218*, 133-147.

(3) Hamachi, T.; Nishimura, K.; Kouno, H.; Kawashima, Y.; Tateishi, K.; Uesaka, T.; Kimizuka, N.; Yanai, N. Porphyrins as Versatile, Aggregation-Tolerant, and Biocompatible Polarizing Agents for Triplet Dynamic Nuclear Polarization of Biomolecules. *J. Phys. Chem. Lett.* **2021,** *12*, 2645-2650.

(4) Gonen, O.; Levanon, H. Time-Resolved EPR Spectroscopy of Electron Spin Polarized ZnTPP Triplets Oriented in a Liquid Crystal. *J. Phys. Chem.* **1985,** *89*, 1637-1643.

(5) Gnezdiiov, O. I.; Mambetov, A. E.; Obynochny, A. A.; Salikhov, K. M. Time-Resolved EPR Spin Exchange in Study of Electron Spin Polarization and Mixed Solutions of Porphyrin Stable Free Radicals. *Appl. Magn. Reson.* **2003,** *25*, 157-198.

(6) Yamauchi, S.; Takahashi, K.; Islam, S. S. M.; Ohba, Y.; Tarasov, V. Time-Resolved High-Frequency EPR Studies on Magnesium and Zinc Tetraphenylporphines in Their Lowest Excited Triplet States. *J. Phys. Chem. B* **2010,** *114*, 14559-14563.

(7) Yamabayashi, T.; Atzori, M.; Tesi, L.; Cosquer, G.; Santanni, F.; Boulon, M. E.; Morra, E.; Benci, S.; Torre, R.; Chiesa, M.; Sorace, L.; Sessoli, R.; Yamashita, M. Scaling Up Electronic Spin Qubits into a Three-Dimensional Metal-Organic Framework. *J. Am. Chem. Soc.* **2018,** *140*, 12090-12101.

(8) Yu, C. J.; Krzyaniak, M. D.; Fataftah, M. S.; Wasielewski, M. R.; Freedman, D. E. A concentrated array of copper porphyrin candidate qubits. *Chem. Sci.* **2019,** *10*, 1702-1708.

(9) von Kugelgen, S.; Krzyaniak, M. D.; Gu, M.; Puggioni, D.; Rondinelli, J. M.; Wasielewski, M. R.; Freedman, D. E. Spectral Addressability in a Modular Two Qubit System. *J. Am. Chem. Soc.* **2021,** *143*, 8069-8077.

(10) Hamachi, T.; Nishimura, K.; Tateishi, K.; Uesaka, T.; Kimizuka, N.; Yanai, N. Porphyrins as Versatile, Aggregation-Tolerant, and Biocompatible Polarizing Agents for Triplet Dynamic Nuclear Polarization of Biomolecules. *J. Phys. Chem. Lett.* **2021,** *12*, 2645-2650.

(11) Yamauchi, S.; Matsukawa, Y.; Ohba, Y.; Iwaizumi, M. State Mixings in the Excited Triplet and Singlet States of Fluorine-Substituted Magnesium Tetraphenylporphines Studied by Optical and Time-Resolved EPR Spectroscopy. *Inorg. Chem.* **1996,** *35*, 2910-2914.

(12) MATLAB, version 9.5.0.944444 (R2018b), The MathWorks Inc., Natick, Massachusetts,. **2018**.

(13) Stoll, S.; Schweiger, A. EasySpin, a comprehensive software package for spectral simulation and analysis in EPR. *J. Magn. Reson.* **2006,** *178*, 42-55.

(14) GaussView, Version 6.0.16, Dennington, Roy; Keith, Todd A.; Millam, John M. Semichem Inc., Shawnee Mission, KS, . **2016**.

(15) Lindsey, J. S.; Schreiman, I. C.; Hsu, H. C.; Kearney, P. C.; Marguerettaz, A. M. Rothemund and Adler-Longo Reactions Revisited: Synthesis of Tetraphenylporphyrins under Equilibrium Conditions. *J. Org. Chem.* **1987,** *52*, 827-836.

(16) Das, S. K.; Song, B.; Mahler, A.; Nesterov, V. N.; Wilson, A. K.; Ito, O.; D'Souza, F. Electron Transfer Studies of High Potential Zinc Porphyrin–Fullerene Supramolecular Dyads. *J. Phys. Chem. C* **2014,** *118*, 3994-4006.

(17) Spellane, P. J.; Gouterman, M.; Antipas, A.; Kim, S.; Liu, Y. C. Porphyrins. 40. Electronic spectra and four-orbital energies of free-base, zinc, copper, and palladium tetrakis(perfluorophenyl)porphyrins. *Inorg. Chem.* **1980,** *19*, 386-391.

(18) Hirata, S.; Totani, K.; Zhang, J.; Yamashita, T.; Kaji, H.; Marder, S. R.; Watanabe, T.; Adachi, C. Efficient Persistent Room Temperature Phosphorescence in Organic Amorphous Materials under Ambient Conditions. *Adv. Funct. Mater.* **2013,** *23*, 3386-3397.

(19) Hirata, S.; Totani, K.; Yamashita, T.; Adachi, C.; Vacha, M. Large reverse saturable absorption under weak continuous incoherent light. *Nat. Mater.* **2014,** *13*, 938-946.

(20) Yamauchi, S.; Tanabe, M.; Ohba, Y.; Sugisaki, K.; Toyota, K.; Sato, K.; Takui, T.; Saltsman, I. Complete assignment of spin sublevels in the lowest excited triplet state of corrole compounds by time-resolved EPR spectroscopy. *Chem. Phys. Lett.* **2012,** *521*, 64-68.

(21) Levanon, H.; Vega, S. Analysis of the transient EPR signals in the photoexcited triplet state. Application to porphyrin molecules. *J. Chem. Phys.* **1974,** *61*, 2265-2274.

(22) Ishii, K.; Abiko, S.; Kobayashi, N. Time-Resolved Electron Spin Resonance of Gallium and Germanium Porphyrins in the Excited Triplet State. *Inorg. Chem.* **2000,** *39*, 468-472.

(23) Maruani, J. On anisotropic saturation of ESR lines in molecular triplet states. *Chem. Phys. Lett.* **1970,** *7*, 29-30.

(24) Yu, H. L.; Lin, T. S.; Weissman, S. I.; Sloop, D. J. Time resolved studies of pentacene triplets by electron spin echo spectroscopy. *J. Chem. Phys.* **1984,** *80*, 102-107.

(25) Fischer, P. H. H.; Denison, A. B. Anisotropic saturation of the electron spin resonance in the photo-excited triplet state of pyrene-*d*-10. *Mol. Phys.* **1969,** *17*, 297-304.

(26) Richert, S.; Limburg, B.; Anderson, H. L.; Timmel, C. R. On the Influence of the Bridge on Triplet State Delocalization in Linear Porphyrin Oligomers. *J. Am. Chem. Soc.* **2017,** *139*, 12003-12008.

(27) Rega, N.; Cossi, M.; Barone, V. Development and validation of reliable quantum mechanical approaches for the study of free radicals in solution. *J. Chem. Phys.* **1996,** *105*, 11060-11067.

(28) Kay, C. W. M. The Electronic Structure of the Photoexcited Triplet State of Free-Base (Tetraphenyl)porphyrin by Time-Resolved Electron-Nuclear Double Resonance and Density Functional Theory. *J. Am. Chem. Soc.* **2003,** *125*, 13861-13867.

(29) Ong, J.-L.; Sloop, D. J.; Lin, T.-S. Deuteration effect on the spin dynamics of the photo-excited triplet state of pentacene in p-terphenyl crystals. *Chem. Phys. Lett.* **1995,** *241*, 540-546.

Chapter 3. Guest responsive triplet quantum coherence in a flexible MOF towards quantum sensing

3-1. Introduction

Among the quantum technologies, quantum sensing will have an impact on a wide range of fields, including chemistry[1] and biology[2] using the quantum properties of qubit. An important parameter for quantum sensing is the time over which the coherence of spin correlations is preserved.[3] Since the sensitivity of quantum sensing depends on coherence time, a long coherence time is highly desirable.[4]

Molecular qubits have uniform structures and can be precisely controlled, which is advantageous for quantum sensor.[5-18] Furthermore, their small size allows them to closely approach the target analyte. Although some radical is known to show long coherence time (T_2) over several microseconds,[19] it is still not easy to achieve microsecond-scale T_2 at room temperature for many molecular qubits. Furthermore, it remains unclear how to make molecular qubits responsive and selective to specific analytes.

One strategy to gain responsivity to analytes is employing porous materials such as metal–organic frameworks (MOFs) or covalent–organic frameworks (COFs). There are few examples of quantum sensing using MOFs containing paramagnetic species.[20-21] In these reports, the hyperfine interaction between electron spins and nuclear spins was used to sense analytes, but this method left a major challenge in that it could not distinguish compounds composed of the same nuclear species, such as benzene and toluene, for example. Another way to sense analytes are using the modulation of the coherence time, known as relaxometry. However, since qubits exposed in the nanopores of MOFs and COFs can undergo significant relaxation from the motion of the qubit itself, it is necessary to design the environment around the qubit appropriately to have a sufficiently long T_2.

The photoexcited triplet state of organic dyes is an excellent candidate for qubits because they can create highly polarized electronic states even at room temperature (Figure 3-1a).[22-25] Furthermore, it has long been known that the triplet state of pentacene doped in dense *p*-terphenyl crystals exhibits a long T_2 on the microsecond scale even at room temperature.[22] However, except for a few pioneering examples,[7, 12-13, 17] photoexcited triplets are largely unexplored in the context of qubits and have never been used for quantum sensing because they are buried in dense matrix

crystals and cannot approach the target analyte. As with other paramagnetic qubits, the response of triplet qubits to target analytes based on hyperfine spectroscopy and relaxometry is expected.[20] The characteristic of triplets is that they have an anisotropic and large (~GHz) zero-field splitting (ZFS) interaction, so that the molecular motion of the qubit causes a pronounced relaxation based on orientation change with respect to the magnetic field.[26] Therefore, when target analytes are incorporated into the nanopores and the environment around the qubit changes, it is expected that the changes can be sensitively captured through relaxometry.

Chapter 3 describes a material design towards quantum sensing using triplet qubits and MOFs. MOFs make the analyte molecules accessible to triplet qubits, and the coherence time T_2 of the triplet qubits is changed by flexibly changing the MOF structure through adsorption of the guest analyte. This method can show different T_2 responses for a wider variety of organic compounds.

MIL-53 was selected as a flexible MOF that exhibits guest-responsive structural change, termed breathing behavior.[27-29] The N-substituted tetracene, 5,12-diazatetracene (DAT), was employed as the triplet qubit.[25] Compared with conventional pentacene, DAT has the advantages of good solubility and superior air-stability.

A variety of additional guest analyte molecules were introduced into DAT-accommodated MIL-53 and evaluated T_2 of the DAT triplet using pulsed EPR (Figure 3-1b and 3-1c). Analyte molecules have nuclear spins, such as that on protons, which usually work as noise to shorten T_2. Interestingly, the T_2 of DAT in MIL-53 shows various T_2 depending on the type of guest analyte, with the longest T_2 being longer than 1 μs at room temperature. This can be mainly attributed to the local molecular density around the DAT and has led to a new concept of quantum sensing by controlling the dynamics of qubits.

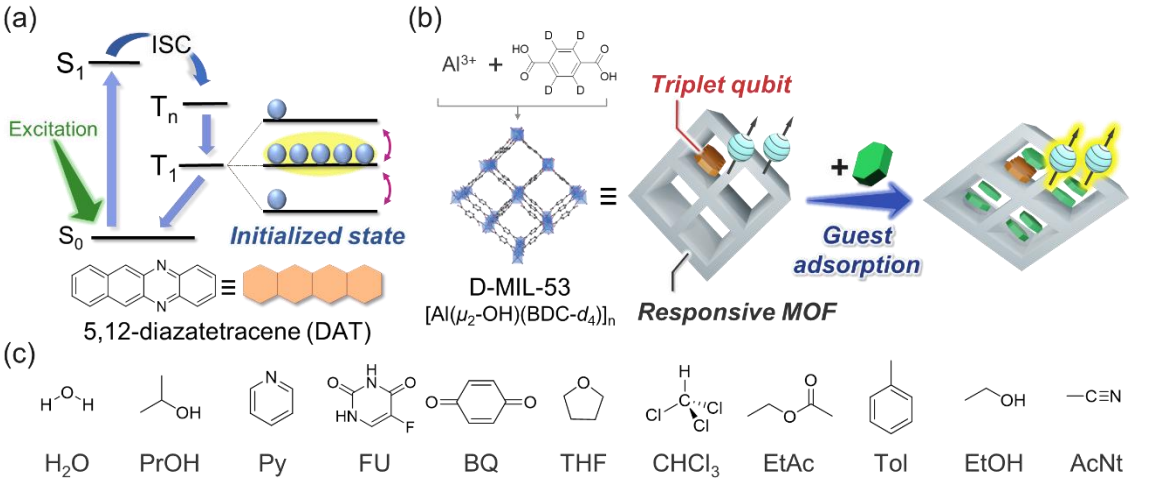

Figure 3-1. (a) Initialization of the triplet qubit. Spin polarization between two of the three triplet sublevels generated by photoexcitation and following spin-selective intersystem crossing (ISC) can be used as qubits. (b) Response of triplet qubits to the guest-induced structural change of a flexible MOF. DAT and D-MIL-53 are employed as triplet qubits and the flexible MOF, respectively. (c) Guest analyte molecules used in this research. H_2O, 2-propanol (PrOH), pyridine (Py), 5-fluorouracil (FU), *p*-benzoquinone (BQ), THF, chloroform ($CHCl_3$), ethyl acetate (EtAc), toluene (*h*-Tol), ethanol (EtOH), and acetonitrile (AcNt) are introduced to D-MIL-53⊃DAT.

3-2. Experimental section

3-2-1. Materials

All reagents were used as received unless otherwise noted. Aluminum chloride hexahydrate ($AlCl_3 \cdot 6H_2O$) and *p*-benzoquinone (BQ) were purchased from Sigma-Aldrich. *p*-Terphenyl was purchased from FUJIFILM Wako Pure Chemical and purified by zone melting. *o*-Phenylenediamine, potassium dichromate ($K_2Cr_2O_7$), and ethylenediamine-*N,N,N′,N′*-tetraacetic acid, tetrasodium salt tetrahydrate (Na_4-EDTA) were purchased from FUJIFILM Wako Pure Chemical. 2,3-Dihydroxynaphthalene and 5-fluorouracil (FU) were purchased from TCI. Glacial acetic acid and oxalic acid dihydrate were purchased from Kishida Chemical. Terephthalic acid-d_4 (BDC-d_4) (ring-d_4, 98 atom%) was purchased from Cambridge Isotope Laboratories, Inc. 5,12-Diazatetracene (DAT) and deuterated MIL-53 (D-MIL-53) were prepared following the literature with slight modifications.[25, 30]

3-2-2. Characterizations

Solution-state ^{1}H-NMR (400 MHz) spectra were recorded on a JEOL JNM-ECZ400 spectrometer using tetramethylsilane (TMS) as the internal standard. Elemental analysis was carried out using a Yanaco CHN Corder MT-5 at the Elemental Analysis Center, Kyushu University. UV–Vis absorption spectra were obtained on a JASCO V-670 spectrophotometer. Fluorescence spectra were obtained using a JASCO FP-8700 fluorescence spectrometer. Thermogravimetric analysis curves were obtained on a Rigaku Thermo Plus EVO2 under N_2.

3-2-3. Time-resolved EPR measurements and pulsed EPR measurements

EPR measurements were performed on a Bruker E680 operated at X-band (~9.6 GHz) using 2 mm glass capillaries placed into 4 mm quartz EPR tubes. A Bruker standard dielectric resonator was used as a microwave resonator (ER4118X-MD5W) using TE011 mode. The samples were excited at a wavelength of 532 nm, excitation light intensity of 2–3 mJ/pulse, pulse width of 5–12 ns, and repetition rate of 30 Hz using a Spectra-Physics Quanta-Ray YAG laser. The microwave intensity were ~0.06 mW for time-resolved measurements. For pulsed EPR measurements, ~2 μW microwave was amplified by a 1 kW amplifier and then attenuated by an attenuator to π/2 pulses with a pulse width of 16 ns. 16 ns and 24 ns microwave pulses were used as π/2 pulse and π pulse, respectively. Temperature was controlled by flowing liquid helium using an Oxford Mercury iTC. The echo decay measurements were conducted using a two-pulse spin echo sequence. The first π/2 pulse was irradiated 0.3 μs after laser excitation and the pulse interval τ was varied. T_2 was obtained by single exponential fitting of decay curves.

3-2-4. Synthesis of DAT

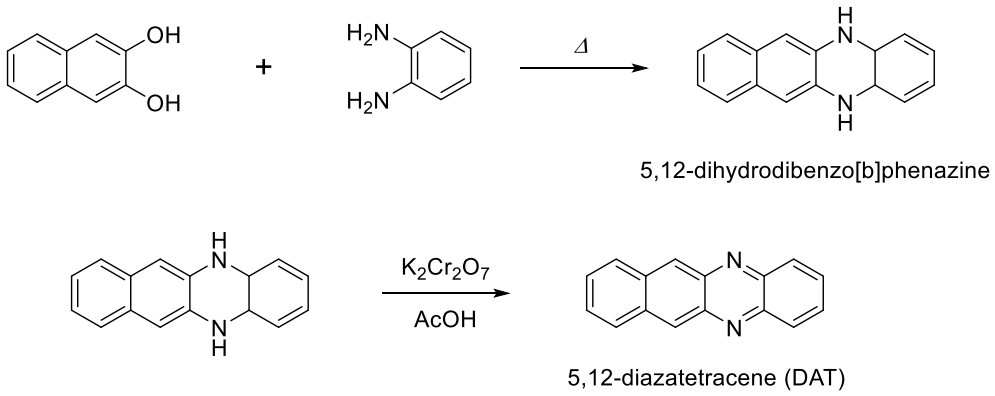

Figure 3-2. Synthetic scheme of DAT.

A mixture of 2,3-dihydroxynaphthalene (2.00 g, 12.5 mmol) and *o*-phenylenediamine (1.35 g, 12.5 mmol) was put into a 50 mL flask and heated to 200 ℃ for 1 h under N_2 atmosphere. After filtering and washing the crude product with methanol, 5,12-dihydrodibenzo[b]phenazine was obtained as a yellow solid and used in the next step without further purification.

5,12-Dihydrodibenzo[b]phenazine (2.04 g, 8.69 mmol) was added to 60 mL of glacial acetic acid to produce a suspension. $K_2Cr_2O_7$ (5.32 g, 18.0 mmol) in 20 mL water was slowly added dropwise, and the mixture was stirred overnight in the dark at room temperature. After neutralization, the organic layer was extracted with $CHCl_3$, dried with anhydrous Na_2SO_4, and concentrated under reduced pressure. Recrystallization from toluene gave 5,12-diazatetracene (DAT) as a reddish-orange solid (yield: 47%). ^{1}H-NMR (400 MHz, $CDCl_3$, TMS): δ (ppm) = 8.92 (s, 2H), 8.23 (dd, 2H), 8.13 (dd, 2H), 7.81 (dd, 2H), 7.54 (dd, 2H). Elemental analysis for $C_{16}H_{10}N_2$: calculated (%) H 4.38, C 83.46, N 12.17; found (%) H 4.30, C 83.50, N 12.03.

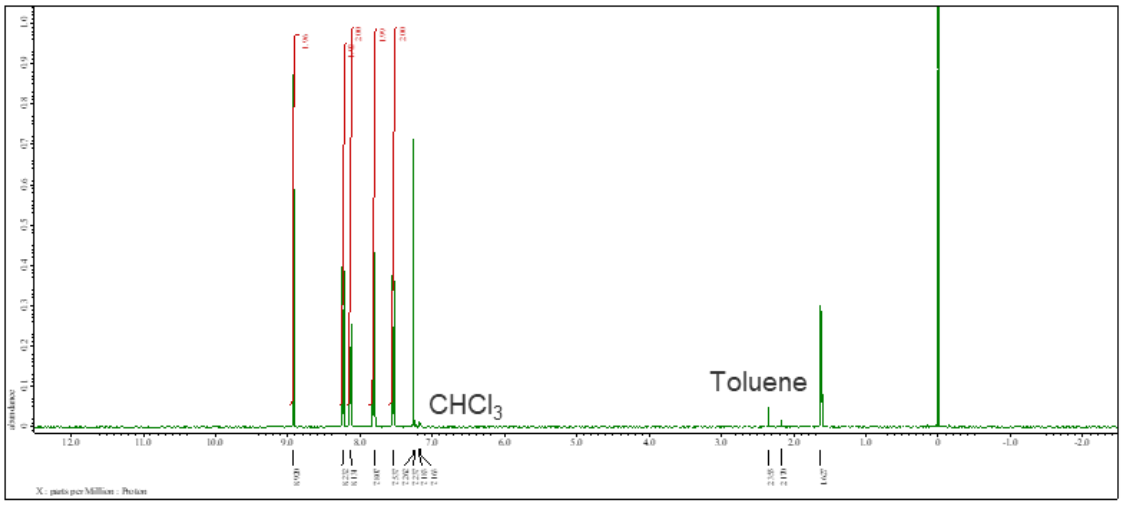

Figure 3-3. ^{1}H NMR spectrum (9.4 T, $CDCl_3$) of DAT.

3-2-5. Synthesis of D-MIL-53

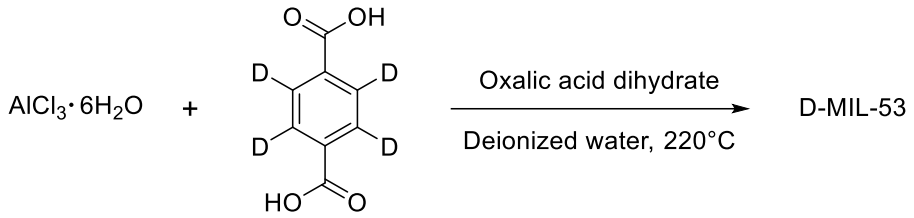

Figure 3-4. Synthetic scheme of D-MIL-53.

MIL-53 [Al(μ_2-OH)(BDC)]$_n$ was synthesized according to the previous report,[31] using oxalic acid as modulator. To suppress the relaxation of electron spins by hyperfine interaction, the ligands of MIL-53 was deuterated (D-MIL-53; [Al(μ_2-OH)(BDC-d_4)]$_n$).

$AlCl_3 \cdot 6H_2O$ (966 mg, 4 mmol), oxalic acid dihydrate (504 mg, 4 mmol), and terephthalic acid-d_4 (BDC-d_4) were added to 30 mL deionized H_2O and put into a 50 mL Teflon-lined autoclave. The mixture was sonicated, heated at 220 ℃ for 72 h, and cooled to room temperature over 24 h in an oven. After filtering and washing the product with DMF and methanol, a colorless powder was obtained.

To remove the residual BDC-d_4 ligands from D-MIL-53, the obtained powder was added to 15 mL DMF and heated to 120 ℃ for 16 h in the oven again. The resulting product was filtered and washed with DMF and methanol. These procedures were repeated until the peak from BDC-d_4 was no longer observed in thermogravimetric measurements (at least three times). The product was then activated at 150 ℃ for 3 h.

In ambient air, activated MIL-53 immediately adsorbs water molecules and forms hydrated structures[32] (denoted as D-MIL-53⊃ H_2O). Elemental analysis for $[C_8H_{1.08}D_{3.92}O_5Al_1]\cdot 1.0(H_2O)$: calculated (%) H 3.06, C 41.75, N 0.00; found (%) H 3.05, C 41.80, N 0.00.

3-2-6. Introduction of qubit and guests into D-MIL-53

D-MIL-53 (50 mg) was put into a 6 mL vial and dried under reduced pressure at room temperature over 3 h. The vial was placed in the dark for 1 h at room temperature after adding 2.5 mL dichloromethane solution of DAT (1 mM). The mixture was centrifuged, washed with fresh dichloromethane (1.0 mL, seven times), and dried under vacuum at 100 °C for 3 h. D-MIL-53⊃DAT was obtained as a yellow powder.

In the ambient air, D-MIL-53⊃DAT quickly absorbs water and forms the hydrated structure (denoted as D-MIL-53⊃[DAT + H_2O]).

The following 11 guests were additionally introduced into D-MIL-53⊃DAT: H_2O, 2-propanol (PrOH), pyridine (Py), 5-fluorouracil (FU), *p*-benzoquinone (BQ), THF, chloroform ($CHCl_3$), ethyl acetate (EtAc), toluene (*h*-Tol), ethanol (EtOH), and acetonitrile (AcNt) (Figure 3-5). Guest molecules were selected to cover as wide a range of volumes as possible based on the previous reports.[32, 28-29] In addition, for liquid guests, those with boiling points high enough but not too high were selected not to be evacuated during sample preparation and to be introduced by vapor diffusion.

Guest analytes except for FU and BQ were introduced by exposing D-MIL-53⊃DAT to each guest vapor. D-MIL-53⊃DAT was put into a 6 mL vial and dried under reduced pressure at 80 °C for 3 h. The vial was placed in a Schlenk flask containing a small amount of solvent containing activated 3A molecular sieves and stored in the dark overnight.

The introduction of FU and BQ into the nanochannels of D-MIL-53⊃DAT was performed by the sublimation method.[33] D-MIL-53⊃DAT was evacuated at room temperature for 3 h. FU (35 mg) or BQ (60 mg) were added to D-MIL-53⊃DAT and the mixtures were put into a 30 mL Schlenk flask. After 1 h of evacuation, guests were sublimated and absorbed directly into the nanopores of the MOF at 175 °C for FU and 80 °C for BQ under reduced pressure for 1 h. Residual guests were eliminated at 175 °C or 80 °C under vacuum until the PXRD peaks of bulk FU and BQ were no longer observed. D-MIL-53⊃[DAT + FU] and D-MIL-53⊃[DAT + BQ] were obtained as a pale-yellow powder and a yellow powder, respectively.

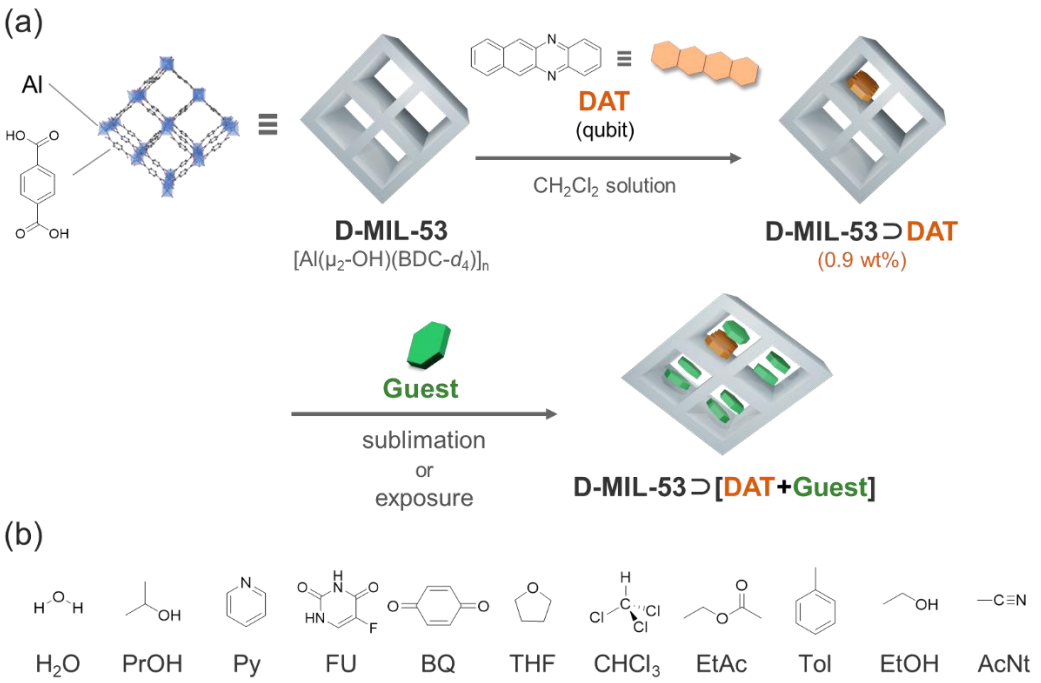

Figure 3-5. (a) Scheme of introduction of DAT and guest molecules into D-MIL-53. DAT was firstly introduced into the MOF by soaking CH_2Cl_2 solution. The guests were accommodated by sublimation (for solid guests) or exposure (for liquid guests). (b) Guest molecules used in this work.

3-2-7. Estimation of guest density in D-MIL-53 pore

The number of guest molecules per unit cell of D-MIL-53 (n_{guest}) was calculated from the following equation:

$$n_{guest} = \frac{w_{loss}(m_{MOF} + n_{DAT}m_{DAT})}{m_{guest}(1 - w_{loss})} \quad (3.1)$$

where w_{loss}, n_{DAT}, m_{MOF}, m_{DAT} and m_{guest} are weight loss (weight of guest) as a percentage of total weight, the number of DAT molecules per unit cell of D-MIL-53, the molecular weight of a unit cell of D-MIL-53 (equivalent to 4 times chemical formula), the molecular weight of DAT, and the molecular weight of the guest, respectively. The guest accessible pore volume per MOF unit cell (V_{pore}) of MIL-53⊃water was obtained as 638 Å^3 by Platon software. By subtracting this V_{pore} from the volume of the MOF unit cell of MIL-53⊃H_2O (V_{MOF}, 977 Å^3),[27] the volume of the framework ($V_{structure}$) was estimated as 339 Å^3. This $V_{structure}$ was assumed to be same for all the D-MIL-53⊃[DAT + guest]. The percentage of guest occupied volume was estimated by the following equation,

$$guest\ occupied\ volume\ (\%) = \frac{100 n_{guest} V_{guest}}{V_{MOF} - V_{structure}} = \frac{100 n_{guest} V_{guest}}{V_{pore}} \quad (3.2)$$

where V_{guest} is the volume of the guest molecule obtained from its steric parameters (Table 3-1).[29] The MOF unit cell V_{MOF} of some of D-MIL-53⊃[DAT + guest] was estimated by PXRD peak positions using the program DICVOL[34] (Table 3-2). For D-MIL-53⊃[DAT + guest] containing THF, $CHCl_3$, EtAc, *h*-Tol, EtOH, and AcNt as the guest, V_{MOF} was estimated by using the unit cell volume of MIL-53 (Fe)⊃guest,[28] considering a linear relationship between the unit cell volumes of MIL-53 (Al)⊃guest and MIL-53 (Fe)⊃guest (Figure 3-6).

Table 3-1. Steric parameters of the guest molecules: *L*, *h* and *e* are the maximum length, the intermediate length, and the thickness of molecules, respectively. V_{guest} was determined by $L \times h \times e$.

Guest	*L* (Å)	*h* (Å)	*e* (Å)	V_{guest} (Å^3)
PrOH	6.5	5.2	4.7	158.9
FU	6.9	6.7	3.5	160.2
EtAc	6.2	5.7	3.4	120.2

Table 3-2. Unit cell parameters for MIL-53 (Al) with guest molecules.

Guest	*a* (Å)	*a*' (Å)	*b* (Å)	*c* (Å)	*β* (°)	V_{MOF} (Å^3)	Crystal system
H_2O[a)]	19.513	18.913	7.612	6.576	104.24	977	monoclinic
PrOH	19.133	18.161	10.844	6.663	108.34	1312	monoclinic
Py	17.547	-	12.181	6.703	-	1433	orthorhombic
FU[b)]	17.984	-	11.749	6.810	-	1438	orthorhombic
BQ	18.642	-	11.916	6.757	-	1501	orthorhombic

a' is the reduced unit cell edge length and $a' = a\cos(\beta-\pi/2)$.

a) Reported in Ref. 32.

b) Reported in Ref. 30.

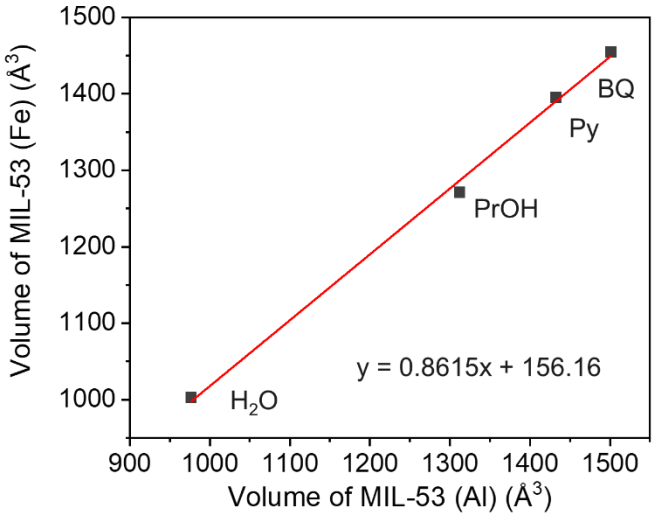

Figure 3-6. Plot of the volumes of MIL-53 (Fe)⊃guest against those of MIL-53 (Al)⊃guest. The volumes of MIL-53 (Al) with THF, $CHCl_3$, EtAc, *h*-Tol, EtOH and AcNt were estimated from this relationship using reported values of MIL-53 (Fe)[28] due to the evaporation of these guests during the PXRD measurements.

3-2-8. Molecular dynamics (MD) simulations

3-2-8-1. Models construction for MD simulations

To construct model structures, the reported experimental crystal structures of MIL-53 in degassed and H_2O-solvated phases were refered,[32] and optimized the infinite crystal structure using Crystal17 program[35-36] under periodic boundary condition. For the optimization, the pob-TZVP-rev2 basis set[37] for all atoms and PBE functional[38] together with Grimme D3 type dispersion correction were employed.[39] The shrinking parameters were set to 2 and 2, and cell parameters were fixed to the experimental ones. Similarly, the MIL-53 in BQ-solvated phase were optimized using the crystal structure of the desolvated phases after changing the cell parameters to the estimated one in Table 3-1. After the optimization of all three systems, each model structure of the 2 × 2 × 4 supercell (16 unit cells) were constructed, where the 4 cells correspond to the pore direction. One DAT molecule was introduced into each model using the insert-molecule tool in GROMACS.[40] According to the experimental estimation of the amount of solvent molecules, 64 H_2O molecules and 64 BQ molecules are added into each model respectively after the introduction of the DAT molecule.

3-2-8-2. Details of MD simulations

The force field parameters for the metal cluster of the MIL-53 were generated by using the Seminario methods[41] in the MCPB.py modelling tool[42] of AmberTools18[43] with the general AMBER force field (GAFF).[44] The Lennard-Jones parameters for the Al atoms and the O atoms coordinating to the Al atoms were taken from the universal force field[45] and the Mulliken partial charges were taken for the literature.[46] The topologies files for the H_2O, BQ, DAT molecules were prepared as follows. The geometries of the three molecules were optimized using density functional theory at the B3LYP/6-311+G(d, p) level of theory. The Mulliken atomic charges were obtained from the single point calculation at HF/6-31G* level of theory. The optimization and charge evaluation were conducted using Gaussian 16 Rev. C. 01.[47] Using the obtained geometries and charges, the amber topology files were generated by the antechamber package[48] with GAFF force field. The amber topology files were converted into a GROMACS format using the python script, Acpype.[49]

For the equilibration of the solvents, first, energy minimization of the systems was performed based on the steepest descent algorithm with the threshold of the maximum force, 10.0 kJ/mol/nm.

Second, NVT equilibration for 20 ns at 300 K were carried out for relaxation of the introduced solvent molecules within the pore, fixing the atomic positions of the MIL-53.

The main MD simulations with the canonical ensemble were performed without any restraints for 200 ns, and the snapshots were collected every 5 ps. To keep the temperature at 300 K, the velocity rescale thermostat was used.[50] Dynamics were propagated with a leapfrog integrator using a time step of 1 fs for the equilibration procedure, and of 2 fs for the main MD simulation, while preserving bond lengths using LINCS.[51] The geometric mixing rules were applied for cross-interactions. The particle-mesh Ewald scheme[52] was used for calculating the long-range electrostatic interactions, while short range contributions were computed with a cutoff distance of 11 Å. All simulations were carried out under periodic boundary conditions using GROMACS software version 2020.5.[40]

3-3. Results and discussion

3-3-1. Characterizations of D-MIL-53⊃DAT

DAT was introduced into partially deuterated MIL-53 [Al(μ_2-OH)(BDC-d_4)]$_n$ (denoted as D-MIL-53⊃DAT; BDC-d_4 = perdeuterated terephthalate) by simply soaking D-MIL-53 in a dichloromethane solution of DAT, according to previous report.[30] The introduction of DAT qubits into D-MIL-53 was confirmed from UV-vis absorption measurement (Figure 3-7). The absorption of D-MIL-53⊃[DAT+H_2O] shows absorption peaks at 450, 480, and 515 nm derived from π–π* transitions. This is consistent with the absorption peaks of DAT molecularly dispersed in *p*-terphenyl crystal and is clearly different from the red-shifted peaks of DAT in its aggregated solid state, as previously reported.[25]

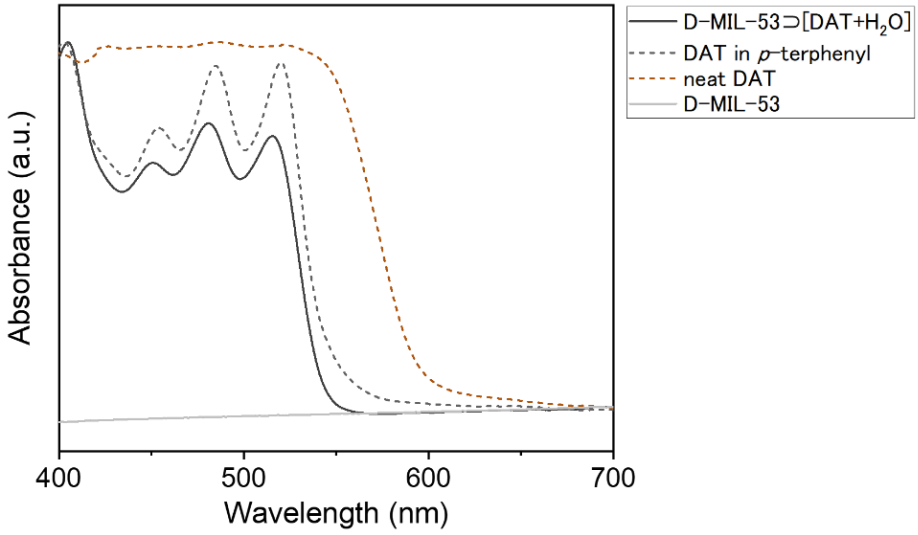

Figure 3-7. UV-vis absorption spectra of D-MIL-53⊃DAT with H_2O (black line), 0.1 mol% DAT doped in *p*-terphenyl crystal (gray dot line), neat DAT (brown dot line), and D-MIL-53 (gray solid line).

The amount of DAT molecules in D-MIL-53 was calculated by UV–Vis absorbance after digesting D-MIL-53⊃DAT in aqueous Na_4-EDTA solution. DAT was extracted from 20.0 mg D-MIL-53⊃DAT using 4.0 mL dichloromethane after adding 4.0 mL aqueous Na_4-EDTA solution (125 mM). The absorbance at 475 nm of the dichloromethane solution of DAT was 0.055 in a 1 mm cell for 20.0 mg of D-MIL-53⊃[DAT + H_2O] (Figure 3-8). From the calibration curve, the concentration of the solution was calculated to be 0.175 mM. Therefore, the total amount of DAT in the 4.0 mL dichloromethane solution was found to be 0.70 μmol (= 0.16 mg). Since 7.8 wt% of water was contained in D-MIL-53⊃[DAT + H_2O] (from the TGA curve shown later), the weight of D-MIL-53⊃DAT without water was determined to be 18.44 mg (21.74 μmol). Thus, the number of DAT molecules per unit cell of D-MIL-53 was estimated to be 0.70/21.74 = 0.032, which corresponds to 0.87 wt% of DAT in D-MIL-53⊃DAT.

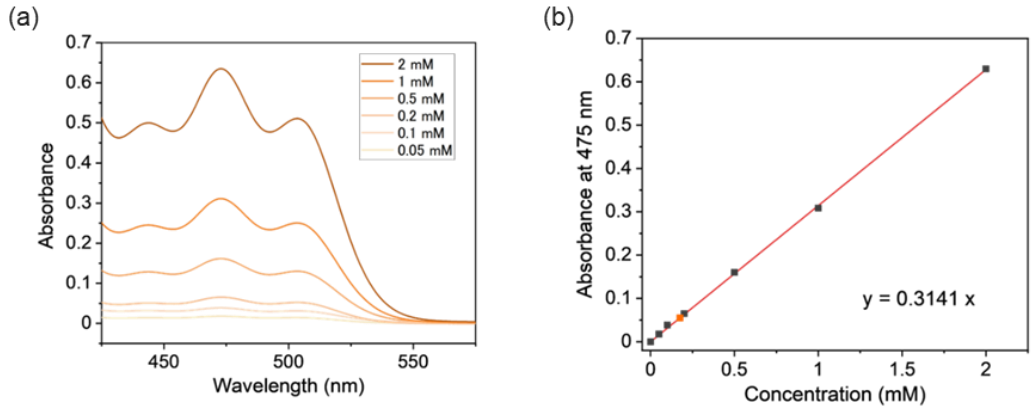

Figure 3-8. (a) UV-vis absorption spectra of a series of DAT standard dichloromethane solutions (0.05, 0.1, 0.2, 0.5, 1, 2 mM). (b) The calibration line obtained from the absorbance of DAT dichloromethane solutions (0.05 mM, 0.1 mM, 0.2 mM, 0.5 mM, 1 mM and 2 mM) at 475 nm using 1 mm quartz cell. The absorbance at 475 nm was 0.055 when 20.0 mg of D-MIL-53⊃[DAT + H_2O] was digested to 4 mL dichloromethane solution (shown as orange dot). From the calibration curve, the concentration of DAT in the solution was calculated to be 0.175 mM.

The formation of MIL-53 structure was confirmed by measuring PXRD patterns (Figure 3-9). The obtained peak pattern of D-MIL-53 was matched with simulated structure, the pattern was kept for D-MIL-53⊃[DAT + H_2O] under soaking of 1 mM DAT solution in dichloromethane. As the concentration of the DAT solution is increased, the structure of obtained MOF changes gradually, supporting the accommodation of DAT in the MOF nanopores.

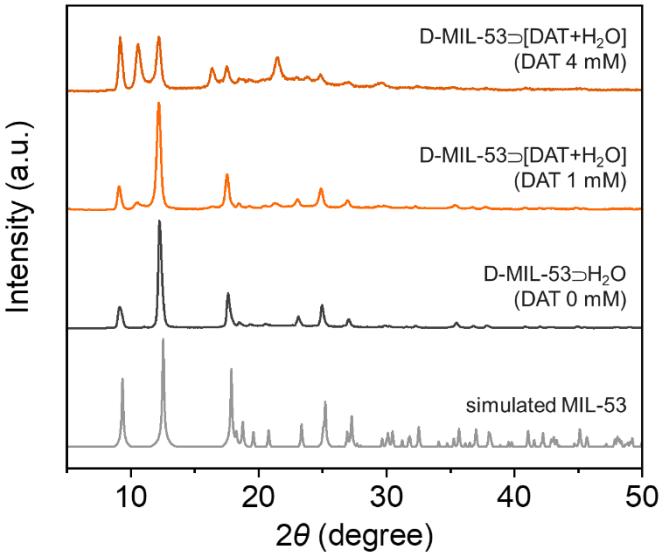

Figure 3-9. PXRD patterns of D-MIL-53⊃[DAT + H_2O] prepared with DAT in dichloromethane 4 mM (brown) and 1 mM (orange) solution, D-MIL-53⊃H_2O (black), and its simulated pattern (gray).

3-3-2. Characterizations of D-MIL-53⊃[DAT+guest]

The following 11 guests were additionally introduced into D-MIL-53⊃DAT: H_2O, 2-propanol (PrOH), pyridine (Py), 5-fluorouracil (FU), *p*-benzoquinone (BQ), THF, chloroform ($CHCl_3$), ethyl acetate (EtAc), toluene (*h*-Tol), ethanol (EtOH), and acetonitrile (AcNt). FU and BQ were introduced by sublimation, and other guests were introduced by exposing D-MIL-53 to each vapor. Guest molecules were selected to cover as wide a range of volumes as possible based on the previous reports.[27-29] In addition, for liquid guests, the guests were selected considering that their boiling points high enough not to be evacuated during sample preparation and not too high to be introduced by vapor diffusion.

UV–vis absorption spectra of DAT in the guest-accommodated samples are slightly different from guest-free D-MIL-53⊃DAT (Figure 3-10), except for D-MIL-53⊃[DAT + BQ] which absorption of BQ are overlapped, suggesting the successful accommodation of the guests. In addition, the change in spectra is not significant for all guests other than BQ. This indicates that the interaction between DAT and the guest molecules is small in the ground state and that DAT is not aggregated by the introduction of guests.

The structural change of the MOF after guest insertion was confirmed from the transformation of the PXRD patterns (Figure 3-11). Due to the desorption of the guest molecules during measurements, only guests with high-boiling points and solid guests were measured. Different PXRD patterns were observed for each guests, as reported in previous report.[28] The structural parameters were obtained from Rietveld refinement and summarized in Table 3-2. For other guest molecules, the parameters were estimated from a relationship between MIL-53 (Al) and MIL-53 (Fe)[28] (Figure 3-6).

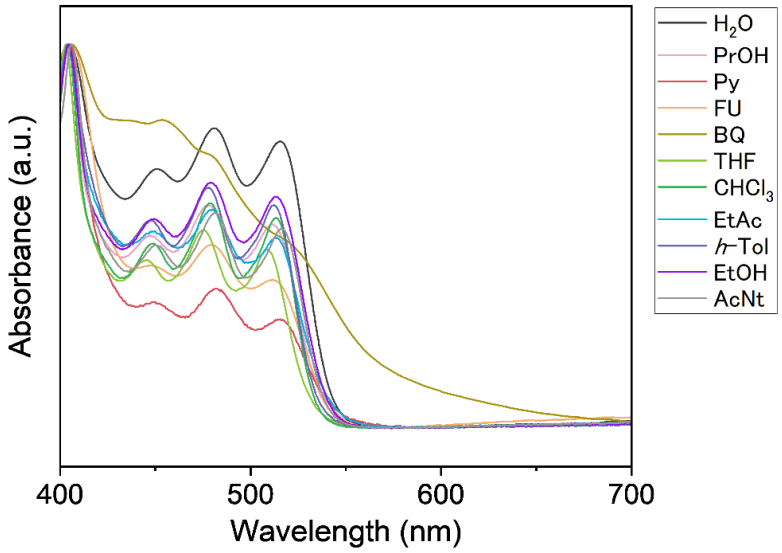

Figure 3-10. UV-vis absorption spectra of D-MIL-53⊃DAT with H_2O (black), PrOH (pink), Py (red), FU (orange), BQ (yellow), THF (pale green), $CHCl_3$ (green), EtAc (blue), *h*-Tol (dark blue), EtOH (purple), and AcNt (gray). For D-MIL-53⊃[DAT + BQ], the absorption of DAT overlapped with that of BQ.

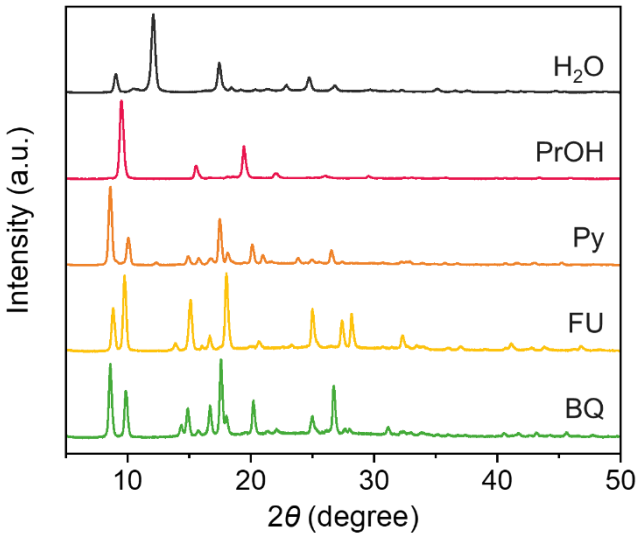

Figure 3-11. PXRD patterns of D-MIL-53⊃[DAT + H_2O] (black), D-MIL-53⊃[DAT + PrOH] (red), D-MIL-53⊃[DAT + Py] (orange), D-MIL-53⊃[DAT + FU] (yellow), and D-MIL-53⊃[DAT + BQ] (green).

3-3-3. EPR properties of D-MIL-53⊃[DAT+guest]

The coherence times (T_2) of the photoexcited triplets of DAT in D-MIL-53 were measured by pulsed EPR at room temperature with a spin echo sequence varying the pulse intervals (Figure 3-12a). Measurements were taken at the magnetic field of the high-field and low-field peaks of the EPR spectra shown later, respectively, and both decay curves are shown (Figure 3-12c). The decay of echo intensity was fitted with a single exponential function and T_2 was obtained as the decay constant. While DAT shows electron spin echo envelope modulation (ESEEM) due to hyperfine coupling with ^{1}H nuclei and ^{14}N nuclei at higher magnetic field, it does not affect the estimation of T_2. The T_2 values obtained at the higher and lower magnetic fields are similar (Table 3-3).

A relatively short T_2 of around 0.1 μs is observed for D-MIL-53⊃DAT without any guest analyte (termed 'empty'). No echo signals are detected when *h*-Tol, EtOH, or AcNt are introduced as guests, probably due to the shortening of T_2 (< 0.1 μs). This is not surprising, since proton nuclear spins usually work as noise and reduce coherence time.[3] Meanwhile, interestingly, the introduction of some guest molecules such as Py, FU, BQ, and THF clearly elongate T_2 of the DAT triplets, despite the increase in proton and other nuclear spins that could cause spin relaxation. The T_2 of DAT in the presence of FU and BQ are over 1 μs, which are notably long as molecular qubits at room temperature[53]. To confirm the measurements were run in the spin dilute regime, the T_2 were measured with different laser powers (Figure 3-13). As expected from the low concentration of DAT in the sample (0.87 wt%), the change of T_2 was small and intermolecular interactions between electron spins of DAT triplets could be ignored.

The T_2 value was plotted against the cell volume of pristine MIL-53 (Figure 3-12b). With increasing cell volume, T_2 shows a non-monotonic trend, becoming longer and then shorter. Interestingly, triplet qubit and flexible MOF hybrids exhibit different coherence times for various guest molecules at room temperature.

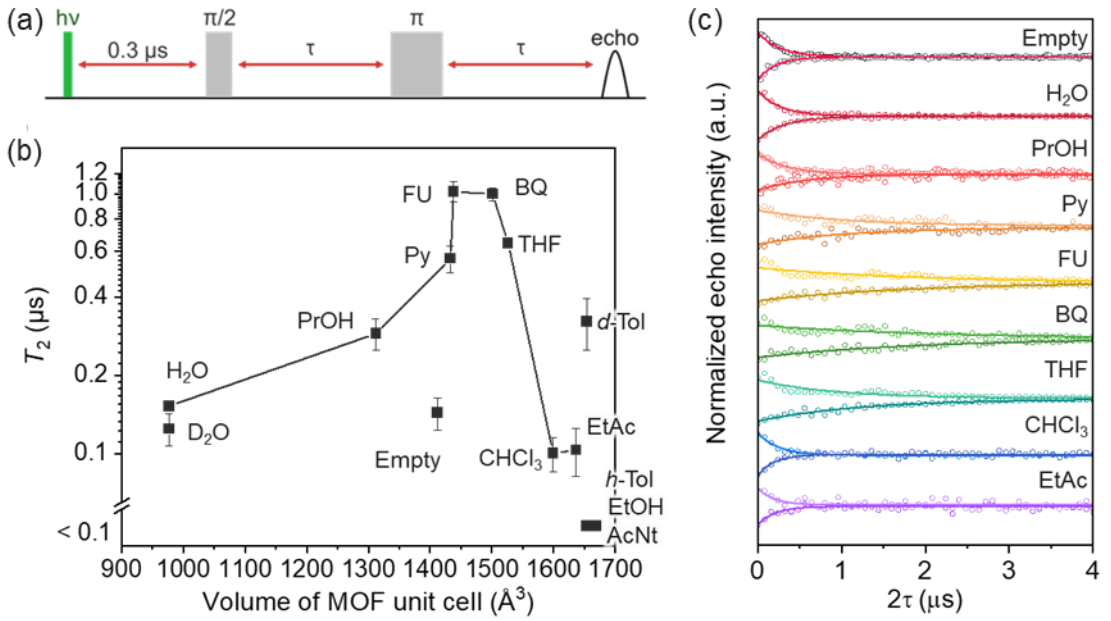

Figure 3-12. (a) Spin echo sequence used for T_2 measurement. The intervals of microwave pulses and echo detection were varied. (b) Plot of T_2 and the fit error obtained by the single-exponential fitting of the spin echo decay curves against the unit cell volume of MIL-53. Only the T_2 obtained from the low field peaks where the effect of ESEEM was small is plotted. For the empty, FU and THF samples, the means and the standard errors of three measurements are shown. Errors of the H_2O and THF samples were small and buried in the symbol. (c) Spin echo decay curves after pulsed photoexcitation at 532 nm for empty (D-MIL-53⊃DAT) and guest-filled (D-MIL-53⊃[DAT + guest]) samples at room temperature. The decay curves of each sample at the magnetic field corresponding to the higher and lower EPR peaks (Figure 3-14) are shown at the top and bottom, respectively. Single-exponential fitting curves for each sample are also shown. Echo signals were not observed when the guest was *h*-Tol, EtOH, or AcNt.

Table 3-3. Unit cell parameters for MIL-53 (Al) with guest molecules. T_2 were obtained from pulsed EPR measurements while other parameters were obtained from time-resolved EPR measurements.

Guest	T_2 (μs)		T_1 (μs)		Relative populations (P_x : P_y : P_z)	$\|D\|$ (MHz)	$\|E\|$ (MHz)
	High (378 mT)	Low (305 mT)	High (378 mT)	Low (305 mT)			
Empty	0.133 ± 0.002 [a]	0.144 ± 0.002 [a]	1.609 ± 0.087	1.450 ± 0.089	1.00 : 0 : 0	1610	160
H_2O	0.136 ± 0.007	0.156 ± 0.005	4.472 ± 0.179	3.935 ± 0.139	0.95 : 0 : 0.05	1610	160
PrOH	0.615 ± 0.014	0.290 ± 0.041	2.560 ± 0.066	2.133 ± 0.056	1.00 : 0 : 0	1610	160
Py	0.523 ± 0.074	0.564 ± 0.066	4.399 ± 0.133	3.886 ± 0.103	1.00 : 0 : 0	1610	160
FU	1.000 ± 0.107 [a]	1.020 ± 0.091 [a]	4.612 ± 0.118	3.999 ± 0.101	0.95 : 0 : 0.05	1610	160
BQ	1.079 ± 0.121	0.999 ± 0.057	5.660 ± 0.302	5.132 ± 0.290	0.75 : 0.25 : 0	1610	160
THF	0.470 ± 0.024 [a]	0.648 ± 0.012 [a]	3.343 ± 0.081	3.160 ± 0.081	0.95 : 0 : 0.05	1610	160
$CHCl_3$	0.125 ± 0.011	0.101 ± 0.015	1.371 ± 0.037	1.128 ± 0.025	0.95 : 0.05 : 0	1610	160
EtAc	0.096 ± 0.032	0.104 ± 0.022	1.684 ± 0.059	1.548 ± 0.048	0.90 : 0.10 : 0	1610	160
h-Tol	< 0.1	< 0.1	3.009 ± 0.189	2.986 ± 0.151	0.95 : 0 : 0.05	1610	160
EtOH	< 0.1	< 0.1	1.226 ± 0.070	1.047 ± 0.061	0.85 : 0.15 : 0	1610	160
AcNt	< 0.1	< 0.1	1.001 ± 0.093	0.978 ± 0.097	0.80 : 0.20 : 0	1610	160

a) The means and the standard errors of three measurements are shown instead of fit errors.

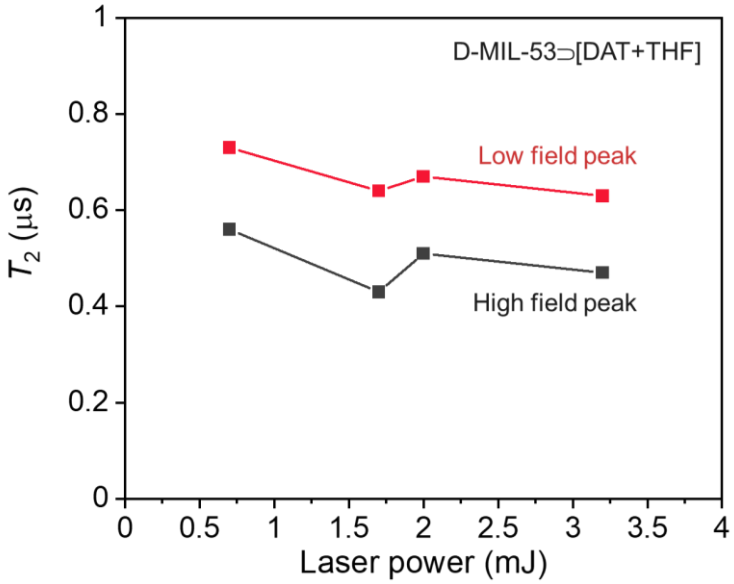

Figure 3-13. Plot of T_2 against the excitation laser power for the high field peak (black line, 378 mT) and the low field peak (red line, 305 mT) of D-MIL-53⊃[DAT + THF].

To obtain information about the interaction of DAT with guest molecules, time-resolved EPR spectra were obtained (Figure 3-14a). All the samples show similar EPR spectra typical for a polarized DAT triplet and it is consistent with the echo-detected field swept spectra obtained from the pulsed EPR measurements (Figure 3-15). There is no significant motional narrowing as in the EPR spectrum of the triplet state in solution,[54] indicating that the incorporation of DAT into the MOF nanopores effectively suppresses its rotation. The EPR spectra were simulated using the EasySpin toolbox[55] in MATLAB (Table 3-3). While large spin polarization of DAT were kept after guest accommodations, the polarization pattern (P_x : P_y : P_z) were slightly changed depends on the guests. There were no significant change in zero-field splitting (ZFS) parameters (D and E) among the samples.

The spin–lattice relaxation time (T_1) was estimated from the decay of the EPR signal after light irradiation (Figure 3-14b). Even under the continuous microwave irradiation which makes the decay faster, the T_1 value for each sample is more than an order of magnitude longer than the corresponding T_2 value (Figure 3-16).

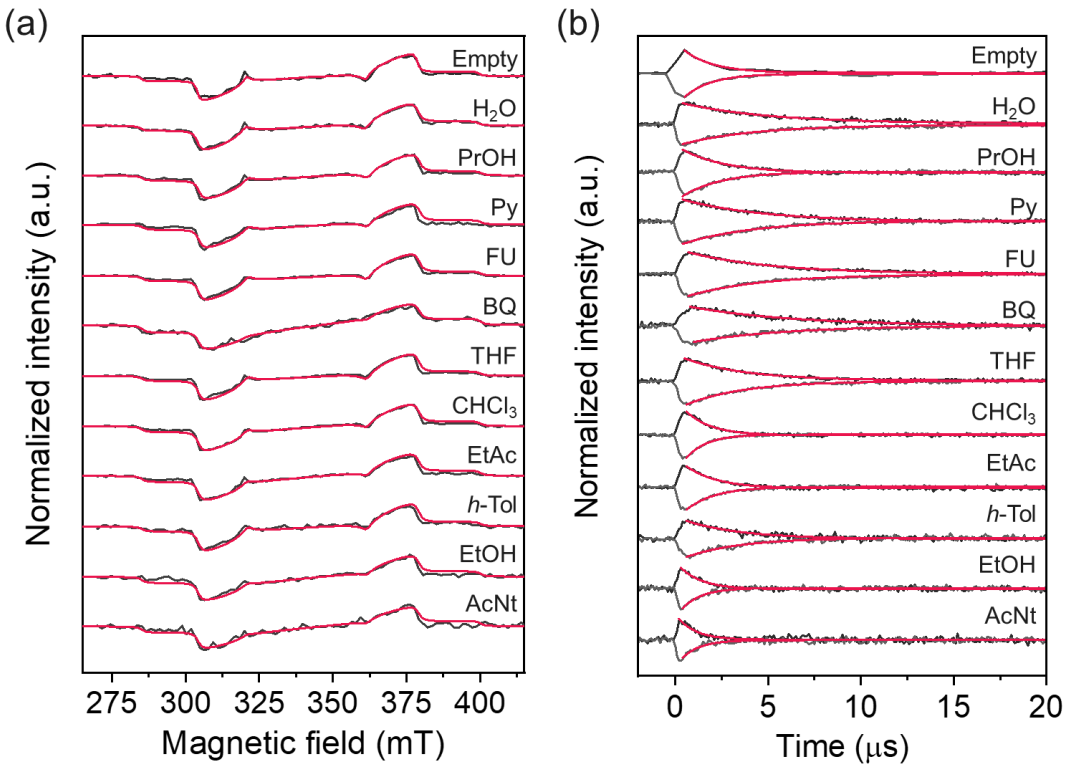

Figure 3-14. (a) Time-resolved EPR spectra at 0.1–0.5 μs for empty (D-MIL-53⊃DAT) and guest-filled (D-MIL-53⊃[DAT + guest]) samples at room temperature. The simulated EPR spectra are shown as red lines. (b) Decays of the EPR peaks at higher and lower magnetic field after pulsed photoexcitation at 532 nm for empty (D-MIL-53⊃DAT) and guest-filled (D-MIL-53⊃[DAT + guest]) samples at room temperature. Decay curves were fitted by a single exponential function and the fitting results are shown as red curves.

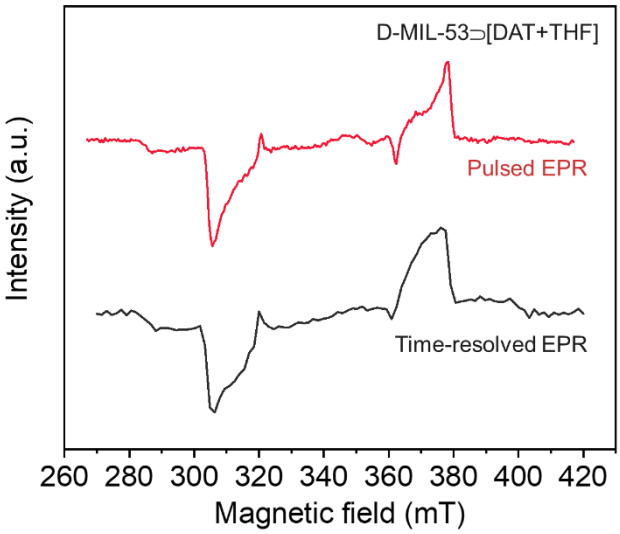

Figure 3-15. Comparison of the echo-detected field swept spectrum from pulsed EPR (red line) and time-resolved CW-EPR spectrum (black line) of D-MIL-53⊃[DAT + THF]. The slight changes might be due to the difference in spectral resolution between time-resolved CW-EPR and pulsed EPR, or difference in relaxation times for each peak.

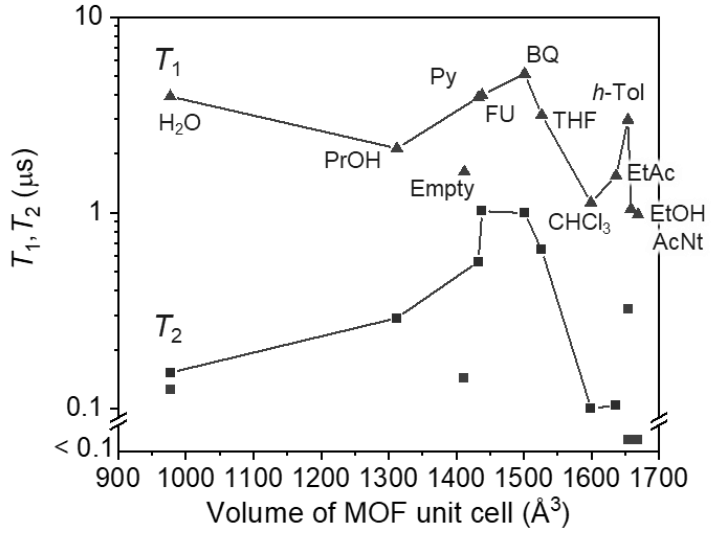

Figure 3-16. Plot of T_1 (triangle) and T_2 (square) obtained by the single-exponential fitting of time-resolved EPR signal decay and the spin echo decay curves, respectively, against the unit cell volume of MIL-53. Only the values obtained from the low field peaks were shown.

3-3-4. Possible decoherence mechanisms

There are several differences before and after the guest introduction to D-MIL-53⊃DAT, thus guest-responsive behavior of T_2 would come from the difference. One possible factor is interactions between DAT and guest molecules. However, as mentioned above, UV–vis absorption spectra of D-MIL-53⊃[DAT + guests] are not different from the guest-free sample (Figure 3-10), and no significant interactions between DAT and guests are indicated. When the dielectric constants of the liquid guests were plotted against T_2, no correlation was also shown (Figure 3-17). Therefore, the change in T_2 is not comes from the electronic interactions.

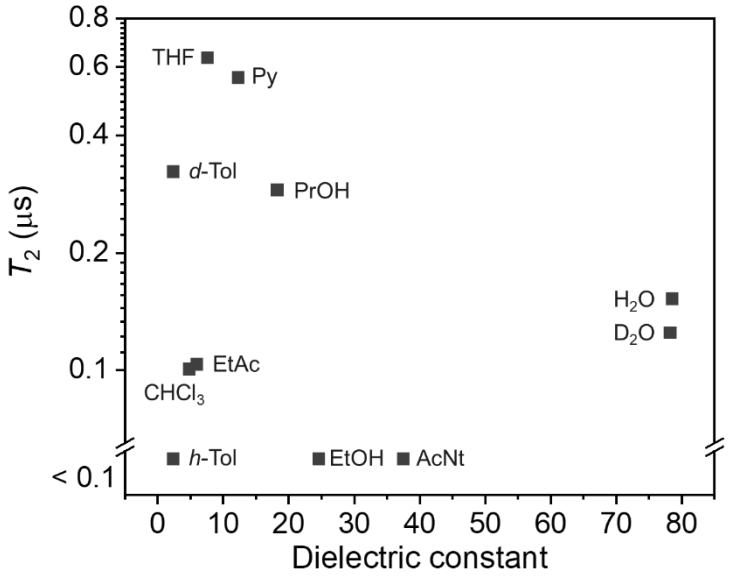

Figure 3-17. Plot of T_2 of D-MIL-53⊃[DAT + guest] samples against the dielectric constants of the guests. Only liquid guests are plotted.

According to the time-resolved EPR spectra, the polarization pattern and the relative zero-field populations (P_x : P_y : P_z) were slightly changed depends on the guests (Figure 3-14, Table 3-3). The slight changes were probably due to the change in vibronic spin-orbit coupling[56], but the T_2 values were unrelated to the relative populations (Figure 3-18). Thus, the DAT structure would be kept after guest introductions.

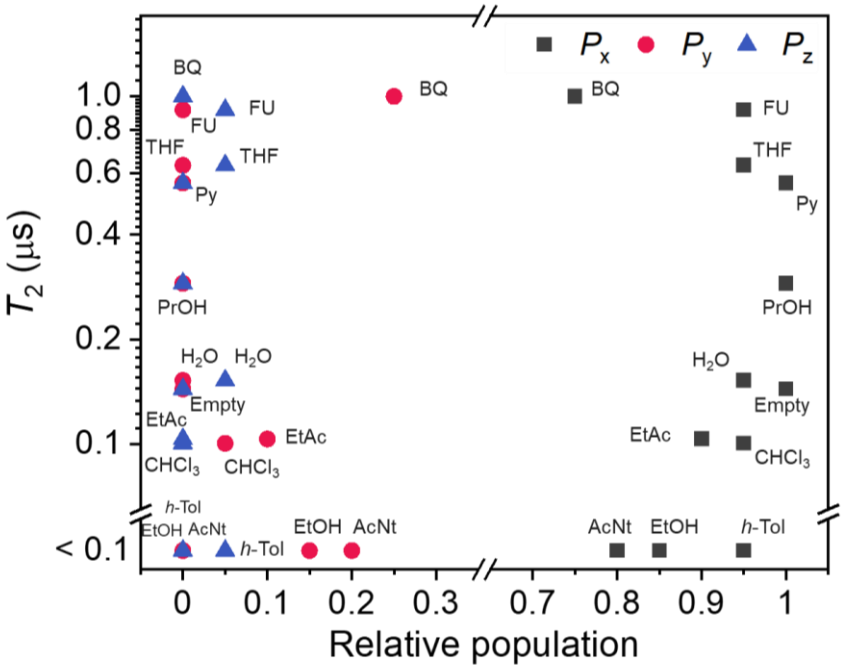

Figure 3-18. Plot of T_2 against relative populations (P_x : P_y : P_z) of empty (D-MIL-53⊃DAT) and guest-filled (D-MIL-53⊃[DAT + guest]) samples.

In general, the spin–spin relaxation time (T_2) of organic molecules are written as equation (1.62). There are three terms that affects the relaxation time: (i) spin–lattice relaxation (T_1), (ii) relaxation from spin coupling between electron spins (T_{ee}), (iii) relaxation from hyperfine coupling between electron spin and surrounding nuclear spins (T_{en}). The factors discussed in former sections would not affect these three relaxations.

The T_1 were estimated from the decays in time-resolved EPR, and significantly longer than T_2 for all samples (Figure 3-14b and Table 3-3), indicating that the spin–lattice relaxation and would not have major role in spin–spin relaxation. Indeed, for D-MIL-53⊃DAT, T_2 and T_1 were 0.144 μs and 1.450 μs, respectively. Thus, the value of $(1/T_2 - 1/2T_1)$, which reflects the relaxation rate not due to the spin–lattice relaxation (i.e. spin–spin coupling), was calculated as 6.60 μs^{-1} (Table 3-4). This is significantly different from the value for D-MIL-53⊃[DAT+BQ] of 0.90 μs^{-1} (T_2 = 0.999 μs, T_1 = 5.132 μs). Therefore, the effect of spin–spin coupling terms should be main factor for spin–spin relaxation. Meanwhile, there are positive relationship between T_1 and T_2. Since the spin–spin dipolar coupling can induce spin–lattice relaxations,[26] these relaxations are probably due to the similar origins.

Table 3-4. Relationship between T_2, T_1 and other relaxation factors. The value of $1/T_2 - 1/2T_1$ indicates the contribution of other relaxation processes than spin–lattice relaxation.

Guest	T_2 (μs)[a]	T_1 (μs)[a)]	$1/T_2$ (μs^{-1})	$1/2T_1$ (μs^{-1})	$1/T_2 - 1/2T_1$ (μs^{-1})	Contribution of spin–lattice relaxation in T_2 (%)[b)]
Empty	0.144	1.450	6.94	0.345	6.60	4.97
H_2O	0.156	3.935	6.41	0.127	6.28	1.98
PrOH	0.290	2.133	3.45	0.234	3.21	6.80
Py	0.564	3.886	1.77	0.129	1.64	7.26
FU	1.020	3.999	0.98	0.125	0.86	12.8
BQ	0.999	5.132	1.00	0.097	0.90	9.73
THF	0.648	3.160	1.54	0.158	1.38	10.3
$CHCl_3$	0.101	1.128	9.90	0.443	9.46	4.48
EtAc	0.104	1.548	9.62	0.323	9.29	3.36
h-Tol	< 0.1	2.986	> 10	0.167	> 9.83	< 1.67
EtOH	< 0.1	1.047	> 10	0.478	> 9.52	< 4.78
AcNt	< 0.1	0.978	> 10	0.511	> 9.49	< 5.11

a) the values in lower magnetic field were used.

b) calculated from $(1/2T_1) / (1/T_2) = T_2 / 2T_1$.

The spin–spin interaction of electron spins contains two types of interactions: (i) intermolecular

interaction and (ii) intramolecular interaction. The former one is an interaction between triplets in different DAT molecules. Because of low concentration of DAT in the sample (0.87 wt%), the T_2 was not dependent to triplet concentration (Figure 3-13), and this could be neglected. The latter one is an interaction between electron spins within a single DAT triplet. Triplet electron spin has the dipolar interaction in the composing two spins, and the interaction is called as zero-field splitting (ZFS). The ZFS parameters (D and E) are estimated from the time-resolved EPR spectra and found to be independent to guest species (Table 3-3). According to this result, the ZFS interaction does not appear to affect the T_2, however the ZFS parameters are anisotropic to magnetic field, there remains the possibility that the fluctuation of ZFS by molecular motions induce the spin–spin relaxation.

For the third term (hyperfine interaction), there are two types of nuclear spins with large gyromagnetic ratio (^{1}H, ^{19}F) in the system: spins on the guest molecules and OH protons attached to aluminum metals (the MOF ligands were deuterated and can be negligible). To clarify the relationship between T_2 and hyperfine coupling between DAT and guest molecules, the T_2 and the number of ^{1}H and ^{19}F spins from guest analytes inside a unit cell (Figure 3-19). If the nuclear spins of guest molecules are dominant to the relaxation, the T_2 should be shorter with the increase of the number of nuclear spins, but such behavior was not observed. Note that some guests with methyl groups like toluene might be exceptional because methyl protons can have significant effect for relaxation (Figure 3-20). The hyperfine coupling between the OH proton and DAT should also exist. While the hyperfine interaction would not be the dominant factor because the strength (~ MHz) is usually much weaker than ZFS interactions (~ GHz), the degree of fluctuation of hyperfine interaction can be weakened when the molecular motions are suppressed by guests.

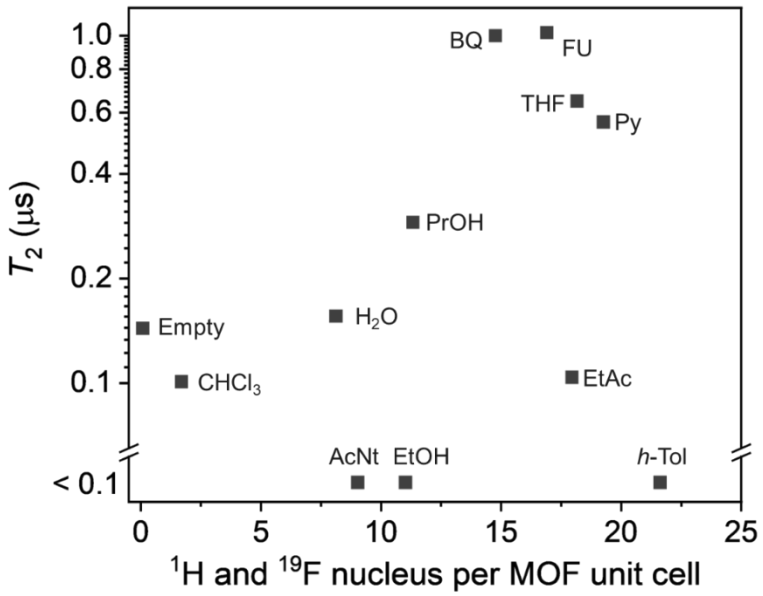

Figure 3-19. Plot of T_2 against the number of ^{1}H and ^{19}F spins from guest analytes of empty (D-MIL-53⊃DAT) and guest-filled (D-MIL-53⊃[DAT + guest]) samples in a unit cell.

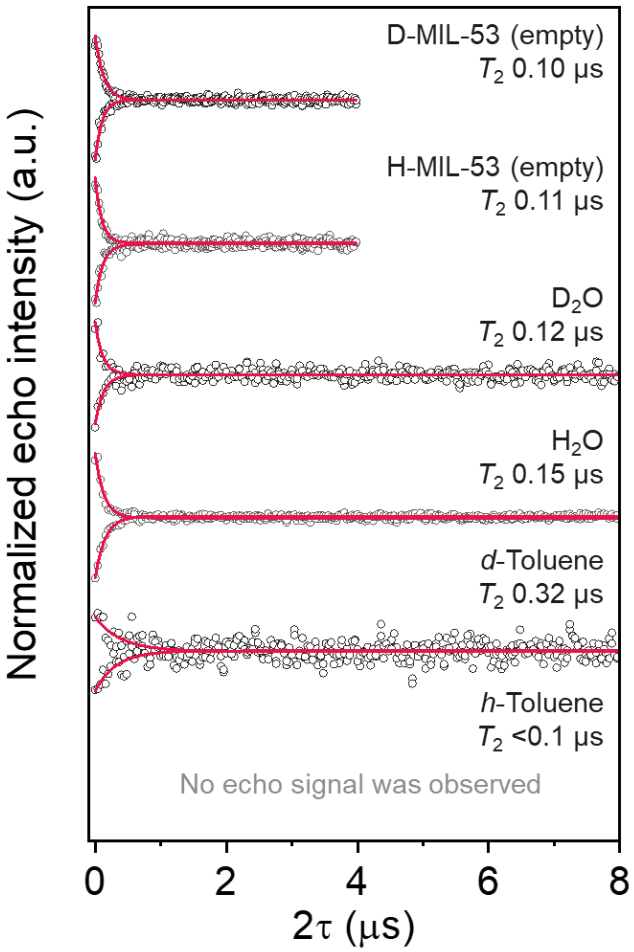

Figure 3-20. Spin echo decay curves after pulsed photoexcitation at 532 nm for D-MIL-53⊃DAT, H-MIL-53⊃DAT, D-MIL-53⊃[DAT + D_2O], D-MIL-53⊃[DAT + H_2O], D-MIL-53⊃[DAT + *d*-Tol], and D-MIL-53⊃[DAT + *h*-Tol] (from top to bottom) at room temperature. Decay curves of each sample at the magnetic field corresponding to the higher and lower EPR peaks (Figure 3-14a) are shown at the top and bottom, respectively. Single-exponential fitting curves for each sample are also shown. Echo signal was not observed for D-MIL-53⊃[DAT + *h*-Tol].

3-3-5. Relationship between coherence time and qubit mobility

The porosity of the MOF pore is important factor that affect the molecular motion around qubit. To gain insight into the local molecular density around DAT in the MOF nanopores, thermogravimetric analysis (TGA) was performed (Figure 3-21). From the TGA curves, the volume fraction of the pore volume occupied by the guest was estimated (Table 3-5). The MOF cell volume minus the framework volume was approximated as the guest accessible pore volume, and the volume fraction of the pore volume occupied by the guest was estimated.

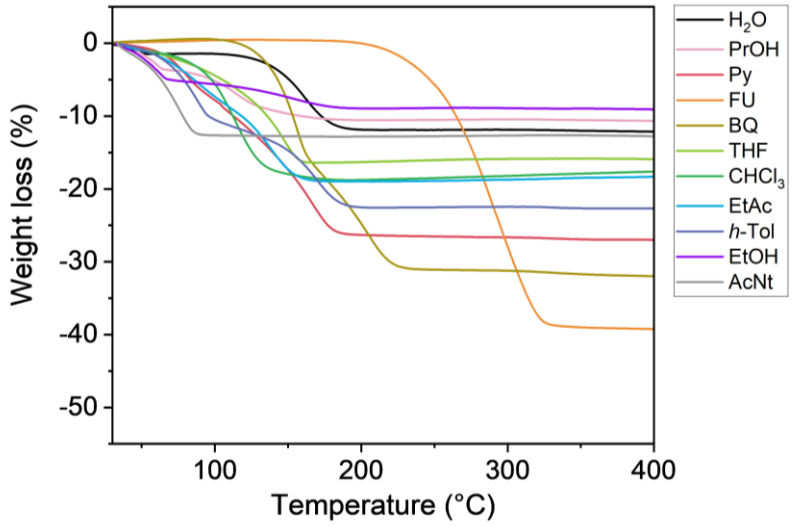

Figure 3-21. TGA curves of D-MIL-53⊃DAT with H_2O (black), PrOH (pink), Py (red), FU (orange), BQ (yellow), THF (pale green), $CHCl_3$ (green), EtAc (blue), *h*-Tol (dark blue), EtOH (purple), and AcNt (gray). TGA curves were obtained under N_2 atmosphere with a heating rate of 5 °C/min.

Table 3-5. Estimation of guest occupied volume (%) of D-MIL-53⊃[DAT+guest] for each guest.

Guest	Weight loss (%)	m_{guest} (g/mol)	n_{guest} [a]	V_{guest} (Å^3) [a]	V_{MOF} (Å^3) [a]	V_{pore} (Å^3) [a]	Guest occupied volume (%)
H_2O	7.81	18.02	4.022	39.17 [b]	977	638	24.7
PrOH	10.14	60.10	1.607	158.9	1312	973	26.2
Py	26.18	79.10	3.836	151.9 [b]	1433	1094	53.3
FU	39.00	130.08	4.205	160.2	1438	1099	61.3
BQ	31.68	108.10	3.670	190.9 [b]	1501	1162	60.3
THF	16.00	72.11	2.260	203.7 [b]	1526	1187	38.8
$CHCl_3$	18.34	119.38	1.610	140.6 [b]	1599	1261	18.0
EtAc	18.70	88.11	2.234	120.2	1637	1298	20.7
h-Tol	22.48	92.14	2.693	231.2 [b]	1654	1315	47.3
EtOH	8.94	46.07	1.823	119.5 [b]	1659	1320	16.5
AcNt	12.52	41.05	2.983	99.11 [b]	1669	1330	22.2

a) the values in lower magnetic field were used.

b) calculated from $(1/2T_1) / (1/T_2) = T_2 / 2T_1$.

Interestingly, the larger the volume fraction occupied by the guest, the longer the T_2 (Figure 3-22). *h*-Tol does not fit this trend, and it is possible that the rotation of the methyl group is responsible for shortening T_2.[3] When perdeuterated toluene (*d*-Tol) is introduced as a guest, T_2 for the DAT triplet is extended to ~0.3 μs (Figure 3-20), which matches the trend for the other guest molecules. This suggests that, in the absence of a particularly relaxing substituent such as a methyl group, the higher the volume fraction occupied by guest (or local molecular density), the more the motility of DAT is suppressed and the longer T_2 is.

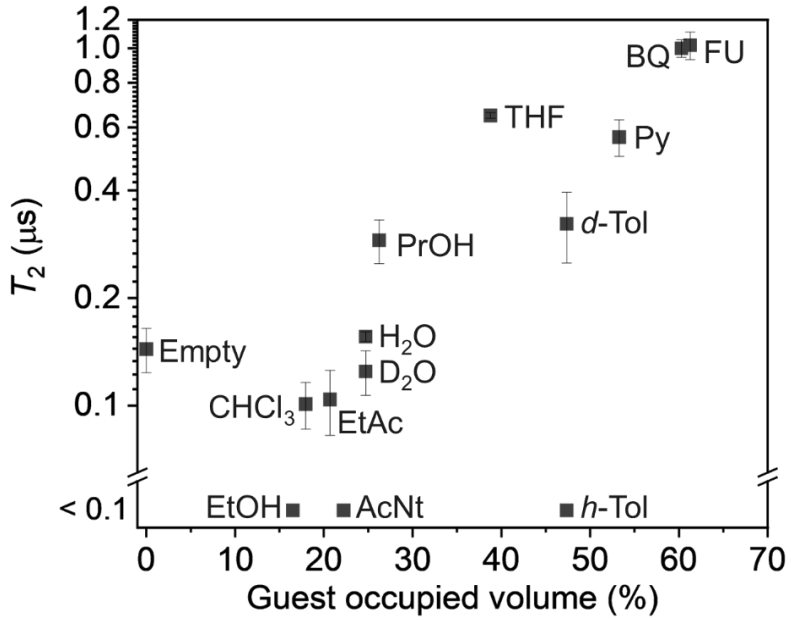

Figure 3-22. T_2 and volume fraction occupied by the guest are plotted for empty (D-MIL-53⊃DAT) and guest-filled (D-MIL-53⊃[DAT + guest]) samples. The means and the standard errors of three measurements are shown for the empty, FU and THF samples, and the fit errors obtained by the single-exponential fitting of the spin echo decay curves are shown for other samples. For the H_2O and THF samples, errors were small and buried in the symbols.

Further analysis using experimental techniques such as solid-state nuclear magnetic resonance (NMR) and terahertz spectroscopy may reveal the detailed dynamics of DAT, but it is difficult to get such insights because the amount of DAT incorporated in the MOF is only 0.87 wt% and there are much larger amounts of the host ligands and other guest molecules. Indeed, deuterated DAT (95 % D) was synthesized and introduced into MIL-53 composed of protonated (non-deuterated) terephthalate, but any ^{2}H NMR signal were not detected even after integrating 1000 scans with 15 kHz magic angle spinning at 9.4 T.

Instead, molecular dynamics (MD) simulation was performed to get insights about the DAT dynamics in MIL-53. Three representative systems, empty (MIL-53⊃DAT), MIL-53⊃[DAT + H_2O], and MIL-53⊃[DAT + BQ] were selected as model, which showed different guest density and either longer or shorter T_2. The simulation was conducted at 300 K for 0.2 μs. To evaluate the rotational and translational motions, the distances between aluminum atom and the four carbon atoms were used (Figures 3-23 and 3-24, Table 3-6).

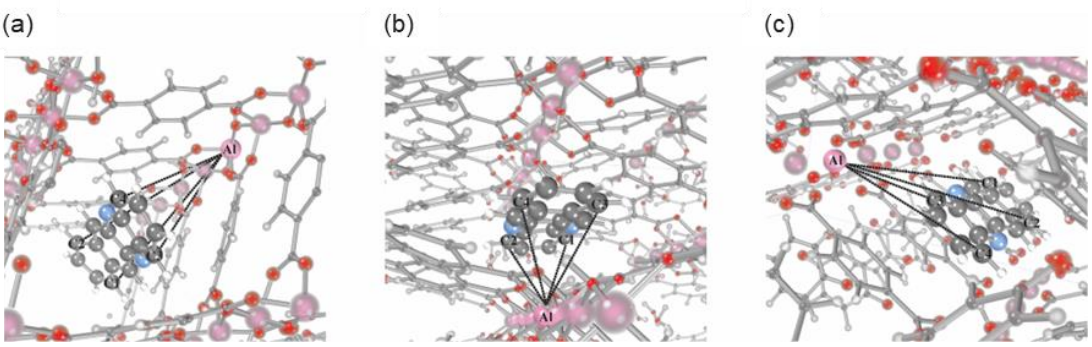

Figure 3-23. Locations of the aluminum atom and the selected four carbon atoms of the DAT molecule to define the four specific distances in the (a) empty, (b) H_2O-solvated and (c) BQ-solvated phases. The dashed four lines in each phase represent these distances which were chosen to analyze the mobility of DAT molecule inside the MIL-53 pore during the MD simulations.

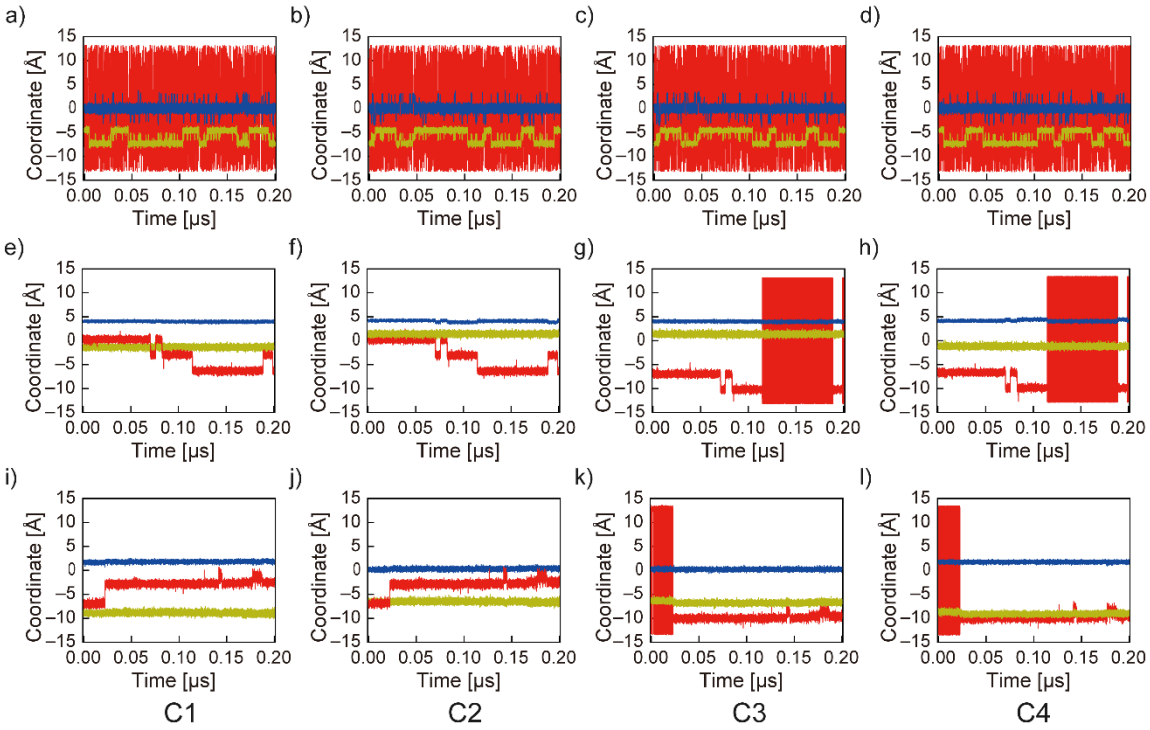

Figure 3-24. The plots of cartesian coordinates, x (blue), y (ocher) and z (red) of the four carbon atoms shown in Figure 3-23 during the MD simulation. The origin of the cartesian coordinates is Al atom shown in Figure 3-23. The plots of (a-d) empty, (e-h) H_2O-solvated and (i-l) BQ-solvated phases are shown. Note: The frequent change of the sing for z coordinate, which corresponds to the one-dimensional pore direction of MIL-53, is attributed to the crossing of the boundary of the model cell under the periodic boundary condition.

Table 3-6. Standard deviations of change of the distances between Al atom in the MIL-53 and the four C atoms in DAT shown in Figure 3-23 for three investigated empty, H_2O-solvated, and BQ-solvated phases.

Phase	Al–C1 / Å	Al–C2 / Å	Al–C3 / Å	Al–C4 / Å
Desolvated	2.8	2.8	2.9	2.8
H_2O-solvated	1.5	1.5	2.3	2.3
BQ-solvated	0.7	0.8	0.9	0.7

In the empty sample, the distances of all directions changed drastically, indicating the presence of both rotational and translational motions. In the case of MIL-53⊃[DAT + H_2O], the displacement in the z (pore) direction was observed, while only fluctuated movements in the x and y directions were observed, which means translational motion in the pore direction is dominant. Importantly, judging from the standard deviation shown in Table 3-6, much less displacements were observed for MIL-53⊃[DAT + BQ], which showed the longest T_2, implying the DAT mobility is significantly suppressed in this system. These results support that the DAT motions can contribute to spin relaxation processes.

As mentioned previously, The DAT triplet has anisotropic zero-field splitting (ZFS) parameters, *D* and *E*, which can be altered by the change of molecular orientation by rotational motions. In addition, since μ-OH groups bridging aluminum metals were not deuterated, the hyperfine interaction between the proton and DAT remained and could be modulated by the translational motion of DAT. Therefore, the fluctuations of anisotropic ZFS parameters and hyperfine interactions based on the molecular motion of DAT would cause the spin–spin relaxation.[57]

Note that the T_2 of D-MIL-53⊃[DAT + H_2O] was comparable to the empty sample, while the result of MD simulation implies D-MIL-53⊃[DAT + H_2O] has less motion than the empty sample. The possible reason is difference in the dynamics of the Al-OH groups. The root mean square fluctuation (RMSF) value of the OH groups, which indicate how much the OH is dynamic, was found to be larger in MIL-53⊃[DAT + H_2O] (Figure 3-25). This intense motion may bring additional relaxation sources to the D-MIL-53⊃[DAT + H_2O] system.

Although the mobility changes in DAT can affect the linewidths of the EPR spectra, almost no change as observed in these systems.[26] Even for the empty sample, which is considered to have the highest mobility of DAT in the present systems, the spectral shape is completely anisotropic and solid-like. This is consistent with the MD simulation result (Figure 3-24) that the timescale of the rotation is around tens of nanoseconds. Thus, even under empty situation, the rotational motions of DAT are sufficiently slower than EPR timescale (~ 100 ps) and might bring no notable changes.

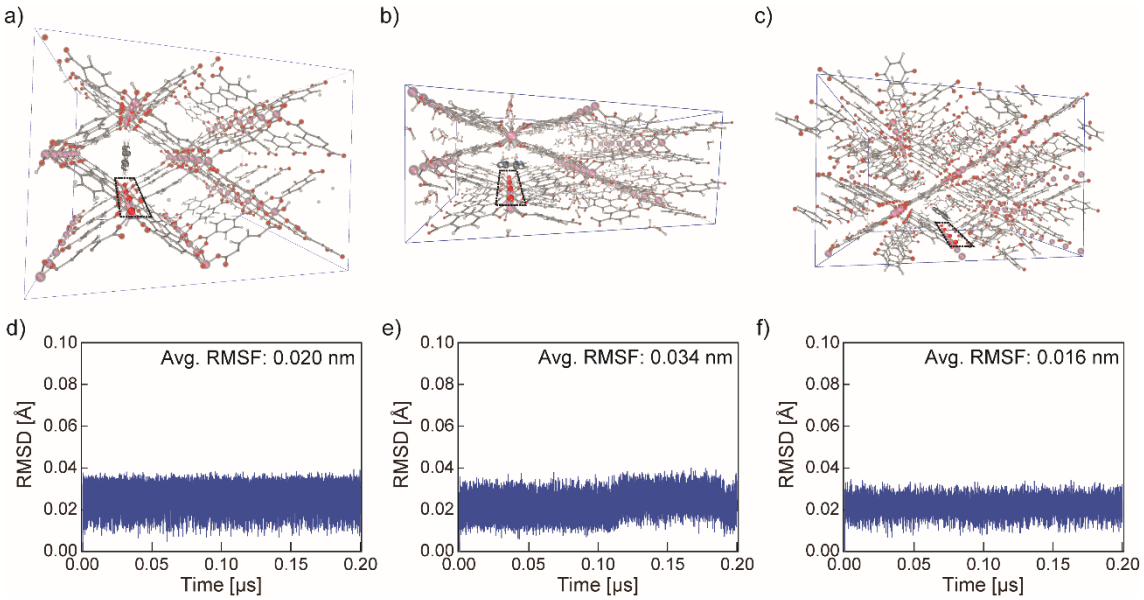

Figure 3-25. The four μ-OH groups that are close to the DAT molecule shown in the black dashed line in the (a) empty, (b) H_2O-solvated and (c) BQ-solvated phases and used to evaluate the root mean square deviation (RMSD) and root mean square fluctuation (RMSF), which are shown in (d), (e), and (f), respectively.

To support the idea that DAT dynamics can be a main factor determining T_2, T_2 was measured at lower temperatures in the empty, guest-free state (D-MIL-53⊃DAT) (Figure 3-26). The T_2 of the DAT triplet, which is 0.1 μs at room temperature, is longer at 100 and 50 K at 1.0 and 2.8 μs, respectively. Conversely, in *p*-terphenyl, which is a solid and dense crystal, the DAT triplet shows a long T_2 of 2.4 μs, even at room temperature. These results also indicate that the dynamics of DAT is important for spin–spin relaxation process.

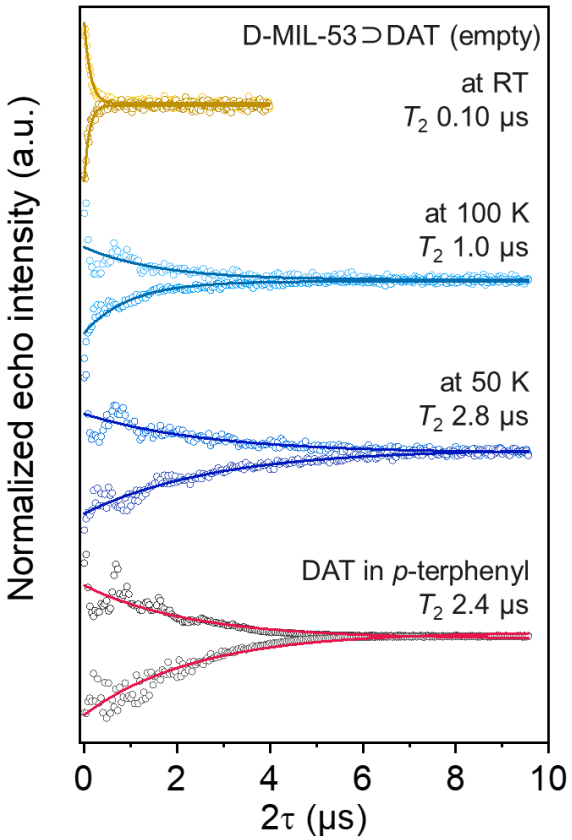

Figure 3-26. Spin echo decay curves after pulsed photoexcitation at 532 nm for the empty sample (D-MIL-53⊃DAT) at room temperature, 100 K, and 50 K (top to bottom), and for DAT doped in *p*-terphenyl crystal at room temperature. Decay curves of each sample at the magnetic field corresponding to the higher and lower EPR peaks (Figure 3-14a) are shown at the top and bottom, respectively.

3-4. Conclusion

In this chapter, the response of quantum coherence to diverse molecules was demonstrated by hybridizing triplet qubits in flexible MOFs. The photoexcited triplet, which is initializable at room temperature and exhibits a long coherence time (T_2), was used as qubits, and the MOF, which can flexibly change its structure upon adsorption of various analyte molecules, was used to make the qubits responsive. This proof-of-concept result will stimulate the development of many hybrid quantum sensors using various combinations of MOFs and qubits in the future. The triplet-MOF complex will provide an ultra-sensitive and highly selective quantum sensing platform that will have impact in a wide range of fields such as analytical chemistry, life sciences, and medicine.

3-5. References

(1) Üngör, O.; Ozvat, T. M.; Ni, Z.; Zadrozny, J. M. Record Chemical-Shift Temperature Sensitivity in a Series of Trinuclear Cobalt Complexes. *J. Am. Chem. Soc.* **2022,** *144*, 9132-9137.

(2) Zhang, T.; Pramanik, G.; Zhang, K.; Gulka, M.; Wang, L.; Jing, J.; Xu, F.; Li, Z.; Wei, Q.; Cigler, P.; Chu, Z. Toward Quantitative Bio-sensing with Nitrogen-Vacancy Center in Diamond. *ACS Sens.* **2021,** *6*, 2077-2107.

(3) Jackson, C. E.; Moseley, I. P.; Martinez, R.; Sung, S.; Zadrozny, J. M. A reaction-coordinate perspective of magnetic relaxation. *Chem. Soc. Rev.* **2021,** *50*, 6684-6699.

(4) Degen, C. L.; Reinhard, F.; Cappellaro, P. Quantum sensing. *Rev. Mod. Phys.* **2017,** *89*.

(5) Kirner, S. V.; Arteaga, D.; Henkel, C.; Margraf, J. T.; Alegret, N.; Ohkubo, K.; Insuasty, B.; Ortiz, A.; Martin, N.; Echegoyen, L.; Fukuzumi, S.; Clark, T.; Guldi, D. M. On-off switch of charge-separated states of pyridine-vinylene-linked porphyrin-C60 conjugates detected by EPR. *Chem. Sci.* **2015,** *6*, 5994-6007.

(6) Bayliss, S. L.; Laorenza, D. W.; Mintun, P. J.; Kovos, B. D.; Freedman, D. E.; Awschalom, D. D. Optically addressable molecular spins for quantum information processing. *Science* **2020,** *370*, 1309–1312.

(7) Christensen, J. A.; Zhou, J.; Tcyrulnikov, N. A.; Krzyaniak, M. D.; Wasielewski, M. R. Spin-Polarized Molecular Triplet States as Qubits: Phosphorus Hyperfine Coupling in the Triplet State of Benzoisophosphinoline. *J. Phys. Chem. Lett.* **2020,** *11*, 7569-7574.

(8) Giménez-Santamarina, S.; Cardona-Serra, S.; Clemente-Juan, J. M.; Gaita-Arino, A.; Coronado, E. Exploiting clock transitions for the chemical design of resilient molecular spin qubits. *Chem. Sci.* **2020,** *11*, 10718-10728.

(9) Jellen, M. J.; Ayodele, M. J.; Cantu, A.; Forbes, M. D. E.; Garcia-Garibay, M. A. 2D Arrays of Organic Qubit Candidates Embedded into a Pillared-Paddlewheel Metal-Organic Framework. *J. Am. Chem. Soc.* **2020,** *142*, 18513-18521.

(10) Wasielewski, M. R.; Forbes, M. D. E.; Frank, N. L.; Kowalski, K.; Scholes, G. D.; Yuen-Zhou, J.; Baldo, M. A.; Freedman, D. E.; Goldsmith, R. H.; III, T. G.; Kirk, M. L.; James K. McCusker; Ogilvie, J. P.; Shultz, D. A.; Stoll, S.; Whaley, K. B. Exploiting chemistry and molecular systems for quantum information science. *Nat. Rev. Chem.* **2020,** *4*, 490–504.

(11) Harvey, S. M.; Wasielewski, M. R. Photogenerated Spin-Correlated Radical Pairs: From Photosynthetic Energy Transduction to Quantum Information Science. *J. Am. Chem. Soc.* **2021,** *143*, 15508-15529.

(12) Kothe, G.; Lukaschek, M.; Yago, T.; Link, G.; Ivanov, K. L.; Lin, T. S. Initializing 2^{14} Pure 14-Qubit Entangled Nuclear Spin States in a Hyperpolarized Molecular Solid. *J. Phys. Chem. Lett.* **2021,** *12*, 3647-3654.

(13) Maylander, M.; Chen, S.; Lorenzo, E. R.; Wasielewski, M. R.; Richert, S. Exploring Photogenerated Molecular Quartet States as Spin Qubits and Qudits. *J. Am. Chem. Soc.* **2021,** *143*, 7050-7058.

(14) von Kugelgen, S.; Krzyaniak, M. D.; Gu, M.; Puggioni, D.; Rondinelli, J. M.; Wasielewski, M. R.; Freedman, D. E. Spectral Addressability in a Modular Two Qubit System. *J. Am. Chem. Soc.* **2021,** *143*, 8069-8077.

(15) Yamashita, M. Next Generation Multifunctional Nano-Science of Advanced Metal Complexes with Quantum Effect and Nonlinearity. *Bull. Chem. Soc. Jpn.* **2021,** *94*, 209-264.

(16) Yu, C. J.; von Kugelgen, S.; Laorenza, D. W.; Freedman, D. E. A Molecular Approach to Quantum Sensing. *ACS*

Cent. Sci. **2021,** *7*, 712-723.

(17) Jacobberger, R. M.; Qiu, Y.; Williams, M. L.; Krzyaniak, M. D.; Wasielewski, M. R. Using Molecular Design to Enhance the Coherence Time of Quintet Multiexcitons Generated by Singlet Fission in Single Crystals. *J. Am. Chem. Soc.* **2022,** *144*, 2276-2283.

(18) Kirk, M. L.; Shultz, D. A.; Hewitt, P.; Chen, J.; van der Est, A. Excited State Magneto-Structural Correlations Related to Photoinduced Electron Spin Polarization. *J. Am. Chem. Soc.* **2022,** *144*, 12781-12788.

(19) Yong, L.; Harbridge, J.; Quine, R. W.; Rinard, G. A.; Eaton, S. S.; Eaton, G. R.; Mailer, C.; Barth, E.; Halpern, H. J. Electron spin relaxation of triarylmethyl radicals in fluid solution. *J. Magn. Reson.* **2001,** *152*, 156-161.

(20) Sun, L.; Yang, L.; Dou, J. H.; Li, J.; Skorupskii, G.; Mardini, M.; Tan, K. O.; Chen, T.; Sun, C.; Oppenheim, J. J.; Griffin, R. G.; Dinca, M.; Rajh, T. Room-Temperature Quantitative Quantum Sensing of Lithium Ions with a Radical-Embedded Metal-Organic Framework. *J. Am. Chem. Soc.* **2022,** *144*, 19008-19016.

(21) Zhang, J.; Liu, L.; Zheng, C.; Li, W.; Wang, C.; Wang, T. Embedded nano spin sensor for in situ probing of gas adsorption inside porous organic frameworks. *Nat. Commun.* **2023,** *14*, 4922.

(22) Sloop, D. J.; Yu, H. L.; Lin, T. S.; Weissman, S. I. Electron spin echoes of a photoexcited triplet: Pentacene in *p*-terphenyl crystals. *J. Chem. Phys.* **1981,** *75*, 3746-3757.

(23) Yamauchi, S. Recent Developments in Studies of Electronic Excited States by Means of Electron Paramagnetic Resonance Spectroscopy. *Bull. Chem. Soc. Jpn.* **2004,** *77*, 1255-1268.

(24) Oxborrow, M.; Breeze, J. D.; Alford, N. M. Room-temperature solid-state maser. *Nature* **2012,** *488*, 353-356.

(25) Kouno, H.; Kawashima, Y.; Tateishi, K.; Uesaka, T.; Kimizuka, N.; Yanai, N. Nonpentacene Polarizing Agents with Improved Air Stability for Triplet Dynamic Nuclear Polarization at Room Temperature. *J. Phys. Chem. Lett.* **2019,** *10*, 2208-2213.

(26) Yamauchi, S.; Takahashi, A.; Iwasaki, Y.; Unno, M.; Ohba, Y.; Higuchi, J.; Blank, A.; Levanon, H. The Lowest Photoexcited Triplet State of Subphthalocyanine in Solid and Fluid Environments. Time-Resolved Electron Paramagnetic Resonance Studies. *J. Phys. Chem. A* **2003,** *107*, 1478-1485.

(27) Loiseau, T.; Serre, C.; Huguenard, C.; Fink, G.; Taulelle, F.; Henry, M.; Bataille, T.; Férey, G. A rationale for the large breathing of the porous aluminum terephthalate (MIL-53) upon hydration. *Chem. Eur. J.* **2004,** *10*, 1373-1382.

(28) Millange, F.; Serre, C.; Guillou, N.; Ferey, G.; Walton, R. I. Structural effects of solvents on the breathing of metal-organic frameworks: an in situ diffraction study. *Angew. Chem. Int. Ed. Engl.* **2008,** *47*, 4100-4105.

(29) Férey, G.; Serre, C. Large breathing effects in three-dimensional porous hybrid matter: facts, analyses, rules and consequences. *Chem. Soc. Rev.* **2009,** *38*, 1380-1399.

(30) Fujiwara, S.; Matsumoto, N.; Nishimura, K.; Kimizuka, N.; Tateishi, K.; Uesaka, T.; Yanai, N. Triplet Dynamic Nuclear Polarization of Guest Molecules through Induced Fit in a Flexible Metal–Organic Framework. *Angew. Chem. Int. Ed. Engl.* **2022,** *61*, e202115792.

(31) Canossa, S.; Gonzalez-Nelson, A.; Shupletsov, L.; Del Carmen Martin, M.; Van der Veen, M. A. Overcoming Crystallinity Limitations of Aluminium Metal-Organic Frameworks by Oxalic Acid Modulated Synthesis. *Chem. Eur. J.* **2020,** *26*, 3564-3570.

(32) Loiseau, T.; Serre, C.; Huguenard, C.; Fink, G.; Taulelle, F.; Henry, M.; Bataille, T.; Férey, G. A rationale for the large breathing of the porous aluminum terephthalate (MIL-53) upon hydration. *Chemistry* **2004,** *10*, 1373-1382.

(33) Yanai, N.; Kitayama, K.; Hijikata, Y.; Sato, H.; Matsuda, R.; Kubota, Y.; Takata, M.; Mizuno, M.; Uemura, T.; Kitagawa, S. Gas detection by structural variations of fluorescent guest molecules in a flexible porous coordination polymer. *Nat. Mater.* **2011,** *10*, 787-793.

(34) Boultif, A.; Louër, D. Indexing of powder diffraction patterns for low-symmetry lattices by the successive dichotomy method. *J. Appi. Cryst.* **1991,** *24*, 987-993.

(35) Dovesi, R.; Saunders, V. R.; Roetti, C.; Orlando, R.; Zicovich-Wilson, C. M.; Pascale, F.; Civalleri, B.; Doll, K.; Harrison, N. M.; Bush, I. J.; D'Arco, P.; Llunell, M.; Causà, M.; Noël, Y.; Maschio, L.; Erba, A.; Rerat, M.; Casassa, S. *R. Dovesi et al. CRYSTAL17 User's Manual* University of Torino: Torino, 2017.

(36) Dovesi, R.; Erba, A.; Orlando, R.; Zicovich‐Wilson, C. M.; Civalleri, B.; Maschio, L.; Rérat, M.; Casassa, S.; Baima, J.; Salustro, S.; Kirtman, B. Quantum-mechanical condensed matter simulations with CRYSTAL. *WIREs Comput. Mol. Sci.* **2018,** *8*, e1360.

(37) Vilela Oliveira, D.; Laun, J.; Peintinger, M. F.; Bredow, T. BSSE-correction scheme for consistent gaussian basis sets of double- and triple-zeta valence with polarization quality for solid-state calculations. *J. Comput. Chem.* **2019,** *40*, 2364-2376.

(38) Perdew, J. P.; Burke, K.; Ernzerhof, M. Generalized Gradient Approximation Made Simple. *Phys. Rev. Lett.* **1996,** *77*, 3865-3868.

(39) Grimme, S. Semiempirical GGA-type density functional constructed with a long-range dispersion correction. *J. Comput. Chem.* **2006,** *27*, 1787-1799.

(40) Abraham, M. J.; Murtola, T.; Schulz, R.; Páll, S.; Smith, J. C.; Hess, B.; Lindahl, E. GROMACS: High performance molecular simulations through multi-level parallelism from laptops to supercomputers. *SoftwareX* **2015,** *1-2*, 19-25.

(41) Seminario, J. M. Calculation of intramolecular force fields from second-derivative tensors. *Int. J. Quantum Chem.* **1996,** *60*, 1271-1277.

(42) Li, P.; Merz, K. M., Jr. MCPB.py: A Python Based Metal Center Parameter Builder. *J. Chem. Inf. Model.* **2016,** *56*, 599-604.

(43) Case, D. A.; Ben-Shalom, I. Y.; Brozell, S. R.; Cerutti, D. S.; III, T. E. C.; Cruzeiro, V. W. D.; Darden, T. A.; Duke, R. E.; Ghoreishi, D.; Gilson, M. K.; Gohlke, H.; Goetz, A. W.; Greene, D.; Harris, R.; Homeyer, N.; Huang, Y.; Izadi, S.; Kovalenko, A.; Kurtzman, T.; Lee, T. S.; LeGrand, S.; Li, P.; Lin, C.; Liu, J.; Luchko, T.; Luo, R.; Mermelstein, D. J.; Merz, K. M.; Miao, Y.; Monard, G.; Nguyen, C.; Nguyen, H.; Omelyan, I.; Onufriev, A.; Pan, F.; Qi, R.; Roe, D. R.; Roitberg, A.; Sagui, C.; Schott-Verdugo, S.; Shen, J.; Simmerling, C. L.; Smith, J.; SalomonFerrer, R.; Swails, J.; Walker, R. C.; Wang, J.; Wei, H.; Wolf, R. M.; Wu, X.; Xiao, L.; York, D. M.; Kollman, P. A. *D. A. Case et al. AMBER 2018*, University of California: San Francisco, 2018.

(44) Wang, J.; Wolf, R. M.; Caldwell, J. W.; Kollman, P. A.; Case, D. A. Development and testing of a general amber force field. *J. Comput. Chem.* **2004,** *25*, 1157-1174.

(45) Rappe, A. K.; Casewit, C. J.; Colwell, K. S.; III, W. A. G.; Skiff, W. M. UFF, a Full Periodic Table Force Field for Molecular Mechanics and Molecular Dynamics Simulations. *J. Am. Chem. Soc.* **1992,** *114*, 10024-10035.

(46) Ramsahye, N. A.; Maurin, G.; Bourrelly, S.; Llewellyn, P.; Loiseau, T.; Ferey, G. Charge distribution in metal organic framework materials: transferability to a preliminary molecular simulation study of the CO(2) adsorption in the MIL-53 (Al) system. *Phys. Chem. Chem. Phys.* **2007,** *9*, 1059-1063.

(47) Frisch, M. J.; Trucks, G. W.; Schlegel, H. B.; Scuseria, G. E.; Robb, M. A.; Cheeseman, J. R.; Scalmani, G.; Barone, V.; Petersson, G. A.; Nakatsuji, H.; Li, X.; Caricato, M.; Marenich, A. V.; Bloino, J.; Janesko, B. G.; Gomperts, R.; Mennucci, B.; Hratchian, H. P.; Ortiz, J. V.; Izmaylov, A. F.; Sonnenberg, J. L.; Young, D. W.; Ding, F.; Lipparini, F.; Egidi, F.; Goings, J.; Peng, B.; Petrone, A.; Henderson, T.; Ranasinghe, D.; Zakrzewski, V. G.; Gao, J.; Rega, N.; Zheng, G.; Liang, W.; Hada, M.; Ehara, M.; Toyota, K.; Fukuda, R.; Hasegawa, J.; Ishida, M.; Nakajima, T.; Honda, Y.; Kitao, O.; Nakai, H.; Vreven, T.; Throssell, K.; J. A. Montgomery, J.; Peralta, J. E.; Ogliaro, F.; Bearpark, M. J.; Heyd, J. J.; Brothers, E. N.; Kudin, K. N.; Staroverov, V. N.; Keith, T. A.; Kobayashi, R.; Normand, J.; Raghavachari, K.; Rendell, A. P.; Burant, J. C.; Iyengar, S. S.; Tomasi, J.; Cossi, M.; Millam, J. M.; Klene, M.; Adamo, C.; Cammi, R.; Ochterski, J. W.; Martin, R. L.; Morokuma, K.; Farkas, O.; Foresman, J. B.; Fox, D. J. *M. J. Frisch et al. Gaussian 16, Revision C.01*, Gaussian, Inc.: Wallingford CT, 2016.

(48) Wang, J.; Wang, W.; Kollman, P. A.; Case, D. A. Automatic atom type and bond type perception in molecular mechanical calculations. *J. Mol. Graph. Model.* **2006,** *25*, 247-260.

(49) Silva, A. W. S. d.; Vranken, W. F. ACPYPE - AnteChamber PYthon Parser interfacE. *BMC Research Notes* **2012,** *5*, 367.

(50) Bussi, G.; Donadio, D.; Parrinello, M. Canonical sampling through velocity rescaling. *J. Chem. Phys.* **2007,** *126*, 014101.

(51) Hess, B.; Bekker, H.; Berendsen, H. J. C.; Fraaije, J. G. E. M. LINCS: A linear constraint solver for molecular simulations. *J. Comput. Chem.* **1997,** *18*, 1463-1472.

(52) Darden, T.; York, D.; Pedersen, L. Particle mesh Ewald: An N·log(N) method for Ewald sums in large systems. *J. Chem. Phys.* **1993,** *98*, 10089-10092.

(53) Dai, Y. Z.; Dong, B. W.; Kao, Y.; Wang, Z. Y.; Un, H. I.; Liu, Z.; Lin, Z. J.; Li, L.; Xie, F. B.; Lu, Y.; Xu, M. X.; Lei, T.; Sun, Y. J.; Wang, J. Y.; Gao, S.; Jiang, S. D.; Pei, J. Chemical Modification toward Long Spin Lifetimes in Organic Conjugated Radicals. *Chemphyschem* **2018,** *19*, 2972-2977.

(54) Fujisawa, J.-i.; Ohba, Y.; Yamauchi, S. A Time-Resolved Electron Paramagnetic Resonance Study of Excited Triplet Porphyrins in Fluid Solution. *J. Am. Chem. Soc.* **1997,** *119*, 8736-8737.

(55) Stoll, S.; Schweiger, A. EasySpin, a comprehensive software package for spectral simulation and analysis in EPR. *J. Magn. Reson.* **2006,** *178*, 42-55.

(56) Sakamoto, K.; Hamachi, T.; Miyokawa, K.; Tateishi, K.; Uesaka, T.; Kurashige, Y.; Yanai, N. Polarizing agents beyond pentacene for efficient triplet dynamic nuclear polarization in glass matrices. *Proc. Natl. Acad. Sci. U. S. A.* **2023,** *120*, e2307926120.

(57) Mirzoyan, R.; Kazmierczak, N. P.; Hadt, R. G. Deconvolving Contributions to Decoherence in Molecular

Electron Spin Qubits: A Dynamic Ligand Field Approach. *Chem. Eur. J.* **2021,** *27*, 9482-9494.

Chapter 4. Room-temperature quantum coherence of high-spin quintet state generated by singlet fission

4-1. Introduction

Quantum information science (QIS) utilizes the principles of quantum mechanics for various applications such as quantum computing,[1-2] quantum communication,[3-4] and quantum sensing.[5-7] The most basic information unit in QIS is a quantum bit (qubit). Among various types of qubit, those using molecular materials generally have the following advantages: the ability to precisely create a specific qubit structure, the ability to control qubit properties by changing the chemical structure, and the scalability to integrate many qubits.[8-10]

Higher spin systems of molecules, such as the quartet state (S = 3/2)[11-12] or quintet state (S = 2),[13-16] are advantageous in quantum spin manipulation because they are composed of multiple spins (i.e., two-qubit operations), such as the CNOT gate, and can generate quantum entanglement, which is a type of correlation between qubits.[17] The sensitivity of quantum sensing can be improved by exploiting quantum entanglement; for example, N-entangled qubit systems can enhance the sensitivity by a factor of $\sqrt{N}$ in a Ramsey relaxometry protocol.[6] One of the photophysical processes that can create a multiplet state is singlet fission (SF).[13-16] SF is a process in which two triplet excitons (T_1) are generated from one photoexcited singlet (S_1) and has been studied mainly in the energy field to improve the efficiency of solar cells.[18-20] This process produces a quintet triplet pair state ^{5}TT consisting of four spins as an intermediate. In addition, by using the reverse process of SF, triplet-triplet annihilation,[21] the information in the quintet state can be optically detected as delayed fluorescence from the S_1 state.

However, only a few cases of ^{5}TT quantum coherence have been observed so far, and these cases are limited to cryogenic temperatures.[22, 19, 14-15] Most of the reported examples are based on molecular crystals of tetracene derivatives, where the two triplet excitons move apart, weakening the exchange interaction J and causing mixing between ^{1}TT and ^{5}TT, and then the triplets come close to each other again, producing a strongly exchange-coupled ^{5}TT. In this mechanism, delicate control of molecular packing is required to make the interaction between chromophores strong enough to cause SF but weak enough to suppress the triplet diffusion.[14] Especially at room temperature, the triplet diffusion is so pronounced that the ^{5}TT pairs quickly dissociate to form non-correlated T+T states, and no coherence can be observed.[22]

Another mechanism for SF-based ^{5}TT generation is the modulation of exchange interactions between chromophores by molecular motion, causing the conversion of ^{1}TT to ^{5}TT.[23-24, 13] Such a conformational change has been observed in intramolecular SF systems consisting of discrete molecules of covalently linked acene units dispersed in a low-temperature glass matrix, and may also occur in acene dimers doped in molecular crystals.[25, 24] However, while molecular motion is necessary for the generation of ^{5}TT, decoherence may be induced by fluctuations in the zero-field splitting interaction.[26] In other words, it remains unclear what kind of molecular motion can simultaneously achieve efficient ^{5}TT generation and noise-suppressed qubits.

Chapter 4 describes how to generate a room-temperature quantum coherence of ^{5}TT multiexcitons preventing the decoherence. MOFs are useful materials for the delicate control of chromophore motion.[16] By integrating chromophores into the ligand, the distance and angle between chromophores can be precisely regulated in MOFs.[27-29] Unlike dense molecular crystals, MOFs have nanoscale voids in the crystals, which allow the chromophores to move, and this movement can be controlled by the topology of the network and the local molecular density around the chromophores.

As a proof-of-concept, a UiO-type[30] pentacene-based MOF (Pn-MOF) was synthesized by combining diamagnetic Zr ions with a dicarboxylate ligand containing pentacene,[31-33] which is the most representative chromophore exhibiting exothermic SF. The non-interpenetrated UiO-type structure can prevent π-stacking between pentacene planes, which gives the pentacene units enough motion to make the conversion from ^{1}TT to ^{5}TT (Figure 4-1).

The dense integration in the Pn-MOF makes the pentacene motion sufficiently suppressive that the quantum coherence of ^{5}TT generated by microwave irradiation was observed for over hundred nanoseconds even at room temperature. Furthermore, the phase and amplitude of quantum beating can be dependent on the molecular motion. The decay of the echo signal from the quintet observed by pulsed electron paramagnetic resonance (EPR) was considerably longer than the decay of the quintet-derived signal in continuous-wave time-resolved electron paramagnetic resonance (CW-TREPR) measurements, suggesting that two components with different degree of order exist and the highly crystalline domains present as minor components in the disordered MOF structure exhibit the long quantum coherence. These results reveal how molecular motions should be designed to achieve quantum coherence of multilevel distinct quantum systems, referred to as

qudits, even at room temperature. This provides a fundamental guideline for the future development of molecular-based QIS.

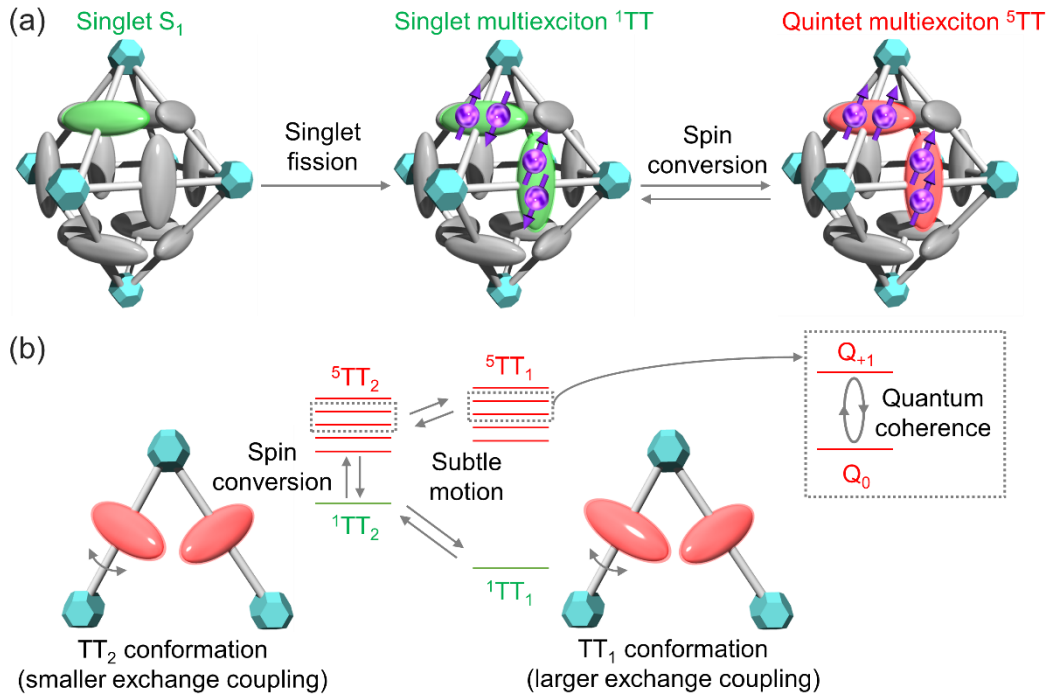

Figure 4-1. Schematic image of Quintet multiexciton generation and its quantum coherence in a MOF. (a) Singlet fission (SF) followed by spin evolution via modulation of exchange interactions results in the formation of quintet multiexciton ^{5}TT in a MOF. (b) Suppressed chromophore motion in a MOF enables not only the spin conversion from ^{1}TT to ^{5}TT but also the quantum coherence of ^{5}TT over hundred nanoseconds even at room temperature.

4-2. Experimental section

4-2-1. Materials

All reagents were used as received unless otherwise noted. Dry tetrahydrofuran (THF) was prepared by treating with Molecular Sieves 4A 1/8, Wako. Liquid paraffin, n-butyl lithium in hexane, and zirconium tetrachloride ($ZrCl_4$) were purchased from Sigma-Aldrich. p-toluene sulfonic acid, tin(II) chloride dihydrate ($SnCl_2 \cdot 2H_2O$), sodium chlorite ($NaClO_2$), sodium dihydrogen phosphate (NaH_2PO_4), and acetic acid were purchased from FUJIFILM Wako Pure Chemical. 4-Bromobenzaldehyde, ethylene glycol, 6,13-pentacenedione, and 2-methyl-2-butene were purchased from TCI.

4-2-2. Characterizations

^{1}H-NMR (400 MHz) spectra were recorded on a JEOL JNM-ECZ400 spectrometer using TMS as the internal standard. Elemental analysis was carried out using a Yanaco CHN Corder MT-5 at the Elemental Analysis Center, Kyushu University. Powder X-ray diffraction (PXRD) patterns were measured on a Bruker D2 Phaser (Cu-Kα, 30 kV, 10 mA). For making the simulated structure and corresponding simulated PXRD pattern, Materials Studio software was used (Accelrys, Material Studio Release Notes, Release 4.2, Accelrys Software, San Diego 2006). The geometry and unit cell were optimized by Materials Studio Forcite tool.[34] Scanning electron microscopy (SEM) image was collected by a Hitachi SU8000 with accelerating voltage of 2.3 kV. Thermogravimetric analysis was conducted on a Rigaku Thermo Plus EVO2 under N_2. N_2 adsorption isotherm measurements were carried out on a Bel BELSORP-max. UV–Vis absorption spectra were obtained on a JASCO V-670 spectrophotometer. FT-IR spectra were recorded on a SHIMADZU IRTracer-100 with a Smiths DuraSamplIR II ATR device.

4-2-3. TAS measurements

The femtosecond transient absorption spectroscopy (fs-TAS) and nanosecond transient absorption spectroscopy (ns-TAS) experiments were performed using home-built pump-probe setups. A Ti:sapphire regenerative amplifier (Spectra-Physics, Spitfire Ace) was utilized as the light source, (pulse duration: 120 fs, repetition rate: 1 kHz, pulse energy: 4 mJ/pulse, central wavelength: 800 nm), seeded by a Ti:sapphire femtosecond mode-locked oscillator (Spectra-Physics, Tsunami) with a pulse duration of 120 fs, a repetition rate of 80 MHz, and a pulse energy of 10 nJ/pulse. For fs-TAS, one of the outputs from the amplifier was directed towards an optical parametric amplifier (Light Conversion, TOPAS), where the output wavelength was tuned to 600 nm for use as the pump pulse. The other output was focused on a sapphire crystal (3 mm thickness), generating white light in the 450-750 nm range for use as the probe pulse. For ns-TAS, output pulses from an optical parametric oscillator (Light Conversion, NT242, central wavelength: 600 nm, pulse duration: 3 ns) using the THG of a Nd:YAG laser as the excitation pulse. was utilized as a pump pulse. The magic angle (~54.7°) was adopted between the pump and probe polarizations. The probe pulse that passed through the sample was dispersed by a polychromator (JASCO, CT-10, 300 grooves/500 nm) and detected by a multichannel detection system with a CMOS sensor (UNISOKU, USP-PSMM-NP). The Pn-MOF sample was enclosed between quartz glass plates under an inert gas atmosphere. The TAS measurements were conducted in a semi-transparent position on the Pn-MOF sample.

4-2-4. Time-resolved EPR measurements and pulsed EPR measurements

Time-resolved EPR measurements were carried out at room temperature using an X-band (9.682 GHz in the CWEPR and 9.589 GHz in the pulsed EPR) CW/FT EPR spectrometer (ELEXSYS II E580) with a dielectric resonator employing a quadrature detection. Samples were photoexcited by the second harmonics (532 nm) of a Nd:YAG laser (Continuum, Minilite II, fwhm ~5 ns). A laser depolarizer (SIGMA KOKI, DEQ 1N) was placed between the laser exit and the microwave cavity. Repetition rate and pulse energy were 10 Hz, and 1 mJ/pulse, respectively. The CW-TREPR spectra were obtained by employing a transient mode in the Bruker Elexsys spectrometer with a microwave power of 4.7 mW. The TREPR signals were directly amplified by a video amplifier using a control program (Xepr) for a digitizer of SpecJet-II. The TREPR data were smoothed for denoising by using a binomial weighted moving average to time-course with a window of 300 ns for the spectra and the 2D plot. The spin echo measurements in Figure 4-25 were performed by using PatternJet-II controlled by the Xepr program. Pulse sequence of the Hahn echo detection (laser–τ_{delay}–$\pi/2$–τ_{echo}–π–τ_{echo}–echo) was employed in the pulse-EPR measurements. The power of microwave pulse was set to maximize the intensity of the spin echo signal of oxidized pentacene species observed in the absence of the laser irradiations following the CWTREPR measurement. In this the pulse durations were x = 16 ns and t_2 = 32 ns, respectively. The echo detected field sweep measurements of the triplet pairs were performed by using τ_{delay} = 1.1 μs, τ_{echo} = 200 ns, x = 8 ns and t_2 = 16 ns, and the magnetic field was varied. Transient nutation measurements were performed by varying x from 0 to 400 ns.

Pn-MOF was put into 2 mm capillaries, with or without paraffin. The capillaries were degassed at room temperature with an oil pump and sealed with a flame.

4-2-5. Computational simulations of EPR

4-2-5-1. Time-resolved EPR

Time-development of the singlet, triplet, and quintet characters for the different exciton-pair conformations together with the *J* values were calculated by using coupled stochastic-Liouville equations.[35] Details of the applied parameters for the multiexciton conformations, the kinetics are listed in Table 4-3, 4-4 and 4-5 to compute the CW-TREPR data and the pulsed EPR data, respectively. The singlet, triplet and quintet diagonal terms in density matrix elements were used to obtain delay time dependences of the excitons of ρ_{SS}^{TT1}, ρ_{SS}^{TT2}, $\rho_{m_\mathrm{S}m_\mathrm{S}}^{\mathrm{TT1}}$, $\rho_{m_\mathrm{S}m_\mathrm{S}}^{\mathrm{TT2}}$, $\rho_{mm}^{\mathrm{T1S0}}$, $\rho_{SS}^{\mathrm{T+T}}$, $\rho_{mm}^{\mathrm{T+T}}$ and $\rho_{m_\mathrm{S}m_\mathrm{S}}^{\mathrm{T+T}}$ where *m* (= +1, 0, -1) represents the quantum number of the triplet sublevels. From Figure 4-16a, the following relations were used: ${}^5\mathrm{TT}_1 = \sum_{m_S}\rho_{m_\mathrm{S}m_\mathrm{S}}^{\mathrm{TT1}}$, ${}^5\mathrm{TT}_2 = \sum_{m_S}\rho_{m_\mathrm{S}m_\mathrm{S}}^{\mathrm{TT2}}$, ${}^3\mathrm{T}_1\mathrm{S}_0 = \sum_m \rho_{mm}^{\mathrm{T1S0}}$, ${}^1\mathrm{TT}_1 = \rho_{SS}^{\mathrm{TT1}}$, ${}^1\mathrm{TT}_2 = \rho_{SS}^{\mathrm{TT2}}$, SCTP = $\rho_{SS}^{\mathrm{T+T}} + \sum_m \rho_{mm}^{\mathrm{T+T}} + \sum_{m_S}\rho_{m_\mathrm{S}m_\mathrm{S}}^{\mathrm{T+T}}$.[35]

From the spin-correlated triplet pair model, coupled stochastic-Liouville equation can be described in ${}^5(\mathrm{TT})_{m\mathrm{S}}$ - ${}^3(\mathrm{TT})_m$ -^{1}(TT) three-level systems where m_S = +2, +1, 0, -1, -2, and *m* = +1, 0, −1, assuming that the quintet-triplet and the singlet-triplet interconversions are ignored in the strongly coupled TT states. The quintet-triplet-singlet (Q-T-S) mixings are considered in the T+T states. In the strongly coupled TT, ${}^5(\mathrm{TT})_{m\mathrm{S}}$ -^{1}(TT) two level system is considered for the quintet generation. For m_S = ±1, ${}^3(\mathrm{TT})_m$ with *m* = ±1 participate in the Q-T-S mixings, respectively, as the three-level systems in the T+T. For m_S = 0, ${}^5(\mathrm{TT})_0$ - ${}^3(\mathrm{TT})_0$ -^{1}(TT) mixing may occur in the T+T. This is because ${}^5(\mathrm{TT})_0$, ${}^3(\mathrm{TT})_0$ and ^{1}(TT) diabatic levels are very close each other for the small exchange coupling in the presence of the strong external magnetic field. The following relations are thus obtained, based upon a previous report:[35]

$$\dot{\boldsymbol{\rho}}_{\mathrm{TT1}} = -i\left[\begin{pmatrix} E_{\mathrm{Q}_{ms}}^{\mathrm{TT1}} & 0 \\ 0 & E_{\mathrm{S}}^{\mathrm{TT1}} \end{pmatrix}, \boldsymbol{\rho}_{\mathrm{TT1}}\right] - k_{12}\boldsymbol{\rho}_{\mathrm{TT1}} + k_{21}\boldsymbol{\rho}_{\mathrm{TT2}} - k_{\mathrm{DISS}}\boldsymbol{\rho}_{\mathrm{TT1}} - \begin{pmatrix} 0 & \frac{k_{\mathrm{REC}}\rho_{\mathrm{Q}_{ms}\mathrm{S}}^{\mathrm{TT1}}}{2} \\ \frac{k_{\mathrm{REC}}\rho_{\mathrm{SQ}_{ms}}^{\mathrm{TT1}}}{2} & k_{\mathrm{REC}}\rho_{\mathrm{SS}}^{\mathrm{TT1}} \end{pmatrix} + k_{\mathrm{Back}}\boldsymbol{\rho}_{\mathrm{T+T}} \quad (4.1)$$

$$\dot{\boldsymbol{\rho}}_{\mathrm{TT2}} = -i\left[\begin{pmatrix} H_{\mathrm{Q}_{ms}\mathrm{Q}_{ms}}^{\mathrm{TT2}} & H_{\mathrm{Q}_{ms}\mathrm{S}}^{\mathrm{TT2}} \\ H_{\mathrm{SQ}_{ms}}^{\mathrm{TT2}} & H_{\mathrm{SS}}^{\mathrm{TT2}} \end{pmatrix}, \boldsymbol{\rho}_{\mathrm{TT2}}\right] + k_{12}\boldsymbol{\rho}_{\mathrm{TT1}} - k_{21}\boldsymbol{\rho}_{\mathrm{TT2}} \quad (4.2)$$

$$\dot{\boldsymbol{\rho}}_{\mathrm{T+T}} = -i\left[\begin{pmatrix} H^{\mathrm{T+T}}_{\mathrm{Q}_{ms}\mathrm{Q}_{ms}} & H^{\mathrm{T+T}}_{\mathrm{Q}_{ms}\mathrm{T}_m} & H^{\mathrm{T+T}}_{\mathrm{Q}_{ms}\mathrm{S}} \\ H^{\mathrm{T+T}}_{\mathrm{T}_m\mathrm{Q}_{ms}} & H^{\mathrm{T+T}}_{\mathrm{T}_m\mathrm{T}_m} & H^{\mathrm{T+T}}_{\mathrm{T}_m\mathrm{Q}_{ms}} \\ H^{\mathrm{T+T}}_{\mathrm{SQ}_{ms}} & H^{\mathrm{T+T}}_{\mathrm{Q}_{ms}\mathrm{T}_m} & H^{\mathrm{T+T}}_{\mathrm{SS}} \end{pmatrix}, \boldsymbol{\rho}_{\mathrm{T+T}}\right] + k_{\mathrm{DISS}}\boldsymbol{\rho}_{\mathrm{TT1}} - k_{\mathrm{Back}}\boldsymbol{\rho}_{\mathrm{T+T}}$$
$$- \begin{pmatrix} 0 & \frac{k_T\rho^{\mathrm{T+T}}_{\mathrm{Q}_{ms}\mathrm{T}_m}}{2} & \frac{k_S\rho^{\mathrm{T+T}}_{\mathrm{Q}_{ms}\mathrm{S}}}{2} \\ \frac{k_T\rho^{\mathrm{T+T}}_{\mathrm{T}_m\mathrm{Q}_{ms}}}{2} & k_T\rho^{\mathrm{T+T}}_{\mathrm{T}_m\mathrm{T}_m} & \frac{(k_S+k_T)\rho^{\mathrm{T+T}}_{\mathrm{T}_m\mathrm{S}}}{2} \\ \frac{k_S\rho^{\mathrm{T+T}}_{\mathrm{SQ}_{ms}}}{2} & \frac{(k_S+k_T)\rho^{\mathrm{T+T}}_{\mathrm{ST}_m}}{2} & k_S\rho^{\mathrm{T+T}}_{\mathrm{SS}} \end{pmatrix} \tag{4.3}$$

where superscripts in the density matrices represent the strongly-coupled TT_1 with large J_1, the thermally activated TT_2 with the intermediate coupling of J_2 ~ -10 GHz, and the de-coupled T+T site, respectively. E_{Qms} and E_S are the eigenenergies in TT_1. In the subscripts, $^5(TT)_{mS}$ = $Q_{mS,}$ and $^1(TT)$ = S are attributable. $H_{Qms\,Qms}$, $H_{Qms\,S}$, H_{SQms} and H_{SS} are respective diagonal and off-diagonal terms of the spin Hamiltonians ($\boldsymbol{H}_{\mathrm{TT2}}$, and $\boldsymbol{H}_{\mathrm{T+T}}$) on the basis spin system of $^5(TT)_{mS}$ and $^1(TT)$ in the TT_1 state. k_{12} and k_{21} are site exchange rate constants determined by the vibration frequency ($\bar{\nu}_{\mathrm{vib}}$) between TT_1 and TT_2 sites with $k_{12} = k_{21}\exp(-\Delta E_{12}/k_BT)$. k_{DISS} and k_{Back} represent the T+T dissociation rate, and the back-reaction rate from the T+T state to the TT_1 state, respectively. k_T and k_S represent recombination rates from the T+T states via the singlet and triplet characters, respectively. $k_T = k_S = 10^5\ s^{-1}$ was assumed in the present calculations. The density matrices are thus represented, as follows.

$$\boldsymbol{\rho}_{\mathrm{TT1}} = \begin{pmatrix} \rho^{\mathrm{TT1}}_{\mathrm{Q}_{ms}\mathrm{Q}_{ms}} & \rho^{\mathrm{TT1}}_{\mathrm{Q}_{ms}\mathrm{S}} \\ \rho^{\mathrm{TT1}}_{\mathrm{SQ}_{ms}} & \rho^{\mathrm{TT1}}_{\mathrm{SS}} \end{pmatrix} \tag{4.4}$$

$$\boldsymbol{\rho}_{\mathrm{TT2}} = \begin{pmatrix} \rho^{\mathrm{TT2}}_{\mathrm{Q}_{ms}\mathrm{Q}_{ms}} & \rho^{\mathrm{TT2}}_{\mathrm{Q}_{ms}\mathrm{S}} \\ \rho^{\mathrm{TT2}}_{\mathrm{SQ}_{ms}} & \rho^{\mathrm{TT2}}_{\mathrm{SS}} \end{pmatrix} \tag{4.5}$$

$$\boldsymbol{\rho}_{\mathrm{T+T}} = \begin{pmatrix} \rho^{\mathrm{T+T}}_{\mathrm{Q}_{ms}\mathrm{Q}_{ms}} & \rho^{\mathrm{T+T}}_{\mathrm{Q}_{ms}\mathrm{T}_m} & \rho^{\mathrm{T+T}}_{\mathrm{Q}_{ms}\mathrm{S}} \\ \rho^{\mathrm{T+T}}_{\mathrm{T}_m\mathrm{Q}_{ms}} & \rho^{\mathrm{T+T}}_{\mathrm{T}_m\mathrm{T}_m} & \rho^{\mathrm{T+T}}_{\mathrm{T}_m\mathrm{S}} \\ \rho^{\mathrm{T+T}}_{\mathrm{SQ}_{ms}} & \rho^{\mathrm{T+T}}_{\mathrm{ST}_m} & \rho^{\mathrm{T+T}}_{\mathrm{SS}} \end{pmatrix} \tag{4.6}$$

Coupled time-differential equations in the 12 (for $m_S = \pm 2$ with S) or 17 (for $m_S = \pm 1$ or 0 with $m = \pm 1$ or with $m = 0$) elements in equation (4.15)-(4.17) are described by regenerating a $\vec{\boldsymbol{\rho}}$ vector composed of these elements. Then, the following master equation is obtained:

$$\frac{\partial\vec{\boldsymbol{\rho}}}{\partial t} = \boldsymbol{L}\vec{\boldsymbol{\rho}} \tag{4.7}$$

where $\boldsymbol{L}$ is summarized in Table 4-1 and 4-2. In these tables, $\rho_{\mathrm{QQ1}} = \rho^{\mathrm{TT1}}_{\mathrm{Q}_{m_S}\mathrm{Q}_{m_S}}$, $\rho_{\mathrm{QS1}} = \rho^{\mathrm{TT1}}_{\mathrm{Q}_{m_S}\mathrm{S}}$, $\rho_{\mathrm{SQ1}} = \rho^{\mathrm{TT1}}_{\mathrm{SQ}_{m_S}}$, $\rho_{\mathrm{SS1}} = \rho^{\mathrm{TT1}}_{\mathrm{SS}}$, $\rho_{\mathrm{QQ2}} = \rho^{\mathrm{TT2}}_{\mathrm{Q}_{m_S}\mathrm{Q}_{m_S}}$, $\rho_{\mathrm{QS2}} = \rho^{\mathrm{TT2}}_{\mathrm{Q}_{m_S}\mathrm{S}}$, $\rho_{\mathrm{SQ2}} = \rho^{\mathrm{TT2}}_{\mathrm{SQ}_{m_S}}$, $\rho_{\mathrm{SS2}} = \rho^{\mathrm{TT2}}_{\mathrm{SS}}$, $\rho_{\mathrm{QQ(T+T)}} = \rho^{\mathrm{T+T}}_{\mathrm{Q}_{m_S}\mathrm{Q}_{m_S}}$, $\rho_{\mathrm{QT(T+T)}} = \rho^{\mathrm{T+T}}_{\mathrm{Q}_{m_S}\mathrm{T}_m}$, $\rho_{\mathrm{QS(T+T)}} = \rho^{\mathrm{T+T}}_{\mathrm{Q}_{m_S}\mathrm{S}}$, $\rho_{\mathrm{TQ(T+T)}} =$

$\rho^{\mathrm{T+T}}_{\mathrm{T}_m\mathrm{Q}_{m_\mathrm{S}}}$, $\rho_{\mathrm{TT(T+T)}} = \rho^{\mathrm{T+T}}_{\mathrm{T}_m\mathrm{T}_m}$, $\rho_{\mathrm{TS(T+T)}} = \rho^{\mathrm{T+T}}_{\mathrm{T}_m\mathrm{S}}$, $\rho_{\mathrm{SQ(T+T)}} = \rho^{\mathrm{T+T}}_{\mathrm{SQ}_{m_\mathrm{S}}}$, $\rho_{\mathrm{ST(T+T)}} = \rho^{\mathrm{T+T}}_{\mathrm{ST}_m}$, $\rho_{\mathrm{SS(T+T)}} = \rho^{\mathrm{T+T}}_{\mathrm{SS}}$ are attributable in equation (4.4)-(4.6).

From equation (4.6), the nine adiabatic-state populations ($\boldsymbol{\rho}^{\mathrm{T+T}_{\mathrm{ii}}}$) where i = 1, 2, ⋯, 9 in the dissociated multiexciton is obtained from the diagonal terms of $\boldsymbol{\rho}^{\mathrm{T+T}}_{1-9} = \boldsymbol{U}^{t}_{\mathrm{T+T}}\boldsymbol{\rho}^{\mathrm{T+T}}\boldsymbol{U}_{\mathrm{T+T}}$ in the SCTP eigenstates calculated by the eigenvectors $\boldsymbol{U}_{\mathrm{T+T}}$ obtained by diagonalizing the spin Hamiltonian of $\boldsymbol{H}_{\mathrm{T+T}}$, where,

$$\boldsymbol{\rho}^{\mathrm{T+T}} = \begin{pmatrix} \ddots & \vdots & \vdots & \vdots & \vdots & \vdots & \vdots \\ 0 & \rho^{\mathrm{T+T}}_{\mathrm{Q}_{ms}\mathrm{Q}_{ms}} & 0 & \rho^{\mathrm{T+T}}_{\mathrm{Q}_{ms}\mathrm{T}_+} & \rho^{\mathrm{T+T}}_{\mathrm{Q}_{ms}\mathrm{T}_0} & \rho^{\mathrm{T+T}}_{\mathrm{Q}_{ms}\mathrm{T}_-} & \rho^{\mathrm{T+T}}_{\mathrm{Q}_{ms}\,\mathrm{S}} \\ 0 & \vdots & \ddots & \vdots & \vdots & \vdots & \vdots \\ 0 & \rho^{\mathrm{T+T}}_{\mathrm{T}_+\mathrm{Q}_{ms}} & 0 & \rho^{\mathrm{T+T}}_{\mathrm{T}_{+1}\mathrm{T}_{+1}} & 0 & 0 & \rho^{\mathrm{T+T}}_{\mathrm{T}_{+1}\mathrm{S}} \\ 0 & \rho^{\mathrm{T+T}}_{\mathrm{Q}_{\mathrm{T}_0}ms} & 0 & 0 & \rho^{\mathrm{T+T}}_{\mathrm{T}_0\mathrm{T}_0} & 0 & \rho^{\mathrm{T+T}}_{\mathrm{T}_0\mathrm{S}} \\ 0 & \rho^{\mathrm{T+T}}_{\mathrm{T}_-\mathrm{Q}_{ms}} & 0 & 0 & 0 & \rho^{\mathrm{T+T}}_{\mathrm{T}_-\mathrm{T}_-} & \rho^{\mathrm{T+T}}_{\mathrm{T}_{-1}\mathrm{S}} \\ \cdots & \rho^{\mathrm{T+T}}_{\mathrm{SQ}_{ms}} & \cdots & \rho^{\mathrm{T+T}}_{\mathrm{ST}_{+1}} & \rho^{\mathrm{T+T}}_{\mathrm{ST}_0} & \rho^{\mathrm{T+T}}_{\mathrm{ST}_{-1}} & \dfrac{\sum_{m_\mathrm{S}} \rho^{\mathrm{T+T}}_{\mathrm{SS}}}{5} \end{pmatrix} \tag{4.8}$$

Using the SCTP model, the TREPR spectra (SP) are calculated as follows:

$$SP = -imag \int_0^{\pi}\int_0^{\pi} \sin\theta \, d\theta \, d\varphi \left\{ \sum_{m_\mathrm{S}} \left(\rho^{\mathrm{TT1}}_{m_\mathrm{S},m_\mathrm{S}-1} + \rho^{\mathrm{TT2}}_{m_\mathrm{S},m_\mathrm{S}-1} \right) + \sum_{i\neq k} \rho^{\mathrm{T+T}}_{i,k} + \sum_{m=1,0} \rho^{\mathrm{T1S0}}_{m,m-1} \right\} \tag{4.9}$$

where θ and φ are the polar and azimuth angles of the external magnetic field applied with respect to the principal axis system in the $\mathrm{T_A}$ triplet in the zero-field splitting interaction and,

$$\begin{pmatrix} \rho^{\mathrm{TT1}}_{m_\mathrm{S},m_\mathrm{S}-1} \\ \rho^{\mathrm{TT2}}_{m_\mathrm{S},m_\mathrm{S}-1} \end{pmatrix}$$

$$= \omega_1 \begin{pmatrix} -\left(-\omega_0 + E^{\mathrm{TT1}}_{\mathrm{Q}_{m_\mathrm{S}}} - E^{\mathrm{TT1}}_{\mathrm{Q}_{m_\mathrm{S}-1}}\right) + i\left(k_{12} + \dfrac{1}{T_{2\mathrm{Q}}}\right) & -ik_{21} \\ -ik_{12} & -\left(-\omega_0 + E^{\mathrm{TT2}}_{\mathrm{Q}_{m_\mathrm{S}}} - E^{\mathrm{TT2}}_{\mathrm{Q}_{m_\mathrm{S}-1}}\right) + i\left(k_{21} + \dfrac{1}{T_{2\mathrm{Q}}}\right) \end{pmatrix}^{-1}$$

$$\times \begin{pmatrix} \rho^{\mathrm{TT1}}_{m_\mathrm{S}m_\mathrm{S}} - \rho^{\mathrm{TT1}}_{m_\mathrm{S}-1,m_\mathrm{S}-1} \\ \rho^{\mathrm{TT2}}_{m_\mathrm{S}m_\mathrm{S}} - \rho^{\mathrm{TT2}}_{m_\mathrm{S}-1,m_\mathrm{S}-1} \end{pmatrix} \{S(S+1) - m_S(m_S-1)\} \tag{4.10}$$

with

$$imag\left(\rho^{\mathrm{T+T}}_{i,k}\right) = \left\langle i\middle|\hat{S}_y\middle|k\right\rangle^2 \frac{\omega_1\left(\rho^{\mathrm{T+T}}_{ii} - \rho^{\mathrm{T+T}}_{kk}\right)T_2}{1 + (\varepsilon_i - \varepsilon_k - \omega_0)^2 T_2^2} \tag{4.11}$$

and

$$imag\left(\rho^{\mathrm{T1S0}}_{m,m-1}\right) = \frac{2\omega_1\left(\rho^{\mathrm{T1S0}}_{mm} - \rho^{\mathrm{T1S0}}_{m-1,m-1}\right)T_2}{1 + (\varepsilon_m - \varepsilon_{m-1} - \omega_0)^2 T_2^2} \tag{4.12}$$

Equation (4.12) represents the EPR line shape in the T_1S_0 pair state generated by the triplet-triplet annihilation process via the strongly coupled ^{3}TT states. Thus, the population dynamics of $\dot{\rho}_{mm}^{\mathrm{TT1}} = k_{\mathrm{Back}}\,\rho_{\mathrm{T}_m\mathrm{T}_m}^{\mathrm{T+T}}$ is incorporated in equation (4.7) and $\rho_{mm}^{\mathrm{T1S0}} = \rho_{mm}^{\mathrm{TT1}}$ is substituted to equation (4.12) to obtain the isolated triplet product caused by the triplet-triplet annihilation.

In equation (4.11), $\langle i|\hat{S}_y|k\rangle^2$, ε_i and ε_k are obtained from the eigenvectors $\boldsymbol{U}_{\mathrm{T+T}}$ and the eigenvalues by diagonalizing the spin Hamiltonian of $\boldsymbol{H}_{\mathrm{T+T}}$ to determine the eigenstates of $|i\rangle = \sum_j^9 c_{ij}\,|\mathrm{TT}\rangle_j$.

In the zero-field splitting interaction of $\boldsymbol{H}_{\mathrm{TTZFS}}$ (= $\boldsymbol{S}_1\boldsymbol{D}_1\boldsymbol{S}_1$ + $\boldsymbol{S}_2\boldsymbol{D}_2\boldsymbol{S}_2$), $\boldsymbol{S}_i$ is the *i*-th triplet spin operator (i = 1 and 2 for A and B moieties, respectively in the T_AT_B multiexciton), and $\boldsymbol{D}_i$ represents the ZFS tensor of the individual triplet. The matrix of the $\boldsymbol{H}_{\mathrm{TTZFS}}$ tensor is dependent on the orientation of the principal axes in the $\boldsymbol{D}_2$ tensor (X_2, Y_2, Z_2) with respect to the principal axes in $\boldsymbol{D}_1$ tensor (X_1, Y_1, Z_1), the geometries of the second pentacene groups were generated by using Euler rotation angles (α, β, γ) with respect to the principal axes in $\boldsymbol{D}_i$ as in equation (1.39)-(1.41)

Direction for the second triplet-state position in TT was set by the polar angles (θ_2 and ϕ_2) with respect the (X_1, Y_1, Z_1) principal axes. The direction of the external magnetic field ($\boldsymbol{B}_0$) was set by the polar angles (θ, ϕ). Thus, $\cos^2\theta_{\mathrm{D}}$ where θ_{D} is the angle between $\boldsymbol{B}_0$ and the inter-spin vector as the principal axis in $\boldsymbol{H}_{\mathrm{TTss}} = D_{\mathrm{SS}}\,(\cos^2\theta_{\mathrm{D}} - 1/3)(3\boldsymbol{S}_{1\mathrm{Z}}\boldsymbol{S}_{2\mathrm{Z}} - \boldsymbol{S}_1\boldsymbol{S}_2)$ is defined for each $\boldsymbol{B}_0$ direction, as reported previously.

Table 4-1. Matrix elements of L in $\partial\vec{\boldsymbol{\rho}}/\partial t = L\rho$ described in the basis spin system of $\widehat{\boldsymbol{H}}_{\mathrm{TT1}}$ utilized for $m_{\mathrm{S}} = \pm 2$ mixed with singlet states.[a)]

ρ_{QQ1}	$-k_{12}$ $-k_{\mathrm{DISS}}$				k_{21}				k_{Back}			
ρ_{QS1}		$-k_{12}-k_{\mathrm{DISS}}-$ $k_{\mathrm{REC}}/2-i($ $E^{\mathrm{TT1}}_{\mathrm{Q}_{ms}}$-$E^{\mathrm{TT1}}_{\mathrm{S}})$				k_{21}				k_{Back}		
ρ_{SQ1}			$-k_{12}-k_{\mathrm{DISS}}-$ $k_{\mathrm{REC}}/2+i($ $E^{\mathrm{TT1}}_{\mathrm{Q}_{ms}}$-$E^{\mathrm{TT1}}_{\mathrm{S}})$				k_{21}				k_{Back}	
ρ_{SS1}				$-k_{12}$ $-k_{\mathrm{DISS}}-$ k_{REC}				k_{21}				k_{Back}
ρ_{QQ2}	k_{12}				$-k_{21}$	$iH^{\mathrm{TT2}}_{\mathrm{SQ}_{ms}}$	$-iH^{\mathrm{TT2}}_{\mathrm{Q_{ms}S}}$					
ρ_{QS2}		k_{12}			$iH^{\mathrm{TT2}}_{\mathrm{Q_{ms}}s}$	$-i(H^{\mathrm{TT2}}_{\mathrm{Q_{ms}Q_{ms}}}$ $-H^{\mathrm{TT2}}_{\mathrm{SS}})-k_{21}$		$-i$ $H^{\mathrm{TT2}}_{\mathrm{Q_{ms}S}}$				
ρ_{SQ2}			k_{12}		$-i$ $H^{\mathrm{TT2}}_{\mathrm{SQ}_{ms}}$		$i(H^{\mathrm{TT2}}_{\mathrm{Q_{ms}Q_{ms}}}-$ $H^{\mathrm{TT2}}_{\mathrm{SS}})-k_{21}$	$iH^{\mathrm{TT2}}_{\mathrm{SQ}_{ms}}$				
ρ_{SS2}				k_{12}		$-iH^{\mathrm{TT2}}_{\mathrm{SQ}_{ms}}$	$iH^{\mathrm{TT2}}_{\mathrm{Q_{ms}S}}$	$-k_{21}$				
$\rho_{\mathrm{QQ(T+T)}}$	k_{DISS}								- k_{Back}	$iH^{\mathrm{T+T}}_{\mathrm{SQ}_{ms}}$	$-iH^{\mathrm{T+T}}_{\mathrm{Q_{ms}}s}$	
$\rho_{\mathrm{QS(T+T)}}$		k_{DISS}							$iH^{T+T}_{\mathrm{Q_{ms}S}}$	$-i(H^{\mathrm{T+T}}_{\mathrm{Q_{ms}Q_{ms}}}$ $-H^{\mathrm{T+T}}_{SS})-k_{\mathrm{S}}$ $/2-k_{\mathrm{Back}}$		$-i$ $H^{\mathrm{T+T}}_{\mathrm{Q}ms\,\mathrm{S}}$
$\rho_{\mathrm{SQ(T+T)}}$			k_{DISS}						$-i$ $H^{\mathrm{T+T}}_{\mathrm{SQ}_{ms}}$		$i(H^{\mathrm{T+T}}_{\mathrm{Q_{ms}Q_{ms}}}-$ $H^{\mathrm{T+T}}_{\mathrm{SS}})-$ $k_{\mathrm{S}}/2-k_{\mathrm{Back}}$	$iH^{\mathrm{T+T}}_{\mathrm{SQ}_{ms}}$
$\rho_{\mathrm{SS(T+T)}}$				k_{DISS}						$-iH^{\mathrm{T+T}}_{\mathrm{SQ}_{ms}}$	$iH^{\mathrm{T+T}}_{\mathrm{Q_{ms}S}}$	$-k_{\mathrm{S}}$ $-k_{\mathrm{Back}}$

[a)] The basis set was obtained by diagonalizing the spin Hamiltonian of $\widehat{\boldsymbol{H}}_{\mathrm{TT1}}$. The matrix identified by the bold frame is replaced by Table 4-2 for $m_{\mathrm{S}} = \pm 1$ and $m_{\mathrm{S}} = 0$ coupled with $m = \pm 1$ and $m = 0$, respectively.

Table 4-2. Matrix elements of L in $\partial\vec{\boldsymbol{\rho}}/\partial t = \boldsymbol{L\rho}$ described for the T+T states when $m_S = \pm 1$ ($m_S = 0$) are mixed with $m = \pm 1$ ($m = 0$), respectively, together with the singlet T+T state. Q and T denote Q_{m_S} and T_m of the T+T multiexciton, respectively.

T+T	QQ	QT	QS	TQ	TT	TS	SQ	ST	SS
QQ	$-k_{Back}$	iH_{TQ}	iH_{SQ}	$-iH_{QT}$			$-iH_{QS}$		
QT	iH_{QT}	$-i(H_{QQ} - H_{TT}) - k_{Back} - k_T/2$	iH_{ST}		$-iH_{QT}$			$-iH_{QS}$	
QS	iH_{QS}	iH_{TS}	$-i(H_{QQ} - H_{SS}) - k_{Back} - k_S/2$			$-iH_{QT}$			$-iH_{QS}$
TQ	$-iH_{TQ}$			$-i(H_{TT} - H_{QQ}) - k_{Back} - k_T/2$	iH_{TQ}	iH_{SQ}	$-iH_{TS}$		
TT		$-iH_{TQ}$		iH_{QT}	$-k_{Back} - k_T$	iH_{ST}		$-iH_{TS}$	
TS			$-iH_{TQ}$	iH_{QS}	iH_{TS}	$-i(H_{TT} - H_{SS}) - k_{Back} - k_T/2 - k_S/2$			$-iH_{TS}$
SQ	$-iH_{SQ}$			$-iH_{ST}$			$-i(H_{SS} - H_{QQ}) - k_{Back} - k_S/2$	iH_{TQ}	iH_{SQ}
ST		$-iH_{SQ}$			$-iH_{ST}$		iH_{QT}	$-i(H_{SS} - H_{TT}) - k_{Back} - k_T/2 - k_S/2$	iH_{ST}
SS			$-iH_{SQ}$			$-iH_{ST}$	iH_{QS}	iH_{TS}	$-k_{Back} - k_S$

4-2-5-2. Pulsed EPR

The nutation profiles and the echo-detected field swept spectrum of the triplet pair are computed from the expectation values of the transverse magnetization of $\langle S_y \rangle$ in the quintet wavefunctions based upon the report by Gierer et al.[36] on the radical pairs. After the pulse durations of x (s) and t_2 (s) in the first and second pulses, respectively in Figure 4-25a, $\langle S_y(\tau_{delay}, x) \rangle$ is represented for a specific field direction, as follows:

$$\langle S_y(\tau_{delay}, x) \rangle = \sum_{m_S=-2,-1,0,+1} I_{m_S,m_S+1}(\tau_{delay}) \left(\frac{\omega_{m_S}}{\omega'_{m_S}}\right)^2 \sin\{\omega'_{m_S} x\} \cos\{\omega'_{m_S} t_2\} \times exp\left[-\frac{x}{T_{2D}}\left\{1 - \frac{1}{2}\left(\frac{\omega_{m_S}}{\omega'_{m_S}}\right)^2\right\}\right] \quad (4.15)$$

with

$$I_{m_S,m_S+1}(\tau_{delay}) = \rho^{\mathrm{TT1}}_{m_S,m_S+1}(\tau_{delay}) + \rho^{\mathrm{TT2}}_{m_S,m_S+1}(\tau_{delay}) \quad (4.16)$$

where

$$\begin{bmatrix} \rho^{\mathrm{TT1}}_{m_S,m_S+1}(\tau_{delay}) \\ \rho^{\mathrm{TT2}}_{m_S,m_S+1}(\tau_{delay}) \end{bmatrix} = \begin{pmatrix} \left(-\omega_0 - E^{\mathrm{TT1}}_{\mathrm{Q}m_S} + E^{\mathrm{TT1}}_{\mathrm{Q}m_S+1}\right) - i\left(k_{12} + \frac{1}{T_{2\mathrm{Q}}}\right) & ik_{21} \\ ik_{12} & \left(-\omega_0 - E^{\mathrm{TT2}}_{\mathrm{Q}m_S} + E^{\mathrm{TT2}}_{\mathrm{Q}m_S+1}\right) - i\left(k_{21} + \frac{1}{T_{2\mathrm{Q}}}\right) \end{pmatrix}^{-1} \times \begin{bmatrix} -\rho^{\mathrm{TT1}}_{m_S m_S}(\tau_{delay}) + \rho^{\mathrm{TT1}}_{m_S+1,m_S+1}(\tau_{delay}) \\ -\rho^{\mathrm{TT2}}_{m_S m_S}(\tau_{delay}) + \rho^{\mathrm{TT2}}_{m_S+1,m_S+1}(\tau_{delay}) \end{bmatrix} exp\left(-\frac{\tau_{delay}}{T_1}\right) \quad (4.17)$$

and

$$\omega'_{m_S} = \sqrt{{\omega_{m_S}}^2 + \left(-\omega_0 - E^{\mathrm{TT1,2}}_{\mathrm{Q}m_S} + E^{\mathrm{TT1,2}}_{\mathrm{Q}m_S+1}\right)^2} \quad (4.18)$$

where ω_0 is the angular frequency of the microwave.

Equation (4.15) and (4.16) represent y-magnetization responses by the first and second microwaves with an angular frequency of ω_0 in the quintet states those of which are in equilibrium between TT_1 and TT_2 states, as detailed in the previous studies in dimer systems. Method to compute the sublevel populations [$\rho^{\mathrm{TT1}}_{m_S m_S}(\tau_{delay})$ and $\rho^{\mathrm{TT2}}_{m_S m_S}(\tau_{delay})$] after the SF

and sublevel energies ($E_{Q m_S}^{TT1}$ and $E_{Q m_S}^{TT2}$) in the presence of the external magnetic field are detailed in the previous reports. [24, 35] T_{2D} = 150 ns and T_1 = 3.8 μs are employed as the decoherence time and the spin–lattice relaxation time in equation (4.15) and (4.17), respectively. k_{12} and k_{21} represent rate constants of the conformational changes between TT_1 and TT_2. It is noted that such quick conformation changes themselves do not induce the decoherences in $\rho_{m_S m_{S+1}}^{TT1}$ and $\rho_{m_S m_{S+1}}^{TT2}$ because the nutation frequency of the quintet EPR transitions in equation (4.18) is not altered by the exchange process with k_{12} and k_{21}. The echo signals are thus obtained as follows:

$$Echo(\tau_{delay}, x) = -\int_0^{\pi}\int_0^{\pi} imag\langle S_y(\tau_{delay}, x)\rangle \sin\theta \, d\theta \, d\phi \qquad (4.19)$$

where θ and ϕ are the polar and azimuth angles of the external magnetic field applied with respect to the principal axis system in the T_A triplet in the zero-field splitting interaction (Figure 4-30). In equation (4.15), the off-resonance effect described in the parentheses is ignored because of the significantly reduced y-magnetization response when T_{2Q} = 100 ns is applied at the off-resonance in equation (4.3). This may correspond to the sharp angle selectivity of the quantum gate (Figure 4-30) at the specific field position of B_0 = 348.1 mT for the sharp resonance polarization in Figure 4-25c. However, minor off-resonance effects are included in the nutation components of 31 and 25 MHz in Figure 4-26c considering that the nutation frequency of the radical is 12 MHz in Figure 4-27b, because 31 and 25 MHz in Figure 4-26c are slightly higher than $\sqrt{6}\times12$ (= 29) and 2×12 (= 24) MHz, respectively.

The red spectrum in Figure 4-25c shows the computed echo signal of equation (4.15) at τ_{delay} = 1.1 μs with substituting x = 5 ns and t_2 = 13 ns as a function of the external magnetic field B_0. For the nutation profiles in Figure 4-26a and 4-26b, equation (4.15) is plotted as a function of x for τ_{delay} = 1.1 μs at B_0 = 348.1 mT applying t_2 = 16 ns. For the delay time dependence of the echo signal (Figure 4-26d), the echo signal of equation (4.15) is plotted as a function of τ_{delay} at the field position of 352 mT. The initial response function of equation (4.16) to all the field directions was also mapped to visualize angle selectivity of the y-magnetization for all the four quantum gates. (Figure 4-30)

4-2-6. THz spectroscopy measurements

Terahertz (THz) spectra of MOF were measured by THz-TDS spectrometer (Advantest TAS7400) in a transmission setup. The frequency resolution of the spectra obtained by the system was 7.6 GHz. The number of accumulations was 1024 at room temperature. MOF in paraffin was measured with polyethylene (PE) cell, and solid MOF samples were measured without PE cell.

3-2-7. Synthesis of PDBA

PDBA was prepared according to our previously reported method.[37]

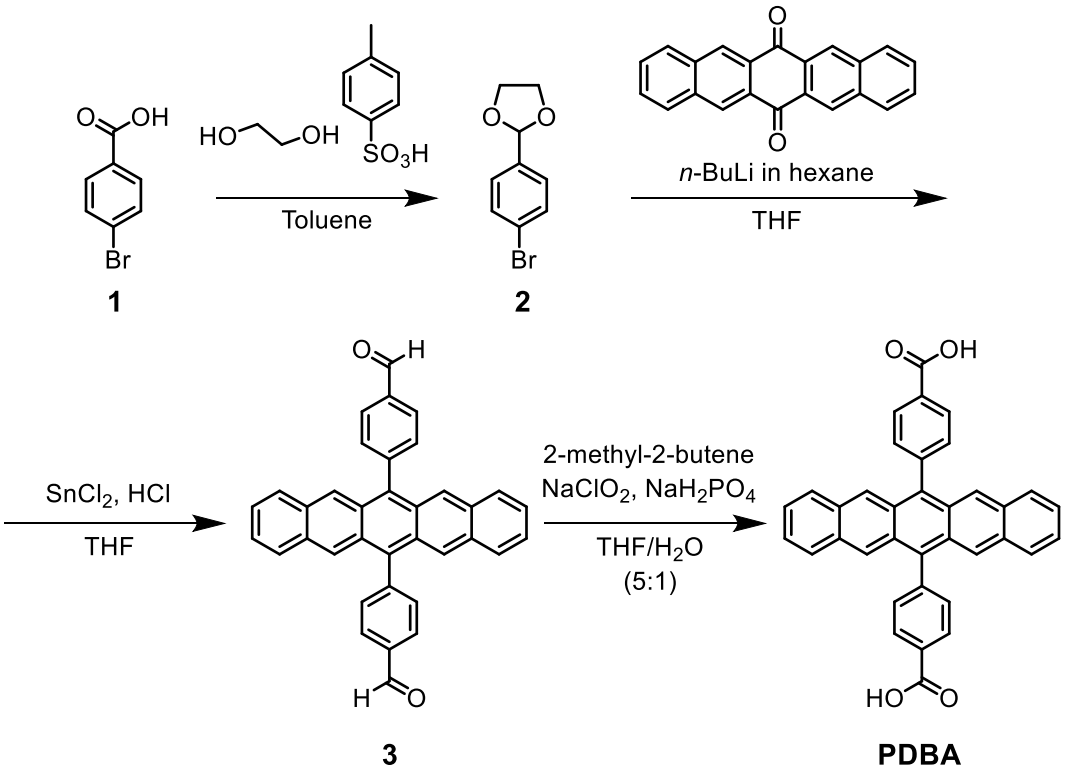

Figure 4-2. Synthetic route of PDBA (4,4'-(pentacene-6,13-diyl)dibenzoic acid).

3-2-7-1. Synthesis of 2-(4-bromophenyl)-1,3-dioxolane (2)

60 mL of a toluene solution of 4-Bromobenzaldehyde (5.0 g, 27 mmol), ethylene glycol (4.3 g, 54 mmol) and *p*-toluene sulfonic acid (0.17 g, 0.90 mmol) was refluxed with a Dean-Stark trap for 8 h. The solution was neutralized with 50 mL K_2CO_3 aqueous solution, then extracted with ethyl acetate (3×50 mL). The organic layer was dehydrated by Na_2SO_4, filtrated and dried under reduced pressure. The orange crude oil was purified using silica gel column chromatography (chloroform/hexane = 1/1), giving a compound **2** as yellow oil. Yield: 5.24 g (85 %). ^{1}H-NMR (400 MHz, DMSO-d_6, TMS): δ = 7.57-7.64 (d, 2H), 7.35-7.45 (d, 2H), 5.73 (s, 1H), 3.90-4.08 (m, 4H).

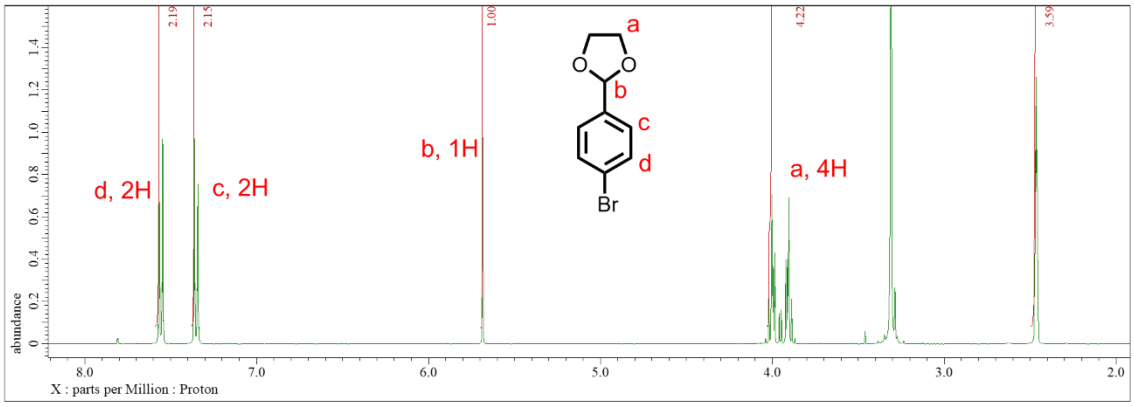

Figure 4-3. ^{1}H NMR spectrum (9.4 T, DMSO-d_6) of 2-(4-bromophenyl)-1,3-dioxolane.

3-2-7-2. Synthesis of 4,4'-(pentacene-6,13-diyl)dibenzaldehyde (3)

n-Butyl lithium in hexane (2.5 M, 6.0 mL, 15 mmol) was dropped to a solution of **2** (3 g, 13.1 mmol) in dry THF (120 mL) at -78 ˚C under N_2 atmosphere. A 20 mL THF solution of 6,13-pentacenedione (1.24 g, 4.0 mmol) was added after stirring for 1 h at -78 ˚C. The reaction was warmed to room temperature and stirred for 24 h. A saturated aqueous NH_4Cl (150 mL) was added to quench the reaction. The mixture was filtered and dried under vacuum. The dark-red oil-like crude was dissolved in 30 mL THF, and added $SnCl_2 \cdot 2H_2O$ (4.2 g, 22 mmol) and 9 mL conc. HCl. To avoid the light exposure, the reaction mixture was covered by an aluminum foil and stirred at room temperature for 24 h. The resulting solution was added 150 mL H_2O and extracted with chloroform (3×100 mL). The organic layer was dehydrated by Na_2SO_4, filtrated, and dried under vacuum. Silica gel column chromatography (chloroform/hexane = 1 : 1) gave **3** as a dark purple powder. Yield: 1.61 g (82 %). ^{1}H-NMR (400 MHz, DMSO-d_6, TMS): δ = 10.32 (s, 2H), 8.32 (t, 4H), 8.25(s, 4H), 7.90–7.95 (d, 4H), 7.84–7.88 (m, 4H), 7.31-7.35 (m, 4H).

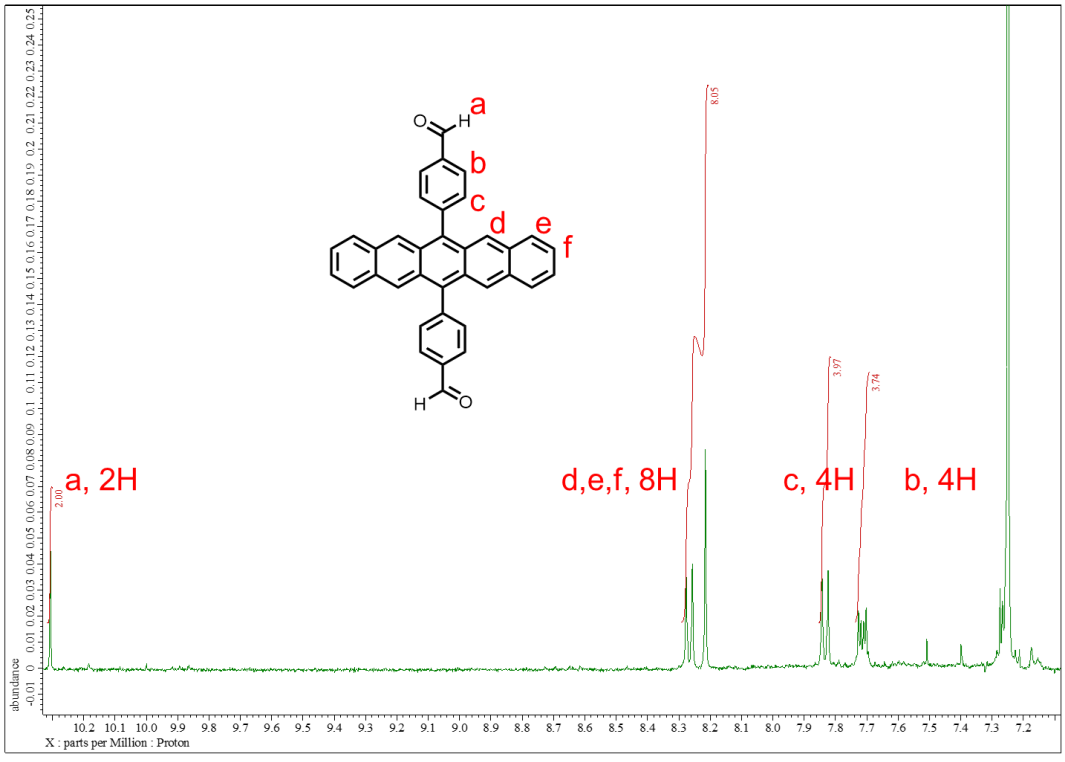

Figure 4-4. ^{1}H NMR spectrum (9.4 T, DMSO-d_6) of 4,4'-(pentacene-6,13-diyl)dibenzaldehyde.

3-2-7-3. Synthesis of 4,4'-(pentacene-6,13-diyl)dibenzoic acid (PDBA)

3 (1.61 g, 3.31 mmol) and 2-methyl-2-butene (35 mL, 331 mmol) were dissolved in THF (200 mL) at 0 °C under Ar atmosphere. $NaClO_2$ (1.2 g, 13.2 mmol) and NaH_2PO_4 (2.50 g, 20.9 mmol) in H_2O (40 mL) was added to the suspension and stirred for 3 h. The reaction was slowly warmed to room temperature and stirred for 24 h under dark. After removing THF under reduced pressure, the residue was diluted with water and washed with chloroform and methanol, giving compound PDBA as a dark purple powder. Yield: 1.05 g (65 %) ^{1}H-NMR (400 MHz, DMSO-d_6, TMS): δ = 8.32-8.37 (d, 4H), 8.25 (s, 4H), 7.85-7.88 (q, 4H), 7.78-7.82 (d, 4H). MS (MALDI-TOF-MS): m/z [M+] calculated $C_{36}H_{22}O_4$, 518.57; found 518.33. Elemental analysis for $C_{36}H_{22}O_4 \cdot 2H_2O$: calculated (%) H 4.73, C 77.97, N 0.00; found (%) H 4.92, C 77.90, N 0.13.

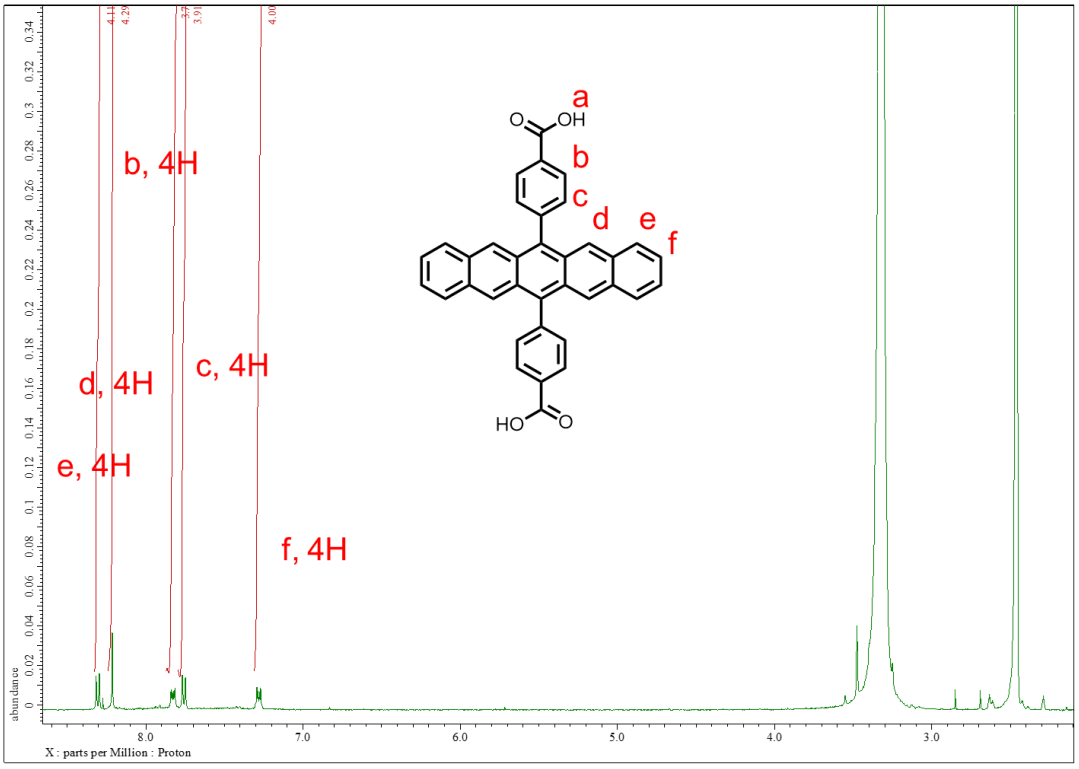

Figure 4-5. ^{1}H NMR spectrum (9.4 T, DMSO-d_6) of PDBA.

3-2-8. Synthesis of Pn-MOF

$ZrCl_4$ (9 mg, 0.0385 mmol) and acetic acid (220 μL, 3.85 mmol) in 2.26 mL of DMF were ultrasonically dissolved in a 6 mL screw vial. After stirring for 6 h at room temperature, PDBA (20 mg, 0.0385 mmol) was added, and the mixture was ultrasonicated again. The obtained purple solution was degassed by freeze-pump-thaw for 2 times in a 10 mL ampule and flame-sealed under vacuum. The degassed sample was wrapped with aluminum foil to minimize light exposure and kept in an oven at 403 K for 48 h. The mixture was cooled to room temperature over 72 h, filtered and soaked in methanol for 12 h. After removing the solvent by filtration and drying for 5 h at 323 K, dark green powder was obtained.

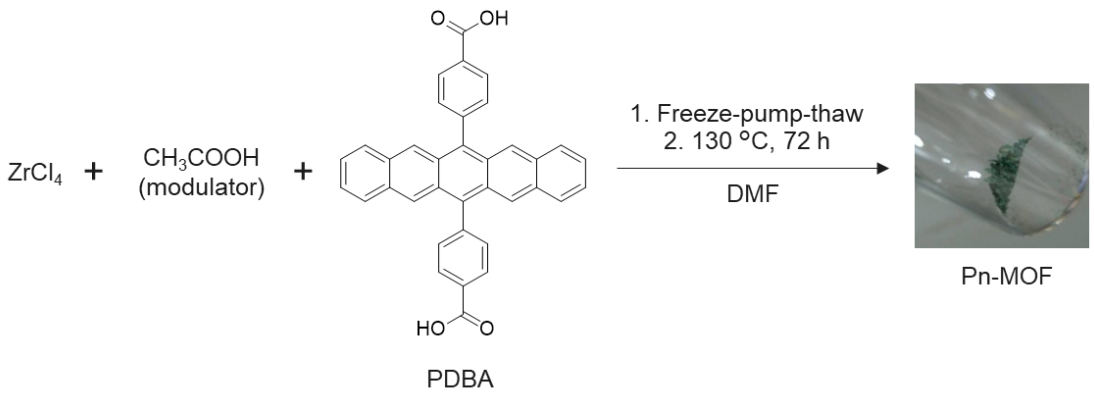

Figure 4-6. Synthetic scheme of Pn-MOF.

4-3. Results and discussion

4-3-1. Characterizations of Pn-MOF

Dicarboxylate-containing pentacene, PDBA was employed as a ligand to insert pentacenes into a MOF structure.[37-38] The energy levels of excited states of PDBA were estimated from time-dependent density functional theory (TD-DFT) calculations. B3LYP/6-31G (d,p) and ωB97X/6-31G (d,p) were used from the ground state optimization and excited state calculations, respectively. It was confirmed that PDBA has the similar S_1 (2.34 eV) and T_1 (0.93 eV) energy levels compared with those of pentacene (S_1: 2.45 eV, T_1: 0.89 eV),[39] and exothermic SF is expected to occur for PDBA as well. Pn-MOF with pentacene integrated in a UiO-type structure was synthesized by a hydrothermal method using $ZrCl_4$ and PDBA in the presence of acetic acid as the modulator in deaerated DMF at 403 K. The coordination of the carboxylic acid of PDBA to the Zr-based cluster was confirmed by the shift to lower wavenumber of the peak originating from carbonyl stretching from 1685 cm^{-1} to 1595 cm^{-1} (asymmetric) and 1540 cm^{-1} (symmetric) (Figure 4-7).[40]

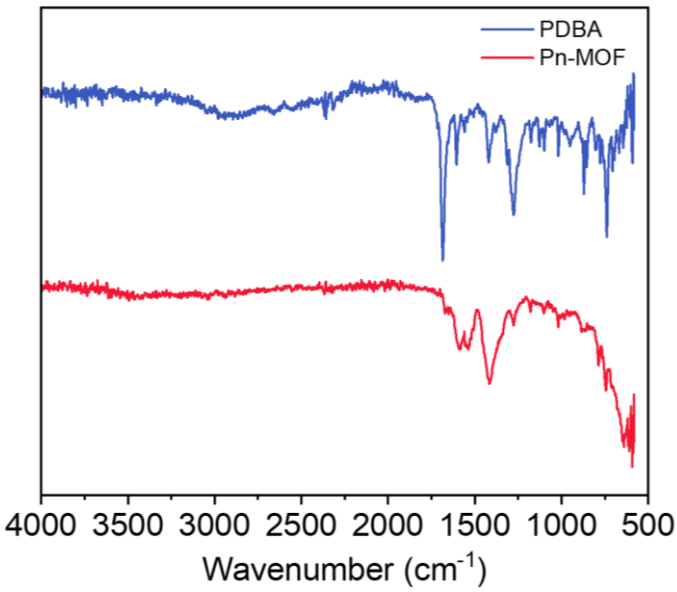

Figure 4-7. FT-IR spectra of PDBA (blue line) and Pn-MOF (red line) at room temperature.

The structure of Pn-MOF was confirmed by powder X-ray diffraction (PXRD) measurements. The peak positions of the experimental PXRD pattern of Pn-MOF matches well with those of the simulated pattern (Figure 4-8). The simulated structure with UiO-68 type topology using PDBA as a ligand is shown in Figure 4-9. The center-to-center distance between the nearest pentacene moieties is 1 nm and the dihedral angle is 120 degrees. The distance between the nearest carbons of the nearest pentacene pair is 0.35 nm, which is close enough for SF to occur. The distance between the second nearest pentacene sites is 1.5 nm and the dihedral angle is 90 degrees. The relatively broad PXRD peaks of Pn-MOF suggest that the structure is partially disordered.[41] Scanning electron microscopy (SEM) images of Pn-MOF showed a rounded morphology with a grain size of approximately 50-100 nm (Figure 4-10), suggesting not high crystallinity of Pn-MOF, consistent with the PXRD results.

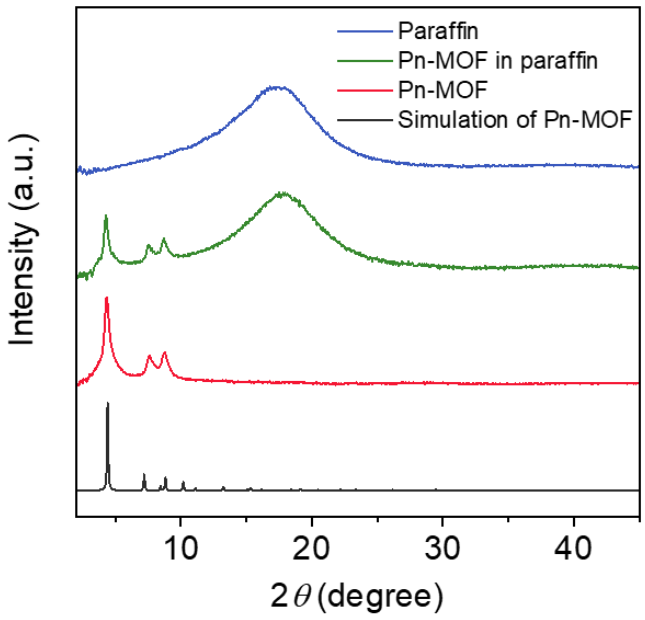

Figure 4-8. Simulated PXRD pattern of Pn-MOF (black line) and experimental PXRD patterns of Pn-MOF (red line), Pn-MOF in paraffin (green line), and paraffin (blue line).

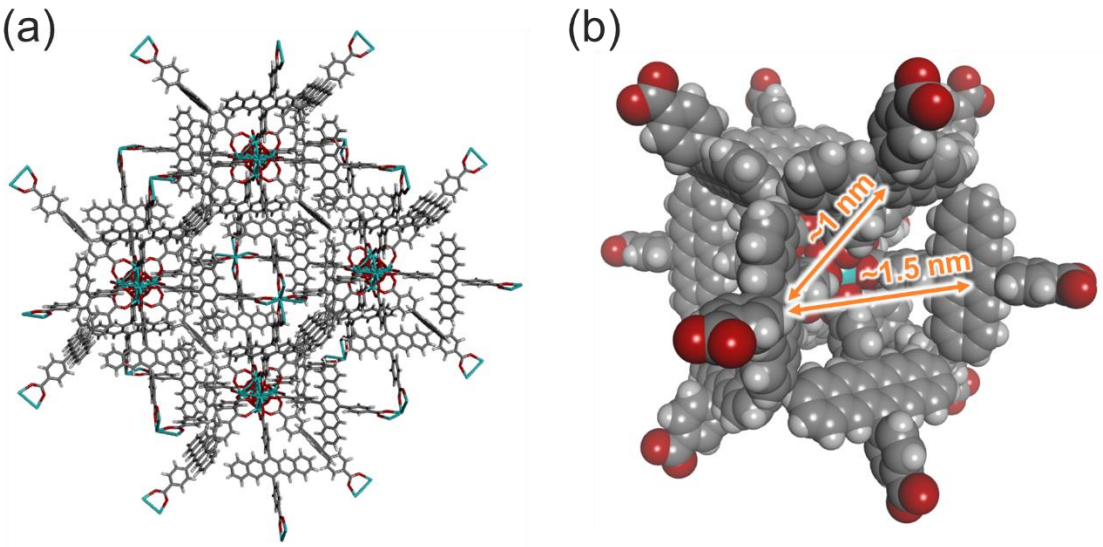

Figure 4-9. (a) Simulated structure of Pn-MOF with UiO-68 type topology. (b) The nearest and second nearest pentacene moieties in Pn-MOF.

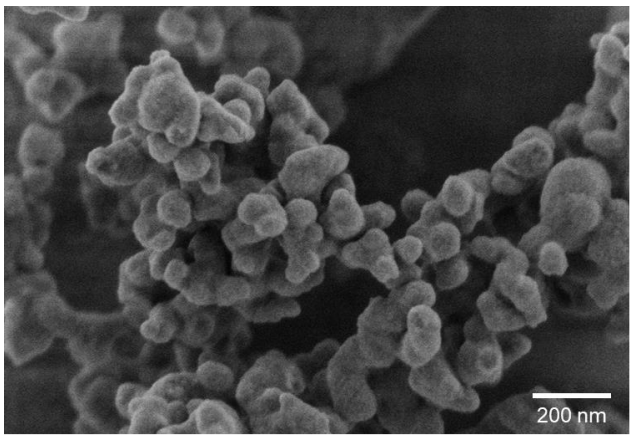

Figure 4-10. SEM image of Pn-MOF.

In Pn-MOF, pentacene moieties do not form π-stacking with each other, which is expected to suppress immediate deactivation of triplet dimer by triplet-triplet annihilation (TTA) and to fluctuate the exchange interaction by changing the dihedral angle between pentacene units. Such moderate inter-pentacene interactions were also confirmed by UV-visible absorption measurements (Figure 4-11). The 0-0 absorption peak of the π-π* transition of the pentacene moiety was located at 602 nm in DMF solution of PDBA, while the absorption peak of Pn-MOF showed a slight broadening and red-shift to 612 nm, indicating the presence of excitonic interactions between the pentacene moieties. On the other hand, in the neat PDBA solid, the absorption peak was located at a longer wavelength of 622 nm with more broadening. This indicates that the interaction is properly modulated in Pn-MOF by preventing π-stacking between pentacene moieties.

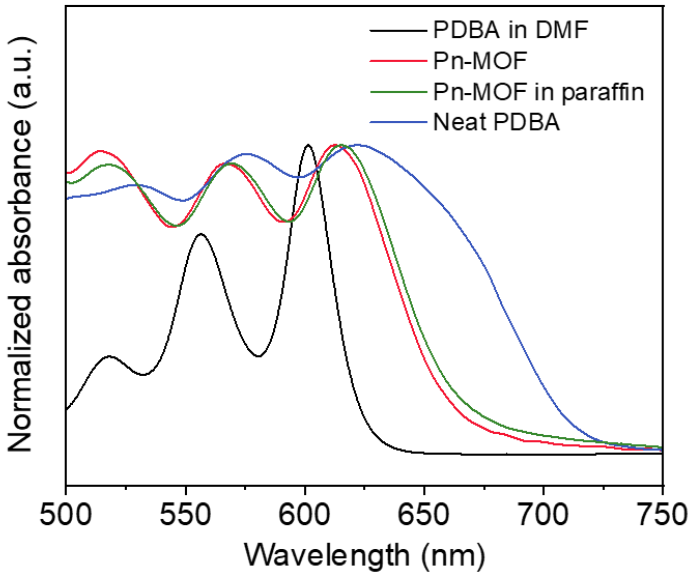

Figure 4-11. UV-vis absorption spectra of 1 mM PDBA in DMF (black line), Pn-MOF (red line), neat PDBA solid (blue line), and Pn-MOF in paraffin (green line).

From thermogravimetric analysis (TGA), it was found that Pn-MOF has high thermal stability up to about 573 K and also adsorbs water from the air into its nanopores (Figure 4-12). The existence of nanopores in Pn-MOF was also confirmed by nitrogen gas adsorption measurements at 77 K after activation of Pn-MOF at 373 K under vacuum (Figure 4-13). The adsorption isotherm of Pn-MOF showed a steep rise in the low-pressure region, which is typical for microporous materials and classified as IUPAC type I. Gradual rise was also observed in the high-pressure region, implying the broad distribution of the pore sizes and the existence of defects. Once the nanoporous structure of Pn-MOF was confirmed, Pn-MOF was soaked in paraffin. Paraffin is non-volatile, useful for dispersing MOF solids, and is sometimes used for time-resolved transient EPR measurements as an inert matrix. The PXRD pattern of activated Pn-MOF soaked in paraffin retained the original peaks, indicating that the UiO-68 type topology was preserved (Figure 4-9). The UV-Vis absorption peak shift of Pn-MOF was very small (612 nm to 615 nm) before and after the paraffin soaking (Figure 4-11). Therefore, it is likely that paraffin in the MOF nanopores does not have any strong interactions with chromophores, and inter-chromophore interactions were not affected by the introduction of guest paraffin molecules.

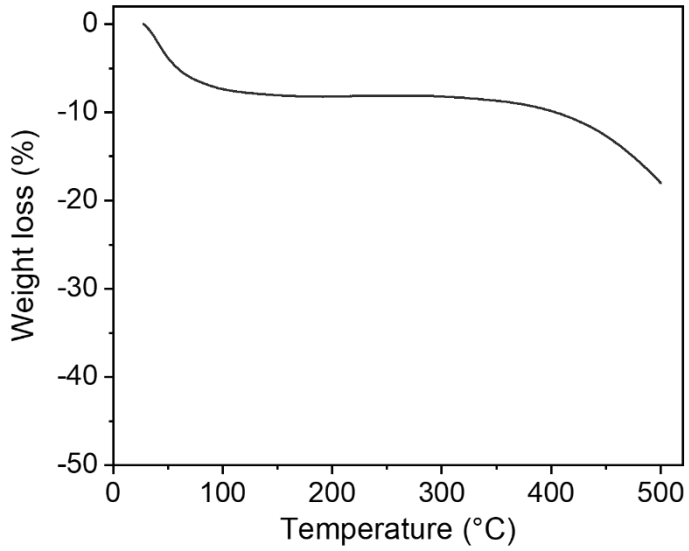

Figure 4-12. TGA curve of Pn-MOF under N_2 atmosphere. The heating rate of the measurement was 5 °C/min. Weight loss below 100 °C is attributed to the uptake of water from the air into the pores of the Pn-MOF.

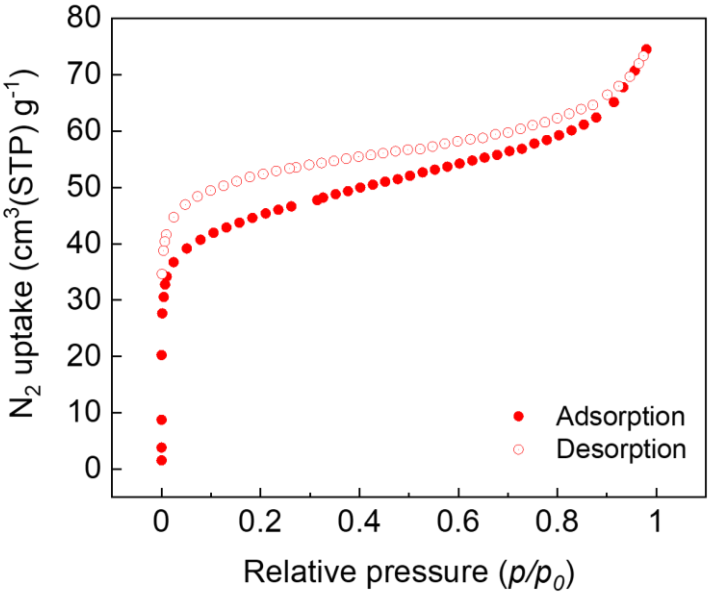

Figure 4-13. Nitrogen adsorption isotherm of Pn-MOF at 77 K. The filled circle represents the adsorption and open circle represents desorption, respectively.

4-3-2. Singlet fission in Pn-MOF

To investigate the SF dynamics in Pn-MOF in paraffin, pump-probe type transient absorption spectroscopy (TAS) was carried out in the 460-550 nm range (Figure 4-14), commonly employed for tracking SF dynamics in pentacene-based systems. Upon excitation by an ultrashort pump pulse at 600 nm, a broad transient absorption spectrum was observed around 450-500 nm, typically attributed to the feature of S_1-S_n absorption of pentacene chromophore. The spectrum subsequently transformed to a different shape with a peak at 530 nm within a hundred picoseconds (Figure 4-14a and 4-14b). Since the signal at 530 nm is indicative of T_1-T_n absorption of pentacene chromophore,[42, 32] the ultrafast generation of the triplet pair state through SF was confirmed. It is possible to assign the second component as the triplet-pair state with singlet multiplicity, ^{1}TT, because the spin multiplicity is conserved in the ultrafast timescale.

Global analysis was performed assuming a sequential model with two components to analyze time constants and spectral features (Figure 4-14b and 4-14c). The first and second components of the evolution-associated spectra (EAS) can reasonably be assigned from their shapes to the spectra from S_1 and ^{1}TT, respectively. The S_1 state was converted to the ^{1}TT state with a time constant of 16.8 ± 0.1 ps, followed by negligible decay (>1 ns) in the current time window. The time scale of transition was slower than the typical timescale of SF in pentacene crystal (~100 fs), but still much quicker than the time scale of the typical intersystem crossing of pentacene in solution (> 1 ns). The ^{1}TT generation process likely outcompetes other photophysical processes such as intersystem crossing in a single chromophore. This is consistent with successful fine tuning of moderate intermolecular interaction required for efficient ^{5}TT generation.

Then the kinetics of the triplet pair state via nanosecond TAS in the Pn-MOF was investigated (Figure 4-14d), which is crucial for QIS. Although the spectral shape was almost constant over time (Figure 4-15), multi-component decay profile was observed. This complex kinetics suggests alternating spin multiplicity via interaction fluctuation impacts the deactivation of the triplet pair state. Low-temperature (150 K) measurements clearly revealed slowed-down dynamics in the nanosecond timescale without altering the spectral shape (Figure 4-14d and 4-15), providing compelling evidence of the role of conformational fluctuation in the electron-spin coupled dynamics.

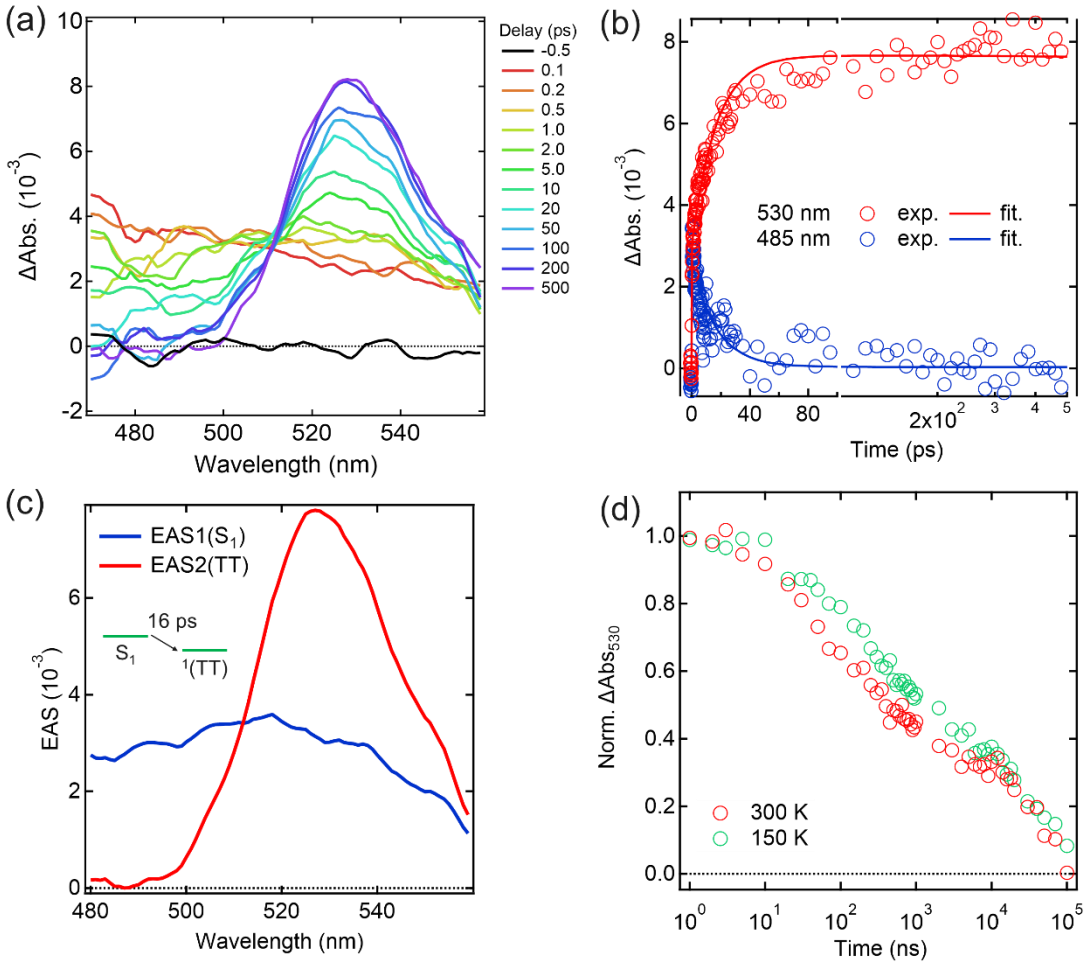

Figure 4-14. (a) Experimentally observed spectral evolution of the fs-TAS (excitation wavelength: 600 nm) of Pn-MOF in paraffin. (b) Temporal change of transient absorption at selected wavelengths and fitting curves from global analysis. (c) Evolution associated spectra (EAS) obtained from global analysis based on the sequential model based on two components. EAS1 and EAS2 indicate the first and second components of EAS, respectively. (d) Temperature dependence of the transient absorption at 530 nm of Pn-MOF.

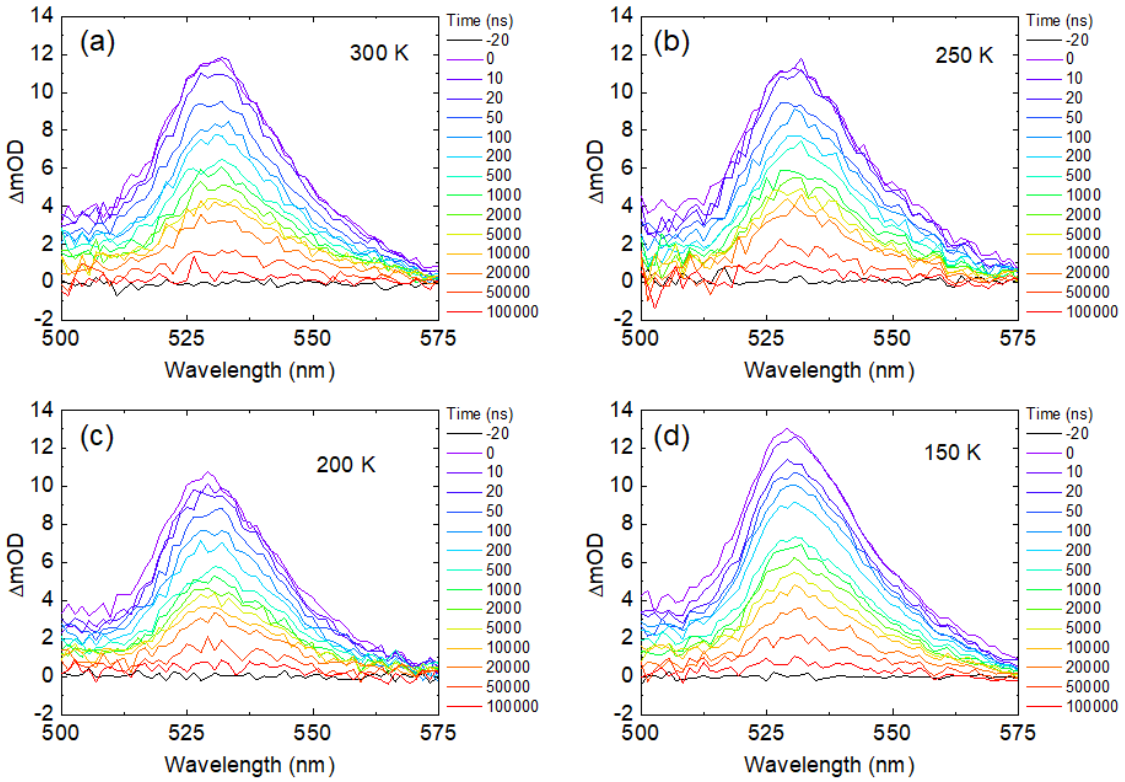

Figure 4-15. Transient absorption spectra of Pn-MOF at (a) 300 K, (b) 250 K, (c) 200 K, and (d) 150 K. The TAS spectra in this spectral range are insensitive to spin multiplicity, as no significant spectral change was observed.

4-3-3. Formation of quintet state

To quantitatively explore the spin dynamics in Pn-MOF, continuous-wave time resolved-EPR (CW-TREPR) measurements of Pn-MOF in paraffin were performed at room temperature. Spin polarization signals with typical A/A/E/A/E/E pattern of quintet (A and E represent microwave absorption and emission, respectively) and E/A pattern of triplet were observed on inner and outer side of the spectra, respectively (Figure 4-16a).

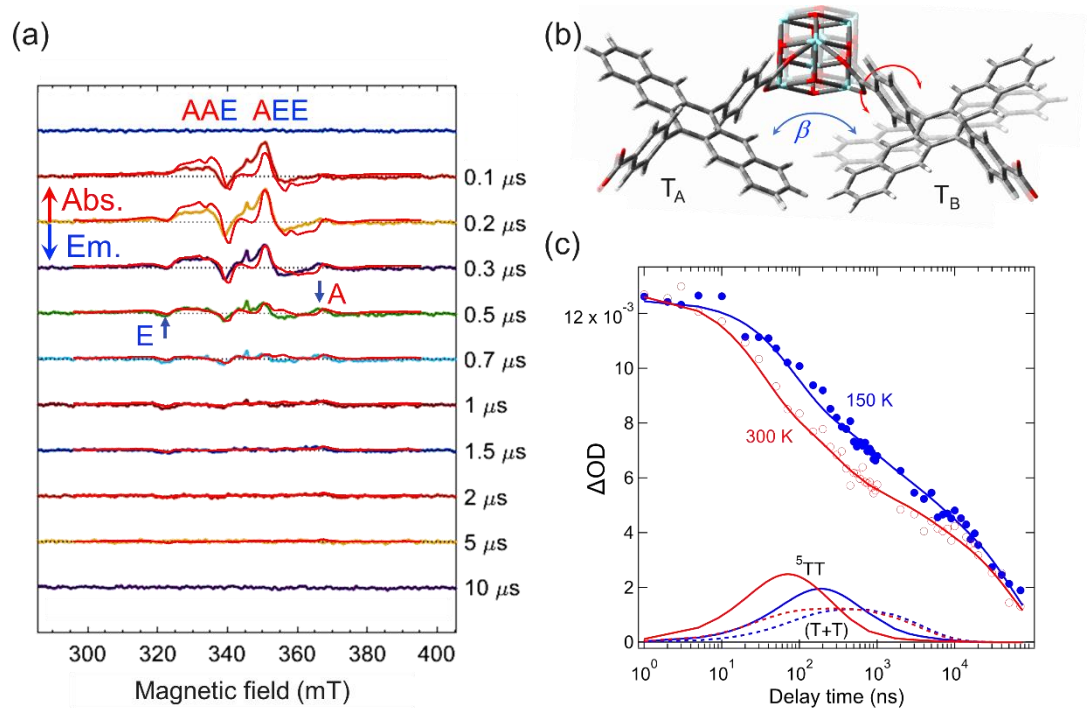

Figure 4-16. (a) TREPR spectra for different delay times of Pn-MOF in paraffin at room temperature. Spectrum simulations by the rotation model analysis in Figure 4-17 are shown by the red lines. (b) Conformations of the quintet TT_1 and TT_2. The blue arrow represents dihedral angle (β) of the aromatic plane in T_B relative to T_A in the T_AT_B pair. (c) Decay profiles of the absorbance changes in nanosecond-TAS (ΔOD) by the multiexcitons at temperatures of 300 K (red circles) and 150 K (blue circles), together with simulated profiles by the rotation model analysis (red and blue lines). Contributions of ^{5}TT and SCTP (T+T) are shown by the solid and dashed lines, respectively, at 300 K (red line) and 150 K (blue line).

According to the TAS data, the EPR silent ^{1}TT state should be initially populated by SF. The spin conversion from ^{1}TT to ^{5}TT has been explained by the modulation of spin–spin exchange coupling J, where $6J = E(^1\text{TT}) - E(^5\text{TT})$, with a conformational change in the covalently linked chromophore dimers. In this case, the chromophores remain strongly coupled to each other even though the conformation of the dimer changes. In contrast to in dense organic crystals, triplet hopping forms weakly coupled triplet pairs, and mixing occurs between ^{1}TT and ^{5}TT, which are close to each other in energy level. The triplets then re-encounter to produce a strongly coupled ^{5}TT. The MOF in this work is a unique system that combines the characteristics of both dimers and crystals because it has a structure in which many chromophores are accumulated, but also has nanopores inside the crystal, which allows the chromophores to rotate and change their interactions. Therefore, it is appropriate to analyze the system using a model that assumes both *J*-modulation in the strongly coupled TT pair and spin mixing in the weakly coupled TT pair (Figure 4-17).

The ^{5}TT formation by the modulation of J through the chromophore rotations within the strongly coupled triplet pair in the 1 nm separated nearest pair shown in Figure 4-9 (Figure 4-17a) competes with the initial exciton migration to form the separated multiexcitons (Figure 4-17b and 4-17c). Depending on local exciton mobility by crystallinity or disorder, the weakly coupled triplet pair (Figure 4-17b) and the non-correlated two triplets T+T (Figure 4-17c) can separately be generated by the exciton migration. The quick triplet exciton dissociation at the crystalline domain would preferentially produce well-separated non-correlated T+T and does not contribute to the electron spin polarization. In contrast, the weakly coupled triplet pair states are anticipated to be generated at the disorder region of the MOF to form the spin correlated triplet pair (SCTP) (T+T) causing the nine adiabatic states (|1>, |2>, ⋯ and |9>) by quantum superpositions of the nine of singlet, triplet and quintet diabatic characters, as shown in Figure 4-17b. These SCTP contributions are observed at the peak positions of the outermost magnetic fields (321 and 365 mT) exhibiting the E/A spin polarization pattern in Figure 4-16a by the spin-spin exchange coupling of J = 1 mT in the 1.5 nm separated exciton pair (Figure 4-9).

Using the model in Figure 4-17, time-developments of the singlet, triplet and quintet diabatic characters were computed for the three different exciton-pair conformations (TT_1, TT_2, and weakly coupled (T+T)) together with the different J values to reproduce the time-dependent EPR data using the density matrix formalism analysis (Table 4-3).

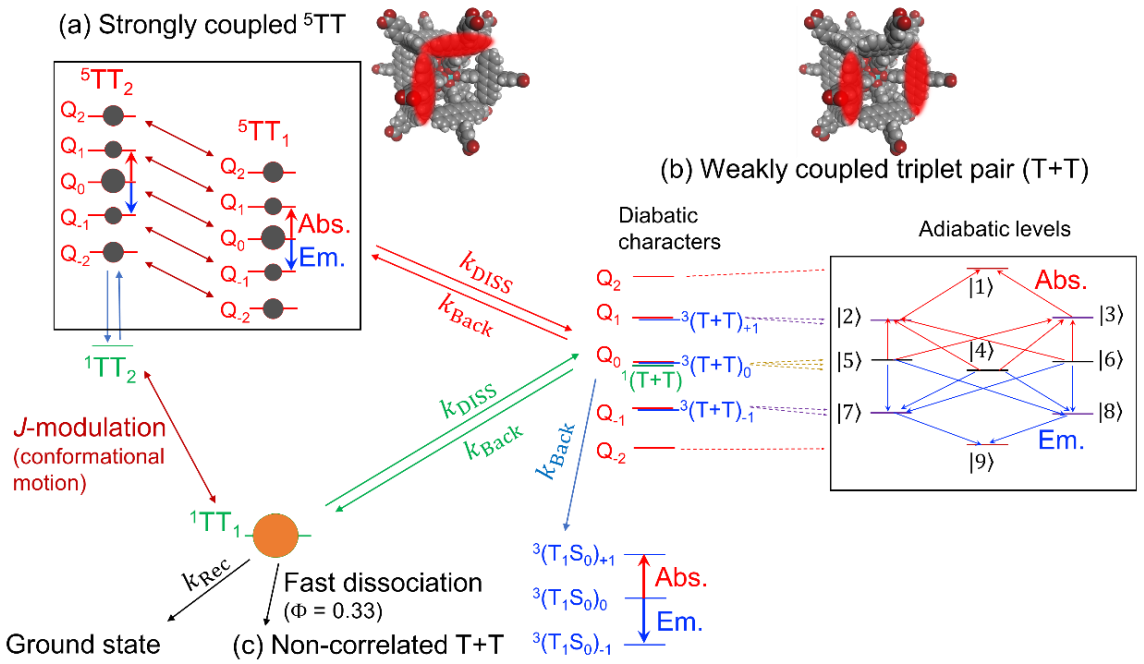

Figure 4-17. Model of the density matrix formalism analysis. Different multiexcitons, (a) strongly coupled triplet pair ^{5}TT (^{5}TT$_1$ and ^{5}TT$_2$), (b) weakly coupled spin correlated triplet pair (T+T), and (c) non-correlated two triplets T+T, are included with considering molecular rotation, exciton migration and re-encounter processes.

Table 4-3. Parameters for computations of the delay time dependence of the EPR spectra and absorbance changes in paraffin, considering the conformation motions between TT_1 and TT_2 states by the multiexciton motions with the frequency of $\bar{\nu}_{vib}$ in the model of Figure 4-17.[24, 35]

		J /MHz	D /MHz [a]	E /MHz [a]	D_{SS} / MHz	Euler angles [b] / degrees (α, β, γ)	Polar angles [c] / degrees	$\bar{\nu}_{vib}$/ cm^{-1}	ΔE_{12} / cm^{-1} [d]	k_{Diss} [e] / s^{-1} k_{Back} [e] / s^{-1}	k_{Rec} [e] / s^{-1}
150 K	TT_1	-1.4×10^5	1,225	-20	-95	α = 95 β = 164 γ = -30	θ_2 =70 φ_2 =160	15	30	8.0×10^5 (1.2×10^6)	1.6×10^7 (2.0×10^7)
	TT_2	-1.9×10^4	1,164	-20	-95	α = 90 β = 113 γ = 0	θ_2 =70 φ_2 =160				-
	T+T	28	1,225	-20	-45	α = 0 β = 125 γ = 0	θ_2 =101 φ_2 =210	-	-	2.3×10^5 (2.8×10^5)	-
300 K	TT_1	-1.4×10^5	1,200	-20	-105	α = 90 β = 130 γ = -20	θ_2 =70 φ_2 =160	14	30	3.0×10^6 (3.0×10^6)	5.6×10^7 (5.6×10^7)
	TT_2	-1.9×10^4	1,140	-20	-105	α = 90 β = 150 γ = -40	θ_2 =70 φ_2 =160				-
	T+T	28	1,200	-20	-45	α = 0 β = 125 γ = 0	θ_2 =101 φ_2 =210	-	-	1.1×10^6 (1.1×10^6)	-

a) Zero-field splitting parameters in $\boldsymbol{H}_{zfs} = D\{S_z^2 - S(S+1)/3\} + E\left(S_x^2 - S_y^2\right)$ for each triplet in the T_AT_B multiexciton. b) Conformation of the principal axes in $\boldsymbol{H}_{zfs}$ of the T_B component with respect to the principal axes of T_A component in the T_AT_B multiexciton with the x-convention.

c) Direction for the T_B component was set by the polar angles (θ_2 and φ_2) with respect the (X_1, Y_1, Z_1) principal axes in T_A. d) The energy gap between TT_1 and TT_2 states represented by $\Delta E_{12} = E(TT_2) - E(TT_1)$. e) The kinetic parameters are shown in the parentheses to fit the transient absorbance changes (Figure 4-14) of the triplet excitons in the absence of the external magnetic field by the present vibronic model analysis.

These diabatic spin characters in Figure 4-17 are described by the density matrix formalism of the equation of motions as follows:

$$\dot{\boldsymbol{\rho}}_{\mathrm{TT1}} = -i\left[\widehat{\boldsymbol{H}}_{\mathrm{TT1}}, \boldsymbol{\rho}_{\mathrm{TT1}}\right] - (k_{12} + k_{\mathrm{DISS}})\boldsymbol{\rho}_{\mathrm{TT1}} + k_{\mathrm{Back}}\boldsymbol{\rho}_{\mathrm{T+T}} + k_{21}\boldsymbol{\rho}_{\mathrm{TT2}} + \widehat{\boldsymbol{K}}_{\mathrm{Rec}}\boldsymbol{\rho}_{\mathrm{TT1}} \tag{4.20}$$

$$\dot{\boldsymbol{\rho}}_{\mathrm{TT2}} = -i\left[\widehat{\boldsymbol{H}}_{\mathrm{TT2}}, \boldsymbol{\rho}_{\mathrm{TT2}}\right] - k_{21}\boldsymbol{\rho}_{\mathrm{TT2}} + k_{12}\boldsymbol{\rho}_{\mathrm{TT1}} \tag{4.21}$$

$$\dot{\boldsymbol{\rho}}_{\mathrm{T+T}} = -i\left[\widehat{\boldsymbol{H}}_{\mathrm{T+T}}, \boldsymbol{\rho}_{\mathrm{T+T}}\right] + k_{\mathrm{DISS}}\boldsymbol{\rho}_{\mathrm{TT1}} - k_{\mathrm{Back}}\boldsymbol{\rho}_{\mathrm{T+T}} - \widehat{\boldsymbol{K}}_{\mathrm{T}}\boldsymbol{\rho}_{\mathrm{T+T}} \tag{4.22}$$

where $\boldsymbol{\rho}$ represents the density matrix for TT_1, TT_2, and T+T states and are numerically solved with the spin Hamiltonian $\widehat{\boldsymbol{H}}$ composed of the Zeeman interaction ($\widehat{\boldsymbol{H}}_{\mathrm{TTz}}$), the zero-field splitting interactions ($\widehat{\boldsymbol{H}}_{\mathrm{TTzfs}}$) in the individual two triplets, the spin–spin dipolar coupling ($\widehat{\boldsymbol{H}}_{\mathrm{TTss}}$) between the triplets, and the exchange interaction ($\widehat{\boldsymbol{H}}_{\mathrm{TTex}}$), as reported previously. Because $\widehat{\boldsymbol{H}}_{\mathrm{TTzfs}}$ and $\widehat{\boldsymbol{H}}_{\mathrm{TTss}}$ are anisotropic and dependent on the TT conformations, the *J* values are also altered by the molecular motions, resulting in the anisotropic electron spin polarization in Figure 4-16a caused by the conformation dynamics. This exchange process by k_{12} and k_{21} in equation (4.20) and (4.21) is thus regarded as the noise to fluctuate the *J* corresponding to the Debye exponential model.[43]

The EPR spectra were simulated as shown by the red lines in Figure 4-16a. The electron spin polarization pattern (A/A/E/A/E/E) in the quintet is sensitive to the mutual orientations of the excitons in the TT and are generated by fluctuation of the exchange coupling. The simulation of the EPR spectra was started with the dihedral angle (β = 130 degrees) between the aromatic planes in TT_1 as shown in Figure 4-16b. Then the effects of the molecular conformation angles of T_B (equation 4.14) in the T_A-T_B pairs on the electron spin polarization of the quintet state were carefully examined. The dihedral angles (β) of the TT_1 or TT_2 states significantly alter the spin polarization pattern (Figure 4-18).

To examine whether the uniqueness of the motion is extracted from the spectrum, the angle distributions in the TT_2 conformations were also considered with fixing the TT_1 conformation (β = 130 degrees) by averaging the five transverse magnetizations with weighting 1:4:6:4:1 amplitude for β = 130, 140, 150, 160 and 170 degrees in the TT_2, as shown by the blue line in Figure 4-19. Also, averaging by the angle distribution is performed in the TT_1 conformation, as shown in Figure 4-19. Because the 130-150° spectrum (solid red lines in Figure 4-19) well agrees with the averaged spectra (dashed blue lines in Figure 4-19), it is concluded that the computation obtained by the 130-150° angle change may include the inhomogeneous distribution in the conformations with a large variation of ±20 degrees. Within this inhomogeneity, the average angle

β = 150 degrees is extracted for the T_B moiety in the TT_2 state as imposed in Figure 4-16b, denoting that the conformation changes by molecular rotations (red arrows in Figure 4-16b) are coupled to the modulation of the exchange interaction in Table 4-3. The stronger J (= -1.4×10^5 MHz) in the TT_1 than that (J = -1.9×10^4 MHz) in the TT_2 is consistent with the dimer model average geometry of TT_1 and TT_2 causing contact edge-to-edge separations (0.29 nm and 0.30 nm, respectively) between carbon atoms in the Pn moieties in Figure 4-16b based on the simulated structure (Figure 4-9). This supports the molecular rotation along with the Pn-ligating direction for the J-modulation.

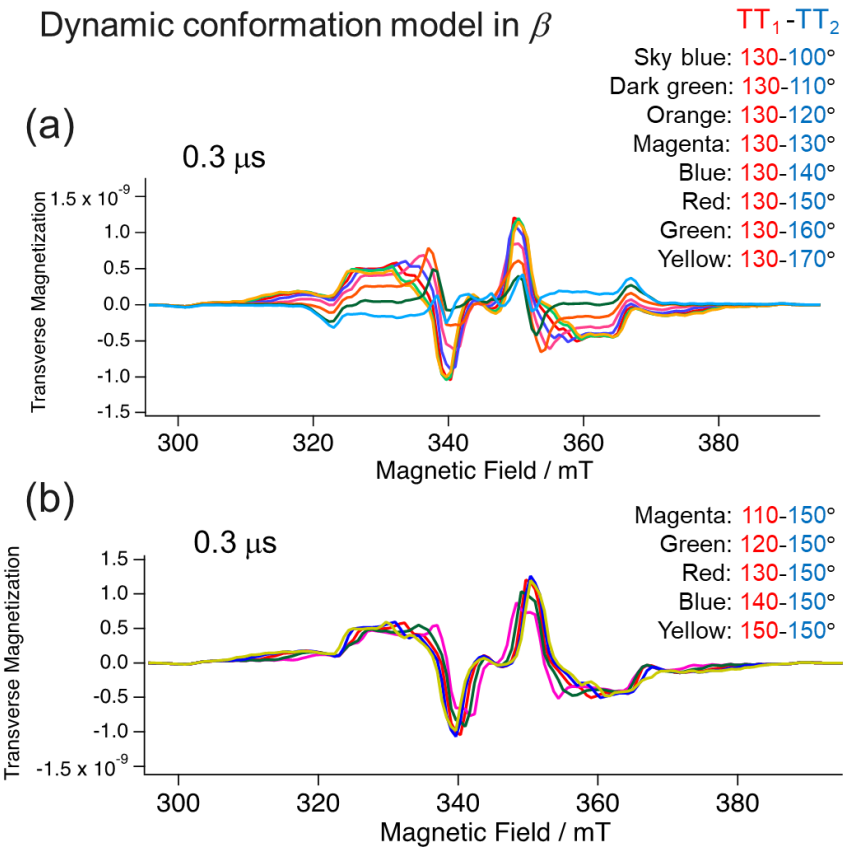

Figure 4-18. Effects of the conformation angles of β in the TT_1 (red) and TT_2 (blue) on the spin-polarized EPR spectra of the multiexcitons at the delay time of 0.3 μs. The other parameters are fixed and are listed in Table 4-3.

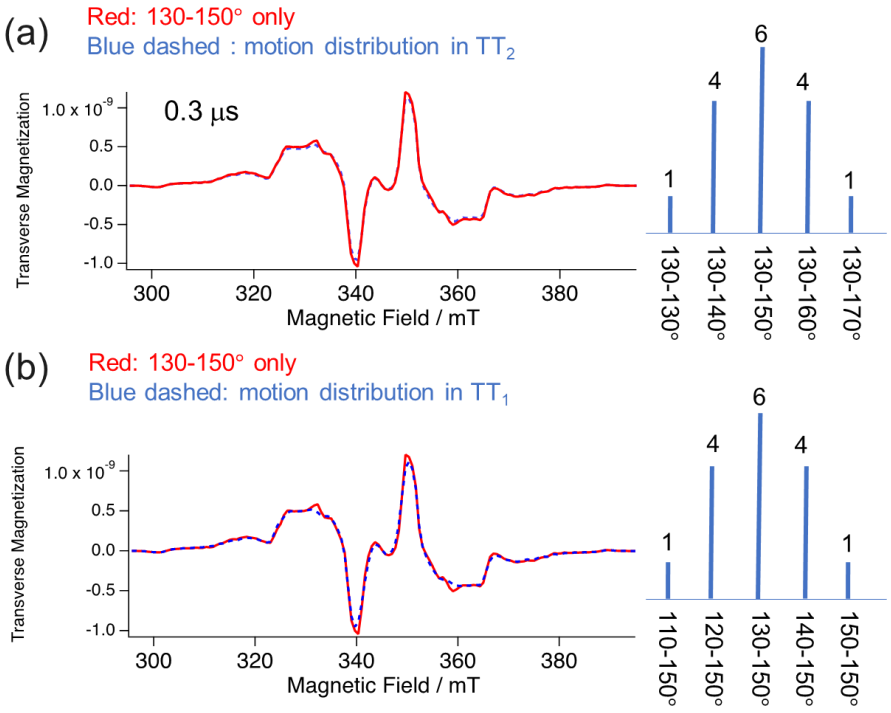

Figure 4-19. Comparisons between the computed EPR spectra obtained by considering the conformation change between TT_1 (β = 130 degrees) and TT_2 (β = 150 degrees) in the red solid lines and spectra (blue dashed lines) obtained by summing the data in Figure 4-18 with weighting 1:4:6:4:1 amplitudes for β = 130, 140, 150, 160 and 170 degrees in the TT_2 in (a) and with the 1:4:6:4:1 amplitudes for β = 110, 120, 130, 140 and 150 degrees in the TT_1 in (b). The bars in the right represent the distributions of the molecular conformations to obtain the dashed lines.

Longer lived multiexciton EPR signals are also obtained at 150 K (Figure 4-20). Better agreement of fitting was obtained at 150 K than at 300 K. This may be due to the activation of several different low-frequency modes of conformational change at higher temperatures, making a perfect fit at 300 K difficult by considering only a single mode of conformational change. By the simulation with setting β = 125 degrees and θ = 40 degrees in TT_1 with varying the TT_2 conformation (Figure 4-21 and Table 4-4), the center field absorptive spectrum is obtained when the motion between β = 125 degrees in TT_1 and β = 110 degrees in TT_2 was considered, as shown by the red line in Figure 4-21.

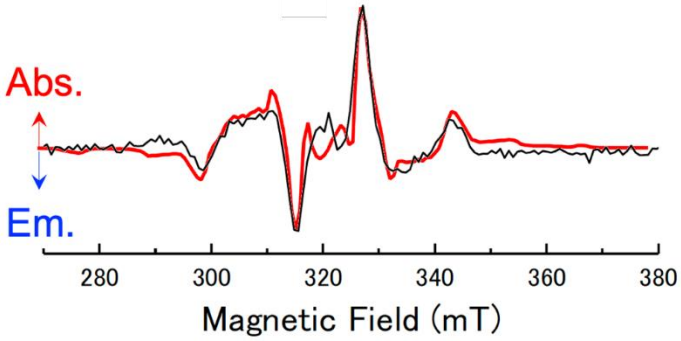

Figure 4-20. Time-resolved EPR spectra of Pn-MOF in paraffin at 150 K obtained at 1 μs after the laser pulse. The measurements were carried out using a home-built X-band (~9 GHz) used in Chapter 2. The red line is obtained by the rotation model analysis in Figure 4-17 using the parameters in Table 4-3 that explained the TAS profile in Figure 4-16c.

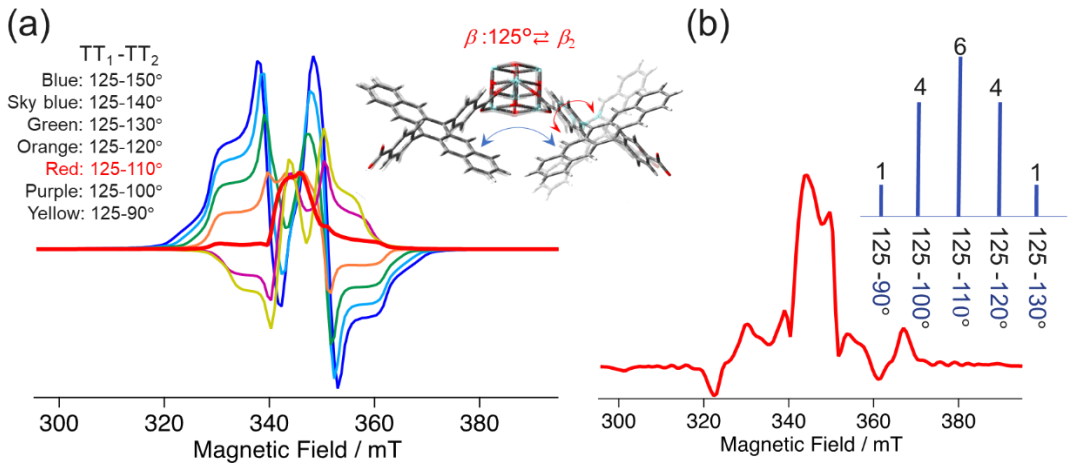

Figure 4-21. (a) Simulation of quintet state in time-resolved EPR spectra at 0.1 μs computed by several TT_2 conformations. (b) Averaged spectrum considering the distribution in the TT_2 conformations.

Table 4-4. Parameters for computations of the delay time dependence of the EPR spectra in paraffin in Figure 4-22b, considering the conformation motions between TT_1 and TT_2 states. [24, 35]

		J /MHz	D /MHz [a)]	E /MHz [a)]	D_{SS} / MHz	Euler angles [b)] / degrees (α, β, γ)	Polar angles [c)]/ degrees	$\bar{\nu}_{vib}$/ cm^{-1}	ΔE_{12} / cm^{-1} [d)]	k_{Diss} [e)]/ s^{-1} / k_{Back} [e)]/ s^{-1}	k_{Rec} [e)]/ s^{-1}
300 K	TT_1	-1.7×10^5	1,200	-20	-45	α = 90 β = 125 γ = -30	θ_2 =40 φ_2 =160	1.9	30	3.0×10^6	5.6×10^7
	TT_2	-2.2×10^4	1,140	-20	-45	α = 90 β = 110 γ = 40	θ_2 =40 φ_2 =160				-
	T+T	28	1,200	-20	-45	α = 0 β = 125 γ = 0	θ_2 =101 φ_2 =210	-	-	1.1×10^6	-

Computation of the time development of the transverse magnetization was also performed using the above conformation motion (Figure 4-22b) and added to the data in Figure 4-16a to obtain the data (red lines) shown in Figure 4-22c. The better fit with the experimental results strongly supports that the highly heterogeneous conformation motions dominate the multiexciton dynamics. The time development of spin polarization coincides with the nanosecond-TAS data, demonstrating that the ^{5}TT should be formed by the large and disorder conformational motions depicted in Figure 4-16b. The reliability of the present numerical model analysis was confirmed by reproducing the EPR patterns of previous rigid tetracene dimers (Figure 4-23).[15] Interestingly, the EPR pattern of Pn-MOF could not be reproduced well without taking motility into account, confirming that the pentacene moieties in the Pn-MOF has rotational dynamics.

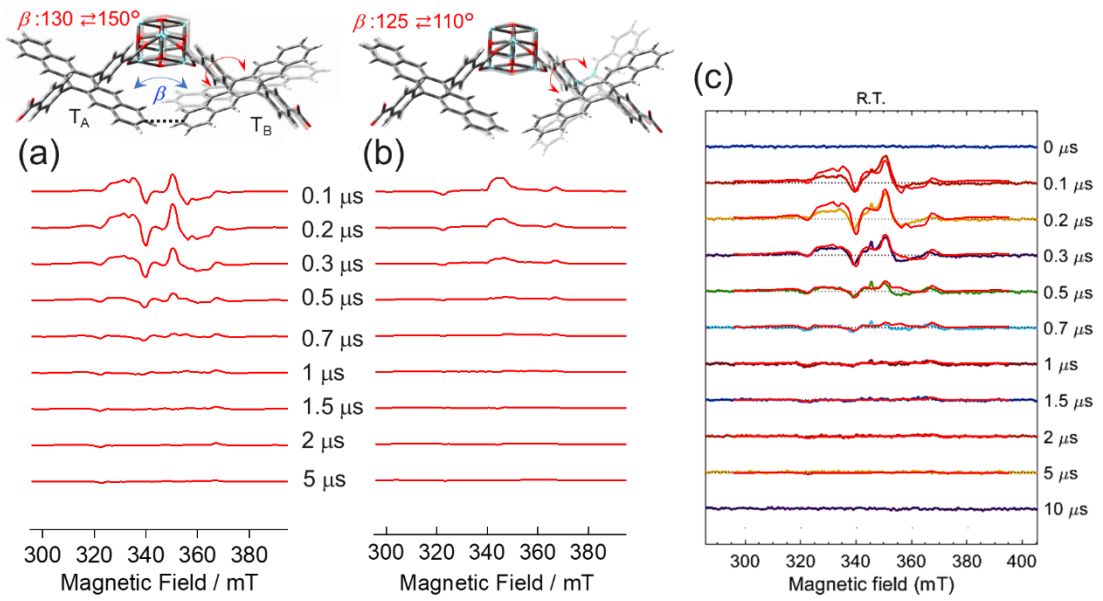

Figure 4-22. (a) Computed time evolution of the transverse magnetization spectrum using the conformation model between β = 130 degrees and 150 degrees. (b) Computed time evolution of the transverse magnetization spectrum with using the motion between β = 125 degrees and 110 degrees. (c) Comparison of experimental spectra in Figure 4-16 and computed spectra obtained by adding the data (b) to (a). Note that the time dependence of the transient EPR spectrum in Figure 4-22b is obtained using the same kinetic parameters of $k_{Diss} = 3.0\times10^{6}$ (s^{-1}), $k_{Back} = 1.1\times10^{6}$ (s^{-1}) and $k_{Rec} = 5.6\times10^{7}$ (s^{-1}) as used for Figure 4-22a (Table 4-3, 300 K), denoting that the nanosecond-TAS decay in Figure 4-16c is unaffected by incorporating the different conformation dynamics.

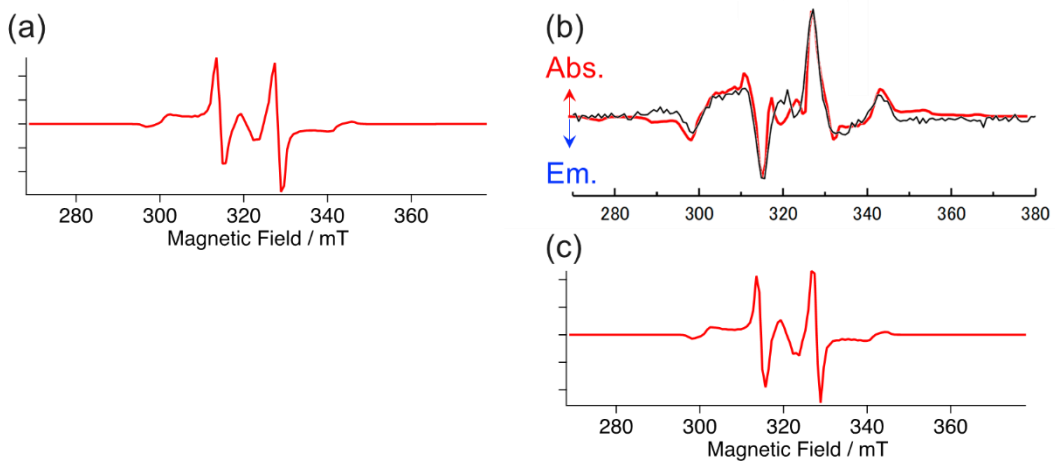

Figure 4-23. (a) Computed spin polarized EPR spectrum of the quintet TT state of the tetracene dimer (TIPS-BP1') conformationally defined by the rigid linkage in Ref. 15. The calculation is performed using the sublevel populations obtained at 0.2 μs in the TT_1 state considering the *J*-modulation between J_1 = 1.4×10^6 MHz and J_2 = -5.6×10^4 MHz with a common T_AT_B conformation defined by (α, β, γ) = (0°, 111°, 0°) and (θ_2, φ_2) = (70°, -90°) in the TT_1 and TT_2 states with D =1322 MHz and D_{SS} = -55 MHz. These angle parameters are characterized as the T_B conformations with respect to the principal axis system of the T_A in the T_AT_B multiexciton and are consistent with the reported dimer geometry. This spin-polarized EPR spectrum demonstrates validity and compatibility of the present numerical model with the reported theory in Ref. 15. (b) Same as Figure 4-20 observed at 150 K in the present MOF sample. (c) Computed spin polarized EPR spectrum of the quintet TT state for the pentacene dimer obtained with D = 1265 MHz and D_{SS} = -55 MHz. The other parameters are identical with those for (a). The better fit is obtained based upon the structure in Figure 4-16b as an average dihedral angle (140°) between β = 164° and 113° in Table 4-3.

As a result, the time evolution of the EPR spectra were successfully reproduced by the model of Figure 4-17 in which the hopping-dissociation (k_{DISS}) and re-encounter (k_{Back}) to form the quintet ^{5}TT, triplet $^3(T_1S_0)$, and singlet ^{1}TT via triplet-triplet annihilation of $^3(T+T)_0$ are considered together with the *J*-modulation between TT_1 and TT_2 to generate the anisotropy in the quintet sublevel populations (Figure 4-16a, red lines). This analysis was also applied to understand the time development of the transient absorption signals in paraffin for $t \geq 1$ ns in the absence of the magnetic field. Notably, the profiles (solid lines in Figure 4-16c) of the sum of the triplet excitons ($^5TT_1 + {}^5TT_2 + {}^3T_1S_0 + {}^1TT_1 + {}^1TT_2$ + SCTP (T+T) + non-correlated T+T) are consistent with the deactivation kinetics of the spin-polarized exciton pairs with ^{5}TT and (T+T) in Figure 4-16a. Quick nanoseconds decays in Figure 4-16c are originating from the singlet deactivation process ($k_{Rec} = 5.6\times10^7$ s^{-1} at room temperature) of ^{1}TT that is in equilibrium with ^{5}TT and (T+T). The longer-lived transient absorption profile at 150 K than at 300 K is due to slower singlet deactivation ($k_{Rec} = 2.0\times10^7$ s^{-1}).

It is possible to reproduce the nanosecond-TAS decay profile even in a scenario that does not include the *J*-modulation, where first (T+T) is generated by triplet diffusion and then ^{5}TT is generated by re-encounter (Figure 4-24). However, in this scenario, the ^{5}TT should still be hardly generated at 100 ns after photoexcitation, which contradicts the actual result that the EPR spectrum at 100 ns showed a strong ^{5}TT-derived signal (Figure 4-16a). This confirms that *J*-modulation plays a major role in the generation of ^{5}TT.

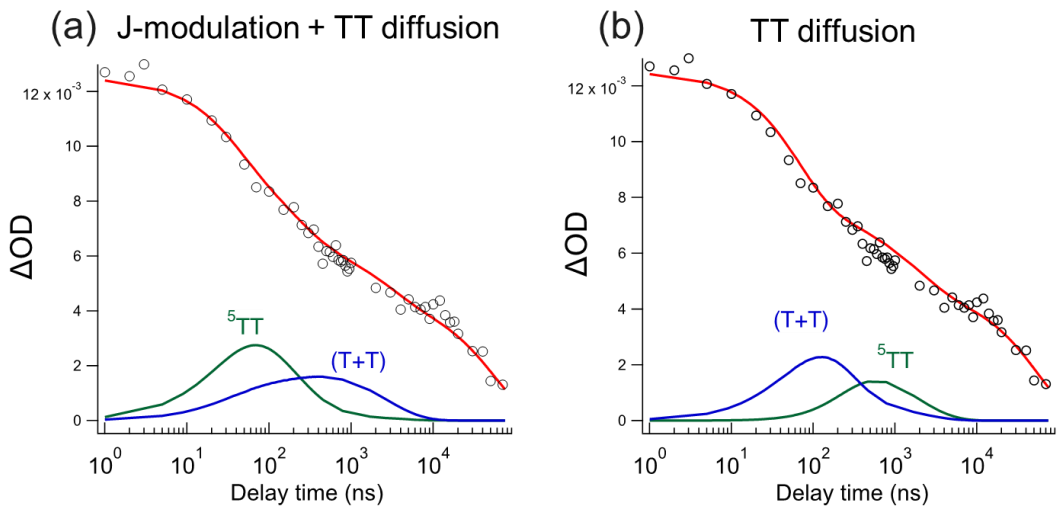

Figure 4-24. Computed nanosecond-TAS decay profiles using two different models at room temperature. In (a), the red profile (Figure 4-16c) is obtained with considering the *J*-modulation between J_1 = -1.4×10^5 MHz and J_2 = -1.9×10^4 MHz in TT_1 and TT_2, respectively in Table 4-3. In (b), $J_1 = J_2 =$ -1.4×10^5 MHz is set assuming that the *J* is frozen in the strongly coupled state. In this model (TT diffusion model), the TA decay profile is reproduced with k_{DISS} = 4.0×10^6 s^{-1}, k_{Back} = 4.0×10^6 s^{-1}, and k_{Rec} = 2.4×10^7 s^{-1}. The green and blue profiles are contributions of the strongly coupled ^{5}TT and the SCTP (T+T). In model (a), the quick ^{5}TT rise within 100 ns is consistent with the observation of the AAEAEE polarized quintet multiexciton at 100 ns in Figure 4-16a. In model (b), however, the contribution of the quintet state is minor at 100 ns and thus is inconsistent with the AAEAEE polarization at 100 ns.

4-3-4. Room-temperature quantum coherence of quintet state

To directly control the four spin qubits of the quintet multiexciton at room temperature, transient nutation microwave pulse sequence was applied using an X-band pulsed EPR spectroscopy (Figure 4-25a and 4-25b). Although the quintet states are significantly minor at the later delay time exceeding 1 μs in Figure 4-16a and 4-16c because of the quick deactivation in the strongly coupled TT pair to the ground state, interestingly, the echo detected EPR spectrum of the quintet is observed even at τ_{delay} = 1.1 μs (Figure 4-25c). This suggests that some of the strongly coupled TT states survive while other dominant TT states undergo quick deactivation and dissociation by hot exciton characters with relatively large angular molecular rotation shown in Figure 4-16b. Such hot multiexcitons should also be subject to significant transverse spin relaxation and not contribute to the echo signal.

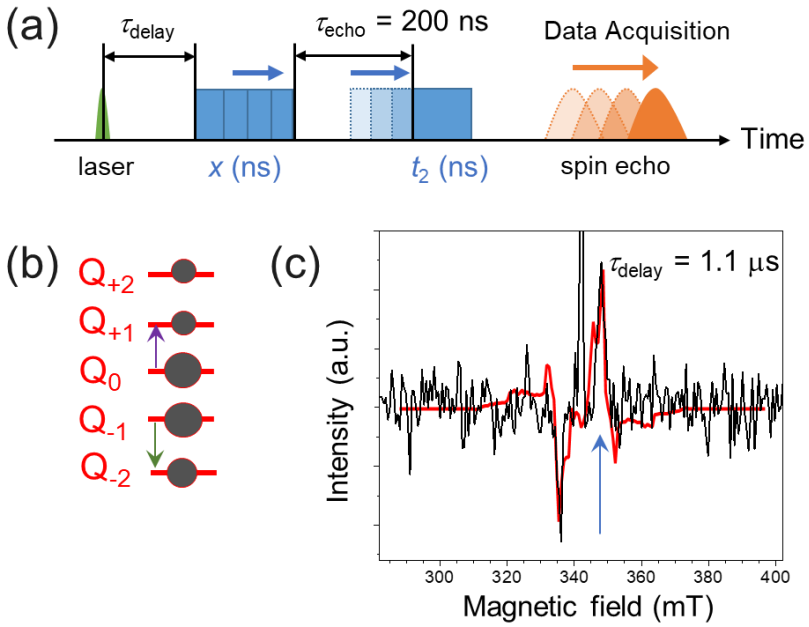

Figure 4-25. (a) Pulse sequence of the transient nutation measurement. (b) Two main quantum gates detected by the pulsed microwave at B_0 = 348.1 mT in the quintet sublevels. (c) Echo detected EPR spectrum at τ_{delay} = 1.1 μs. The durations of the first and second pulses are x = 8 ns and t_2 = 16 ns, respectively. Fitting result using parameters listed in Table 4-5 is shown as a red line.

At the field strength of B_0 = 348.1 mT (blue arrow in Figure 4-25c), the microwave-induced spin coherence of the quintet was appeared as shown in Figure 4-26a. This profile is successively explained by the superpositions of the nutation frequencies (ω_{m_S}) contributed by the quintet quantum gates of $\Delta m_s = \pm 1$ in Figure 4-25b (Figure 4-17a) described by the following equation,

$$\omega_{m_S} = \frac{g\mu_B B_1}{\hbar}\sqrt{S(S+1) - m_S(m_S \pm 1)} \tag{4.23}$$

where m_s (= 0, ±1, and ±2) represent the quintet sublevel quantum numbers causing the transitions of $\Delta m_s = \pm 1$ with $S = 2$ in Figure 4-17a (detailed analysis method is described in Table 4-5). A decoherence time constant of T_{2D} = 150 ns is employed. This is consistent with the transverse relaxation time of T_2 = 122 ns in Figure 4-27d. B_1 is the microwave field strength in equation (4.23) and is set to be B_1 = 0.45 mT. The nutation frequency varies with the quantum gate: $\omega_{m_S} = \sqrt{6}g\mu_B B_1/\hbar$ for the gates (Q_0, $Q_{\pm1}$) between Q_0 and $Q_{\pm1}$ and $\omega_{m_S} = 2g\mu_B B_1/\hbar$ for the gates ($Q_{\pm2}$, $Q_{\pm1}$) between $Q_{\pm2}$ and $Q_{\pm1}$. Therefore, anisotropic quintet sublevel distribution by the S-Q_{mS} interconversion in Figure 4-17a highly influences the frequencies and amplitudes of the quantum beats induced by the coherent microwave pulses at a field strength of B_0. The quantum beat profile is well reproduced by the dynamic model of the quintet populations considering subtle conformational motion between the dihedral angles of β = 130° and 122° in the T_AT_B exciton pair for TT_1 and TT_2, respectively. In the simulated profile (red lines in Figure 4-26a) a minor lower frequency component (green line in Figure 4-26a) is included by the gates between $Q_{\pm2}$ and $Q_{\pm1}$, denoting that the two different nutation frequencies of 25 and 31 MHz are involved with opposite polarizations (Figure 4-25b) in the experimental profile.

To explicitly understand the spin coherences, the echo intensity at 348.1 mT was plotted as a function of the delay time (τ_{delay}) (Figure 4-26d). The decay time (1.2 μs) of the echo signal of the quintet is much longer than the decay time (0.2 μs) of the quintet signals (blue line in Figure 4-26d) detected by the CW-TREPR and is well fitted by the rotation model calculations (red lines in Figure 4-26a and 4-26d) using $k_{Rec} = 1.5\times10^6$ s^{-1} at room temperature (Table 4-5), implying the species observed in pulsed EPR was different from that in CW-TREPR.

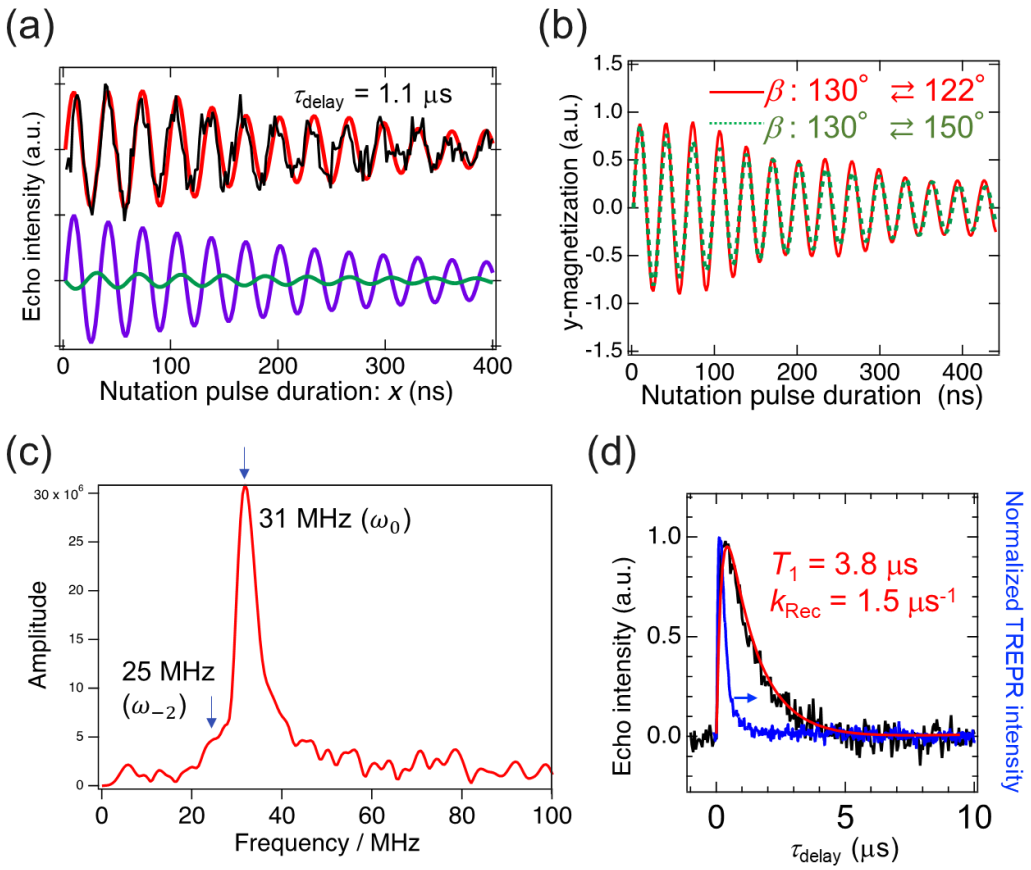

Figure 4-26. (a) Transient nutation profiles as a function of x in Figure 4-25a at τ_{delay} = 1.1 μs using t_2 = 16 ns. The simulated profile is shown by a red line considering the anisotropic sublevel populations. At the bottom, decomposition of the computed nutation data by the gates $Q_{0,\pm1}$ and $Q_{\pm2,\pm1}$ are shown by purple and green lines, respectively. (b) Simulated profiles by the different rotation models. The red solid line corresponding to the red line in (a) is computed by the conformation motion between the dihedral angles of β = 130 degrees and 122 degrees of the T_B molecule in the T_AT_B pair for TT_1 and TT_2, respectively. Green dotted line is obtained with considering the large dihedral angle change between β = 130 degrees and 150 degrees in Figure 4-16b. (c) Fourier transform of the nutation data in (a), (d) Dependence of τ_{delay} on the echo intensity (black line) employing x = 8 ns, t_2 = 16 ns and τ_{echo} = 200 ns with B_1 = 0.45 mT together with delay time dependence of the CW-TREPR intensity at 351 mT in Figure 4-16a (blue line). Fitting result using equation (4.23) and Table 4-5 is shown as a red line.

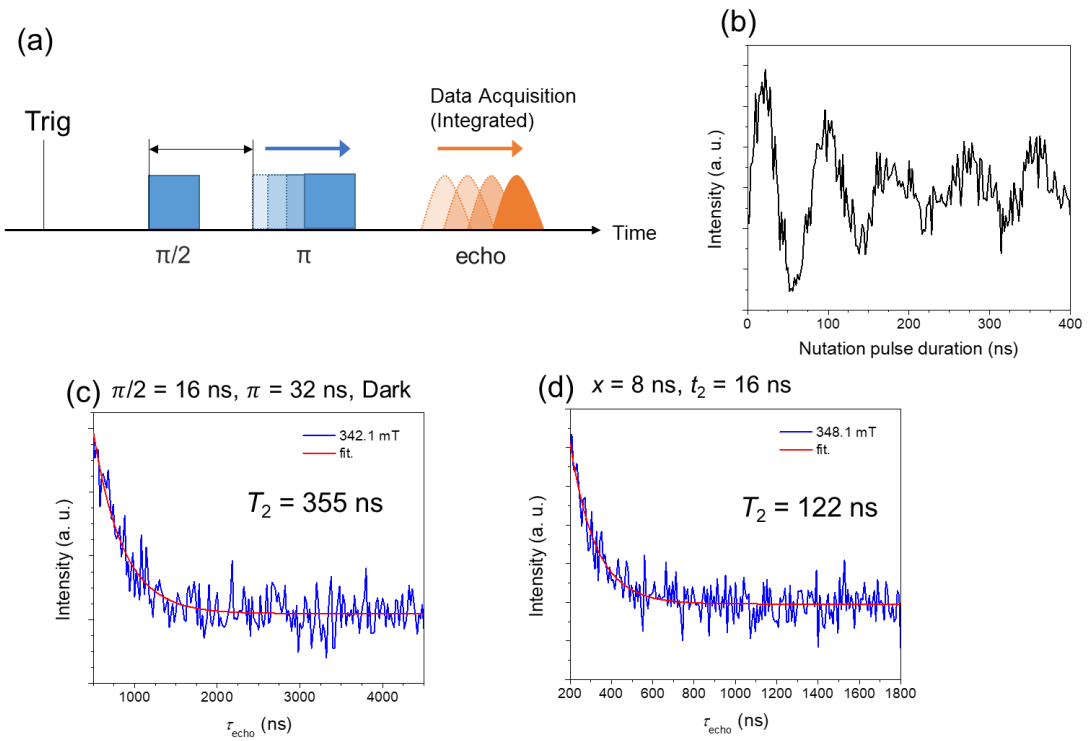

Figure 4-27. (a) Pulse sequence of the spin echo detection (τ_{delay}–π/2–τ_{echo}–π–τ_{echo}–echo) for isolated radical signal at B_0 = 342.10 mT in the dark performed after the CWTREPR experiments. (b) The nutation profile of the radical species obtained by B_1 = 0.45 mT at 342.10 mT with π = 32 ns in the absence of the laser irradiation. The nutation frequency (= 12 MHz) exhibits characteristic of the doublet frequency of $g\mu_B B_1/\hbar$ by S = 1/2 in equation (4.23). (c) The transverse relaxation time of T_2 = 355 ns was obtained by plotting the echo signal with varying τ_{echo} in the radical species in the dark. (d) For the quintet triplet-pairs, T_2 = 122 ns was obtained by plotting the echo signal with varying τ_{echo} at B_0 = 348.10 mT (blue arrow in Figure 4-25c) with x = 8 ns and t_2 = 16 ns at τ_{echo} = 1.1 μs in Figure 4-25a.

Table 4-5. Parameters for computations of the transient nutation and delay time dependence of echo signal at B_0 = 348.1 mT at 300 K (τ_{delay} = 1.1 μs), considering the conformation motions between TT_1 and TT_2 states for computations of the sublevel populations ($\rho^{TT1}_{m_S m_S}$and $\rho^{TT2}_{m_S m_S}$) and the sublevel energies ($E^{TT1}_{Q m_S}$ and $E^{TT2}_{Q m_S}$) in equation (4.3) by the multiexciton motions with the frequency of $\bar{\nu}_{vib}$ in the model of Figure 4-25c. [24, 35]

		J /MHz	D /MHz	E /MHz	D_{SS} / MHz	Euler angles / degrees (α, β, γ)	Polar angles/ degrees	$\bar{\nu}_{vib}$/ cm^{-1}	ΔE_{12} / cm^{-1}	k_{Diss} / s^{-1} a) k_{Back} / s^{-1} a)	k_{Rec} / s^{-1}
300 K	TT_1	-1.7×10^5	1,225	-25	-105	α = 90 β = 130 γ = -20	θ_2 =70 ϕ_2 =160	22	20	$< 10^3$	1.5×10^6
	TT_2	-2.2×10^4	1,164	-25	-105	α = 90 β = 122 γ =-30	θ_2 =70 ϕ_2 =160				-
	T+T a)	-	-	-	-	–	–	-	-	$< 10^3$	-

a) T+T dissociation is not considered ($k_{Diss} < 10^3\ s^{-1}$) in the trap multiexciton.

4-3-5. Origin of coherent quintet

The ^{5}TT-derived signal observed in CW-TREPR was reproduced by a large dihedral motion between β = 130 and 150 degrees, but such a large conformational change would cause a large fluctuation of the zero-field splitting interaction (D), leading to a severe quantum decoherence (Figure 4-28). In fact, the pulse EPR nutation profile could not be reproduced by dihedral motion between β = 130 and 150 degrees but could be reproduced by the subtle conformational motion of 22 cm^{-1} between the dihedral angles of β = 130 and 122 degrees (Figure 4-26b). This suggests that large and small conformational motions coexist in the Pn-MOF as major and minor components, respectively. Since the crystallinity of the Pn-MOF was not good, majority of the MOF structure (source of CW-TREPR signal) should be disordered, resulting in large conformational changes, while the conformational change was suppressed in some minor domains with high crystallinity (source of pulse EPR echo signal). The chromophores in such disordered region should cause the larger dihedral motion and the quicker dephasing in the quintet coherence, and thus do not contribute to the spin echo signal. It is anticipated, however, that the ordered 22 cm^{-1} collective motions occur at the ordered domains most probably in the crystalline region of the MOF with preventions of the conformation motions. These minor TT pairs are possibly responsible for the weak echo signals.

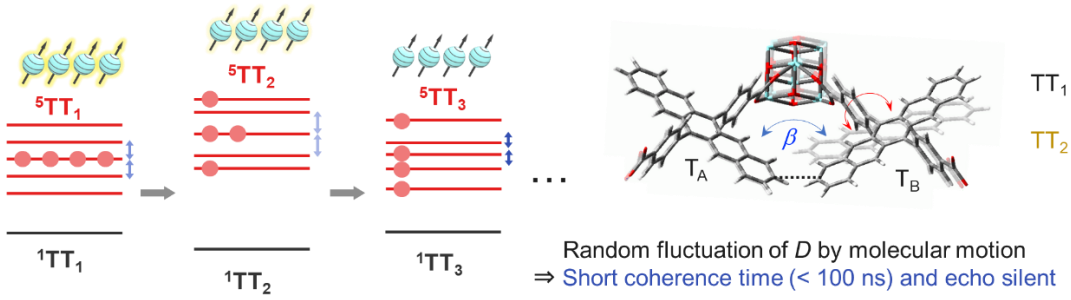

Figure 4-28. Schematic representations of time course of the singlet and quintet TT at the disordered domain in the MOF after the singlet-fission. Because the dipolar interaction (D) in the ^{5}TT is time-dependent, the resonance magnetic field within the quintet sublevel is modulated, causing the spin relaxation and the major echo-silent EPR signal were observed. This is highly distinguished from the species responsible for the echo generated at the minor ordered domain in the MOF sample.

To corroborate this mode of motion, terahertz spectroscopy of Pn-MOF was carried out (Figure 4-29). Although the frequency of the large conformational change (14 cm^{-1}) was outside the measurement range, sharp Lorentzian lines were observed at around 25 cm^{-1} near the simulated frequency of the small conformational change (22 cm^{-1}). Similar low-frequency motion modes have been observed in other MOFs in systems with restricted ligand mobility,[44] supporting the idea that suppressive collective molecular motion is occurring in the Pn-MOF. The sharp terahertz signals indicate that the ordered collective modes (> 22 cm^{-1}) originate from the motion of the entire framework via the metal-ligand coordination bonds. Although the detailed assignment of the collective mode is out of the scope of the current work, these phonon modes might couple with the local molecular rotations of the chromophores.

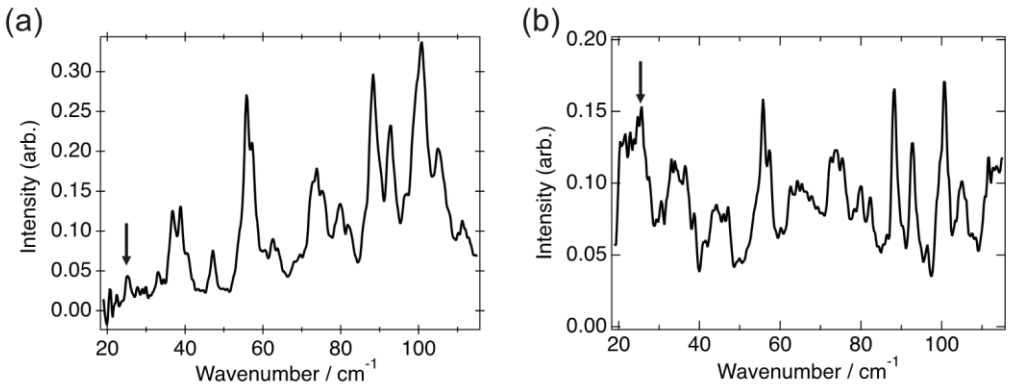

Figure 4-29. THz spectra of Pn-MOF. The spectra were measured using the THz-TDS spectrometer in a transmission set up (a) in the air and (b) in paraffin at room temperature. MOF in paraffin was measured in a polyethylene (PE) cell and the PE cell was not used for (a). The arrows around 25 cm^{-1} correspond to the frequency of the motion for the quintet generation in Figure 4-26. There are several different motions in the solid sample other than 25 cm^{-1}. However, it is in principle important to note from the Redfield theory[45] that the singlet-quintet population mixing is effectively caused when the energy gap by the *J*-coupling is close to the motion frequency in the solid. In addition, TT_2 state needs to be thermally accessible for the spin conversion.

For the singlet-quintet conversion in the strongly coupled TT with the negative exchange coupling, it is essential that the frequency of the *J*-modulation is closer to the frequency relevant to the quintet-singlet energy gap based upon the Redfield theory, as reported previously.[24, 43] In addition, the quintet-singlet energy gap is required to be thermally accessible to get the quintet populations. In the present analysis, quintet-triplet energy gap is set to be ~1 THz corresponding to the -6*J* value (30 cm^{-1}) that is close to the reported values.[46-47] In this case, the higher frequency vibrations (> 50 cm^{-1}) in the THz spectrum should not contribute to minor quintet production because these frequencies are much higher than -6*J*. The broad and congested spectral component around 20-30 cm^{-1} should be responsible for the disordered motions causing the major echo-silent quintet EPR. Therefore, it is reasonable to hypothesize that the low-frequency Debye peak should contribute to the echo-silent quintet due to the disordered, non-state specific vibronic coupling, while the ordered motion characterized by the Lorentzian peak at 25 cm^{-1} should contribute to the minor long-lasting echo due to the ordered molecular motions with the suppressive conformation dynamics.

Specifically, the limited dihedral angle fluctuation in β is revealed to result in superposition of the transverse magnetization by the gates of $Q_{0,1}$ (purple in Figure 4-25b and 4-26a) and $Q_{-2,-1}$ (green in Figure 4-25b and 4-26a) at B_0 = 348.1 mT from Figure 4-30a, while the magnetization by the $Q_{\pm1,\pm2}$ gates are minor for the larger angle-fluctuation case in Figure 4-30b. The hindered rotation thus leads to detections of the high and low frequency nutation components determined by $\omega_0 = \sqrt{6}g\mu_B B_1/\hbar$ and $\omega_{-2} = 2g\mu_B B_1/\hbar$. This is also consistent with the echo-detected EPR spectrum (red line in Figure 4-25c) obtained using this rotation model. These results imply that the quantum beating behavior can be altered by the degree of the structural fluctuation.

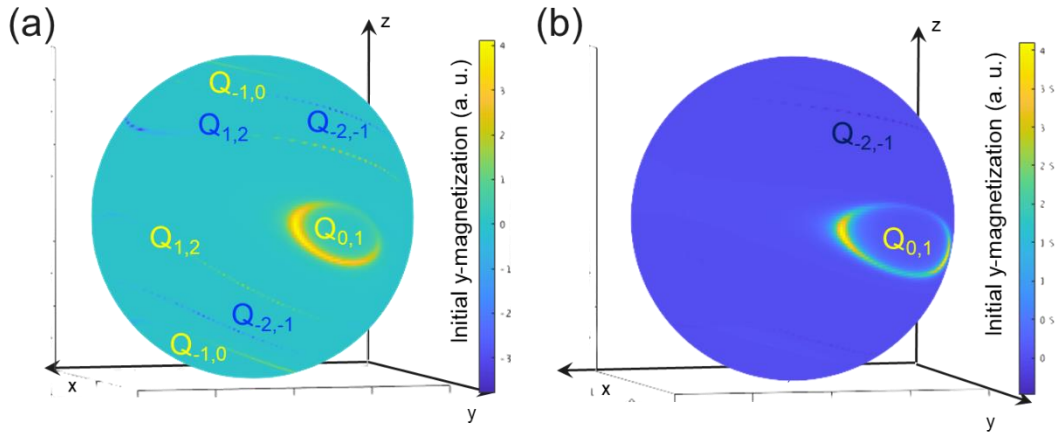

Figure 4-30. Angle selectivity of y-magnetization response for the field directions (B_0 = 348.1 mT) created by the first microwave pulse in the quantum gates obtained from a powder-pattern calculation of the transient nutation profiles of the red solid and green dotted lines in Figure 4-26b for (a) and (b), respectively. The positive magnetization represented by Qm_s,m_{s+1} denotes overpopulation in the sublevel of m_s at the resonance transition between Qm_s and Qm_{s+1} with m_s = -2, -1, 0 and 1. These maps are obtained by plotting transverse magnetization responses (eqation 4.16) by the short first microwave pulse for the four different quantum gates to the magnetic field directions with respect to the molecular frame (x, y, z) of the principal axes of the zero-field splitting interaction of the T_A molecule. In (a), the positive (yellowish) and negative (dark blue) magnetization regions by the $Q_{0,1}$ gates (around the center of the sphere) and by the $Q_{-1,0}$ gates (around the sphere poles) are obtained for the common nutation frequency of 31 MHz. Summation of these four components will result in the superposition of the amplitudes from the high and low frequency components in Figure 4-26a, when the small degree of the molecular rotation is considered. In (b), the amplitude by the $Q_{0,\pm1}$ gates will be minor in the dashed green line of Figure 4-26b when the larger degree of motion is considered (Figure 4-16b).

4-4. Conclusion

In this chapter, the room-temperature quantum coherence of quintet multiexcitons was demonstrated by dense integration of chromophores in porous MOF. For quintets generated by SF, it has been unclear what kind of molecular motion is required to achieve both (i) effective quintet generation and (ii) noise suppressed qubits. This work reveals that low-mobility triplet pairs with small orientation angle changes prevent exciton hopping and recombination. In addition, and importantly, the suppression of transverse relaxation due to fluctuations in the zero-field splitting interaction makes it possible to slow down decoherence and function as qubits even at room temperature. The control of multiple quantum gates is also extremely important for future developments in molecular quantum computing with multiple qubits, such as verification of CNOT gates.

It is significant that not only the generation of quantum coherence by microwave irradiation has been demonstrated at room temperature by simulating chromophore motion in a MOF, but also the details of molecular motion (change in molecular orientation) that enable the realization of room-temperature qubits have been discovered. Precise control of the assembly structure and motion of the chromophores in MOFs is expected to lead to the development of innovative materials useful for the molecular-based QIS.

4-5. References

(1) Ladd, T. D.; Jelezko, F.; Laflamme, R.; Nakamura, Y.; Monroe, C.; O'Brien, J. L. Quantum computers. *Nature* **2010,** *464*, 45-53.

(2) Arute, F.; Arya, K.; Babbush, R.; Bacon, D.; Bardin, J. C.; Barends, R.; Biswas, R.; Boixo, S.; Brandao, F.; Buell, D. A.; Burkett, B.; Chen, Y.; Chen, Z.; Chiaro, B.; Collins, R.; Courtney, W.; Dunsworth, A.; Farhi, E.; Foxen, B.; Fowler, A.; Gidney, C.; Giustina, M.; Graff, R.; Guerin, K.; Habegger, S.; Harrigan, M. P.; Hartmann, M. J.; Ho, A.; Hoffmann, M.; Huang, T.; Humble, T. S.; Isakov, S. V.; Jeffrey, E.; Jiang, Z.; Kafri, D.; Kechedzhi, K.; Kelly, J.; Klimov, P. V.; Knysh, S.; Korotkov, A.; Kostritsa, F.; Landhuis, D.; Lindmark, M.; Lucero, E.; Lyakh, D.; Mandra, S.; McClean, J. R.; McEwen, M.; Megrant, A.; Mi, X.; Michielsen, K.; Mohseni, M.; Mutus, J.; Naaman, O.; Neeley, M.; Neill, C.; Niu, M. Y.; Ostby, E.; Petukhov, A.; Platt, J. C.; Quintana, C.; Rieffel, E. G.; Roushan, P.; Rubin, N. C.; Sank, D.; Satzinger, K. J.; Smelyanskiy, V.; Sung, K. J.; Trevithick, M. D.; Vainsencher, A.; Villalonga, B.; White, T.; Yao, Z. J.; Yeh, P.; Zalcman, A.; Neven, H.; Martinis, J. M. Quantum supremacy using a programmable superconducting processor. *Nature* **2019,** *574*, 505-510.

(3) Muralidharan, S.; Li, L.; Kim, J.; Lutkenhaus, N.; Lukin, M. D.; Jiang, L. Optimal architectures for long distance quantum communication. *Sci. Rep.* **2016,** *6*, 20463.

(4) Bhaskar, M. K.; Riedinger, R.; Machielse, B.; Levonian, D. S.; Nguyen, C. T.; Knall, E. N.; Park, H.; Englund, D.; Loncar, M.; Sukachev, D. D.; Lukin, M. D. Experimental demonstration of memory-enhanced quantum communication. *Nature* **2020,** *580*, 60-64.

(5) Maze, J. R.; Stanwix, P. L.; Hodges, J. S.; Hong, S.; Taylor, J. M.; Cappellaro, P.; Jiang, L.; Dutt, M. V.; Togan, E.; Zibrov, A. S.; Yacoby, A.; Walsworth, R. L.; Lukin, M. D. Nanoscale magnetic sensing with an individual electronic spin in diamond. *Nature* **2008,** *455*, 644-647.

(6) Degen, C. L.; Reinhard, F.; Cappellaro, P. Quantum sensing. *Rev. Mod. Phys.* **2017,** *89*, 035002.

(7) Guo, X.; Breum, C. R.; Borregaard, J.; Izumi, S.; Larsen, M. V.; Gehring, T.; Christandl, M.; Neergaard-Nielsen, J. S.; Andersen, U. L. Distributed quantum sensing in a continuous-variable entangled network. *Nat. Phys.* **2019,** *16*, 281-284.

(8) Zadrozny, J. M.; Gallagher, A. T.; Harris, T. D.; Freedman, D. E. A Porous Array of Clock Qubits. *J. Am. Chem. Soc.* **2017,** *139*, 7089-7094.

(9) Wasielewski, M. R.; Forbes, M. D. E.; Frank, N. L.; Kowalski, K.; Scholes, G. D.; Yuen-Zhou, J.; Baldo, M. A.; Freedman, D. E.; Goldsmith, R. H.; Goodson, T.; Kirk, M. L.; McCusker, J. K.; Ogilvie, J. P.; Shultz, D. A.; Stoll, S.; Whaley, K. B. Exploiting chemistry and molecular systems for quantum information science. *Nat. Rev. Chem.* **2020,** *4*, 490-504.

(10) von Kugelgen, S.; Krzyaniak, M. D.; Gu, M.; Puggioni, D.; Rondinelli, J. M.; Wasielewski, M. R.; Freedman, D. E. Spectral Addressability in a Modular Two Qubit System. *J. Am. Chem. Soc.* **2021,** *143*, 8069-8077.

(11) Maylander, M.; Thielert, P.; Quintes, T.; Vargas Jentzsch, A.; Richert, S. Room Temperature Electron Spin Coherence in Photogenerated Molecular Spin Qubit Candidates. *J. Am. Chem. Soc.* **2023,** *145*, 14064-14069.

(12) Qiu, Y.; Equbal, A.; Lin, C.; Huang, Y.; Brown, P. J.; Young, R. M.; Krzyaniak, M. D.; Wasielewski, M. R.

Optical Spin Polarization of a Narrow-Linewidth Electron-Spin Qubit in a Chromophore/Stable-Radical System. *Angew. Chem. Int. Ed. Engl.* **2023,** *62*, e202214668.

(13) Smyser, K. E.; Eaves, J. D. Singlet fission for quantum information and quantum computing: the parallel JDE model. *Sci. Rep.* **2020,** *10*, 18480.

(14) Jacobberger, R. M.; Qiu, Y.; Williams, M. L.; Krzyaniak, M. D.; Wasielewski, M. R. Using Molecular Design to Enhance the Coherence Time of Quintet Multiexcitons Generated by Singlet Fission in Single Crystals. *J. Am. Chem. Soc.* **2022,** *144*, 2276-2283.

(15) Dill, R. D.; Smyser, K. E.; Rugg, B. K.; Damrauer, N. H.; Eaves, J. D. Entangled spin-polarized excitons from singlet fission in a rigid dimer. *Nat. Commun.* **2023,** *14*, 1180.

(16) Yamauchi, A.; Tanaka, K.; Fuki, M.; Fujiwara, S.; Kimizuka, N.; Ryu, T.; Saigo, M.; Onda, K.; Kusumoto, R.; Ueno, N.; Sato, H.; Kobori, Y.; Miyata, K.; Yanai, N. Room-temperature quantum coherence of entangled multiexcitons in a metal-organic framework. *Sci. Adv.* **2024,** *10*, eadi3147.

(17) Mao, H.; Pazera, G. J.; Young, R. M.; Krzyaniak, M. D.; Wasielewski, M. R. Quantum Gate Operations on a Spectrally Addressable Photogenerated Molecular Electron Spin-Qubit Pair. *J. Am. Chem. Soc.* **2023,** *145*, 6585-6593.

(18) Smith, M. B.; Michl, J. Singlet Fission. *Chem. Rev.* **2010,** *110*, 6891−6936.

(19) Einzinger, M.; Wu, T.; Kompalla, J. F.; Smith, H. L.; Perkinson, C. F.; Nienhaus, L.; Wieghold, S.; Congreve, D. N.; Kahn, A.; Bawendi, M. G.; Baldo, M. A. Sensitization of silicon by singlet exciton fission in tetracene. *Nature* **2019,** *571*, 90-94.

(20) Miyata, K.; Conrad-Burton, F. S.; Geyer, F. L.; Zhu, X. Y. Triplet Pair States in Singlet Fission. *Chem. Rev.* **2019,** *119*, 4261-4292.

(21) Bossanyi, D. G.; Sasaki, Y.; Wang, S.; Chekulaev, D.; Kimizuka, N.; Yanai, N.; Clark, J. Spin Statistics for Triplet-Triplet Annihilation Upconversion: Exchange Coupling, Intermolecular Orientation, and Reverse Intersystem Crossing. *JACS Au* **2021,** *1*, 2188-2201.

(22) Weiss, L. R.; Bayliss, S. L.; Kraffert, F.; Thorley, K. J.; Anthony, J. E.; Bittl, R.; Friend, R. H.; Rao, A.; Greenham, N. C.; Behrends, J. Strongly exchange-coupled triplet pairs in an organic semiconductor. *Nat. Phys.* **2016,** *13*, 176-181.

(23) Collins, M. I.; McCamey, D. R.; Tayebjee, M. J. Y. Fluctuating exchange interactions enable quintet multiexciton formation in singlet fission. *J. Chem. Phys.* **2019,** *151*, 164104.

(24) Kobori, Y.; Fuki, M.; Nakamura, S.; Hasobe, T. Geometries and Terahertz Motions Driving Quintet Multiexcitons and Ultimate Triplet-Triplet Dissociations via the Intramolecular Singlet Fissions. *J. Phys. Chem. B* **2020,** *124*, 9411-9419.

(25) Lubert-Perquel, D.; Salvadori, E.; Dyson, M.; Stavrinou, P. N.; Montis, R.; Nagashima, H.; Kobori, Y.; Heutz, S.; Kay, C. W. M. Identifying triplet pathways in dilute pentacene films. *Nat. Commun.* **2018,** *9*, 4222.

(26) MacDonald, T. S. C.; Collins, M. J. Y. T. M. I.; Kumarasamy, E.; Sfeir, S. N. S. M. Y.; Campos, L. M.; McCamey, D. R. Anisotropic Multiexciton Quintet and Triplet Dynamics in Singlet Fission via Pulsed Electron Spin

Resonance. *J. Am. Chem. Soc.* **2023,** *145*, 15275-15283.

(27) So, M. C.; Wiederrecht, G. P.; Mondloch, J. E.; Hupp, J. T.; Farha, O. K. Metal-organic framework materials for light-harvesting and energy transfer. *Chem. Commun.* **2015,** *51*, 3501-3510.

(28) Joarder, B.; Mallick, A.; Sasaki, Y.; Kinoshita, M.; Haruki, R.; Kawashima, Y.; Yanai, N.; Kimizuka, N. Near-Infrared-to-Visible Photon Upconversion by Introducing an S−T Absorption Sensitizer into a Metal-Organic Framework. *ChemNanoMat* **2020,** *6*, 916-919.

(29) Haldar, R.; Kozlowska, M.; Ganschow, M.; Ghosh, S.; Jakoby, M.; Chen, H.; Ghalami, F.; Xie, W.; Heidrich, S.; Tsutsui, Y.; Freudenberg, J.; Seki, S.; Howard, I. A.; Richards, B. S.; Bunz, U. H. F.; Elstner, M.; Wenzel, W.; Woll, C. Interplay of structural dynamics and electronic effects in an engineered assembly of pentacene in a metal-organic framework. *Chem. Sci.* **2021,** *12*, 4477-4483.

(30) Cavka, J. H.; Jakobsen, S.; Olsbye, U.; Guillou, N.; Lamberti, C.; Bordiga, S.; Lillerud, K. P. A New Zirconium Inorganic Building Brick Forming Metal Organic Frameworks with Exceptional Stability. *J. Am. Chem. Soc.* **2008,** *130*, 13850-13851.

(31) Walker, B. J.; Musser, A. J.; Beljonne, D.; Friend, R. H. Singlet exciton fission in solution. *Nat. Chem.* **2013,** *5*, 1019-1024.

(32) Sanders, S. N.; Kumarasamy, E.; Pun, A. B.; Trinh, M. T.; Choi, B.; Xia, J.; Taffet, E. J.; Low, J. Z.; Miller, J. R.; Roy, X.; Zhu, X. Y.; Steigerwald, M. L.; Sfeir, M. Y.; Campos, L. M. Quantitative Intramolecular Singlet Fission in Bipentacenes. *J. Am. Chem. Soc.* **2015,** *137*, 8965-8972.

(33) Sakai, H.; Inaya, R.; Nagashima, H.; Nakamura, S.; Kobori, Y.; Tkachenko, N. V.; Hasobe, T. Multiexciton Dynamics Depending on Intramolecular Orientations in Pentacene Dimers: Recombination and Dissociation of Correlated Triplet Pairs. *J. Phys. Chem. Lett.* **2018,** *9*, 3354-3360.

(34) Accelrys, Material Studio Release Notes, Release 4.2, Accelrys Software, San Diego. **2006**.

(35) Nakamura, S.; Sakai, H.; Nagashima, H.; Fuki, M.; Onishi, K.; Khan, R.; Kobori, Y.; Tkachenko, N. V.; Hasobe, T. Synergetic Role of Conformational Flexibility and Electronic Coupling for Quantitative Intramolecular Singlet Fission. *J. Phys. Chem. C* **2021,** *125*, 18287-18296.

(36) Gierer, M.; Est, A. v. d.; Stehlik, D. Transient EPR of weakly coupled spin-correlated radical pairs in photosynthetic reaction centres: increase spectral resolution from nutation analysis. *Chem. Phys. Lett.* **1991,** *186*, 238-247.

(37) Fujiwara, S.; Hosoyamada, M.; Tateishi, K.; Uesaka, T.; Ideta, K.; Kimizuka, N.; Yanai, N. Dynamic Nuclear Polarization of Metal-Organic Frameworks Using Photoexcited Triplet Electrons. *J. Am. Chem. Soc.* **2018,** *140*, 15606-15610.

(38) Kawashima, Y.; Hamachi, T.; Yamauchi, A.; Nishimura, K.; Nakashima, Y.; Fujiwara, S.; Kimizuka, N.; Ryu, T.; Tamura, T.; Saigo, M.; Onda, K.; Sato, S.; Kobori, Y.; Tateishi, K.; Uesaka, T.; Watanabe, G.; Miyata, K.; Yanai, N. Singlet fission as a polarized spin generator for dynamic nuclear polarization. *Nat. Commun.* **2023,** *14*, 1056.

(39) Pan, Y. Y.; Huang, J.; Wang, Z. M.; Yu, D. W.; Yang, B.; Ma, Y. G. Computational investigation on the large energy gap between the triplet excited-states in acenes. *RSC Adv.* **2017,** *7*, 26697-26703.

(40) Perego, J.; Bezuidenhout, C. X.; Villa, I.; Cova, F.; Crapanzano, R.; Frank, I.; Pagano, F.; Kratochwill, N.; Auffray, E.; Bracco, S.; Vedda, A.; Dujardin, C.; Sozzani, P. E.; Meinardi, F.; Comotti, A.; Monguzzi, A. Highly luminescent scintillating hetero-ligand MOF nanocrystals with engineered Stokes shift for photonic applications. *Nat. Commun.* **2022,** *13*, 3504.

(41) Ali, M. A.; Ren, J.; Zhao, T.; Liu, X.; Hua, Y.; Yue, Y.; Qiu, J. Broad Mid-Infrared Luminescence in a Metal-Organic Framework Glass. *ACS Omega* **2019,** *4*, 12081-12087.

(42) Musser, A. J.; Liebel, M.; Schnedermann, C.; Wende, T.; Kehoe, T. B.; Rao, A.; Kukura, P. Evidence for conical intersection dynamics mediating ultrafast singlet exciton fission. *Nat. Phys.* **2015,** *11*, 352-357.

(43) Collins, M. I.; Campaioli, F.; Tayebjee, M. J. Y.; Cole, J. H.; McCamey, D. R. Quintet formation, exchange fluctuations, and the role of stochastic resonance in singlet fission. *Commun. Phys.* **2023,** *6*, 64.

(44) Banks, P. A.; Kleist, E. M.; Ruggiero, M. T. Investigating the function and design of molecular materials through terahertz vibrational spectroscopy. *Nat. Rev. Chem.* **2023,** *7*, 480-495.

(45) Matsui, Y.; Kawaoka, S.; Nagashima, H.; Nakagawa, T.; Okamura, N.; Ogaki, T.; Ohta, E.; Akimoto, S.; Sato-Tomita, A.; Yagi, S.; Kobori, Y.; Ikeda, H. Exergonic Intramolecular Singlet Fission of an Adamantane-Linked Tetracene Dyad via Twin Quintet Multiexcitons. *J. Phys. Chem. C* **2019,** *123*, 18813-18823.

(46) Yago, T.; Ishikawa, K.; Katoh, R.; Wakasa, M. Magnetic Field Effects on Triplet Pair Generated by Singlet Fission in an Organic Crystal: Application of Radical Pair Model to Triplet Pair. *J. Phys. Chem. C* **2016,** *120*, 27858-27870.

(47) Bayliss, S. L.; Weiss, L. R.; Mitioglu, A.; Galkowski, K.; Yang, Z.; Yunusova, K.; Surrente, A.; Thorley, K. J.; Behrends, J.; Bittl, R.; Anthony, J. E.; Rao, A.; Friend, R. H.; Plochocka, P.; Christianen, P. C. M.; Greenham, N. C.; Chepelianskii, A. D. Site-selective measurement of coupled spin pairs in an organic semiconductor. *Proc. Natl. Acad. Sci. U.S.A.* **2018,** *115*, 5077-5082.

Chapter 5. Conclusion and future remarks

5-1. Conclusion

Chapter 1 overviewed the basic principles of electron spin-based molecular qubits. The characteristics of molecular qubit systems were described comparing to conventional NV center-based quantum sensor. The important parameters of qubits such as spin polarization and relaxation times were reviewed and the effects of spin interactions to the parameters were also explained. Then recent molecular qubit-based quantum sensing systems and their details were summarized.

In chapter 2, the elongation of the spin relaxation time in the triplet state of zinc porphyrin was achieved while its large spin polarization was kept. The reduction of the spin density on the zinc center by fluorine substitutions weakened the spin–orbit coupling moderately so that the relaxation was suppressed but the spin polarization was unaffected.

Chapter 3 describes a new methodology to recognize analytes inside MOFs from the change of the molecular motions of qubits. The combination of triplet qubits and flexible MOFs was effective for the control of the qubit mobility by the introduction of analyte guests. The change in the mobility was reflected as the alternation of the relaxation times demonstrating the concept of molecular motion-based sensing.

In chapter 4, the first example of room-temperature quantum coherence of 4-spin entangled quintet qubits was demonstrated. While the molecular motions of chromophores are required for generation of the quintet state, the relaxation is caused by the motions same time. This problem was solved by making the qubit motion minimum not to induce the spin relaxation but to mediate the conversion between the singlet and the quintet.

5-2. Future remarks

Although the results mentioned above raise the possibility for quantum sensing of various chemicals at room temperature, there are several challenges towards practical quantum sensing applications. In chapter 3, the guest-responsive behavior of qubits was shown, however, the recognition of guest species that bring similar T_2 like FU and BQ. In addition, the single microwave pulse takes around 200 ns to operate spins. Thus, the T_2 around 1 μs is still inadequate for effective control of spins that enables various sensing protocols including spin echo or ESEEM-based methods. For the operation of quantum entanglement, much longer coherence time is required because the entanglement does not work if any one of the entangled qubits loses the coherence. T_2 of several to ten microseconds is desirable for further applications.

To overcome the first problem of recognizing various targets, the fabrication of a sensor array would be a possible solution. There are hundreds of different olfactory receptors in the human nose, and the activation of the multiple olfactory receptors identifies specific odor molecules. Using this mechanism, identification of specific analyte molecules can be performed by pattern recognition of arrays of different MOF-qubit hybrids (Figure 5-1). While distinguishment of guests is difficult from single MOF-qubit system, an array of multiple MOF-qubit hybrids that show different guest responsivity will realize the recognition of various guest molecules.

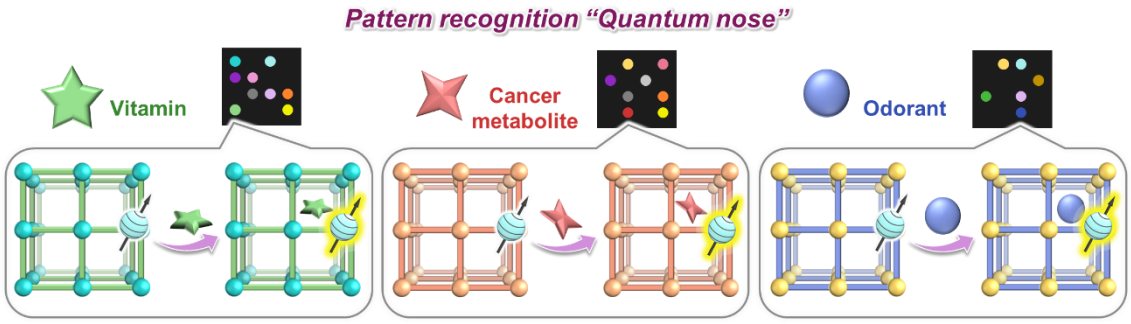

Figure 5-1. Schematic drawing of quantum nose, pattern recognition of specific analyte using qubit-MOF hybrid arrays. By combining the guest-selectivity of MOF and the sensing ability of molecular qubits, and by implementing multiple MOF-qubit hybrids with different guest selectivity or responsivity, quantum sensing of a specific guest is achieved. Reproduced with permission from reference 1. Copyright 2024 American Chemical Society.

Instead of a microwave readout, an optical readout is also preferable for array-based systems from the viewpoint of the spatial resolution to detect the signals of each systems separately. The optical readout of triplets were recently achieved by several groups at room temperature using pentacene-doped *p*-terphenyl systems.[2-3] By applying this technique to MOF-qubit hybrids, higher sensitivity and resolution can be expected.

To elongate T_2 at room temperature, the spin interactions and the fluctuations due to the molecular motions are key factors. Unlike crystal systems, qubits have high freedom of the motions in porous MOF-based systems. Toward longer relaxation time, the freedom should be reduced. For example, pentacene chromophores inside Pn-MOF appeared in chapter 4 are fixed by two carboxylate groups and can rotate around those two points. If the qubits are fixed by multiple points of three or more, they do not rotate, and the fluctuations will be suppressed. When the MOF structure is flexible to the guest, the change in the motion of MOF structure induced by guests can be a detectable for sensing of the guests instead of the qubit motions. In addition to the fluctuation, the spin interactions should be optimized. Qubits with large π conjugation will reduce the dipolar ZFS interaction due to the delocalization of the spins. The spin density on the qubits is also considered, and the nuclear spins on the positions that have high spin density should be replaced by other atoms.

Another way to obtain a long-lived quantum coherence is to convert information of the electron spin to the nuclear spin. Nuclear spins have generally much longer coherence time (~ ms) than electron spins because of their smaller gyromagnetic ratio. The entangled nuclear spin state was created by the spin polarization transfer from the electron spin to the nuclear spins in pentacene.[4] The quantum coherence of nuclear spins can be operated and readout by radio wave as NMR.

Although the quantum sensing using molecular qubits is just beginning and the performance is the same or lower than the conventional sensors, I hope the strategies established in this thesis contribute to the future development of the quantum sensors that exceeds the conventional sensors.

5-3. References

(1) Yamauchi, A.; Yanai, N. Toward Quantum Noses: Quantum Chemosensing Based on Molecular Qubits in Metal-Organic Frameworks. *Acc. Chem. Res.* **2024,** *57*, 2963-2972.

(2) Mena, A.; Mann, S. K.; Cowley-Semple, A.; Bryan, E.; Heutz, S.; McCamey, D. R.; Attwood, M.; Bayliss, S. L. Room-Temperature Optically Detected Coherent Control of Molecular Spins. *Phys. Rev. Lett.* **2024,** *133*, 120801.

(3) Singh, H.; D'Souza, N.; Zhong, K.; Druga, E.; Oshiro, J.; Blankenship, B.; Reimer, J. A.; Breeze, J. D.; Ajoy, A. Room-temperature quantum sensing with photoexcited triplet electrons in organic crystals. *arXiv* **2024**.

(4) Kothe, G.; Lukaschek, M.; Yago, T.; Link, G.; Ivanov, K. L.; Lin, T. S. Initializing 2^{14} Pure 14-Qubit Entangled Nuclear Spin States in a Hyperpolarized Molecular Solid. *J. Phys. Chem. Lett.* **2021,** *12*, 3647-3654.